Search for VHE gamma-ray emission from the globular cluster M13 with VERITAS

Michael Warren McCutcheon*
Department of Physics
McGill University, Montreal

April 11, 2012

A thesis submitted to
McGill University
in partial fulfilment of the requirements
of the degree of
Doctor of Philosophy.

*mccutchm@physics.mcgill.ca

Abstract

Globular clusters, such as M13, are very dense star clusters and are known to contain many more millisecond pulsars per unit mass than the galaxy as a whole. These pulsars are concentrated in the core regions of globulars and are expected to generate relativistic winds of electrons. Such energetic electrons may then interact with the intense field of optical photons, which is supported by the numerous normal stars of the cluster, to generate Very High-Energy (VHE) gamma rays. Herein, this emission model, as implemented by Bednarek & Sitarek [36], is described and justified in more detail and data from observations of M13, undertaken to confront this model, are analysed. No evidence for VHE gamma-ray emission from M13 is found. A decorrelated, integral upper limit of $0.306 \times 10^{-12}\,\mathrm{cm}^{-2}\ \mathrm{s}^{-1}$ above $0.8\,\mathrm{TeV}$, at a confidence level of 95%, is determined. Spectral upper limits are also determined and compared to emission curves presented in [36]. A detailed examination of the parameters of the model is performed and it is found that the predicted curves were based upon over-optimistic estimations of several of these. Nonetheless, the model can be related to existing theories of pulsar winds and, thereby, it is found that the acceleration of electrons in millisecond pulsar winds (outside pulsar light-cylinders) to TeV energies is excluded by these observations, under self-consistent assumptions of the properties of this population of millisecond pulsars.

Resumé

Les amas globulaires, tels que M13, sont des amas d'étoiles très denses et sont connus pour contenir beaucoup plus de pulsars milliseconde par unité de masse que la galaxie dans son ensemble. Ces pulsars sont concentrés dans les régions centrales d'amas globulaires et sont supposés générer des vents relativistes d'électrons. Ces électrons énergétiques peuvent alors interagir avec le champ intense de photons optiques, qui est soutenu par les nombreuses étoiles normales de l'amas, afin de générer des rayons gamma de Très Haute Énergie (THE). Dans la présente thèse, ce modèle d'émission, mis en œuvre par Bednarek & Sitarek [36], est décrit et justifié de manière plus détaillée et des données, recueillies à partir d'observations de M13, ont été analysées dans le but de confronter ce modèle. Aucune preuve d'émission des rayons gamma THE de M13 n'a été trouvée. Une limite supérieure intégrale et décorrélée est déterminée, soit $0.306 \times 10^{-12}\,\mathrm{cm}^{-2}\ \mathrm{s}^{-1}$ en dessus de $0.8\,\mathrm{TeV}$, à un niveau de confiance de 95%. Des limites supérieures spectrales sont également déterminées et comparées aux courbes d'émission présentées dans [36]. L'examen détaillé des paramètres du modèle révèle que les courbes attendues étaient fondées sur des estimations trop optimistes de plusieurs de ces paramètres. Néanmoins, le modèle peut être lié aux théories existantes des vents des pulsars et, ce faisant, à travers ces observations, on trouve que l'accélération des électrons dans les vents des pulsars millisecondes (en dehors des cylindres lumièriques des pulsars) aux énergies TeV est à exclure, selon des hypothèses auto-cohérentes des propriétés de cette population des pulsars millisecondes.

In memory of my mother, Carol.

In honour of my father, Niall.

With love, for Erica.

With hope, for Léah and Adèle.

How must our wonder and admiration be increased when we consider the prodigious distance and multitude of the stars.

— Christian Huygens

The stars that we follow can lead us astray.

— 'The Plough', Neil Hannon

Contents

Disclaimer

To illustrate generic results (such as the performance of the analysis chain) or generic concepts (such as the structure of pulsar wind nebulae) I have, in certain instances, reproduced figures due to other authors. I do not claim copyright on those figures that are explicitly credited to other persons or publications.

Acknowledgements

I offer my most sincere gratitude to my thesis supervisor, Prof. David Hanna, for his support, patience, insight and unwavering critical analysis: any errors remaining in this thesis are due to my own lack of vigilance or excess of intransigence. He also exhibited an unerring application of both 'carrot' and 'stick', as necessary, when an external source of motivation was required: at times the subject of this thesis seemed like a moving target (as much of gamma-ray astronomy seems to be in the *Fermi* era) and it is only by his efforts to expedite the process that it reached a satisfactory conclusion.

I am also deeply indebted to Erica for her patience, even when it ran against her better judgement, and truly remarkable capacity for keeping her frustration in check: thank you for letting me take pride in this work. Thanks also to the members of my family who have had cause to cope with my years and months of pre-occupation and have done so with good grace and humour: Niall, Susan, Alison and Denis.

Thanks are due to all those who were members of the McGill VERITAS group during my association with it, for maintaining an interesting, engaging and challenging environment: John Kildea, who first interested me in VHE astronomy; Luis Valcárcel, who first introduced me to VERITAS; Audrey MacLeod; Roxanne Guenette; Gernot Maier, for an admirable example to follow; Peter Cogan; Mary Bautista; Sean Griffin; Jonathan Tyler; Simon Archambault; and, particularly, Andrew McCann, for much humour, sanity, honesty and support.

My thanks are also due to Maggie Livingstone, for helpful discussions concerning the applicability of this work, an enthusiastic reading of this thesis and suggestions which improved it.

The data analyzed herein would not exist without long years of work by all of the members of the VERITAS collaboration both past and present who have contributed to the design, construction, operation and optimization of

the telescope array. I, along with the VERITAS collaboration as a whole, acknowledge the excellent work of the technical support staff at the Fred Lawrence Whipple Observatory and at the collaborating institutions in the construction and operation of the instrument.

I gratefully acknowledge the financial support provided by the McGill Department of Physics through the Research Assistantship I have held there since January 2006. Through the VERITAS collaboration, this research is supported by grants from the U.S. Department of Energy Office of Science, the U.S. National Science Foundation and the Smithsonian Institution, by NSERC in Canada, by Science Foundation Ireland (SFI 10/RFP/AST2748) and by STFC in the U.K.

Thesis Outline

This thesis describes a search for Very High-Energy (VHE) gamma rays being emitted from a globular cluster. In short, this is expected because globular clusters contain many stars and also many pulsars. To guide the reader to an understanding of this relationship, I will start, after briefly outlining the present state of gamma-ray astronomy at the highest energies (§1.1), by describing the nature of globular clusters and why they should contain so many pulsars (§1.2). I will also justify the choice of the target of this search: M13 (NGC6205).

I will then detail the basic premises at the foundation of the model of emission that has motivated this search and the specific implementation of that model with predictions for M13 [36]. Specifically, I will indicate that pulsars are known to produce winds of very energetic particles and it is the presence of these particles within a globular cluster that ultimately leads to the production of gamma rays (§2). Thus, it will next be necessary to describe the evidence for winds of energetic particles from pulsars (§2.1.1) and also outline the theories that allow us to expect that the energies with which particles are endowed by pulsars are sufficient to generate such energetic gamma rays (§2.1.3). I will then describe the mechanism by which these energetic particles produce gamma rays in the environment of the globular cluster that hosts them (§2.2.1), an environment dominated by the prodigious quantity of stars they contain. Following from these basic premises, I will describe an implementation of this model due to Bednarek & Sitarek [36] which quantitatively connects the pulsar populations of certain globular clusters (and M13 in particular) to the gamma-ray emission that might be expected from them (§2.3).

Having justified the expectation that there should be VHE gamma-ray emission from globular clusters, I will describe the means by which such emission can be detected (§3). In particular, I will detail the Very-Energetic

Radiation Imaging Telescope Array System (§3.2), which was used to collect the data that is herein used to confront the predictions of Bednarek & Sitarek. I will then lay out the processing of data generated by this instrument (§4) and discuss the statistical methods required in its analysis, including background rejection (§4.2.2) and estimation (§4.2.4).

Next, I will specify the criteria for ensuring the quality of data that is passed on to an analysis of this target (§5.1), before providing the details and results of the analysis (§5.3). In short, I will show that there is no evidence for VHE emission from M13 and consequently set rigorously defined (§5.3.2.1), generalized (§5.3.2.2) and universally applicable (§5.3.2.3) upper limits on any flux of VHE gamma-rays from this object. I will then discuss the implications of these results in relation to the predicted flux. Specifically, I will define feasible values for the three key parameters of the model, based primarily on the interpretation of radio and X-ray observations of other pulsars and globular clusters (§6.1). With these feasible values, I will use the results of my analysis, in the context of the predicted level of emission, to determine what portions of the parameter space are mutually inconsistent. This process will demonstrate that the original implementation of this emission model by Bednarek & Sitarek was most likely overly-optimistic (§6.2). Nevertheless, useful limits can be extracted in relation to certain assumptions concerning the energetics of pulsar winds (§6.2.4).

Statement of Original Contributions

Elements of this thesis that constitute original contributions to scientific knowledge are as follows :

- An estimate of the age and spin-down luminosity (and, by extrapolation to the characteristic values, the timing properties) of a hypothetical young pulsar associated with Terzan 5, which could power VHE emission observed in the latter's vicinity (§B).

- The determination of a decorrelated, integral flux upper limit in the VHE domain for M13 (§5.3.2.2): the previous integral flux upper limits for this object were not decorrelated and thus are subject to an assumption concerning the spectral index of a putative source.

- The determination of spectral flux upper limits above 1 TeV for M13 (§5.3.2.3): spectral upper limits have previously been defined for this object, but were derived at lower energies.

- An estimate of the total pulsar population of M13 by extrapolation of the mean radio luminosity distribution function of globular clusters (§6.1.1.1) and by extrapolation of a previously published relationship between X-ray source counts and stellar interaction rate (§6.1.1.2).

- An estimate of the mean spin-down luminosity of the pulsars of M13 by comparison to pulsars from the ATNF database (§6.1.2.2).

- The relation of existing predictions for VHE emission from M13 to current theories of pulsar winds (§6.1.3).

- In particular the results of this thesis, under certain self-consistent assumptions, exclude the efficient acceleration of electrons to TeV energies in pulsar winds (§6.2), a property that has been a canonical assumption for pulsar winds.

Also, during my time as a PhD candidate and member of VERITAS, I have contributed to the overall functioning and operation of the VERITAS collaboration and instrument through :

- The maintenance and development of `loggen` (a WWW portal to the database of information relating to the operating conditions of the telescope array during data-taking), including its integration with the Data Quality Monitoring framework.

- The contribution, to a collaboration-wide analysis software suite, of a class allowing time-wise selection of data within individual data runs.

- Assistance in the design and commissioning of both a LED-flasher calibration source [91] and a focal-plane-mounted digital-camera-based alignment tool [157].

- Numerous trips on-site to fulfil commissioning, maintenance and observational duties.

Part I

Background & Introduction

Chapter 1

Gamma-ray Astronomy and Globular Clusters.

Gamma rays occupy the shortest wavelengths of the electromagnetic spectrum: they are the highest energy[1] and most particle-like form of light. As with all forms of light, they (almost always) travel in straight lines. Thus, if they have been generated deep in space and travel towards Earth, they preserve the direction of their source and, if detected, can be used to infer the existence, location and other properties of that source. In short, they can be used for astronomy [163].

This sets astrophysical gamma rays apart from the equally energetic but much more ubiquitous charged cosmic rays. The latter's paths are distorted and effectively scrambled by their passage through the galactic magnetic field and their arrival direction tells us nothing of their origin. Their existence, however, is enticing: they imply that there are means by which nature can accelerate charged particles to energies we would associate with objects more than a thousand times more massive. This requires that these particles are moving very close to the speed of light, they are said to be highly **relativistic**, and have more energy than it has been possible to afford particles in the laboratory until only very recently. Interestingly, particles moving at these speeds can, under the right circumstances, generate gamma rays of similar energy and so, to learn of the most energetic processes in the universe, we

[1] More than one hundred thousand times more energetic than visible light. To try and put this in context, this thesis will deal with observation of gamma rays with energies of $\sim 1\,\mathrm{TeV}$ (about one thousand billion times more energetic than visible light) which is about the same kinetic energy as a flying mosquito, but carried by a single particle.

must intercept and detect gamma rays. This is the domain of gamma-ray astronomy.

I will define and summarise high- and very-high-energy gamma-ray astronomy and address expectations for very-high-energy gamma-ray emission from globular clusters.

1.1 Gamma-Ray Astronomy

The energy ranges of astronomy are essentially operational definitions: each range is defined by the sensitivity of a particular detection technique. The highest energy gamma rays (those above $\sim 30\,\mathrm{MeV}$) interact with matter predominantly via pair-production. In this process, a gamma ray passing close to an atomic nucleus interacts with the latter's intense Coulomb field and is converted into an electron-positron pair[2] (see Figure 1.1). This pair of

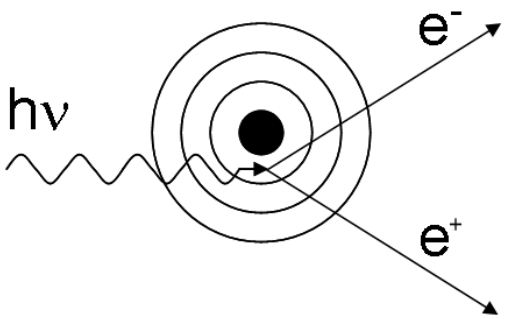

Figure 1.1: An incident gamma ray interacts with the electric field of a nucleus: a larger atomic number (more protons in the nucleus) implies a stronger electric field and greater probability of inducing pair-production. The nucleus absorbs a small amount of momentum in the interaction but its recoil is essentially negligible in comparison to the energy and momentum imparted to the pair of electrons.

particles inherits most of the energy and momentum from the original gamma ray and so they carry on close to the path the gamma ray would have taken. As they do so they will interact with any surrounding matter, frequently

[2] Henceforth, for brevity, I will refer to electrons and positrons collectively as 'electrons'. For most purposes below the sign of the charge is not relevant.

liberating electrons from the atoms and laying down a path of ionization. This process saps the energy of the particles which soon slow to a halt. However, if they are sufficiently energetic they may, before they are brought to a stand-still, emit bremsstrahlung gamma rays which may themselves pair-produce in what is termed an **electromagnetic cascade**. By detecting the ionization paths, the directions of the pair-production products can be determined and, by measuring the total ionization, their energies can be estimated; with this information the direction and energy of the original gamma ray can be reconstructed.

Such a direct approach may only be used by satellites because gamma rays will also interact with the Earth's upper atmosphere in the manner described above. The design employed, see Figure 1.2, is to stack alternating layers of heavy metal conversion foils, to promote pair production, and active tracking layers which can detect the transit of pair-production products and locate the position at which they cross the layer. Beneath these layers is placed a calorimeter, designed to encourage the deposition of the pair-production products' energy in such a way that they will be contained within the detector and the total energy be accurately measured. The whole device is termed a **pair-production telescope** and is the primary tool for observation of **High Energy** (HE) gamma rays.

At higher energies, it becomes increasingly unlikely that the pair-production products will be properly contained within the calorimeter layer. Furthermore, in the production of relativistic particles in astrophysical sources it is less probable for individual particles to reach higher energies: this carries over to the production of gamma rays at these sites and, in general, the flux of gamma rays decreases with increasing energy.[3] This penalises satellite-based detectors because of their modest size: a restriction imposed by the weight limits of launch vehicles. At these very high energies, satellites fail to measure gamma rays adequately and do not intercept enough to be statistically useful. However, when gamma rays of these energies are absorbed by the Earth's atmosphere the latter acts somewhat like the calorimeter layer in a pair-production telescope and it becomes possible to detect gamma rays by observing the upper atmosphere with an **Atmospheric Cherenkov Telescope** (ACT), see §3. Such a telescope monitors a large area of the upper

[3] Specifically, many sources of gamma rays exhibit power-law spectra: *i.e.* a photon flux obeying $\mathrm{d}N \propto \varepsilon^{-\delta}\,\mathrm{d}\varepsilon$ for a number of photons N with energy ε. Thus photons an order of magnitude more energetic arrive less frequently by *multiple* orders of magnitude.

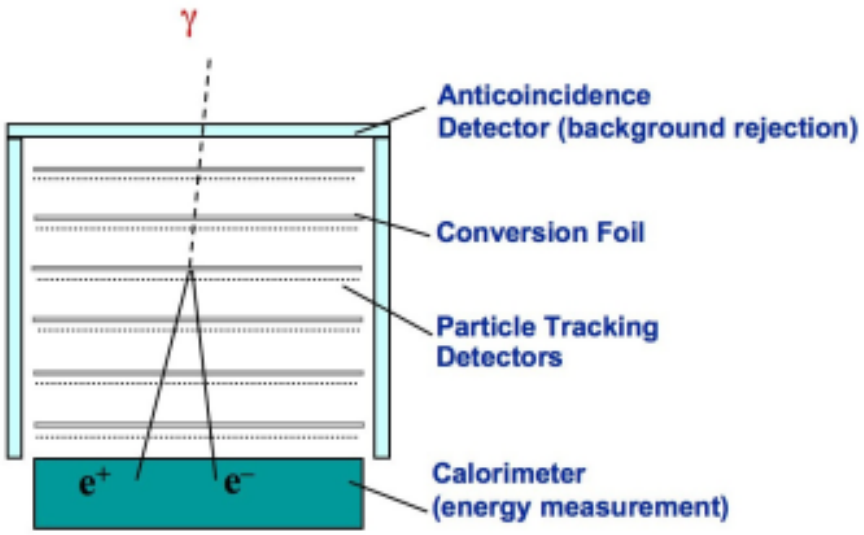

Figure 1.2: Principle of the pair-production telescope. Gamma rays are neutral and pass, without interacting, through a low-density Anticoincidence Detector which allows a veto against energetic charged particles. High-density Conversion Foils increase the likelihood of a gamma ray undergoing pair-production. Created electron pairs are tracked to determine their directions of travel. The electrons then arrive in the Calorimeter where each instigates an electromagnetic cascade which deposits the particle's energy, allowing its measurement. Image credit — *Fermi*/NASA.

atmosphere ($\sim 10^5$ m^2) coincidentally leading to a much greater chance of detecting even a sparse flux. This technique is described in more detail in Chapter 3 and is the principle means of **Very High Energy** (VHE) gamma-ray astronomy.[4]

This distinction between detection techniques leads to the boundary between HE and VHE gamma rays at ~ 100 GeV or ~ 0.1 TeV : below this

[4] At still higher energies (Ultra High Energy, UHE) the tail-end of very large gamma-ray-induced air-showers may be detected directly at ground-level. This is achieved via Cerenkov light produced in tanks of water instrumented with sensitive light detectors. Pioneering (though unsuccessful) efforts in the detection of UHE gamma-ray sources by CASA-MIA [45, 53] (and many others) were followed by success with the Tibet Air-Shower-gamma Experiment [23, 22] and particularly Milagro [10, 11]. This effort continues with HAWC [200].

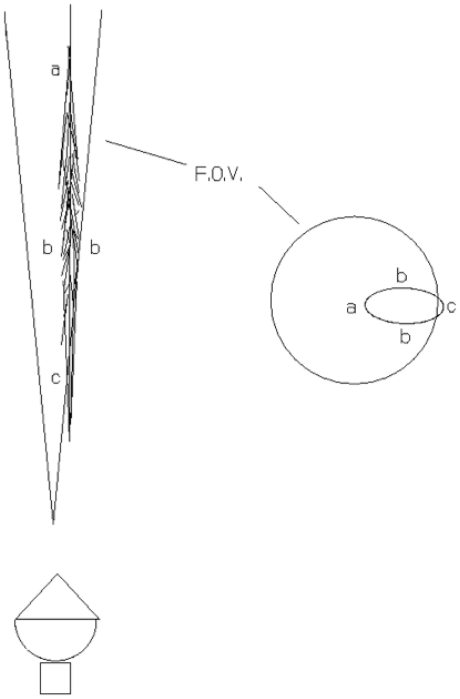

Figure 1.3: An electromagnetic cascade in the upper atmosphere intersects the field of view (F.O.V.) of an Atmospheric Cerenkov Telescope. The telescope may form a fore-shortened image of the cascade from Cerenkov light due to the pair-production products' passage (see §3 for more details). Image credit — T. Weekes: Fig. 2.7 from [207].

satellites are most sensitive; above, ground-based observatories. It is also worth noting one more important difference between these techniques: pair-production telescopes have a very wide field of view such that they may monitor the entire sky over a matter of hours whilst ACTs have narrow fields of view and are obliged to make observations of selected sources. Due to this, the satellite-based observatories are invaluable as path-finders for ACTs.

Below I will briefly summarise the development of these two domains of astronomy and the types of objects they have catalogued as sources, but first I will mention the emission mechanisms which generate gamma rays. As noted above, sources of astrophysical gamma rays correspond to the presence of highly relativistic particles. Such particles can be induced to generate gamma rays by several mechanisms. The acceleration of charged particles to relativistic velocities is generally associated with strong magnetic fields and as the paths of charged particles curve in such fields the centripetal acceleration induces radiation which is observed as **synchrotron radiation**. Synchrotron radiation gamma rays are only ever a small fraction of the radiating particle's energy but can be generated prolifically according to the power

of the accelerator. Many sources identified by HE gamma-ray astronomy produce synchrotron radiation. Another mechanism is **inverse-Compton scattering**, where a relativistic charged particle collides with a low-energy photon imparting to the latter a portion of its energy. In extreme cases the energy of the scattered photon is limited only by the original energy of the charged particle (see §2.2.1 for more details), thus inverse-Compton scattering figures prominently in sources catalogued by VHE gamma-ray astronomy. Frequently, the same object will appear in HE and VHE catalogues: the same population of particles powering both plentiful synchrotron radiation and very energetic inverse-Compton scattering.

1.1.1 HE Gamma-Ray Astronomy—Pair-Production Telescope Satellites

The first primitive pair-production telescope was launched on Explorer XI (1961) and detected 22 gamma rays (with energies $E > 50\,\mathrm{MeV}$) coming from elsewhere than the Earth: the first indication of astrophysical gamma rays. One of the instruments on OSO-3 (the third Orbiting Solar Observatory, 1967–69) was an upgraded version of the Explorer XI instrument and, in detecting 621 astrophysical gamma rays, was able to determine that the flux of astrophysical gamma rays was not uniform but rather was concentrated in the plane of the galaxy.

SAS-2 (the second Small Astronomy Satellite, 1972–73) of NASA was dedicated to gamma-ray astronomy ($E > 20\,\mathrm{MeV}$) but was halted earlier than expected due to a power supply failure. It was soon followed by a European Space Agency satellite of more modest capabilities: COS-B ($E > 30\,\mathrm{MeV}$) had an order of magnitude less effective area[5] but while it was intended to last two years, it instead continued for almost seven (1975–82). Together they mapped out the galactic plane and detected the first point sources and gamma-ray pulsars: gamma-ray astronomy in earnest had begun.

This branch of astronomy being the exclusive domain of satellites, NASA made a major effort over the following decade to advance the technology and sensitivity of these missions, culminating in one of its so-called 'great observatories': the Compton Gamma-Ray Observatory (CGRO, 1991-2000), see Figure 1.4. Aboard this seventeen-tonne satellite were a number of gamma-ray instruments including the Energetic Gamma-Ray Experiment Telescope

[5] A measure of flux sensitivity.

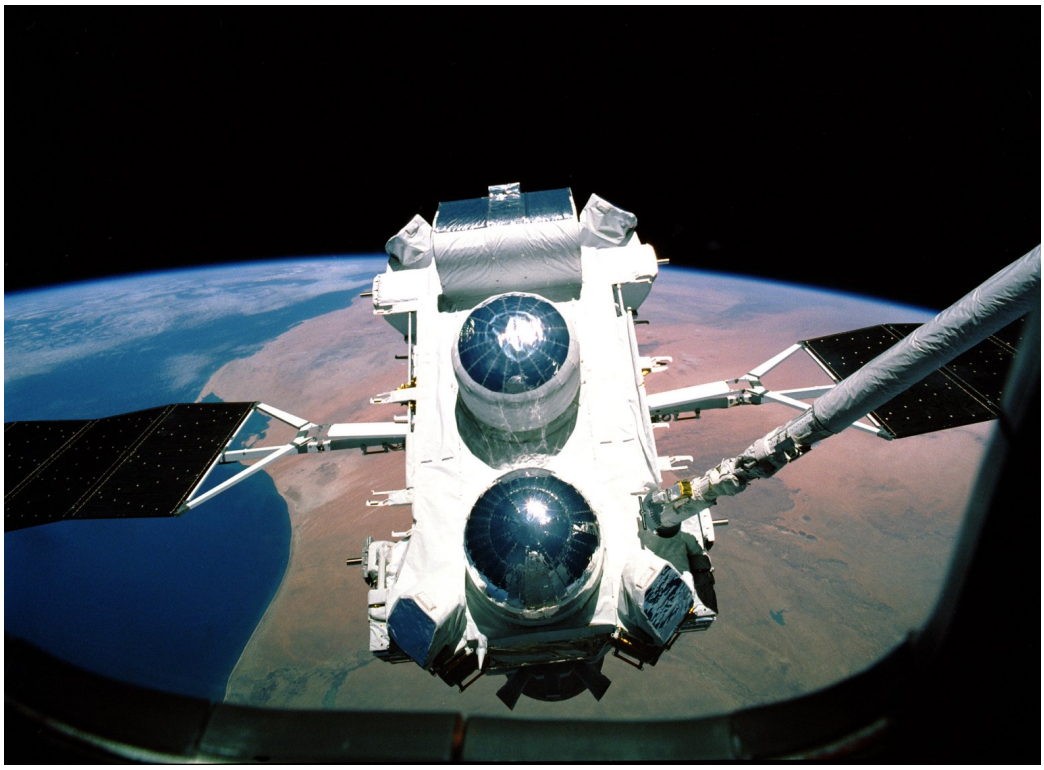

Figure 1.4: The Compton Gamma-Ray Observatory being deployed from the Space Shuttle *Atlantis* with the aid of the Canadarm (April 1991). The reflective outer surfaces of the detectors helped to maintain thermal equilibrium. In addition to the pair-production telescope EGRET (situated in the lower dome in this view), there were three other instruments which were sensitive only at energies $\lesssim 0.1\,\mathrm{GeV}$: the Burst And Transient Source Experiment (BATSE); the Oriented Scintillation Spectrometer Experiment (OSSE); and the Imaging Compton Telescope (COMPTEL). The BATSE array was distributed across the eight corners of the satellite platform; OSSE had four independent detectors housed in the box at the top; and COMPTEL resided in the central dome. Image credit — crew of STS-37, Compton Science Support Center, NASA.

(EGRET, 20 MeV $< E <$ 30 GeV). Unfortunately CGRO was deliberately terminated after the failure of one of its three attitude control gyroscopes required it to be de-orbited before control was lost entirely.[6]

The demise of CGRO left a gap in this energy range filled only recently by the launch of AGILE[7] (2007, 30 MeV $< E <$ 30 GeV) and the *Fermi* Gamma-ray Space Telescope (2008), see Figure 1.5, whose primary science

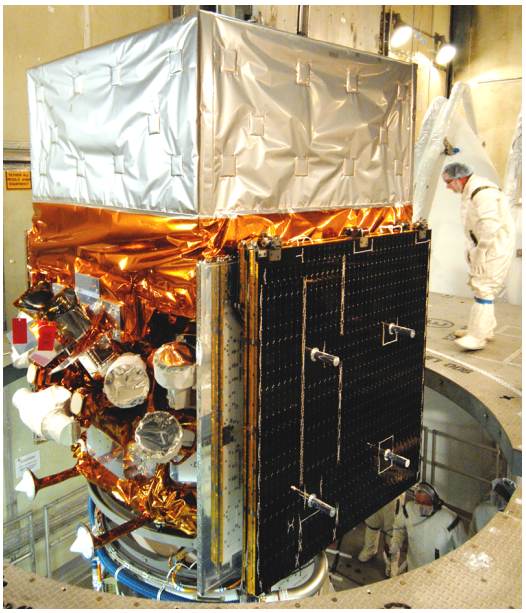

Figure 1.5: The Gamma-ray Large Area Space Telescope before launch, after which it was re-named the *Fermi* Gamma-ray Space Telescope, in honour of Enrico Fermi. On the right are folded solar panels; on top is the Large Area Telescope covered by thermal blankets which also provide protection against micrometeors. Image credit — *Fermi*/NASA.

instrument, the Large Area Telescope (LAT, 20 MeV $< E <$ 300 GeV), improves upon EGRET's sensitivity by more than an order of magnitude and with substantially improved angular resolution and a larger field-of-view [33].

[6] Others of NASA's 'great observatories' such as the Hubble Space Telescope (1990–present) and the *Chandra* X-ray Observatory (1999–present) have proved more enduring, each lasting more than a decade. The Spitzer Space Telescope (2003–present), the infrared 'great observatory', continues to operate with reduced capabilities since the exhaustion of its cryogens in mid-2009.

[7] The *Astro-rivelatore Gamma a Immagini LEggero* is an Italian satellite.

The latter point is of particular importance as it has helped to resolve the mystery posed by the final EGRET catalogue for which more than half of the sources had no identified counterparts, primarily because there were many objects seen at other wavelengths within the range of uncertainty provided by EGRET's source reconstruction.

1.1.1.1 *Fermi* Catalogue

In the first three months of scientific data-taking, the *Fermi* Gamma-ray Space Telescope compiled the most accurate map of the HE gamma-ray sky ever achieved. After a further eight months of collating data the first *Fermi* catalogue was released [1], see Figure 1.6; it represents the state of the art for HE astronomy. The most obvious general feature is the strong flux in and around the galactic plane: this is primarily due to cosmic-ray nuclei throughout the galaxy, colliding with clouds of gas and the particles produced by these collisions ultimately decaying to produce energetic gamma rays [7].

Below are outlined the main classes of source and the particular scenario for each class which is generally assumed to account for particle acceleration and the consequent gamma-ray emission.

Supernova remnants and starburst galaxies. The most energetic events in the galaxy are supernovae: the explosive deaths of massive stars. It is perhaps unsurprising, therefore, that their residue, **SuperNova Remnants** (SNRs), figure prominently in the catalogue of HE gamma-ray sources. As the debris of the explosion sweeps up surrounding ionised gas, a vast, often shell-like, shock wave is set up which concentrates the ambient magnetic field. As the shock front advances, particles may cross back and forth, their paths contorted by the chaotic magnetic fields. With each crossing in the direction of the shock front's motion a given particle is accelerated, resulting in diffusive shock acceleration. Some of the particles ultimately reach TeV energies and their curvature results in GeV synchrotron radiation.

Starburst galaxies represent an extrapolation of this scenario. These are galaxies in the process of large-scale star formation, perhaps due to recent gravitational disturbances as they collide with and absorb smaller galaxies. As a result of this activity, many more heavy stars than would normally be present in a galaxy are being formed, evolving rapidly (as they must) and dying, creating a remarkable over-density of SNRs. A starburst galaxy's emission is thus assumed to be the cumulative emission from its many SNRs.

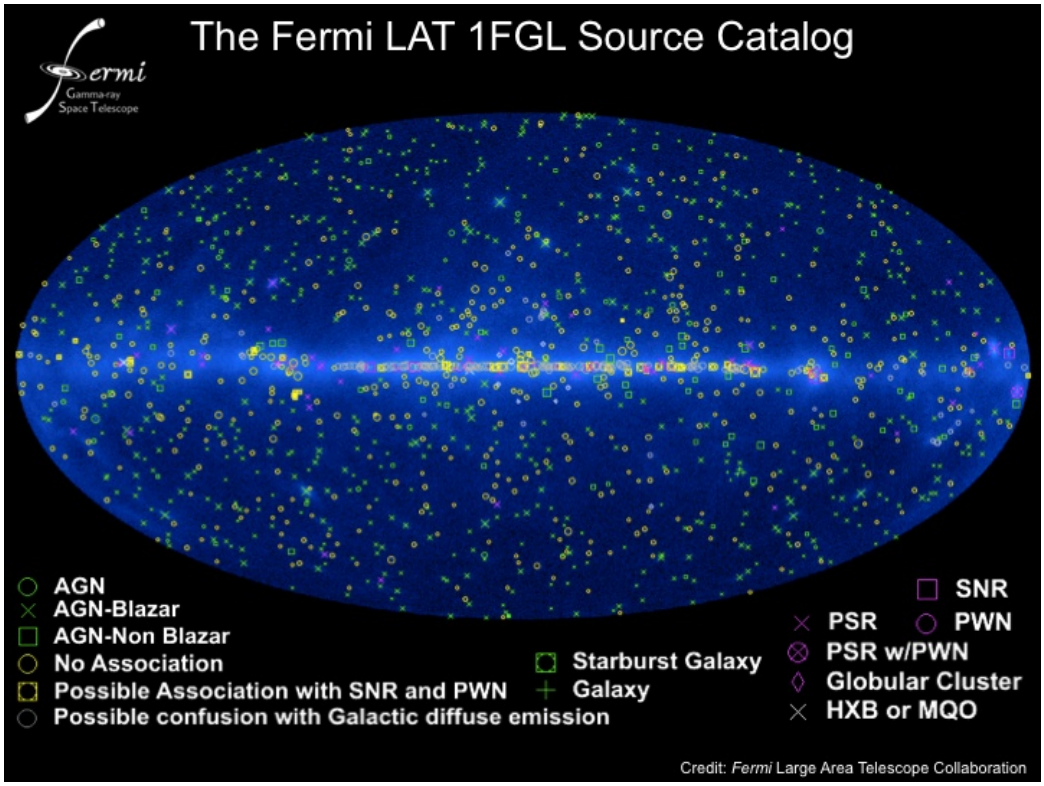

Figure 1.6: The first *Fermi* Catalogue (Aitoff projection of galactic coordinates) [1] consisting 1,451 discrete sources overlayed on the counts map, which is dominated by diffuse emission in the galactic plane. Image credit — *Fermi*/NASA.

Pulsars and pulsar-wind nebulae. A pulsar is a special type of neutron star which itself is the compressed, spent core of a massive star ($M_* \gtrsim 11\,M_\odot$) which has died as a supernova. Pulsars are particular in that they rotate rapidly and exhibit very strong magnetic fields (typically $B \gtrsim 10^8\,\mathrm{G}$). This is an excellent recipe for particle acceleration, see §2.1 for details, and, in particular, synchrotron radiation. In this case, however, the geometry of the magnetic field plays a further role in limiting the radiation into narrow beams which sweep across the sky, much like the light-beams of a lighthouse. If they sweep over the Earth, the source is observed to pulsate at a regular frequency, hence the term 'pulsar'. The particles accelerated close to a pulsar generate this pulsed emission but they also escape into the surrounding space

as a so-called **pulsar wind**: a synergy of the strong magnetic field and the relativistic plasma. As the wind streams away from the pulsar, the particles may be accelerated further, sapping the magnetic field, and eventually crash into the surrounding interstellar medium whence, in a manner similar to the expanding shell of a SNR, they act as a further source of gamma rays: this is a **Pulsar-Wind Nebula** (PWN).

Active galactic nulcei. At the centres of many galaxies reside **Super-Massive Black Holes** (SMBHs) of mass greater than $10^6\,M_\odot$. In many cases, such as our own Milky Way, the central compact object is more-or-less quiescent, perhaps having cleared its immediate surroundings of material. In other cases the centre of the galaxy is dramatically different, the SMBH driving an accretion disk heated to temperatures in excess of 10^6 K and polar jets of highly relativistic particles: this is termed an **Active Galactic Nucleus** (AGN). The mechanism by which these jets are formed and focussed is not well understood, but they are clearly very powerful, very energetic and emit a broad spectrum of synchrotron and inverse-Compton scattered radiation. They may be highly variable and are grouped into numerous subclasses, such as 'quasars' and 'blazars', according to the orientation of the relativistic jet with respect to our viewing angle.

High-mass x-ray binaries / micro-quasars. **High-Mass X-ray Binaries** (HMXBs) consist of a bright, massive, main-sequence star and a compact object of some sort (a neutron star or black hole). and they are usually strong sources of X-rays. For most of these objects, there are competing emission scenarios which fit either type of compact companion and assert either shock acceleration (as in the PWNe), where a wind from the neutron star interacts with that from the massive star, or the formation of accretion-powered relativistic jets (rather like a miniature AGN). In the latter case the system is often referred to as a micro-quasar.

Globular clusters. These are ten-billion-year-old spherical clusters of up to several million stars that are known to contain many more pulsars per unit mass than the galactic plane. That globulars contain an overabundance of pulsars is a property of these clusters which we will address in §1.2.2. *Fermi* has detected eight globular clusters [9] in a study targeting those thirteen deemed most likely to contain many pulsars; M13 was not among

them. The detected flux has been interpreted as the cumulative, unresolved, direct emission due to a large population of pulsars. A further three were firmly identified as sources of HE gamma rays (along with another three only tentatively) in a search of *Fermi* data relating to thirty globulars [196]; a complete list of the objects examined was not provided.

1.1.2 VHE Gamma-Ray Astronomy—Ground-Based ACTs

The working concept of ACTs was simple to implement but was hampered by the overwhelming flux of cosmic rays. Many experiments were attempted without success from the first proof-of-concept of the technique by Jelley & Galbraith in 1952 [82] until the first reliable detection, of steady emission from M1 (the Crab PWN) in 1989 [209], by an imaging ACT at the Fred Lawrence Whipple Observatory (henceforth Whipple) [124]. Whipple went

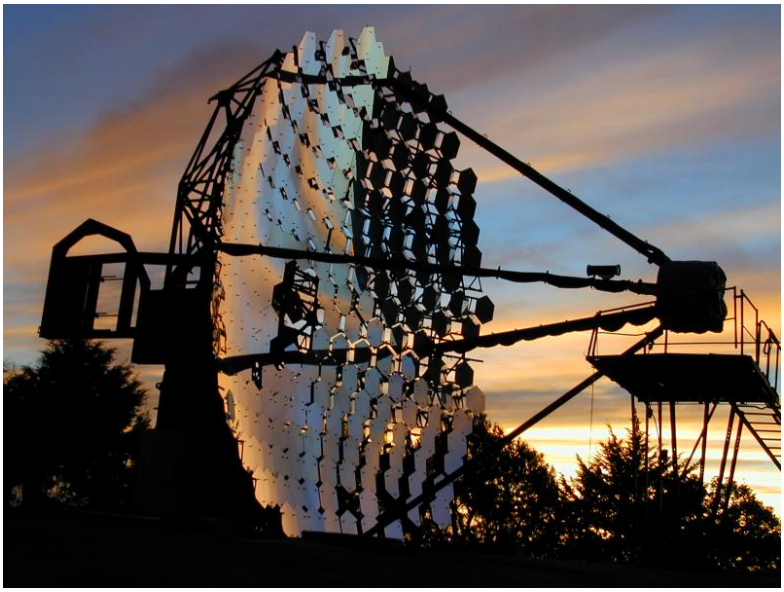

Figure 1.7: The 10 -m ACT at the Fred Lawrence Whipple Observatory. Constructed in 1968, it operated with a single-pixel detector (*i.e.* as an ACT without imaging capabilities) until 1982 when an imaging camera was installed. The telescope was in operation until 2011. Image credit — D. Horan.

on to detect several blazars (the most luminous and energetic form of AGN) [178, 179, 111] and reveal indications of VHE emission from the centre of our own galaxy [134].

The High-Energy Gamma-Ray Astronomy (HEGRA) array, consisting of five telescopes, was the first VHE observatory to use stereoscopic images to reconstruct astrophysical gamma rays. Although the individual telescopes were small compared to Whipple (having a diameter of 3.4 m compared to 10 m), meaning that they could only detect gamma rays above 500 GeV , the greater precision allowed by the stereoscopic technique proved its worth, improving both angular and energy resolution [65]. Consequently, HEGRA was able to provide strong evidence for TeV emission from a SNR (Cassiopeia A) [12] and from another sub-class of AGN (M87) [15] and the detection of an unidentified source (TeV J2032+4130) [13, 14, 49][8].

It was fairly clear that, in order to capitalise on the success of these two trail-blazing instruments, the next generation of VHE observatories required arrays of telescopes with large reflectors. A number of scientific collaborations were formed to realise this paradigm and push ahead in the fledgling field of VHE astronomy.

CANGAROO-III comprised four, 10-m diameter telescopes and operated near Woomera, southern Australia between 2004 and 2010.

H.E.S.S. is an array of four, 12-m telescopes which has been in full operation since 2004. It is situated in Namibia, where it has an excellent viewing angle on the Galactic Centre which allowed it to carry out a very successful survey of that region [19], eventually revealing more than fifty sources [55, 109], the majority of which are associated with PWNe and SNRs but several of which remain unidentified [18]. The mirrors of the original telescopes are being degraded by the desert environment, diminishing the sensitivity of the array over time. However, a process of mirror re-coating and replacement has recently been implemented which will conclude this year. This is intended to coincide with the completion of a $\sim$27-m Very Large Cerenkov Telescope (VLCT) which is to be situated in the centre of the array and whose design allows the detection of gamma rays down to $\sim$20 GeV [172]. The restored original telescopes and addition of the VLCT will inaugurate a second phase of the H.E.S.S. experiment, H.E.S.S. II.

MAGIC operates from near the old HEGRA site at Rocque de los Muchachos on La Palma. MAGIC-I (2004-2009) comprised a single telescope

[8] This was recently determined to be the PWN of a previously undetected pulsar [2, 52].

but that had a fairly sophisticated 17 -m , parabolic reflector. Such reflectors are optimised for a low energy threshold[9] and this allowed MAGIC to detect the Crab pulsar at 25 GeV , nominally in the domain of HE gamma-rays [20]. Since the completion of a second, identical telescope in 2009 (MAGIC-II), MAGIC has been operating in a stereoscopic mode.

VERITAS is an array of four, 12 -m imaging AC telescopes located in southern Arizona, USA. It became fully operational in 2007 and has a continuous program of mirror re-coating in order to maintain optimum optical sensitivity.[10] In addition, the configuration of the array was modified in 2009 to optimise its gamma-ray sensitivity: by optimising the baseline between telescopes, the stereoscopic technique may be used to its full potential. A planned upgrade of the cameras will further increase optical sensitivity.[11] VERITAS is currently the most sensitive instrument in the VHE regime and this contributed to the recent detection of the Crab pulsar at unprecedented energies (above 100 GeV) [205, 156] demonstrating that the prevailing paradigm of pulsed gamma-ray emission is incomplete. This instrument has been used to collect the data analysed for this thesis and is described in detail in §3.2.

1.1.2.1 TeV Catalogue

As noted above, ACTs have a relatively restricted field of view in comparison to pair-production telescopes; sources are detected as essentially discrete objects. The current catalogue of VHE sources is shown in Figure 1.8 against the all-sky map due to *Fermi*.

Relation to HE-astronomy source classes. Most of the HE source-classes have several members which manifest themselves in the VHE domain as well, either because they are especially energetic or powerful or are nearby.

[9] The VLCT for HESS II also uses a parabolic dish.

[10] This maintains both a low energy threshold and large collection area.

[11] As described in §3.1.1.2, the cameras are composed of photo-multiplier tubes and the intrinsic sensitivity of these devices to light may be characterised by the quantum efficiency. The upgrade of VERITAS's cameras will replace all of the existing pixels with photo-multiplier tubes of higher quantum efficiency.

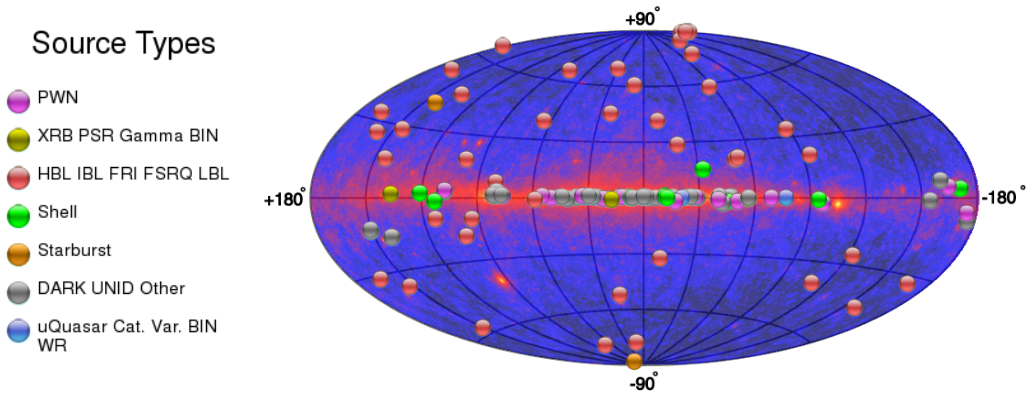

Figure 1.8: The 121 sources detected in VHE gamma rays overlaid on the counts map due to *Fermi* (Aitoff projection of galactic coordinates). XRB is another acronym for HMXB; HBL, IBL, FRI, FSRQ, LBL are classes of AGN; Shell refers to shell-type SNR; uQuasar (implying μ-Quasar) is short for micro-quasar. Image credit — TeVCat due to S. Wakely & D. Horan (http://tevcat.uchicago.edu/).

A notable exception appears to be the pulsars. Only one pulsar has been detected by ACTs: the Crab pulsar by MAGIC and VERITAS (see above). This is largely in line with the theory of pulsar emission of gamma rays which asserts that they are emitted well within the strong magnetic field of the pulsar: this leads to any gamma rays emitted in the VHE band having a strong probability of interacting with the magnetic field and being absorbed in the process of pair-production.[12] In contrast, PWNe figure prominently in the VHE catalogue because at a distance from the pulsar, isolated from its very strong magnetic field, inverse-Compton scattered photons are able to escape unfettered and, in addition, the shock front of the PWN itself provides many target photons for the population of relativistic particles to scatter, in a process termed synchrotron self-Compton[13] [67]. Indeed it is this environment which provided the first incontrovertible detection of a source of VHE gamma rays: the Crab PWN. Thus direct emission from pulsars is

[12] The VERITAS result challenges this scenario somewhat by demonstrating that the highly energetic electrons which emit these gamma rays likely continue to high altitudes, allowing VHE emission where the magnetic field is less stifling. Nonetheless the VHE emission is considerably less powerful than the HE emission.

[13] A population of particles generates broadband synchrotron radiation, a part of which is then inverse-Compton scattered by the same population.

all-but absent from the VHE catalogues but their associated PWNe are the prototypical VHE source. This dichotomy is played out in expectations for emission from globular clusters to which we now devote our attention.

1.2 Globular Clusters as Sources of VHE Gamma-Rays

We have seen that pulsars support HE emission from globulars but that their direct emission is unlikely to contribute significantly to any VHE emission from these objects. However, there remains the possibility of a PWN-like emission where the relativistic particles of the pulsar winds are involved in inverse-Compton scattering. This requires an intense field of target photons which may be supplied by the stars of the globular itself. Given the greater distance of globulars, relative to PWNe in the galactic disc, a great many pulsars may be required to render this flux detectable. Globulars do, in fact, host many pulsars and we will examine why this is so after discussing the defining characteristics of these star clusters.

1.2.1 Globular Cluster Characteristics

The defining trait of globular clusters is that they are old. At up to 12 billion years old [187], they are some of the oldest objects known and place strict lower limits on the age of the universe [135]. Furthermore their constituent stars are all of a similar age, having formed within the first percent of the cluster's life [174]. This is understood to be due to the lives and deaths of the most massive stars of the cluster which which would have occurred early and violently as supernovae. A combination of powerful stellar winds from these massive, highly luminous stars followed by supernovae blasts and the winds of pulsars formed by the aging population of stars [191] would have effectively evacuated any free gas left in the cluster after the initial period of star formation. Thus no material remains from which new stars could form and the stellar population as a whole has aged steadily since the initial formation of the cluster: as time progresses, stars of decreasing mass leave the main sequence to become red giants and eventually white dwarfs.

So, globular clusters have settled into an extended period of slow collapse under gravity. Their orbits outside the plane of the galaxy have ensured that they suffer little disruption, preserving their simple spheroidal form which

Figure 1.9: M13: the great globular cluster in the constellation Hercules. One of 157 known globulars associated with the Milky Way [95]. The intense crowding towards the core is evident. This image covers approximately 14 arcminutes. By comparison the half-light radius is only 1.69 arcminutes. Image credit — OPIOMM (http://www.astro.umontreal.ca/~opiomm/images.html).

lends them their title. Their constituent objects sink towards the centre as the system gravitationally relaxes, leading to a tremendous density of stars. To take M13 as an example (see Figure 1.9), it has a half-mass radius of $\sim 6\,\mathrm{pc}$ and comprises approximately 6×10^5 stars : within 6 pc of the centre there are on the order of three hundred thousand stars similar to our Sun; in contrast, the nearest star to our solar system is 1.3 pc away and within 6 pc there are approximately one hundred stars, most of which are much dimmer than the Sun.

If this simple picture was a complete explanation, the gravitational col-

lapse of typical globulars with ages of $\sim 10\,\mathrm{Gyr}$ would have already advanced into a state of 'core collapse' where the observed density of stars increases without apparent limit towards the centre of the cluster. However, the luminosity profiles of most globulars do not fit this form; instead they are very well described by so-called King models [127] which are characterised by a relatively constant density of stars in a core region surrounded by a zone of steeply declining stellar density itself enclosed by a broad, tenuous envelope stretching out to a tidal radius, more than an order of magnitude larger than that of the core: here the gravitational field of the Galaxy begins to dominate over that of the cluster.[14] Even without core collapse the central stellar density of these objects is remarkable, attaining $\sim 3500\,\mathrm{pc}^{-3}$ in the case of M13, supporting an intense field of optical and infrared photons.

The reason typical globulars are not core-collapsed has to do with a subtlety of the process of relaxation itself. The heavier components of the cluster, including neutron stars and binaries, are subject more to gravitational settling in comparison to the remaining light, main-sequence stars. This results in gravitational segregation or differentiation wherein the populations of heavier objects become more concentrated in the core[15] [87]. Now, it is this migration of binary systems into the core of a globular that acts as a brake on the self-same gradual gravitational collapse for the following reasons: in the extremely dense core of the globular, interactions between unassociated stars become common and, also, there is a tendency for binary systems to become more tightly bound during interactions with single stars [97]. This so-called 'hardening' of binary systems, imparts a significant amount of energy to surrounding stars[16], puffing-out the globular and delaying the overall gravitational collapse of the cluster [86].

The means by which binary systems become more tightly bound are important for understanding the pulsar population of globulars. A binary, when scattering a single star or a less tightly bound binary, will tend to shrink in

[14] In fact, in line with their overall simplicity, globular clusters are a remarkably uniform class of object: they mostly seem to obey a single fundamental correlation between the core concentration (the logarithm of the ratio between the tidal and core radii, as defined in the King model), total luminosity and binding energy (modified slightly by the distance from the galaxy, accounting for its tidal effects) [159].

[15] This is analogous, albeit on a much larger scale, to the formation of a planet which leads to a metallic core with a rocky mantle overlaid by a light, volatile atmosphere.

[16] In fact, the reservoir of energy contained in binaries is sufficient to dissipate the cluster entirely [177] and globulars are believed to be shedding stars, effectively evaporating.

radius, whilst accelerating the single star or softening the other binary. Also, a binary system interacting with a single heavy object, such as a neutron star or a heavy white dwarf, will tend to eject the least massive component and retain the heavy object [116] in a so-called **exchange interaction**. Thus, an interesting side-effect of the processes of gravitational differentiation and binary hardening is to concentrate compact objects, like neutron stars, and binary systems together in the cores of globulars and furthermore to transfer those compact objects into close binary systems with lighter companions. We will now examine how this environment promotes a large population of pulsars.

1.2.2 Binaries and Recycled Pulsars

There are essentially two types of close binary systems of relevance here; each consists of a compact object and non-degenerate companion[17] and they are distinguished by the type of compact object: a **Cataclysmic Variable** (CV) contains a white dwarf; a **Low-Mass X-ray Binary** (LMXB) contains a neutron star. In both cases the compact object is sufficiently close to its companion[18] that its gravitational field is stripping material from the companion's outer layers in a process known as Roche-lobe overflow. The material stripped from the companion star falls onto the compact object, heating it to millions of Kelvin such that it becomes a strong source of thermal X-rays.

CVs may create young pulsars. In the case of a CV, if the white dwarf is composed of oxygen, neon and magnesium [117] (as may occur, for example, if the progenitor star was in the correct mass range [116]) the additional material may raise its mass above the critical threshold for an electron-capture supernova, in a process called accretion-induced collapse. If this occurs, a neutron star is created. In fact, this process may represent a large fraction of the neutron stars retained by a globular during its lifetime [117, 116]and because it is promoted by exchange interactions it significantly enhances the neutron star (and by extension, pulsar) population of a globular.

Now, when neutron stars are born in supernovae they may inherit strong

[17] A star supported by and shining because of nuclear fusion in its core.

[18] This may be because the system is ultra-compact or the non-degenerate companion has advanced to a giant phase in its evolution.

magnetic fields and rapid rotation. By a combination of the geometry of the magnetic field and the rotation of the neutron star, charged particles are accelerated to very near the speed of light, they become highly relativistic, and emit radiation as tight beams or fans which sweep across the sky. If these happen to sweep over the Earth the object is observed as a pulsar. Pulsars gradually slow or 'spin down' after their creation, as the initial rotational kinetic energy is taken up by the accelerated particles and the surrounding plasma which convert it into the radiation of the beams or carry it away as a pulsar wind; they have no consistent power source of their own, in the way that normal stars are powered by nuclear fusion, and their initial, stored energy is progressively dissipated. The rate at which a young pulsar slows is such that it will cease to accelerate particles and hence cease to be luminous within a small fraction of a globular's lifetime. Thus, due to accretion-induced collapse in CVs, there should be many neutron stars in globular clusters but few young pulsars are expected to be seen [46].

LMXBs and recycled pulsars. However, the second type of close binary, the LMXB, represents a means by which a pulsar can be rejuvenated [26]. As material overflows the Roche lobe of the companion star it falls towards the neutron star in a process known as mass transfer. As matter is drawn in to the neutron star, conservation of angular momentum forces it to collapse into a rapidly spinning accretion disc. The disc dissipates some of the gravitational potential energy of the in-falling material, heating itself to millions of Kelvin and emitting X-rays. The material migrates to the inner edge of the disc before falling onto the surface of the pulsar, contributing a fresh supply of angular momentum and energy. Of course, this causes the pulsar's rate of rotation to increase: it is said to have been 'spun up' or 'recycled'. In this way the fastest known pulsars [102] are created, with rotation periods an order of magnitude shorter than those of pulsars fresh from supernovae: these are **millisecond pulsars** (MSPs) [21], having periods of $\sim 1\,\mathrm{ms}$. Now, MSPs typically have very low spin-down rates[19], such that their lifespans are greater than the age of globulars and, as a result, they will have been accumulating in the cores of these clusters over the last 10-billion years [116].

[19] It seems that recycled pulsars have smaller magnetic fields (by many orders of magnitude) compared to young pulsars reducing their coupling to the surrounding plasma and consequently the rate at which their rotational energy is dissipated. This phenomenon is often attributed to the accreted matter 'burying' the magnetic field.

In short, globulars are fertile ground for LMXBs and MSPs[20] and, indeed, these objects are more common in globulars by orders of magnitude compared to the galactic plane [121, 58].

1.2.3 MSP Population

Soon after it became clear that globulars were indeed rich in pulsars, stellar interaction rates in their cores were used to estimate the total population of pulsars in the entire system of galactic globulars with the conclusion that there should be prodigious quantities ($\sim 10^4$) [138], although this initial estimate was undoubtedly hindered by low statistics[21]. This led to an estimate of hundreds of pulsars in the cores of larger globulars and many dozens in more typical ones [198].

Recent simulations indicate that, although a large globular may indeed contain hundreds of neutron stars that have undergone mass transfer ('plausible' pulsars), a large fraction of these binary systems may not necessarily lead to the creation of MSPs [116]. Nonetheless, tens of MSPs are expected in the cores of large globular clusters and indeed there are three clusters that have more than ten pulsars detected in each and a further seven clusters having five or more detected pulsars. In total 143 pulsars are known in globulars[22] and these figures should be considered with the expectation that only 10–20 % of the total globular pulsar population has been seen [181][23].

1.2.4 VHE Predictions and Observations

Recalling the association between pulsars and PWNe and that the latter are commonly VHE sources, it may be expected that the great concentration of pulsars in a globular causes the latter to be a source of VHE gamma rays

[20] Globulars are models of sustainable development: they *reduce* their heavy stars to compact objects, *reuse* them in exchange interactions and *recycle* them into millisecond pulsars.

[21] Only seven globular cluster pulsars had been detected at the time and this study restricted itself to pulsar surveys by northern hemisphere observatories (excluding two pulsars from 47 Tucanae) that did not account for binary acceleration (excluding one pulsar from M15).

[22] See `http://www.naic.edu/~pfreire/GCpsr.html` for an up-to-date listing.

[23] It is perhaps worth noting that this implies up to ~ 750 objects which, in comparison to the tens-of-thousands of some estimates, is much more in line with the earliest expectations of 500–2000 total, based on the integrated radio emission from globulars [79].

in much the same way as a PWN is. This argument was laid out by Smith [190] soon after the discovery of the Crab Nebula in TeV gamma-rays. It was argued simply that some fraction of globular pulsars' spin-down power would be converted into TeV-gamma rays and if that fraction was $\sim 0.1\,\%$ and the number of pulsars $\sim$1000 then certain globulars might be visible to detectors of that era. Under these auspices, Whipple observed M13 in 1998 and detected no evidence of a VHE gamma ray flux [90], setting an integral flux upper limit of $1.08 \times 10^{-11}\,\mathrm{cm}^{-2}\ \mathrm{s}^{-1}$ above 0.5 TeV at a confidence level of 99.9%.

A modern, more nuanced approach argues that it is the wind of relativistic particles from a pulsar that powers a PWN and so the collective winds of numerous pulsars may interact with the ambient environment of the globular to produce TeV gamma rays.[24] The gist of this scenario is that MSPs inject (via their pulsar winds) a population of relativistic particles into the core of a globular. As the relativistic particles diffuse through the core of the cluster they will interact with the intense starlight by inverse-Compton scattering (see §2.2.1 for a detailed discussion) transferring their energy to some of the stellar photons and thereby converting them to VHE gamma rays which escape from the cluster.

1.2.4.1 VHE Emission Models

Two models have been promulgated with regard to this mechanism: one due to Venter, de Jager and Clapson (henceforth VJC09 [201, 202]) and another due to Bednarek and Sitarek (henceforth B&S07 [36]). The models differ primarily in the level of sophistication applied to different components of the model, namely the energy spectrum of the pulsar wind particles, how they diffuse through the cluster and the spatial distribution of target photons.

VJC09 have calculated particle spectra using a precise pulsar magnetosphere model. These spectra are determined as the particles leave the vicinity of a pulsar and for an ensemble of pulsars which serve as the basis for the energy distribution of relativistic particles circulating in the globular. In this model the level of IC emission is related to the ambient magnetic field (they term this the 'nebular field'). This is due to the fact that such a magnetic

[24] We will summarise the evidence for winds from MSPs in §2.1.1; here we shall content ourselves with the fact that globulars are known to be fertile territory for pulsars and that the latter are capable of powering PWNe which feature prominently in the catalogue of VHE sources.

field curves the paths of charged particles helping to retain them in the core where the density of target photons is greatest. There is also a subtle interplay between an increasing magnetic field retaining relativistic particles and cooling them via synchrotron emission. The target photon field is modelled by only two zones: the core and outside that to the half-mass radius of the cluster. Ultimately, this model relates VHE flux to the number of pulsars as a function of the ambient magnetic field within the globular. It should be noted that the specific pulsar magnetospheres they have modelled to provide the injection spectrum of relativistic particles are constructed according to the observed pulsars of 47 Tucanae. To compare this model to other globulars it must be assumed that all globulars host a population of pulsars with a similar distribution of properties.

B&S07 have attempted to construct a model independently of a specific pulsar population: they use a set of 'typical' millisecond pulsar properties to define a reasonable particle injection energy and power, and then scale this according to the number of pulsars. Therefore, this model relates VHE flux to the product of the number of pulsars, $N_{\rm P}$, and the typical efficiency, η, with which they generate relativistic particles. They also suggest that not only will relativistic particles be sourced directly from pulsar winds but also that, due to the extreme density of objects in the cores of globulars, the same pulsar winds may collide. Such colliding winds form shock fronts which can re-distribute the spectrum of wind particles: this leads to a power-law spectrum of particles circulating within the globular some of which have been accelerated to greater energies still. B&S07 assume a range of possible parameters for such a power-law spectrum along with the possibility of a monoenergetic injection spectrum directly from the pulsars, without passing through the shock fronts. For each candidate injection spectrum they use Monte-Carlo simulations to trace the passage of trial particles through ambient magnetic field, tracking their inverse-Compton emission but ignoring synchrotron losses. They model the target photon field with a smooth spatial distribution based on the King model luminosity profile of the specific globular under consideration. Under this paradigm, the VHE flux would be directly related to the number of pulsars in the globular and the efficiency with which they produce relativistic particles in their winds. In this way VHE observations of globulars may provide insight into the pulsar population of these clusters and the composition of pulsar winds.

In making specific predictions, these models both assumed 100 pulsars in any particular globular. They have since been used to interpret observations

made by both H.E.S.S. and MAGIC.

1.2.4.2 VHE Observations

H.E.S.S. observed 47 Tucanae[25] in 2005 [17]: it detected no flux and set an upper limit in the energy range 0.8–48.6 TeV of $6.7 \times 10^{-13}\,\mathrm{cm}^{-2}\ \mathrm{s}^{-1}$ at the 99% confidence level. This upper limit corresponds to 2% of the flux from the Crab Nebula. This result was interpreted in terms of VJC09 as limiting the number of MSPs to less than 80, in the case that the ambient magnetic field is 12 μG. The same result was cast in terms of B&S07 with some scaling to account for a more accurate estimate of the spin-down luminosity of pulsars in this globular and a revised estimate of its distance. It is noted by H.E.S.S. that there is no observational evidence to support the idea of colliding pulsar winds in the globular's core. Nonetheless, the most restrictive constraint, given the various power-law spectra examined by this model and the known twenty-three pulsars, implied that the wind efficiency was only $\sim$1 %, significantly less than for the Crab Nebula which is $\sim$10 %.

MAGIC observed M13 in 2007 and detected no flux [24], setting an integral upper limit of $5.1 \times 10^{-12}\,\mathrm{cm}^{-2}\ \mathrm{s}^{-1}$ above 0.2 TeV. In addition they set differential upper limits at a confidence level of 95% in six spectral energy bins. In interpreting this result it was noted that the energy range of the spectral upper limits was too low (140–1120 GeV) to allow confrontation of VJC09 which predicts peak emission in a fairly narrow band of 1–3 TeV. In relation to B&S07, the strongest constraint provided by the power-law injection spectra was similar to that provided by the HESS result outlined above if one assumes the presence of 100 pulsars in any given globular. In this case, however, the globular contains only five known pulsars and the upper limit corresponds to a wind efficiency of $\sim$10 %. Ignoring the possibility of colliding winds and assuming an injected particle spectrum that was monoenergetic at 1 TeV the limit corresponds to as little as 4 %.

Terzan 5. H.E.S.S. has also observed Terzan 5, the globular hosting the greatest-known population of pulsars [182, 102], very deeply (90 hours of exposure) [100]. They have detected emission from the direction of Terzan 5 with an integral photon flux of $1.2 \times 10^{-12}\,\mathrm{cm}^{-2}\ \mathrm{s}^{-1}$ in the energy range

[25] The globular hosting the second-largest population of detected pulsars, twenty-three in total [145].

0.44–24 TeV .However, the emission is somewhat extended and, critically, its centroid is offset ($4'.0 \pm 1'.9$) from the centre of the cluster; this location and morphology cannot be reconciled with the emission mechanism considered here which is reliant upon the intense photon field in the *core* of the cluster: the peak region of that photon field is, by definition, at the visible centre of the cluster. Nonetheless, the probability that this is the chance overlap of an unassociated source (*e.g.* the PWN of a young pulsar), even in the crowded sky around the galactic centre, is estimated to be only 0.01%. Thus, this detection is intriguing and may highlight what an exceptional object Terzan 5 is (being one of the largest and most dense of all galactic globulars [140])[26]; I consider an explanation for this unusual result in §B.

1.2.4.3 Target Selection

VJC09 makes no specific predictions for globulars visible to VERITAS. On the other hand, B&S07 does make specific predictions for two globulars visible to VERITAS: M13 and M15. Of these two, a greater flux (by a factor of $\sim$1.6) is predicted from M13 given the assumption of 100 pulsars in each cluster. Five pulsars are known in M13 compared to eight in M15 but four of those in M13 have periods less than 4 ms compared to none in M15. Given that faster-spinning pulsars are generally more powerful, this favours M13 for the possibility of yielding a detectable flux. Furthermore, of the six brightest/most massive globulars in the northern hemisphere, M13 is the closest. Thus, for this study M13 was the chosen target.

B&S07 presents a family of predicted emission curves for M13, based on a range of assumptions concerning the spectrum of electrons powered by the pulsar winds: *e.g.* Figure 1.10 shows the set of curves calculated for particular power-law electron spectra as might be expected from colliding pulsar winds, along with the sensitivities of various instruments mentioned above. In the next chapter I will justify and describe the emission model and its implementation in B&S07 in more detail.

[26] There is currently some debate as to whether Terzan 5 is, in fact, a globular cluster in the strictest sense [74, 64, 73, 170].

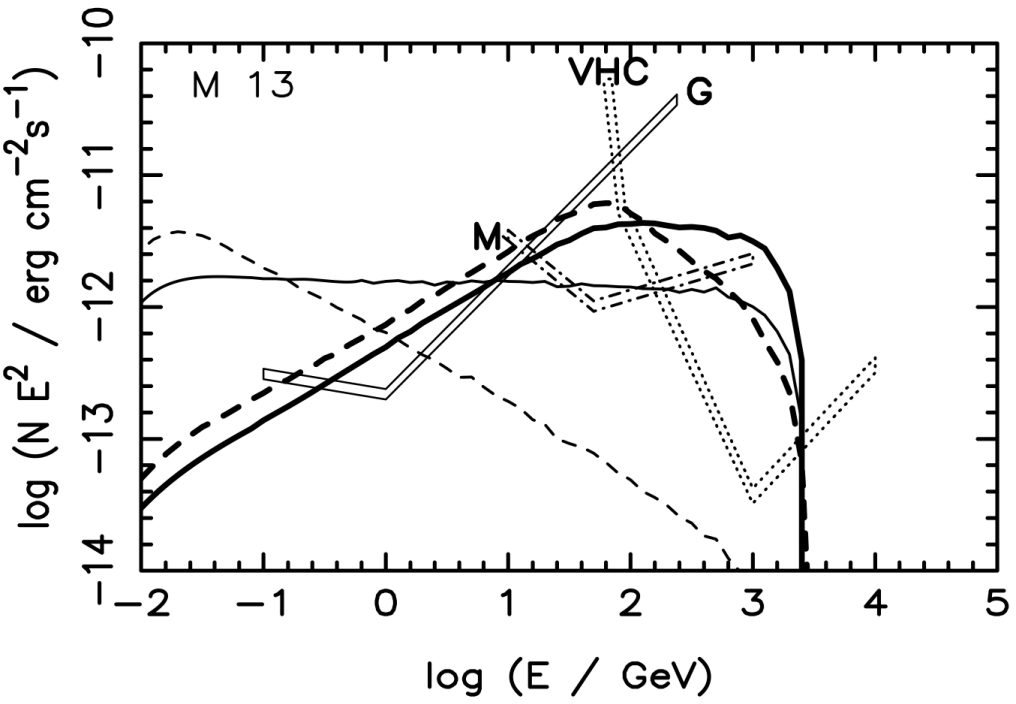

Figure 1.10: Some predicted gamma-ray energy-flux curves for M13 as calculated in B&S07. These curves are determined for various hypothetical power-law spectra of electrons presumed to be generated in the globular cluster by colliding pulsar winds. Each particle spectrum has index 2 (solid lines) or 3 (dashed lines) and low-energy cut-off 1 GeV (thin lines) or 100 GeV (thick lines). The high-energy cut-off of all these spectra is 3 TeV. The sensitivities of various gamma-ray telescopes are indicated by bands labelled VHC (VERITAS, H.E.S.S., CANGAROO), M (MAGIC), G (GLAST, now *Fermi*). Note that, of the ground-based telescopes, only VERITAS and MAGIC are well-situated for observation of this object. For the ground-based telescopes these bands represent detection after 50 hours of observations and for the satellite, after 5 years. The curves due to particle spectra with a low-energy cut-off of 1 GeV are better suited to HE observations by *Fermi* whereas those due to particle spectra with a low-energy cut-off of 100 GeV should be readily accessible to VHE observatories but more challenging for the satellite. Image credit — from Fig. 9 of B&S07.

Chapter 2

Very High-Energy Emission From Globular Clusters

Here I will define why a globular cluster hosting a population of millisecond pulsars should be a source of very high-energy gamma rays in accordance with the model of B&S07. At its simplest level the emission mechanism requires the coexistence of relativistic electrons (having energies of $\sim 1\,\mathrm{TeV}$) with a dense background of optical photons. But a detailed estimate of any expected flux of gamma rays requires careful examination and determination of these populations and their interactions.

Millisecond pulsars are known to generate relativistic-particle winds and because of this a globular cluster containing them will also host a population of relativistic particles. As a large globular cluster may consist of up to a million stars it will also support an intense field of optical and infrared photons, in addition to being suffused with the ubiquitous **Cosmic Microwave Background** (CMB) radiation. Relativistic electrons ejected from the pulsars may, while contained within the globular cluster, scatter from the ambient photons, boosting the latter to gamma-ray energies. These arguments form the basis of the model proposed in B&S07 .

In the following sections I will discuss in more detail the evidence that millisecond pulsars support relativistic winds of particles and how they are expected to accelerate particles to relativistic energies. In so doing, I note that electrons of energy $\sim 1\,\mathrm{TeV}$ are thought likely to be produced by pulsars. I go on to describe the scattering process that converts low-energy photons into gamma rays by their interaction with relativistic charged particles and in particular the regime in which the resultant gamma ray has energy similar

to that of the initial particle energy. Finally, I will describe the specifics of the implementation of the model in B&S07.

2.1 Particle Acceleration in Millisecond Pulsars

Pulsars are rapidly rotating, highly magnetized neutron stars [84, 171, 38]. The combination of these two properties is in itself promising for the acceleration of charged particles because the rapid rotation of such a dense object represents a great store of rotational kinetic energy, $E_{\rm R}$, and the strong magnetic field a means of coupling that source of energy to charged particles. Indeed, pulsars are observed to slow at an appreciable rate which is interpreted as the action of the magnetic field driving charged particles in their immediate vicinities, transferring energy to them and its surrounding plasma. Some portion of the energy is lost to the emission of radiation, as described below, but this is mediated by the acceleration of charges. The rate of slowing, $\frac{{\rm d}\Omega}{{\rm d}t} = \dot{\Omega}$, is thus related to a spin-down luminosity [192] :

$$L_{\text{s-d}} = \dot{E}_{\rm R} = k\frac{\Omega^4\mu^2}{c^3}(1+\sin^2\chi), \quad k = 1 \pm 0.1 \tag{2.1}$$

where Ω is the rotation rate, μ is the magnetic dipole moment of the pulsar, χ is the angle of inclination of the magnetic axis away from the rotation axis and the uncertainty in k is related to the resolution of the simulations used to derive this general result. The energy extracted from a pulsar's rotation must be transported from the neutron star as either radiation or a wind of magnetised plasma.

Pulsars are characterised by the observation of regular pulses of radiation, as viewed from the Earth, and are known to emit a very broad spectrum of radiation. Their discovery, as a class of astronomical object, was made with radio observations [104, 173] but they have since been discovered in every band of radiation, including gamma rays [20, 205]. Such a broad spectrum is often a feature of relativistic charged particles moving in a magnetic field.

The present understanding of pulsar magnetospheres is based largely upon the seminal work of Goldreich & Julian [85], who outlined the main features imposed by a dominant dipole magnetic field of a rotating object both within the **light-cylinder**, where co-rotation is allowed by relativity,

and beyond it. Later work has focussed upon possible acceleration sites for particles within the light-cylinder of such an object, seeking to explain the eponymous pulsed emission. This leads to estimates of the energy that particles should have, upon leaving these acceleration sites, before entering the interstellar medium of a globular cluster.

I will briefly review some of the observational evidence for the association of winds of relativistic particles with MSPs and then outline the theoretical framework which suggests the mechanism(s) for the acceleration of these particles in the magnetosphere of a MSP.

2.1.1 Observational Evidence for Relativistic Pulsar Winds

'Black-widow' pulsars. PSR J1959+204 (PSR B1957+20) is one of the fastest known pulsars and has a low-mass stellar companion which is surrounded by a cloud of ionised gas [80][78]. It is understood that this cloud has been created by the evaporation of the outer layers of the companion itself due to radiation emanating from the shock wave between this gas and the pulsar's wind[1] [194]. A number of other MSP binary systems show similar properties, including three in the globular cluster 47 Tucanae, namely PSR J0024-7204 J, O & R [44] .

Furthermore, the binary system consisting of PSR J1959+204 and its companion has a large relative velocity with respect to the surrounding interstellar medium. This motion generates enough ram pressure to form a bow-shock where the wind from the pulsar is sweeping up and pushing aside the interstellar medium. Within the shell formed by the bow-shock is observed an X-ray emitting tail of material from the pulsar [193](see Figure 2.1). The existence of this tail coupled with its evidently non-thermal emission demands that the pulsar wind is composed (at least in part) of a population of relativistic particles [193].

***Fermi* millisecond pulsars.** Additional evidence for relativistic electrons in association with MSPs may be drawn from the fact that *Fermi* has observed HE gamma-ray emission from known MSPs [3]. Likewise, radiation

[1] The fact that the companion may be completely eroded within the life-span of the pulsar has led to the latter being dubbed a 'black-widow' pulsar in allusion to the species of spider that devours its diminutive partner after copulation.

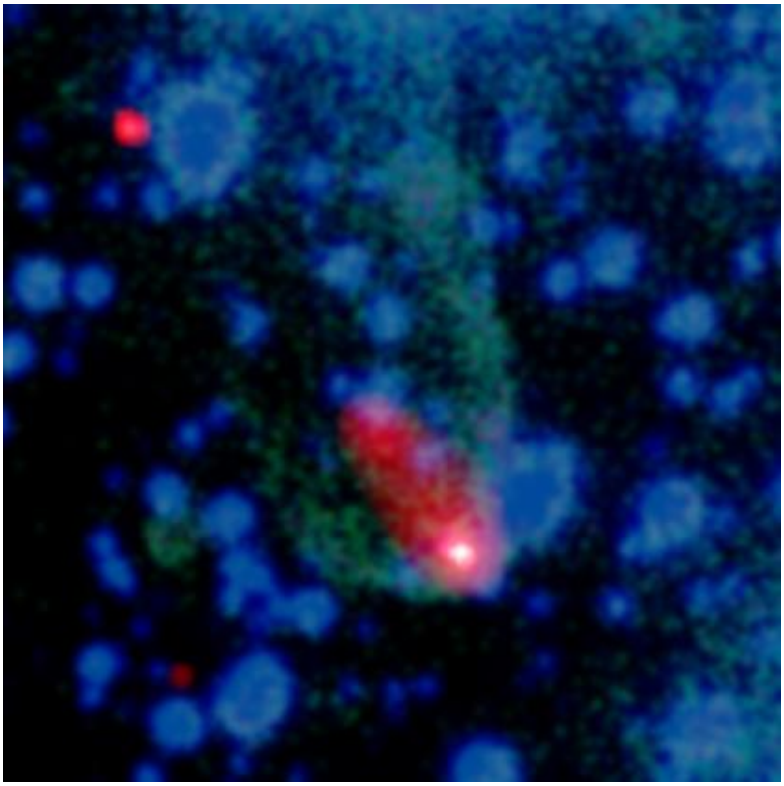

Figure 2.1: A composite X-ray (red/white) and optical (blue/green) image of the region surrounding PSR J1959+204. The bow shock due to the motion of the binary system is the green shell. The elongated, oval region of X-ray emission indicates the presence of relativistic particles filling the cavity in the interstellar medium bored out by the pulsar's motion. Image credit — X-ray: NASA/CXC/ASTRON/B. Stappers *et al.*; Optical: AAO/J. Bland-Hawthorn & H. Jones.

having a similar spectrum has been observed emanating from eight globular clusters [9] where it is interpreted as being the stacked emission from the MSP population of each of these globulars[2]. Such emission is pulsed[3] and this association with the rotation rate of the neutron star is generally as-

[2] Thirteen globulars were examined in this study: M13 (NGC 6502) was not among them.

[3] In the case of the detected globular clusters, the pulsations of the individual pulsars could not be distinguished but the overall spectra were similar to phase-averaged spectra from the known MSPs.

sumed to indicate that it is generated in the vicinity of the pulsar, within the light-cylinder. This region is dominated by the strong dipole magnetic field of the neutron star, as outlined by Goldreich and Julian.

2.1.2 Goldreich & Julian Magnetosphere

Goldreich and Julian [85] developed their model from relatively few assumptions, namely that a pulsar supports an intrinsic dipole field and that it has a conducting surface. For simplicity, it was also assumed that the magnetic and rotational axes are aligned.[4] Given typical characteristics for a pulsar (mass $M = 1\,M_\odot$, radius $R_0 = 10\,\mathrm{km}$, polar magnetic field $B_0 = 10^{12}\,\mathrm{G}$, period $P = 2/\pi\Omega = 1\mathrm{s}$, temperature $T = 10^6\,\mathrm{K}$) they judged that homopolar induction by the intrinsic magnetic field upon the surface would lead to electromagnetic forces more than 10^8 times stronger than the gravitational force upon charges in the surface. This would cause charges to leave the surface and demand that the magnetosphere of the pulsar be filled with a plasma. This plasma would be at least sufficient to supply what has become known as the **Goldreich-Julian charge density**, a co-rotating (on average) charge distribution of the form :

$$\rho_{\mathrm{GJ}} = -\frac{\mathbf{\Omega}\cdot\mathbf{B}}{2\pi c[1-(\Omega r/c)^2\sin^2\theta]} \tag{2.2}$$

expressed in the usual polar coordinates (r, θ, ϕ), with θ measured from the rotation axis. This distribution acts to shield the intense induced electric field along the co-rotating magnetic field lines within the light cylinder. The poloidal component of the magnetic field, that in the (r, θ) plane, is shown in Figure 2.2. The azimuthal (ϕ) component of the field is effectively zero close to the neutron star but becomes increasingly dominant with radius such that the magnetic field lines resemble a tightly wound spiral beyond the light cylinder.

In such an environment, the charges may be thought of as moving force-free but with the constraint that they move along magnetic field lines because the energy of charged particles due to the magnetic field greatly exceeds their kinetic and gravitational energies. In this way, the magnetic field lines also define electric equipotentials: charges can rearrange themselves to eliminate

[4] If the magnetic and rotational axes are anti-aligned, the roles of negatively and positively charged particles are reversed.

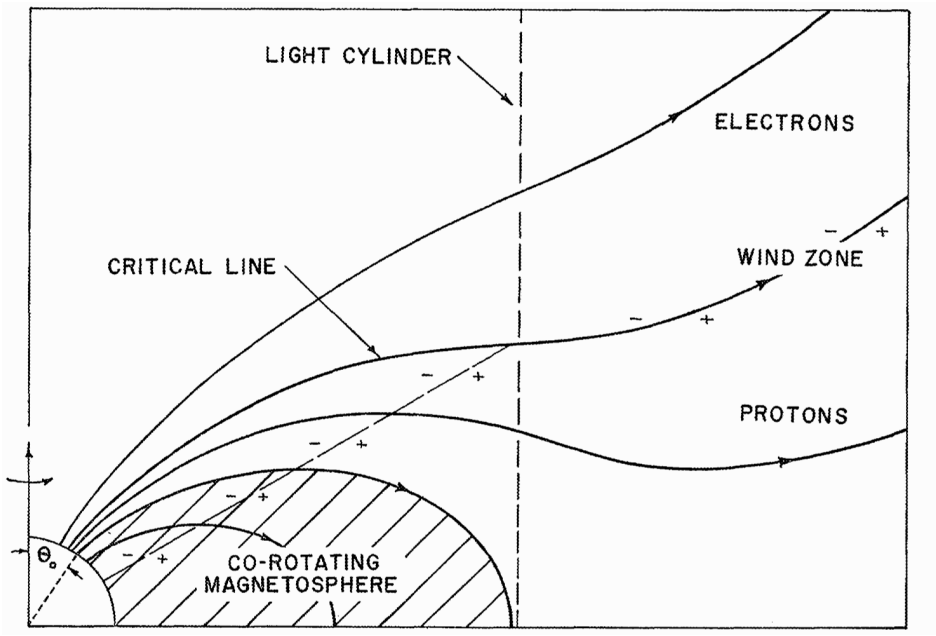

Figure 2.2: Schematic of the poloidal structure of the Goldreich-Julian magnetosphere: Fig. 1 of [85]. The critical field line rests at the potential of the interstellar medium: oppositely charged species stream out above and below this line. The null charge surface is the locus of points where the magnetic field lines are locally perpendicular to the axis of rotation (vertical in this diagram): the co-rotating plasma must be neutral here. It is indicated by the diagonal line from the pulsar's surface to the light cylinder: above the plasma is negative, below it is positive.

any potential difference parallel to the magnetic field lines but not perpendicular. The magnetic field lines can thus be considered as behaving much like wires, the charges being carried freely along them, and the overall potential of the field line is set by the point, θ_0, at which it intersects the pulsar's surface, where homopolar induction maintains a large potential difference between the pole and other parts of the surface. The arrangement of magnetic field lines will dictate the path of any charges flowing from the surface.

The major constraint on the form of the magnetosphere is the light-cylinder: this is defined as the cylindrical radius, $R_{\rm lc}$, about the axis of rotation at which a co-rotating point would have a tangential speed equal to that of light $c = R_{\rm lc}\Omega$. Co-rotation is therefore impossible at and beyond the light cylinder. Magnetic field lines which emanate from the surface relatively far from the axis of rotation have a relatively small radius of curvature and will close within the light cylinder, i.e. they can be traced back to the surface near the other magnetic pole. The field line that closes just within the light cylinder is dubbed the last closed field line. Within the volume defined by this field line, only the afore-mentioned co-rotating charge density exists.

Those lines which are rooted closer to the axis of rotation than the last closed field line will pass beyond the light cylinder and must continue out towards the interstellar medium. As these magnetic field lines represent electric equipotentials those rooted near the pole ($\theta_0 = 0$) will carry a very low potential and those rooted near the last closed field line ($\theta_0 = \arcsin[\sqrt{\Omega R\ c}]$) will carry a very high potential; somewhere between the two must exist a critical field line whose potential is close to that of the interstellar medium. Far from the pulsar, charged particles can move off the weakening magnetic field lines to neutralise the large potential difference :

$$\Delta\Phi \sim \frac{1}{2}\left(\frac{\Omega R}{c}\right)^2 RB_0 = \frac{\Omega^2\mu}{2c^2} \tag{2.3}$$

In this way the open field lines provide a path, all be it a circuitous one, across the large potential difference supported by homopolar induction and particles stream along these field lines from the surface. Above the critical field line electrons must stream out, along the magnetic field lines, towards the small potential of the interstellar medium and likewise protons below the critical field line. So, where the pulsar magnetosphere abuts the interstellar medium, discharge across the magnetic field lines accelerates previously streaming particles to highly relativistic energies; in fact, Goldreich and Julian assert that in this boundary zone much of the angular momentum and

energy carried away from the pulsar by the electromagnetic field is transferred to streaming particles until equipartition is achieved. In principle, charged particles could be accelerated to a maximum energy proportional to the potential difference between the last closed field line and the pole: $E_{e,\max} \sim e\Delta\Phi$, where e is the electron charge. For a 'typical' MSP as defined in B&S07 $(B_0 = 10^9\,\mathrm{G}\,,\ P = 4\,\mathrm{ms}\,)$ $E_{e,\max} \sim 200\,\mathrm{TeV}$. A similar estimate may be arrived at in more modern theories of pulsar winds [27], a subject to which I return in §6.1.3, but this does not form part of the basis of the argument laid out in B&S07 so I shall not dwell on it here.

Being based on so few assumptions, the Goldreich-Julian model is generally assumed to capture the gross features of pulsar magnetospheres but it suffers the critical flaw that it contains no mechanism for generating pulsed emission and particularly gamma-ray emission. Firstly, it is axisymmetric and thus the rotation of the neutron star cannot cause time-dependent emission. Secondly, once the Goldreich-Julian charge density is established around the neutron star, there is no means of accelerating electrons to gamma-ray emitting energies *within the light cylinder*: considered necessary to tie pulsations to the rotation rate of the neutron star. Soon after the proposal of this model, it was argued [160] that most of the features would be preserved in extension to a non-aligned case, one in which the magnetic axis was tilted with respect to the rotation axis; this allows the model to represent, at least in principle, a real pulsar. To remedy the second flaw, much attention was subsequently devoted to locating regions of the inner magnetosphere which might provide exceptions to the Goldreich-Julian rule: gaps[5] in the shielding charge density which could expose charges to the powerful induced electric field. As stated by Mestel [161]

> Much of the discussion ... centres around the domains of validity of the Goldreich-Julian approximation ... and the consequences of its breakdown.

2.1.3 Vacuum Gap Acceleration

Adaptation of the Goldreich-Julian model to allow for particle acceleration has focussed on the creation of so-called vacuum gaps in the co-rotating charge distribution. Such a gap (which may be an under-density rather than a complete evacuation) has an insufficient population of charges to cancel

[5] Some have dubbed this somewhat esoteric sub-field 'gapology' [28].

the induced electric field and instead allows acceleration of charges within the light cylinder. Curvature emission from these charges is used to account for the eponymous pulsed emission[6] from these objects. Acceleration within these vacuum gaps tends to be radiation-reaction limited, achieving a steady state between acceleration and acceleration-induced radiation losses. Thus a significant portion of the particles accelerated in these gaps will accumulate at some maximum energy (e.g [161], [105]). Furthermore, it may be argued, as is assumed in [201] and [202], that whatever spectrum of particle energies exists at the light-cylinder may be preserved as particles continue along field lines towards the interstellar medium. For instance, in the Goldreich-Julian model the poloidal component of the field is asymptotically radial beyond the light-cylinder such that it may be possible to ignore any further loss of energy to curvature radiation as the charges stream out in the relativistic wind.

Three prinicpal geometries of vacuum gaps have been postulated: the polar cap, slot gap and outer gap, see Figure 2.3.

2.1.3.1 Polar-Cap

Proposed by Sturrock [195] it was postulated that the supply of charges from the surface of the pulsar is limited such that the streaming current along open field lines is insufficient to support the Goldreich-Julian density. Those charges which are extracted from the polar cap (the region defined by the base of the open field lines) are thus exposed to an accelerating electric field [164].

Now, accelerated charges will promptly emit curvature radiation which may subsequently be absorbed on the magnetic field through pair-production of electrons. If the magnetic field is strong enough, this process can be so efficient as to create a pair-formation front [92], above which the region of open field lines is populated with a sufficient density of charges to screen the electric field. However, if the magnetic field is weak, as may be expected for MSPs because of their low spin-down rates, pair-production from

[6]This mechanism can account for pulsed optical, non-thermal X-ray and gamma-ray signals for which incoherent emission scenarios are sufficient. As a charge accelerates in one of these vacuum gaps, it does so along a magnetic field line; its path is forced to curve with the magnetic field line and it radiates in response to this lateral acceleration.

Pulsed radio emission requires a rather more complex scenario involving coherent emission.

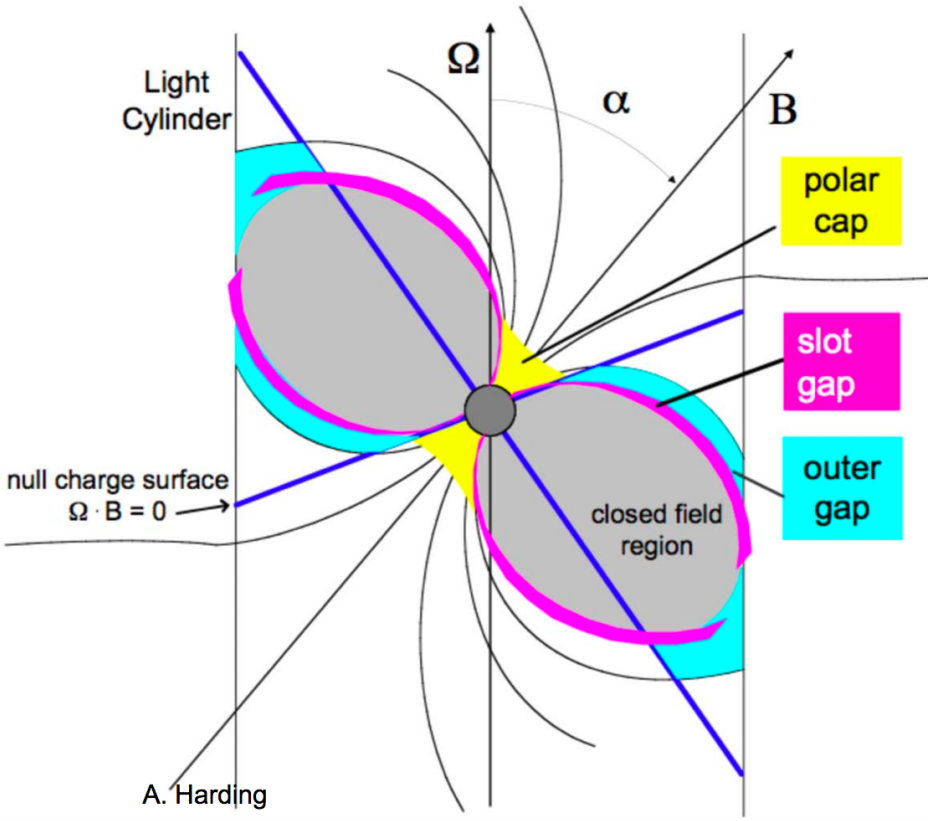

Figure 2.3: The three commonly proposed locations for vacuum gaps in pulsar magnetospheres.

curvature radiation may be limited and a so-called pair-starved polar cap magnetosphere will result [166, 167] in which electrons from the surface can be accelerated all the way to the light cylinder. In this case electrons should attain a curvature radiation-limited Lorentz factor $\sim 10^7$ as they cross the light cylinder [166].

This model has been used to motivate the two main studies [36, 202] concerning VHE gamma-ray emission from globular clusters. However, results from *Fermi* [3] now suggest that only a minority of MSPs conform to the expectations of the pair-starved polar cap model. That is, their pulsed emission is consistent with an origin close to the pulsar's surface where the accelerating electric field is strong but the HE emission is not damped by an intense magnetic field. In contrast, *Fermi* observations prefer high-altitude emission from most MSPs such as that predicted by the 'slot-gap' or 'outer-gap' scenarios of acceleration within the light cylinder. I will briefly indicate that these alternatives can stand in for the polar cap model.

2.1.3.2 Slot-Gap

The slot-gap scenario is an extension of the polar cap model in the case where the magnetic field is strong and most of the region of open field lines is populated by pair production from curvature radiation [92]. In this case, the induced electric field above the pulsar is shielded at high altitudes except for those open field lines rooted at the rim of the polar cap, bordering the last closed field line. At this boundary, between the open and closed portions of the magnetosphere, the bare electric field is partially shielded by the conducting surface of the co-rotating charge density within the last closed field line. Thus charges emitted by the neutron star's surface at the rim of the polar cap remain less energetic than those emitted closer to the pole: they do not emit enough or sufficiently-energetic curvature radiation to establish a pair-formation front at low altitude. Therefore, a narrow region of space charge deficit persists between the last closed field line and the majority of the polar cap: the so-called slot-gap [165].

The electric field in the slot-gap is not as intense as it would be elsewhere above an unshielded polar cap but, because it is not shielded by plasma, it continues to higher altitudes where both field line curvature and the strength of the magnetic field are diminished. Thus particles continue to accelerate to high altitude, even as far as the light cylinder and, again, Lorentz factors of $\sim 10^7$ are expected.

It is not clear, however, how this model can apply to millisecond pulsars as a mechanism for populating the open field lines over the centre of the polar cap is required. It has been speculated [3] that a multipole magnetic field may be present in these objects, providing a much stronger magnetic field near the surface and thus allowing copious acceleration, curvature radiation and pair production at low altitude resulting in a pair-formation front that could shield most of the polar cap. Such a magnetic field would reduce to a dipole field farther out and, in this case, acceleration in the slot gap at high altitude will approximately follow the behaviour of the standard slot gap described here.

2.1.3.3 Outer-Gap

This scenario is constructed using a distinctly different approach to justify the presence of vacuum gaps. It may be argued [112] that the co-rotating plasma is charge-separated: that is to say positive and negative charges do not co-exist. This is justified [113] by the assertion that the powerful gravitational field of the neutron star will strip out any charges of sign opposite to those required by the Goldreich-Julian charge density at a given point: the charge density is reduced to only those charges which are necessary.

Due to homopolar induction, the charge distribution is negative near the poles and positive near the equator and the dividing line, where $\mathbf{\Omega} \cdot \mathbf{B} = 0$ is dubbed the null-charge surface. Furthermore, certain open field lines cross this boundary before passing through the light cylinder. These field lines are rooted in the negative portion of the charge distribution and are unable to supply positive streaming charges across the null-charge surface. The charges cannot be replenished from the surface of the pulsar and inevitably a charge deficit will develop outside the null-charge surface [56]. The region of charge deficit formed in this way has been christened the outer gap.

Given the presence of an outer gap, a self-sustaining process can exist whereby thermal X-rays from the hot surface of the pulsar undergo pair-production with curvature radiation from charges accelerated in the outer gap: the pairs so produced are accelerated in opposite directions, electrons falling and heating the surface and positrons rising, accelerating and generating more curvature radiation [183, 212]. Recent iterations of this model [213] explain well X-ray emission from millisecond pulsars and suggest radiation-reaction limited Lorentz factors $\sim 10^7$ for electrons approaching the light cylinder directly from the outer gap.

2.2 Production of Gamma Rays by Scattering of Stellar Photons

I have outlined the observational evidence for MSPs as sources of relativistic particle winds and touched upon the theoretical bias suggesting that particles may leave the vicinity of these objects with ~ 1 -TeV energies. As highly relativistic electrons move through a globular cluster they will be influenced by the environment of the interstellar medium. The primary feature of this environment is the intense photon field due to the combined luminosity of stars which form the visible component of the globular cluster. There likely also exists a magnetic field in this interstellar medium.

Electrons with energies $\sim 1\,\mathrm{TeV}$, as we can expect from millisecond pulsars, may generate synchrotron emission at lower energies due to their paths bending in the magnetic field. However, emission of gamma-rays in the very-high-energy regime will occur via inverse Compton scattering of ambient photons. The latter could be optical or infra-red photons due to the, approximately black-body, stellar radiation or even less energetic photons from the omnipresent cosmic microwave background radiation.

2.2.1 Inverse Compton Scattering

Inverse Compton (IC) scattering is an expression of one of the most fundamental interactions of quantum electrodynamics allowed by energy and momentum conservation. It involves only one in-going and one out-going photon mediated by a single electron, see Figure 2.4. In the particular case of IC scattering, the energy of the outgoing photon is greater than that of the ingoing one, at the expense of the energy of the electron. This is in contrast to the photon losing energy to the electron, which defines Compton scattering. Such a distinction is essentially one of reference frame and it is instructive to consider instances of IC scattering, (where energy is transfered to the photon in the *observer's* frame of reference) in a different reference frame, one in which the electron is initially at rest (the rest frame)[7] or one in which the centre of momentum of the interacting objects is stationary throughout (the CoM frame). These frames of reference are related by the Lorentz transformations.

[7]Note that the rest frame, by definition, fulfills the definition of Compton scattering, not IC scattering. Nevertheless, it is simply a different view of the exact same process.

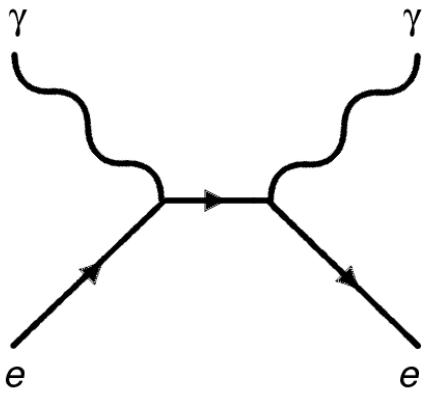

Figure 2.4: The lowest order Feynman diagram for (inverse) Compton scattering. For Compton scattering the electron (e) gains energy; for inverse Compton scattering the photon (γ) gains energy.

Considered from the reference frame of the observer, in the core of a globular cluster highly relativistic electrons move through an isotropic field of low energy photons, see Figure 2.5(a). Individual photons, with energy ε, may encounter an electron at an incident angle θ, with respect to the electron's direction of motion, before being scattered. Using the transforms as defined by Longair (Eq. 4.26 from [142]), in the rest frame the corresponding angle, θ' (see Figure 2.5(b)), is given by :

$$\tan\theta' = \frac{\sin\theta}{\gamma(\cos\theta + \beta)} \tag{2.4}$$

where γ is the Lorentz factor of the electron and βc defines its velocity, both in the observer's frame.

Now, as described by Blumenthal & Gould [42], for our purposes $\beta \approx 1$ and $\gamma \gg 1$ such that $\theta' \simeq 0$ for almost all θ. Thus, for large γ, the situation in the rest frame approximates Compton scattering of an electron by a beam of photons, see Figure 2.6: this putative beam is directed anti-parallel to the electron's observer-frame motion. The photons in the beam have energy $\varepsilon' = \gamma\varepsilon(1 + \beta\cos\theta)$, as given by the Lorentz transformations.

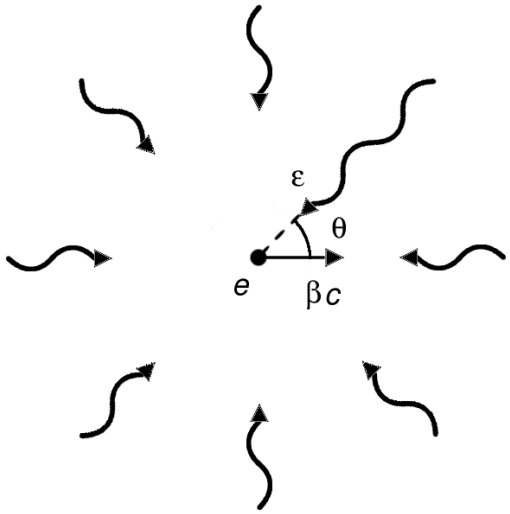

(a) The observer's frame

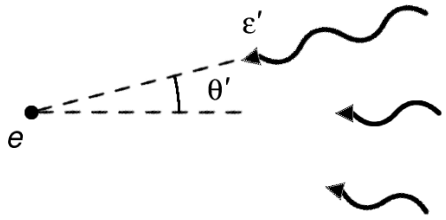

(b) The rest frame

Figure 2.5: Initial geometry of inverse Compton scattering in the observer's and electron rest frames.

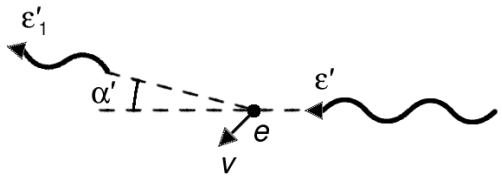

Figure 2.6: Photon scattering angle in the electron rest frame.

2.2.1.1 Scattering Rate and Particle Densities

In the situation described above, in the rest frame, scattering occurs at a rate per electron :

$$\frac{\mathrm{d}N'}{\mathrm{d}t'} = c \int \sigma \, \mathrm{d}n' \tag{2.5}$$

where σ is the interaction cross-section and I follow [42] in defining $\mathrm{d}n'$ as the differential photon density of, for instance, a distribution over energy or frequency ($\mathrm{d}n' = \int \mathrm{d}\varepsilon' \, \mathrm{d}n' / \mathrm{d}\varepsilon'$). They go on to identify that the quantity $\mathrm{d}n / \varepsilon = \mathrm{d}n' / \varepsilon'$ is an invariant under the Lorentz transformations (whereas time dilation requires $\mathrm{d}t = \gamma \, \mathrm{d}t'$), such that the scattering rate in the observer's frame may then be defined :

$$\begin{aligned} \frac{\mathrm{d}N}{\mathrm{d}t} &= \frac{\mathrm{d}N'}{\gamma \, \mathrm{d}t'} && (2.6) \\ &= \gamma^{-1} c \int \sigma \frac{\mathrm{d}n}{\varepsilon} \varepsilon' && (2.7) \\ &= c(1 - \beta \cos\theta) \int \sigma \, \mathrm{d}n && (2.8) \end{aligned}$$

For an isotropic photon field in the observer's frame, averaging over θ removes the trigonometric term but we must also average over the energy distribution of photons (*e.g.* the black-body distribution $\nu(\varepsilon)$), with a possible dependence

of the cross-section upon the photon energy :

$$\frac{\mathrm{d}N}{\mathrm{d}t} = c \int \sigma(\varepsilon)\,\mathrm{d}\varepsilon\,\frac{\mathrm{d}n}{\mathrm{d}\varepsilon} \quad (2.9)$$

$$= c \int \sigma(\varepsilon)\cdot\nu(\varepsilon)\,\mathrm{d}\varepsilon \quad (2.10)$$

Recall that this is the scattering rate *per electron* and, therefore, the flux of gamma rays depends upon the abundance of relativistic electrons and the population of ambient photons and also the probability that the former will scatter the latter, as expressed by the cross-section. Any model of IC scattering of stellar photons to VHE gamma rays must include these elements: the photon density as a function of energy and location in the cluster, the interaction cross-section (including any energy dependence) and the flux of relativistic electrons. I will describe below the implementation of one such model as presented in B&S07 but I will now continue the discussion of IC scattering in order to justify the assertion that it may convert stellar photons into VHE gamma rays.

2.2.1.2 Cross-Section and Scattered Spectrum

The probability for the scattering of a photon from a charged particle is defined at low energies by the Thomson cross-section, which represents the classical limit of the process and rests on the assumption that the photon can be approximated by a continuous wave-form with respect to the charged particle. Scattering in this regime is essentially coherent in the rest frame with the initial and final photon energies being the same and the electron recoil being negligible.

The Thomson cross-section is valid for IC scattering in so far as the photon energy in the centre of momentum frame is much less than that of the electron rest energy. In this case the centre of momentum frame and the rest frame are essentially equivalent and recoil of the electron can be disregarded. For electrons that are relativistic in the observer's frame of reference, the conditions for approximately coherent scattering can still be met *in the rest frame* (*i.e.* $h\nu' = \varepsilon' = \gamma\varepsilon(1+\beta\cos\theta) \ll m_e c^2$) for photons of sufficiently small observer-frame energy (ε). Even in this case, very energetic gamma rays may result: from the rest frame, the scattering is, by definition,

Compton scattering and kinematics[8] dictates :

$$\varepsilon_1' = \frac{\varepsilon'}{1 + (\varepsilon'/mc^2)(1 - \cos\alpha')} \approx \gamma\varepsilon(1 + \beta\cos\theta) \tag{2.11}$$

such that, in transforming energies to the observer's frame[9] (before letting $\beta \to 1$) :

$$\begin{aligned} \varepsilon_1 &= \gamma\varepsilon_1'(1 + \beta\cos(\pi - \alpha')) && (2.12)\\ &\approx \gamma[\gamma\varepsilon(1 + \cos\theta)](1 - \cos\alpha') && (2.13)\\ &\leq 4\gamma^2\varepsilon && (2.14) \end{aligned}$$

where in the last step I choose $\theta = 0$ and $\alpha' = \pi$ to find the upper limit to the energy of the scattered photon. In this way, in a head-on collision between an ambient photon and relativistic electron where the photon's direction of motion is completely reversed, the transformation of the photon energies back and forth from the observer's frame of reference, leads to a significant boost in photon energy. Each change of reference frame involves a factor of γ so that coherent scattering in the rest frame can leave the initial and final photon energies differing by a factor of γ^2. In this manner, energetic gamma rays may be created by IC scattering in the Thomson regime, without approaching the non-classical limit, given a population of sufficiently low energy seed photons and sufficiently energetic electrons: *e.g.* scattering of the cosmic microwave background radiation (up to $10^{-3}\,\mathrm{eV/photon}$) by 5-TeV electrons ($\gamma \sim 10^7$) may produce gamma rays of up to $\sim 0.1\,\mathrm{TeV}$.

Klein-Nishina suppression. If the electron and photon energies are more closely matched, the photon energy in the centre of momentum frame will approach that of the electron. Equivalently, as the photon wavelength approaches that of the Compton wavelength ($\lambda_\mathrm{C} = h/(m_\mathrm{e}c)$) the assumptions allowing validity of the Thomson cross section no longer apply, to wit the simple approximation of a particle being stimulated by a passing electromagnetic field is no longer valid, and a full quantum treatment is required. Such a treatment results in the Klein-Nishina cross section (see §7.1 in [186]) which is identical to the Thomson cross-section in the classical limit but decreases

[8] Refer to §7.1 of [186] for details.

[9] I omit α' from this transformation for simplicity and because it will be used to maximise the function below.

for increasing scattered-photon energy. This is referred to as Klein-Nishina suppression: scattering is less likely for large energy transfer and, for a given electron energy, the suppression is greater with increasing initial photon energy.

For instance, for electrons of Lorentz factor $\gamma \sim 10^7$ moving through a black-body spectrum of characteristic temperature 6000 K , mid-infrared photons are most likely to be scattered (see Figure 2.7), even though the black-body distribution peaks in the optical. Also, the photons most likely to be scattered do so with a Klein-Nishina cross-section which is less than one sixth of the Thomson cross section. Thus, inverse Compton scattering of this black-body radiation is less efficient than that of the cosmic microwave background.

Spectral saturation. However, the former remains significant because of a peculiarity in the spectrum of gamma rays generated by scattering in the Klein-Nishina limit. Essentially, IC scattering in the extreme Klein-Nishina limit is saturated in the sense that the energy of the scattered photon will be almost equal to the initial energy of the electron. This follows from the greater recoil of the electron (in the centre of momentum frame) as larger initial photon energies are considered.

Thus, all scattering of optical photons, representing the bulk of these black-body photons, will lead to gamma rays with similar energies, introducing a distinct peak to the emitted spectrum. This result was derived for $\gamma \gg 1$ by Jones [119] (see also [42]) and is summarised by the following expression which describes the spectral distribution of scattered photons :

$$\frac{\mathrm{d}N}{\mathrm{d}t\ \mathrm{d}\varepsilon_1} = \frac{2\pi r_0^2 c}{\gamma^2} \times \left[2q\ln q - 2q^2 + q + 1 + \frac{1}{2}\frac{(\Gamma q)^2}{1+\Gamma q}(1-q)\right] \times \frac{n(\varepsilon)\,\mathrm{d}\varepsilon}{\varepsilon} \tag{2.15}$$

with :

$$\Gamma = \frac{4\gamma\varepsilon}{mc^2},\ q = \frac{\varepsilon_1}{\Gamma(E_e - \varepsilon_1)}$$

where ε is the initial energy of the photon and γ is the Lorentz factor of the electron, such that $E_e = \gamma mc^2$ is its initial energy.

Figure 2.8(a) shows the (normalised) spectral distributions of photons scattered by 5 -TeV electrons from various target photon energies, with the scattered photon energy in units of the maximum value it can attain as

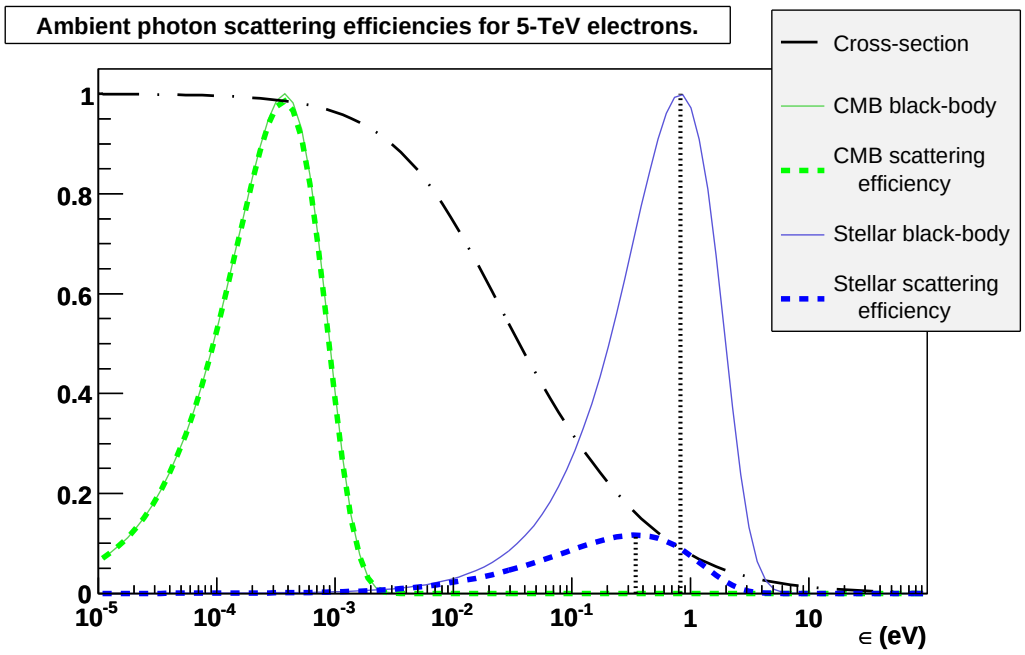

Figure 2.7: The effect of Klein-Nishina suppression on the scattering efficiency of 5 -TeV electrons from the CMB and from stellar photons. The black-body distributions due to the CMB (green, left) and stellar radiation (blue, right) at 6000 K are indicated by thin, solid lines. In both cases the distributions have been normalised for the peak to reach 1. The Klein-Nishina scattering cross-section, as a fraction of the Thomson cross-section, is the black dot-dashed line. The product of each black-body spectrum with the scattering cross-section is indicated by thick dashed lines: these curves demonstrate the efficiency with which black-body photons are scattered by 5 -TeV electrons. The CMB spectrum is scattered with nearly uniform efficiency in the Thomson limit of IC scattering: the distribution of photons that are scattered is not distorted with respect to the original black-body distribution. In comparison, the stellar photons are scattered disproportionately due to the onset of Klein-Nishina suppression: the separation of the most common stellar photon (the peak of the black-body distribution) and the most-likely scattered stellar photon (the peak of the black-body/cross-section product) is indicated by the vertical dotted lines. There is essentially zero separation in the case of the CMB for which Klein-Nishina suppression is effectively negligible. Note that at even greater electron energies the cross-section curve shifts to the left, Klein-Nishina suppression sets in at lower target photon energies and even scattering of CMB photons will be subject to this effect, for electrons an order of magnitude more energetic.

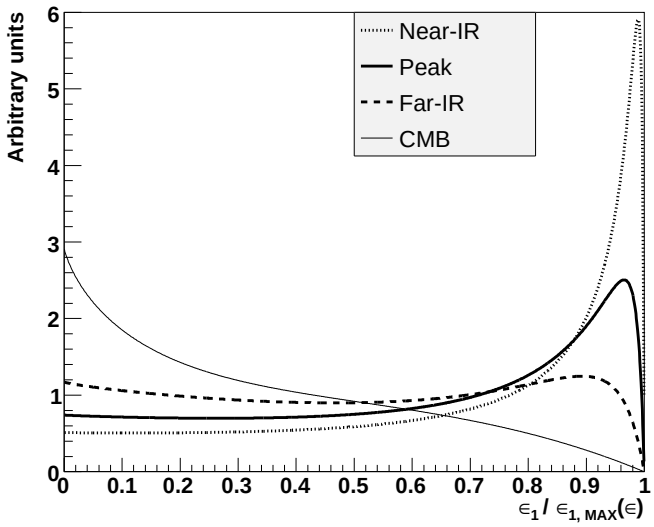

(a) Scattered photon spectrum as fraction of maximum.

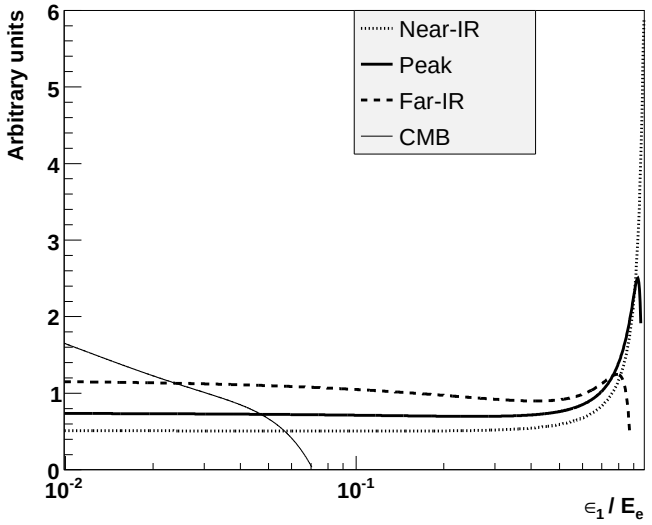

(b) Scattered photon spectrum as fraction of initial electron energy.

Figure 2.8: The normalised spectrum of scattered photons from 5-TeV electrons for various seed photon energies.

allowed by kinematics (energy and momentum conservation) [42] :

$$\varepsilon_{1,\mathrm{MAX}} = E_e \frac{\Gamma}{1+\Gamma} = \frac{4\gamma^2 \varepsilon}{1+\Gamma} \tag{2.16}$$

This demonstrates the strong peak attained in deep Klein-Nishina scattering (large target photon energy).

Figure 2.8(b) shows the same curves but expressed in terms of the initial electron energy, (*i.e.* the total available energy). It can be seen that (Thomson) scattering from CMB photons generates photons of energy $\sim$1% that of the electron energy, gradually sapping an electron's energy over the course of multiple collisions. In comparison, scattering in the deep Klein-Nishina regime preferentially generates photons of energy close to the maximum available: the electron delivers almost all of its energy to the photon in the majority of these collisions.

Thus, VHE emission due to $\sim$1-TeV electrons in globular clusters is possible via the scattering of near infra-red and optical photons. Furthermore, even though the scattering of these photons is strongly suppressed (relative to that of CMB photons), it generates very similar scattered energy regardless of the exact target photon energy, such that scattering from the bulk of the stellar radiation field is cumulative in the domain of VHE gamma-ray emission. These traits lead to the particular form of emission spectra predicted for globular clusters, which is particularly evident for the case of mono-energetic electrons being ejected directly from MSPs (see Figure 2.9) in which case scattering of the CMB contributes a continuum and scattering of the (mostly optical) stellar photon field contributes a prominent peak in the VHE domain.

2.3 Model of VHE Emission

I have identified the supporting observational and theoretical information and the essential components of any model of this emission mechanism. The flux of gamma rays escaping any particular region of the globular cluster in question will depend upon the local density of target photons and the flux of relativistic electrons passing through them. At any point in a globular, the target photon field intensity will be a combination of the CMB and the intensity of light from the surrounding stars. In turn, the population of relativistic electrons circulating in a cluster will be directly related to the

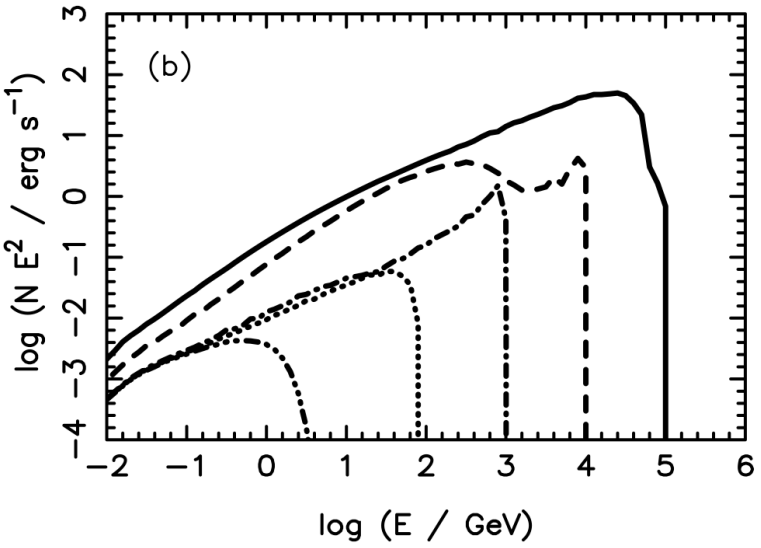

Figure 2.9: Differential gamma-ray energy spectra produced by the IC scattering of the CMB and a globular cluster stellar radiation field by mono-energetic leptons diffusing from the core of the cluster, as presented in B&S07. The modelled globular cluster has a luminosity of $10^6\,L_{\odot}$. Lepton energies are $E_e = 0.01\,\mathrm{TeV}$ (triple-dot-dashed curve), $0.1\,\mathrm{TeV}$ (dotted curve), $1\,\mathrm{TeV}$ (dot-dashed curve), $10\,\mathrm{TeV}$ (dashed curve) and $100\,\mathrm{TeV}$ (solid curve). For each curve the power of electrons injected into the core corresponds to one particle per second. For the 10-TeV curve the 'bump' due to IC scattering of the CMB in the Thomson regime can be contrasted with the 'peak' at the highest energies due to the, strongly suppressed, IC scattering of stellar radiation in the Klein-Nishina regime. At lower electron energies the spectrum is dominated by scattering of stellar radiation. Image credit — from Fig. 2 in B&S07.

total power which pulsars are emitting in the core of a globular. The local flux of relativistic electrons will depend upon how they diffuse through the cluster and also more subtly upon the cooling of the population by radiation and escape. B&S07 lays out a simulation of these density distributions within specific globulars which has yielded predictions of VHE gamma ray flux and I now describe the implementation of this model as described in that work.

2.3.1 Photon Field and Luminosity Profile

The most accessible component of this model is the ambient photon field as observational evidence for the factors contributing to it are well established. Any region of the universe, globular clusters not being exceptions, is bathed in the CMB which has a well defined spectrum and density: it is a black-body with an effective temperature of 2.73 K and has an energy density of 0.25 $\mathrm{eV{\cdot}cm^{-3}}$. In addition to this, the visible stellar population of a globular supplies plentiful optical and infrared photons. B&S07 assumes that the luminous component of each globular is dominated by Sun-like stars producing approximately black-body emission at an effective temperature of 6000 K .

The distributions of stars within globulars are perceived as luminosity profiles which have been the subject of detailed study and have been found to be well parametrised by the King model (initially stated as an empirical law [126], it later received physical explanation and justification [162, 127, 128]). It consists of a family of curves whose shape is defined only by the ratio of a core radius and a limiting tidal cutoff radius, where stars are no longer bound to the cluster but instead orbit the Galaxy directly. The observed luminosity profile of a globular is a projection on the sky of its stellar density. The latter may be derived from the former with only the assumption of spherical symmetry [175, 126]. For the purposes of the model of B&S07, the stellar density as a function of radius, as derived from the King model, is described by an approximation due to Kuranov & Postnov [139]. This amounts to a set of power-laws defined for three regions of a globular with boundaries at the core radius, r_c, half-mass radius, r_h, and tidal radius, r_t :

$$\rho(r) = \begin{cases} \rho_\mathrm{c} & \text{if} \quad r \leq r_\mathrm{c} \\ \rho_\mathrm{c}(r/r_\mathrm{c})^{-2} & \text{if} \quad r_\mathrm{c} < r \leq r_\mathrm{h} \\ \rho_\mathrm{c}\frac{2}{3}(r_\mathrm{t}/r_\mathrm{c})(r/r_\mathrm{c})^{-4} & \text{if} \quad r_\mathrm{h} < r \leq r_\mathrm{t} \end{cases} \tag{2.17}$$

where ρ_c is, by definition, the central stellar density (or equivalently the central luminosity density) and the half-mass radius is related to the other characteristic radii by $r_h = \sqrt{2 r_c r_t / 3}$. The form of the function is parametrised by the ratio of r_t to r_c, which is a legacy of the King model in which it is termed the **concentration**. This model of the stellar density function can be calibrated for any particular globular using the observed core size and concentration (*e.g.* see Table A.2) and the central luminosity density. The latter is defined in [139] to be $\rho_c = L_{tot}/[8\pi\sqrt{\frac{2}{3}} r_c^3 (\sqrt{\frac{r_t}{r_c}} - 1)]$ in terms of a cluster's total luminosity, L_{tot}: this definition ensures that the integral of the approximate model is normalised to the total luminosity.[10] An example, using the parameters of M13, is shown in Figure 2.10(a).[11]

At any point within the globular the intensity of the stellar photon field may be calculated by integration of the stellar density function, weighted by the inverse square law, over the whole cluster. In particular B&S07 states that the energy density of the stellar photon field in the core of a globular having a total luminosity of L_{GC} is given by :

$$U_{ph} = \frac{L_{GC}}{c r_c^2} \frac{18 - 3\sqrt{6} R^{-1/2} - 2R^{-2}}{6(\sqrt{6} R^{1/2} - 2)} \quad , \qquad R = \frac{r_t}{r_c} \tag{2.18}$$

This may be simplified to :

$$U_{ph} \approx \frac{L_{GC}}{c r_c^2} \sqrt{\frac{3}{2}} R^{-1/2} \simeq \frac{L_{GC}}{c r_c r_h} \tag{2.19}$$

where I have used the fact that $r_t \gg r_c$ (*i.e.* $R \gg 1$) in the approximation. As might be expected, for a given total luminosity, a more compact cluster has a greater photon energy density in its core. For the case of M13 this evaluates to $\sim 240\,\mathrm{eV{\cdot}cm^{-3}}$ which greatly exceeds the photon energy density of the

[10] I note also that B&S07 defines a different normalisation for this model: $A = \frac{N_{tot}}{r_c}/[2 - (\frac{3}{2}\frac{r_t}{r_c})^{-1/2} - \frac{2}{9}(\frac{r_t}{r_c})^{-2}]$, where N_{tot} is the total number of stars in the cluster (or equivalently the total luminosity). However, in the context in which this is introduced, it is not clear how this is applied and the units are evidently not those of density. Regardless, [139] is cited explicitly by B&S07 and Fig. 1 of the latter is consistent with the normalisation defined in the former and with Fig. 2.10(a) here.

[11] In light of the smooth, accurate and easily computed function for the stellar density provided by Eq. 27 of [126] and shown in 2.10(a), it is curious that B&S07 (or, indeed, [139]) should have elected to make *any approximation* to a King model instead of using this exact form.

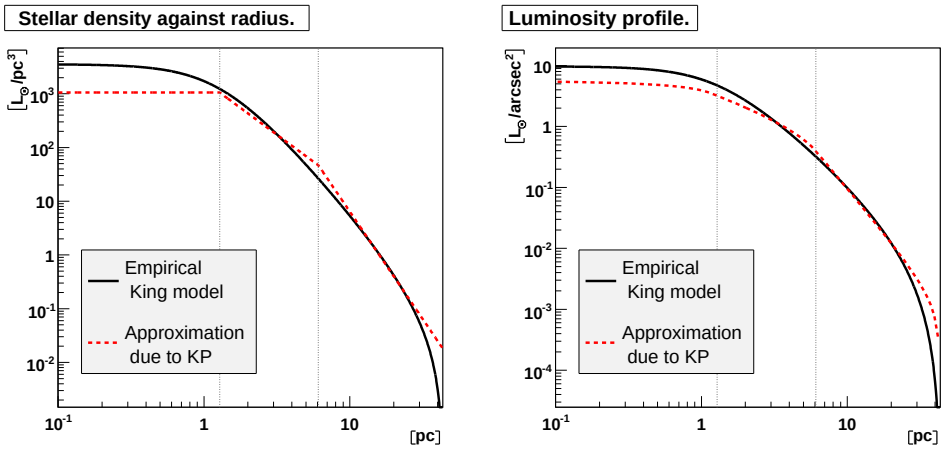

(a) Stellar density function for M13. (b) Brightness profile of M13.

Figure 2.10: The approximation of the stellar density function due to Kuranov & Postnov [139], (a), is uniform within the core radius (left-hand vertical grey line) and a pair of power laws of differing slope outside that. The power-law break is at the half-mass radius (right-hand vertical grey line) and the model ends at the tidal radius (the upper limit of the horizontal axis): beyond this the stellar density for the cluster is zero. Meanwhile, the empirical King model, (b), is an excellent representation of the observed distribution of stars in M13 as projected onto the plane of the sky, (see Fig. 11 of [126]): here the model is calibrated using parameters from the Harris catalogue (2010 version) [95]. The empirical King model may be converted to a stellar density function using integration by parts, which yields Eq. 27 of [126]. This is plotted in (a) where it is clear that the approximation of [139] underestimates the stellar density in the core of the cluster. Conversely, the approximation for the stellar density may be projected onto the plane of the sky (*e.g.* see Eq. 23 of [127]) as a luminosity/brightness profile: the underestimate of the stellar density in the inner regions of the cluster leads to a deficit by a factor of almost two in the surface brightness in the core of the cluster. For both the empirical King model and the approximation, the volume integral out to the tidal radius is within 10% of the cluster's total luminosity.

CMB. The latter, however, being entirely homogeneous becomes comparable to that of stellar photons near the periphery of a typical cluster.

It is worth noting that the scale of the luminosity profile ascribed to a given cluster is dependent upon our knowledge of its distance from us: if a cluster is more distant than assumed, in order to yield the same observed brightness, it must be more luminous by a ratio of factors of $1/d^2$. However, as the rate at which IC-scattered photons are generated would vary linearly with the photon density and that rate would be subject to the same factor of $1/d^2$ in being converted to a flux of gamma rays at the Earth, the observed flux of VHE gamma rays (due to IC scattering of optical photons) is rendered insensitive to the exact distance of the globular in question.

2.3.2 Electron Diffusion and Energy Losses

This model assumes that MSPs situated in the core of a globular generate a population of relativistic electrons which then propagate outwards. To simulate this, Monte Carlo methods are used to track the Bohm diffusion of relativistic electrons injected into the centre of an ambient photon field as that described above. Bohm diffusion is chosen to characterise the propagation of the electrons because an ambient magnetic field is expected to exist within the interstellar medium and this takes into account the increased path-length due to the curvature of an electron's trajectory which, in turn, increases the likelihood of it being scattered before passing out of any given volume. B&S07 estimates the strength of this field to be at least $1\,\mu$G due to the presence of MSPs alone. The presence of a magnetic field acts to restrict diffusion, retaining electrons within the cluster core, though the effect diminishes with increasing electron energy. It is determined in B&S07 (see Fig. 5 in that work) that such a field ensures the majority of emission due to IC scattering, across all energies considered, occurs within 10 pc of the centre of a typical globular. Consequently, they derive emission spectra by summing the simulated emission within such a radius.

The electron population responsible for gamma-ray emission may lose energy in a number of ways as its members propagate through a globular[12]. Electrons may:

- escape from the region densely populated by target photons.

[12] A quantitative estimate of the relative importance of these factors is given in [201].

- lose energy gradually to synchrotron emission as they traverse the ambient magnetic field.
- lose energy gradually to Thomson-regime IC scattering, of appropriately soft target photons.
- lose energy comprehensively in Klein-Nishina-regime IC scattering, of appropriately hard target photons.

The first mechanism is accounted for tacitly by considering emission from within 10 pc of the centre but synchrotron losses are neglected. As simulated electrons propagate through the smoothly varying photon field, determined at each point in the manner described above (§2.3.1), the probability that they undergo IC scattering is tracked and any resultant scattered photons are recorded. Therefore, in B&S07, an emission spectrum is calculated as the total energy lost by the population of electrons through the latter two mechanisms in the list above (though it is the last one in particular that is relevant to VHE emission).

2.3.3 Electron Spectrum and Model Parameters

As may be seen above, the IC-scattered spectrum depends upon the electron energy through both kinematics (Eq. 2.16) and the scattering cross-section (Eq. 2.15). The onset of Klein-Nishina suppression and the associated peak in the scattered spectrum are dependent upon the electron energy (Figure 2.9). As a consequence, the spectrum of electrons injected into the core of a simulated globular is of critical importance. Unfortunately there is little certainty as to the form it should take and B&S07 makes a set of informed guesses in this regard.

The simplest assumption follows from the models of HE pulsar emission noted above (§2.1.3). Radiation-reaction limited acceleration of electrons, within the pulsar magnetosphere, may result in an effectively mono-energetic spectrum of electrons leaving the vicinity of a pulsar. B&S07 examines two possibilities: 1 - and 10 -TeV electrons ($\gamma = 0.2 \times 10^7$ and $\gamma = 2.0 \times 10^7$ respectively) which together bracket the approximate characteristic Lorentz factor suggested by pulsar emission models of $\gamma \sim 10^7$.

B&S07 also entertains the possibility that the winds from MSPs in the core of a globular will develop some sort of termination shock[13]. Their par-

[13] See [122] for an excellent discussion of a pulsar-wind termination shock.

ticular assertion is that pulsars will be so densely packed in the core that the winds will collide between themselves. Such a shock front would effectively randomise the particle energies and result in a power-law injection spectrum. Unfortunately there is a large amount of freedom in specifying the form of such a power-law: the minimum particle energy injected, the maximum particle energy attained against *in situ* losses and the slope of the spectrum are all largely undetermined. B&S07 covers the range of possibilities by examining two particular values of each of these three properties amounting to eight possible combinations. Each assumed injection spectrum is associated with a more-or-less distinct spectrum of emitted gamma rays (see Figure 2.11 and Figure 2.12).

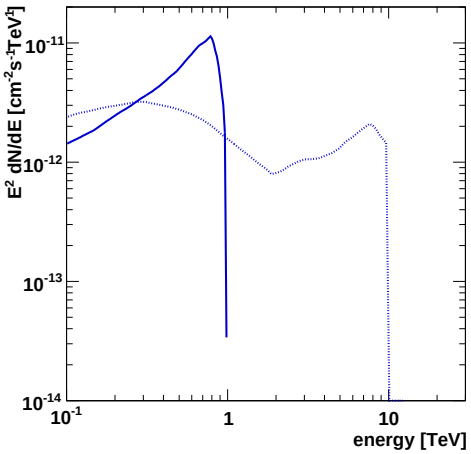

Figure 2.11: Predicted emission spectra in the VHE domain (above 100 GeV) for monoenergetic injection spectra. Solid line 1-TeV electrons, dotted line 10-TeV electrons. Image credit — These curves were extracted from Fig. 10 of B&S07 using the online implementation of Dexter [70] (http://dc.zah.uni-heidelberg.de/sdexter).

Regardless of the form of the injection spectrum, its magnitude must be set by the power output of the MSPs which are its source. Furthermore, as it is the population of injected electrons that powers the IC scattering of ambient photons, the power output of the MSPs is directly related to the level of emitted gamma rays. By this reasoning I introduce the main parameters of the model. The power of the injected electron spectrum will simply be the total power released in the form of relativistic electrons by all the MSPs in

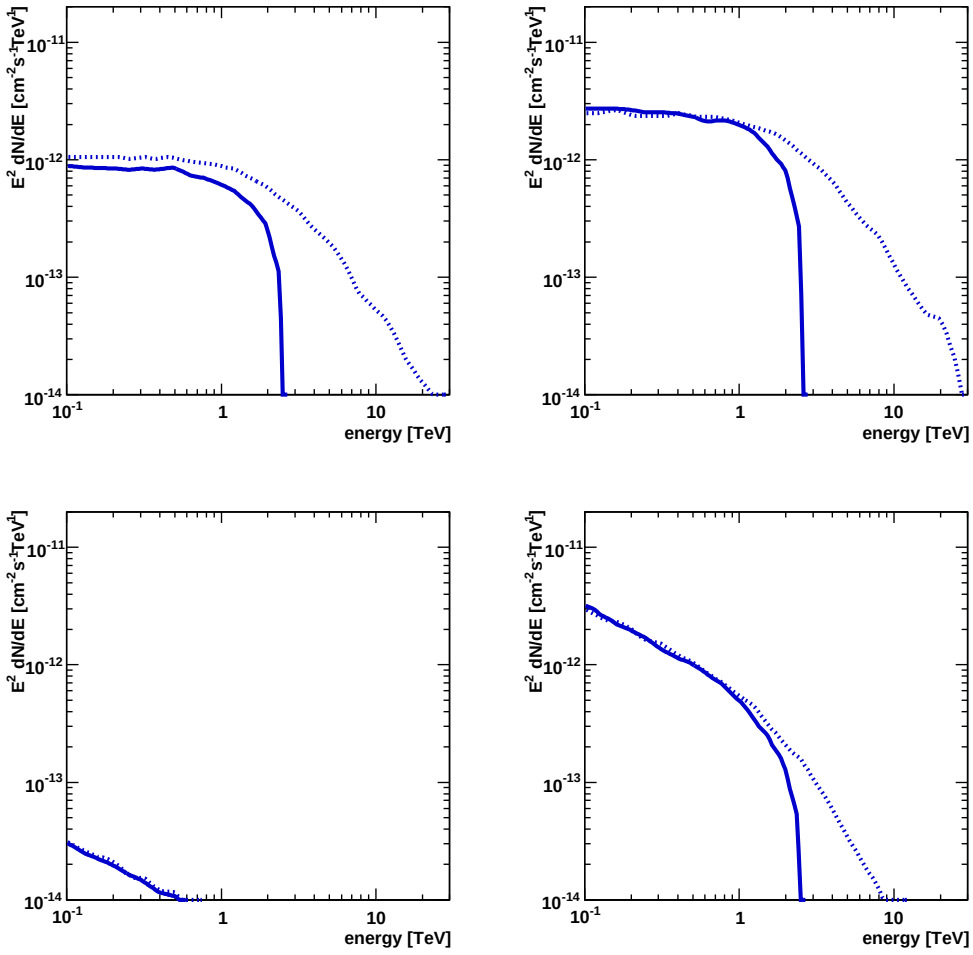

Figure 2.12: Predicted emission spectra in the VHE domain (above 100 GeV) for power-law injection spectra. Top row is index 2 and bottom row is index 3; left column has a minimum injection energy of 100 GeV and right column has a minimum injection energy of 1 GeV. Solid curves have a maximum injection energy of 3 TeV and dotted curves 30 TeV. Image credit — These curves were extracted from Fig. 9 of B&S07 using the online implementation of Dexter [70] (`http://dc.zah.uni-heidelberg.de/sdexter`).

the globular, $L_{\pm}$. This will be a factor of the total spin-down luminosity of the pulsar population and an efficiency with which that power is delivered

to energetic electrons. In turn, the total spin-down luminosity can further be broken down as the product of the average spin-down luminosity and the total number of pulsars.

Thus, the emission models of B&S07 are directly related to essentially three parameters: the total number of pulsars, $N_{\rm P}$, the average spin-down luminosity, $\bar{L}_{\rm s\text{-}d}$, and the efficiency, $\eta_{\pm}$, with which MSP spin-down power is converted into relativistic electrons in the pulsar wind. The energy flux of gamma rays, $\Phi(E)$, will be proportional to the product of these parameters :

$$\Phi(E) \quad \propto \quad L_{\pm} = \eta_{\pm} \bar{L}_{\rm s\text{-}d} N_{\rm P} \tag{2.20}$$

The predicted emission spectra in B&S07 were generated by assigning to these parameters values of $\bar{L}_{\rm s\text{-}d} = 1.2 \times 10^{35}\,{\rm erg\ s^{-1}} \simeq 10^{22}\,{\rm MW}$, $N_{\rm P} = 100$ and $\eta_{\pm} = 0.01$. Now, allowing that I can estimate any two of these parameters, and given a particular measured flux at a particular gamma-ray energy, these emission models allow such a measurement to be converted into an estimate of the remaining parameter. I will return to a detailed discussion of these parameters in §6 where I will attempt to relate VHE gamma-ray observations of M13 to these parameters.

2.3.4 Flaws

Of course no model perfectly represents reality and simplifications are necessary to render all but the most trivial problems tractable. Nonetheless, there are a few elements of this model which may not be as realistic as might be desired. Here I briefly note them and why they might be expected to have a significant impact on the predicted spectra, but it is beyond the scope of this thesis to attempt to account for them.

Stellar photon spectrum. The model presented in B&S07 uses a black-body emission spectrum at a set effective temperature of 6000 K to account for the stellar photon spectrum in all of the globulars considered. However, the observed integrated spectral class is available in the catalogue of globulars [94] for each of the clusters considered. This property is a direct measure of the average stellar photon spectrum in a particular cluster and can easily be interpreted as a mean effective temperature (*e.g.* Table VII [89]).

It is apparent that such a correction could be significant to the VHE flux from a globular when we consider that, in the Klein-Nishina limit which

is of particular importance to emission at these energies, the spectrum of photons scattered from a target black-body distribution is proportional to the square of the characteristic temperature of the target distribution [42]. In the case of M13 which has an integrated spectral class of F6, corresponding to an effective temperature of $\sim$6500 K, this could introduce a correction of approximately 17% to a modelled flux in the VHE domain.

Stellar density function. The approximation to a King-model stellar density function used in B&S07 (that due to Kuranov & Postnov [139]) is seen above to be an underestimate in the inner regions of the cluster. This will certainly lead to underestimation of the stellar photon field intensity in the core of the cluster. Recalling that inverse-Compton scattering is expected to occur mainly in the core, the overall effect of this approximation on the predicted VHE flux is likely to be approximately the factor of two seen *e.g.* in the derived surface-brightness profile. The effect of inverse-square weighting of radiation from distant parts of the cluster will somewhat exacerbate this effect, given that it must suppress the contribution from the over-estimated luminosity in the outer parts of the cluster.

Synchrotron emission. As noted above, synchrotron emission due to propagation through the ambient magnetic field is neglected in this model. This simplification is justified by the observation that the energy density of a 1-μG ambient magnetic field ($U_{\rm B} \sim 10^{-1}\,{\rm eV\cdot cm^{-3}}$) is several orders of magnitude below equipartition with the energy density of the stellar radiation field in the core of a typical globular ($U_{\rm ph} \sim 10^{2}\,{\rm eV\cdot cm^{-3}}$). This argument relies on the fact that the ratio of synchrotron to IC emission power is directly related to the ratio of these energy densities (see §7.2 of [186]) :

$$\frac{P_{\rm Synch}}{P_{\rm Compton}} = \frac{\frac{4}{3}\sigma c \gamma^2 \beta^2 U_{\rm B}}{\frac{4}{3}\sigma c \gamma^2 \beta^2 U_{\rm ph}\left[1 - \frac{63}{10}\frac{\gamma\langle\varepsilon^2\rangle}{mc^2\langle\varepsilon\rangle}\right]} \approx \frac{U_{\rm B}}{U_{\rm ph}} \ll 1 \qquad (2.21)$$

where $U_{\rm ph} = \int \varepsilon\nu\,{\rm d}\varepsilon$ and $\langle\varepsilon^n\rangle = \int \varepsilon^n\nu\,{\rm d}\varepsilon \,/\, \int \nu\,{\rm d}\varepsilon$ for an ambient-photon spectral distribution $\nu(\varepsilon)$. Note that the term in square-brackets contains the leading-order correction from the Klein-Nishina cross-section, but also that in the approximation we have assumed this correction to be small. Thus, we may claim that cooling by IC scattering should dominate over energy losses to synchrotron radiation. However, this assertion relies upon the IC scattering

being in the *Thomson* regime whereas in Eq. 2.21, for sufficiently large γ, the ratio may in fact approach unity. This effect would be exacerbated for larger magnetic fields and the corresponding greater magnetic energy densities, $U_{\rm B} = B^2/2\mu_0$. It should be noted that B&S07 also considered $\sim 10\,\mu$G as a plausible ambient magnetic field.

As VHE emission here relies primarily upon IC scattering of stellar photons by the highest energy electrons in the Klein-Nishina regime, which suffers greatly reduced scattering rates, synchrotron cooling may compete, sapping power from this portion of the electron population. This could become quite significant for ambient fields of only $\sim 10\,\mu$G , as may be seen in the model of [201], which accounted for synchrotron losses but was based on a more rudimentary, two-zone photon field.

2.3.5 Summary

B&S07 determined that substantial VHE emission should occur from globular clusters if, as expected, they contain many MSPs. This follows (with certain caveats regarding the exact target photon field and competing electron-cooling mechanisms) from the known facts that globulars support intense fields of infra-red and optical photons and MSPs power winds of relativistic plasma: the photons acting as plentiful targets for relativistic electrons from the pulsar winds which can transfer their energy to individual photons via inverse-Compton scattering. The major assumption here is that the electrons ejected from the pulsars have $\sim$ TeV energies as they stream outwards in the pulsar winds.

The assertion that this should be the case relies upon pulsar emission models based on curvature radiation from an energetic, but radiation-reaction limited, population of electrons. These models have known some success but are now being seriously challenged by the detailed observations from the *Fermi* satellite: the previously favoured model of MSP emission has already been rendered largely obsolete [203] and a serious re-examination of the framework may be in order [34]. Regardless, gamma-ray emission from MSPs does seem to indicate the presence of highly energetic particles in close proximity with pulsars.

However, underlying the relevance of this is a deeper assumption: that $\sim$ TeV electrons close to a pulsar also imply electrons of similar energy in that pulsar's wind. Little is known with certainty about pulsar winds and least of all how they are 'launched'. A significant obstacle is that they remain

largely dark, likely because they are highly ordered.[14] In fact searching for inverse-Compton scattered photons from globulars may be one of the best ways of probing pulsar winds, where they are bathed in target photons, but not necessarily close to a termination shock. In the absence of more detailed knowledge, at least it does not seem *unreasonable* that some portion of a population of $\sim$ TeV electrons should escape undiminished from the vicinity of a given pulsar.

If these assumptions are accepted, it seems obvious that VHE emission must occur at *some* level in a typical large globular. Furthermore, with predictions that this mechanism can provide substantial emission from particular clusters well-placed for the VERITAS observatory it seems that these assumptions can be tested by the current generation of ACTs.

[14] It can't be stated more elegantly than in [30]: "Theoretical models of MHD winds exhibit negligible radiative emission (by construction), and indeed, there has been no positive observational identification of the winds themselves—observational study of the winds' properties has depended on detection of the winds' consequences. The winds are like a river flowing on dark nights—invisible until the water strikes a dam, or rocks in the stream, when the glimmer of starlight from the spray thrown by the obstacles allows one to infer the river's presence and properties."

Part II

Observation & Analysis

Chapter 3

Detection Technique & Apparatus

Gamma rays cannot penetrate the Earth's atmosphere: upon entering it, they very soon interact with the electric field of an atomic nucleus and are converted, predominantly, into electron-positron pairs. For a sufficiently energetic **primary** (meaning the original particle, of astrophysical origin), the resulting electrons[1] will, as they interact again with the nuclei of atmospheric molecules, lose energy to *bremsstrahlung* photons which will themselves be sufficiently energetic to pair-produce. In this way a cascade of particles results which develops into an **Extensive Air Shower** (EAS). The cascade will grow until the average particle energy is insufficient to drive the production of more electrons, at which point the shower rapidly diminishes as particles continue to lose energy in ionization of the atmosphere.

A similar phenomenon is associated with energetic cosmic rays[2] except that the shower development is not purely electromagnetic, in that some fraction of the shower constituents are produced via strong interactions which can lead to distinct differences in the shape of the shower. This characterisitc can be used to estimate what type of primary created the EAS and will be discussed in more detail in Chapter 4.

A significant side-effect of the particle cascade (though representing an

[1] As we shall see shortly, for our purposes it is only significant that the particles produced are charged, (the sign is irrelevant) and so we will regard electrons and positrons as identical, for the sake of argument.

[2] As distinct from gamma rays, in that they are charged. The vast majority of these are atomic nuclei; mostly protons.

almost insignificant loss of energy) is that the charged constituents of an EAS induce **Cherenkov radiation**, see Figure 3.1. As a charged particle moves through an insulating medium, it induces polarization of the medium's constituent molecules. If the particle moves slowly, the polarization of the medium remains approximately spherically symmetric and no radiation is emitted. However, if the particle moves close to the speed of light in the medium, the distribution of induced dipoles will be asymmetric[3], leading to an effective dipole trailing the charged particle and oriented along its path. Emission can be thought of as a requirement of energy conservation: the effective dipole being trailed around by the particle applies a drag force, the work done by which ends up as electromagnetic radiation via the relaxation of this effective dipole. When the particle exceeds the speed of light in the medium, emission from the effective dipole at different points along the path becomes coherent at a particular angle, constructively interfering in a cone around the trajectory of the particle: this is Cherenkov radiation. The opening angle of the cone is defined by the geometry of electromagnetic radiation spreading from the vicinity of the particle more slowly than the particle's own passage through the medium. As such, it is determined by the speed of the particle relative to that of light and the refractive index of the medium.

The relativistic charged constituents of an EAS individually induce **Atmospheric Cherenkov** (AC) radiation but the emission is coordinated across much of the shower for several reasons. Firstly, through conservation of momentum and the highly relativistic nature of the shower's constituents, the particles' directions of motion are generally similar, such that the axes of the cones of Cherenkov emission are approximately parallel. Secondly, given that the refractive index of air is only slightly larger than 1 (implying that particles in the EAS must be very close to the speed of light in a vacuum in order to induce AC emission) and that the energy of a particle diverges near the speed of light, the AC radiation is emitted at almost the same angle by most of the particles in the shower despite the broad spectrum of energies[4] they possess. Finally, as the shower develops at a rate only slightly faster than the AC radiation passes through the atmosphere, later parts of the shower generate photons only slightly ahead of those from above. The final

[3] The retarded potential ahead of the particle is weaker than that behind.

[4] Necessarily ranging from (almost) the energy of the primary at the start of the shower and diminishing with the shower's development, as that original energy is shared out amongst the shower's constituents.

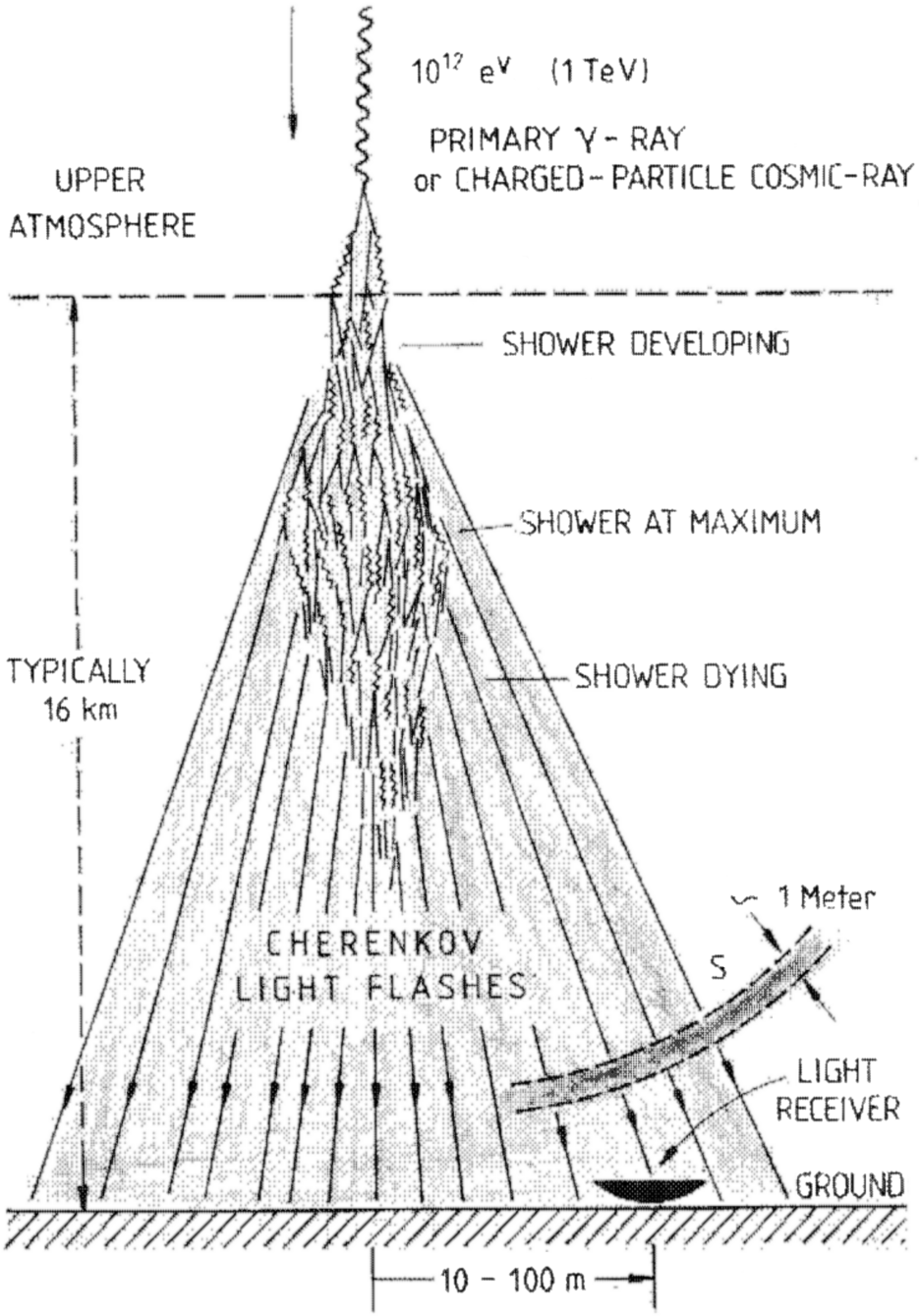

Figure 3.1: An EAS generates a thin shell of photons (labelled 'S' in the figure) which may be detected from the ground. Image credit — figure due to J. Jelley, reproduced in [208].

effect is cumulative, such that the AC radiation due to an EAS is emitted into a cone of $\sim 1^\circ$ around the direction of the primary particle's motion and a large quantity of photons arrive at the ground within a few nanoseconds in a coordinated and approximately uniform **light-pool**. The light-pool illuminates a roughly elliptical patch of ground, with a minor radius of $\sim 100\,\mathrm{m}$ for a characteristic emission height of $\sim 10\,\mathrm{km}$.

The energy emitted as Cherenkov radiation, by path length and angular frequency of light, is given by the Frank-Tamm formula for a non-magnetic medium :

$$\mathrm{d}E = \frac{e^2}{c^2} \int \left(1 - \frac{1}{\beta^2 n(\omega)^2}\right) \mathrm{d}x\, \omega\, \mathrm{d}\omega \tag{3.1}$$

As the refractive index, n, for air is almost constant within the frequency domain of interest (varying by $\sim 0.1\%$ for blue–UV) :

$$\mathrm{d}E = \frac{e^2}{c^2} \cdot \frac{1}{v^2} \left[v^2 - \left(\frac{c}{n}\right)^2\right] \int \mathrm{d}x\, \omega\, \mathrm{d}\omega \tag{3.2}$$

Thus the total intensity depends upon the magnitude of the charge of the particle, e, and upon the amount by which the square of its speed, v^2, exceeds that of light in the medium, $(c/n)^2$, both of these affecting the strength of the induced dipole. As noted above, the speeds of electrons in the shower which are generating AC radiation are all very similar such that the total amount of light emitted closely matches the number of particles in the shower and, consequently, the energy of the primary.

We can also see that the total emitted energy per unit path length as a function of frequency obeys :

$$\frac{\mathrm{d}E}{\mathrm{d}x} \propto \omega^2 \tag{3.3}$$

The spectrum of AC radiation is dominated by large frequency (short wavelength) light; in terms of the number of emitted photons, $\mathrm{d}N\,/\,\mathrm{d}x$ is linear with frequency or inversely proportional to wavelength. In practice, the atmosphere is opaque for wavelengths shorter than 300 nm and the AC flash at ground level peaks in the near-UV at $\sim 310\,\mathrm{nm}$, see Figure 3.2.

In summary, EASs result in a brief, coordinated flash of AC light, brightest in the near-UV and illuminating an elliptical light-pool at the base of the atmosphere. If the AC flash can be observed by a telescope within the light-pool and observing the upper atmosphere, properties of the EAS can

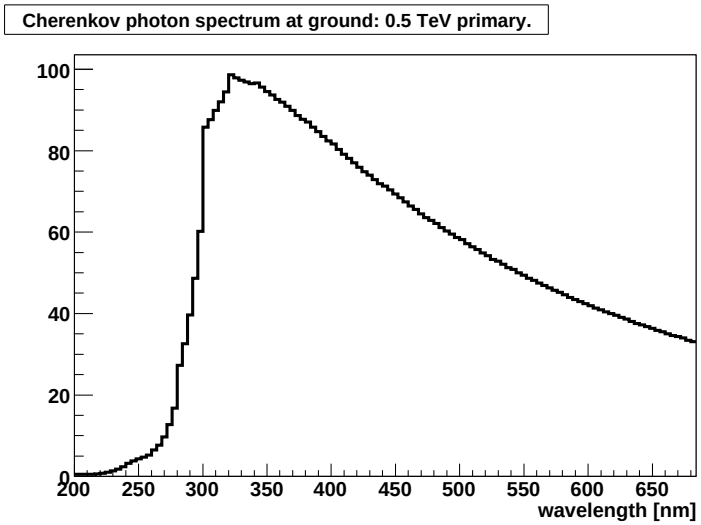

Figure 3.2: The mean spectral distribution of photons at ground level from an EAS due to a 0.5 -TeV gamma-ray primary. At longer wavelengths the spectrum is inversely proportional, as may derived from the Frank-Tamm formula (see main text). At shorter wavelengths the spectrum is dominated by atmospheric absorption. Image credit — G. Maier.

be gleaned.[5] If the orientation of the AC emission relative to the telescope is measured the geometry of the EAS may be reconstructed and the direction of the primary can be estimated. Likewise, if the brightness of the flash can be measured from a sample of the total AC emission, the size of the EAS may be estimated and, accounting for the efficiency with which the detector collects light, the energy of the primary may be estimated[6]. Thus, detection of AC radiation from EASs is a tool for gamma-ray astronomy and, as we shall now discuss, the fact that a telescope need only be within the light-pool of a shower lends this technique to the study of the lowest flux, highest energy gamma rays.

[5] To wax lyrical ... an AC telescope cannot see the radiation it seeks to measure: instead, like a blindfold hunter waiting to detect its prey by the sound if its passage, another of the telescopes' senses has been acutely heightened in order to discern the glimmer of the debris of the gamma ray's collision as it brushes against the atoms of the Earth's atmosphere.

[6] In technical terms, the atmosphere and telescope together form an AC-sampling calorimeter.

3.1 Detecting Gamma Rays

Given sufficiently large flux, the small surface area of a satellite ($\sim 1\,\mathrm{m}^2$) operating above the atmosphere may be adequate to collect enough gamma rays to perform scientific analysis. As many sources of the highest energy gamma rays ($> 1\,\mathrm{GeV}$) exhibit power-law spectra[7] these large fluxes are associated with lower energies. Thus, above $\sim 10\,\mathrm{GeV}$ observations of even the brightest sources will be severely limited by count rates.

However, from beneath the atmosphere an EAS may be detected by observation of its associated AC emission, and with equal efficiency anywhere within the light-pool, due to the latter's uniformity, granting to a detector capable of this an effective area on a par with the area of the light pool $\sim 10^5\,\mathrm{m}^2$ [118]. In turn, such a detector can achieve reasonable count rates for the much lower flux associated with energies above $\sim 100\,\mathrm{GeV}$ [8]. This is the principle behind the AC technique of which the most advanced form uses imaging AC telescopes [208], see Figure 3.3, which capture the form of an EAS as a rough ellipse. The major axis of the ellipse represents a plane through the atmosphere which includes the axis of the EAS and, equivalently, the arrival direction of the primary. The presence of multiple telescopes in the light-pool allows stereoscopic reconstruction of the arrival direction by intersection of these image planes, see §4.1.1.

3.1.1 Design Considerations

Capturing images of EASs from the short-lived burst of AC radiation visible from the ground requires telescopes with large reflectors to gather as much light as possible; with fast acting cameras that may create an image from a brief flash of light; and with a rapid, automated system to determine when an image has been acquired. I will discuss the essential characteristics for each of these systems below and then detail the specific implementation constructed by the VERITAS collaboration in the next section (3.2).

[7] The principle mechanisms (e.g. shock acceleration, see §21 of [143]) for accelerating charged particles to energies required for them to emit gamma rays tend to create power-law spectra, which carry over to the spectra of the photons they emit.

[8] This is the operational distinction between the regime of high- and very-high-energy gamma rays.

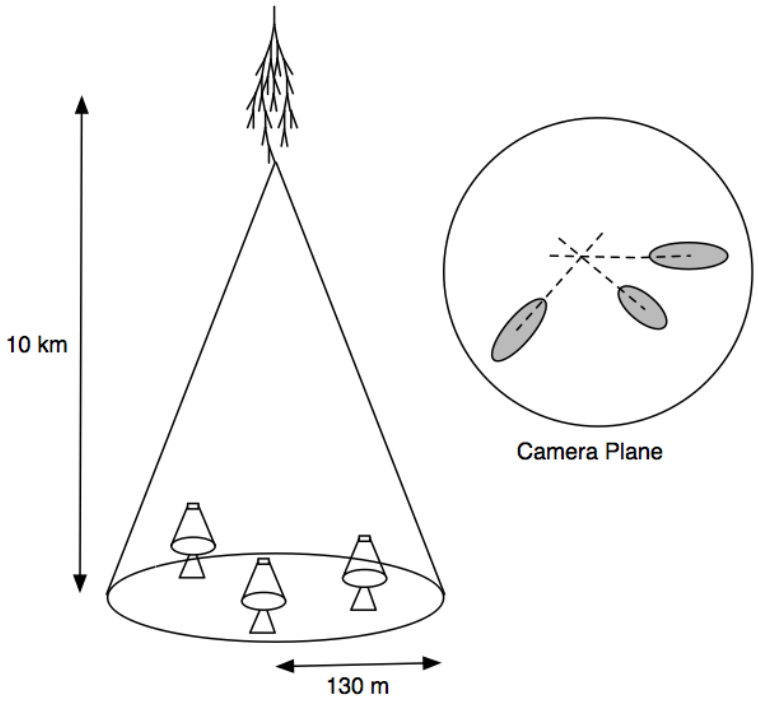

Figure 3.3: In the imaging AC technique an EAS is imaged via AC radiation as an ellipse by each of the telescopes. The intersection of the major axes of the imaged ellipses indicates the direction from which the primary arrived. Image credit — J. Holder; Figure 29.2 from [169].

3.1.1.1 Optics

Given the simple, extended shape of EASs, the optical resolution of the telescopes is not especially critical: the angular resolution for gamma-rays depends upon reconstruction/identification of the axis of the elliptical image which can be $\sim 1^\circ$ across and the optical resolution need only be fine enough to capture the form of this image. It is better to gather enough light to achieve well-defined though coarse images, rather than accurate images that may be indistinct[9], and in the design of these detectors optical precision is sacrificed for reflector area. This results in a **Point-Spread Function** (PSF), being the image formed of a point-like source by an optical system and a proxy for the latter's quality, which would be unsuitably large for

[9]Brightness is preferred over sharpness.

almost all forms of optical astronomy. However this point is moot, in fact the optical resolution tends to be limited by the granularity of the camera and the PSF need only be small enough to be contained by a single pixel. Without the constraint of exquisite optical precision, very large reflectors are made possible by using tessellated reflectors instead of continuous reflecting surfaces: the current generation of imaging AC telescopes have photon collection areas larger than $\sim 10^2\,\mathrm{m}^2$.

3.1.1.2 Camera

All of the AC light due to an EAS that is collected by the reflector arrives at the focal plane of a telescope within a few nanoseconds. To capture an image of an EAS we require a camera which is capable of responding promptly to such a signal. This is because the vast majority of photons that arrive at the focal plane are due to **Night-Sky Background** (NSB) : photons which arrive at random due to sources which include air-glow[10] and Rayleigh scattering of starlight[11] from the Earth's atmosphere. Against this continual trickle of individual photons, the co-ordinated and coherent Cherenkov light arrives rarely but *en masse*, instantaneously outshining the NSB and even direct starlight[12] even though it represents only a fraction of a percent of all photons from the night sky [41, 118, 208].

The NSB introduces, on average, about one photon every 5 ns for a given pixel: to prevent the image of an EAS from being washed-out by noise from the NSB, the duration of a single 'exposure' of the camera should be of a similar order of magnitude. Thus, to isolate AC photons and correctly image the EAS requires a camera with pixels that respond quickly enough to build up a signal from a flash of light which lasts only ~ 2 ns without collecting many photons from the continual background noise.

Such a rapid response requires a camera composed of **Photo-Multiplier**

[10] Phosphorescence due to exposure to the ionising component of sunlight during the day and to cosmic radiation.

[11] Ideally only starlight would contribute to scattered light but other sources of ambient light are also present: moonlight, light pollution, even photons due to EASs outside the field of view.

[12] If NSB photons fall as a persistent drizzle, then starlight is light rain and AC photons from an EAS are a tropical cloudburst. The human eye does not perceive EASs because its response time is longer by many orders of magnitude (~ 0.1 s in darkness) and the total background light over such a stretch of time entirely dilutes any Cherenkov photons.

Tubes (PMTs): analogue electronic devices[13] with the capability of detecting a single photon and with a response time of $\sim 2\,\mathrm{ns}$. Each PMT pixel is a glass vacuum tube whose exposed face is coated inside with a photocathode which is typically composed of alkali metals[14]. The photocathode readily emits electrons when exposed to photons in the optical-to-UV range. Thus, when AC photons strike the face of the PMT a certain fraction pass through the glass window and are absorbed in the photocathode where they may emit so-called photoelectrons. The efficiency with which this occurs is termed the **quantum efficiency**: the mean ratio of photons which result in the emission of photoelectrons to the total incident on the photocathode. The quantum efficiency is a function of the wavelength of the incident photons and, by judicious choice of the photocathode's composition, may provide optimum sensitivity to the spectrum of AC radiation.

Once released, photoelectrons are accelerated towards a dynode which, relative to the photocathode, is held at a much greater potential (typically $\sim 10^2\,\mathrm{V}$ higher). Upon striking the dynode's surface, the electron's energy is dissipated; a fraction of that freeing more electrons which are in turn accelerated towards another dynode, see Figure 3.4. In all, this process is repeated several times on a sequence of dynodes: each time the charge released at the photocathode is effectively multiplied by the liberation of more electrons. Finally the avalanche of electrons reaches the anode of the device; the resulting pulse of current, and attendant dip in the voltage supported across the PMT, corresponds to the detection of photons. An array of PMTs whose signal pulses are captured simultaneously can create an image of an EAS.

3.1.1.3 Trigger

The fact remains, however, that most pulses are caused by NSB photons and the AC flash is of such short duration that for the vast majority of the time there is nothing to see in terms of AC radiation but plenty of unwanted signals from the NSB. Only small portions of the continuous stream of data from all the pixels in the camera are needed: these are **events** consisting a

[13] These differ from digital devices, such as the CCD in a common camera, in that they produce a continuous signal. Though the PMT signal is eventually digitized for data storage, the complete waveform is available to the trigger system (see §3.1.1.3).

[14] Alkali metals have the lowest first ionization energies of all elements and consequently are those which most readily lose electrons.

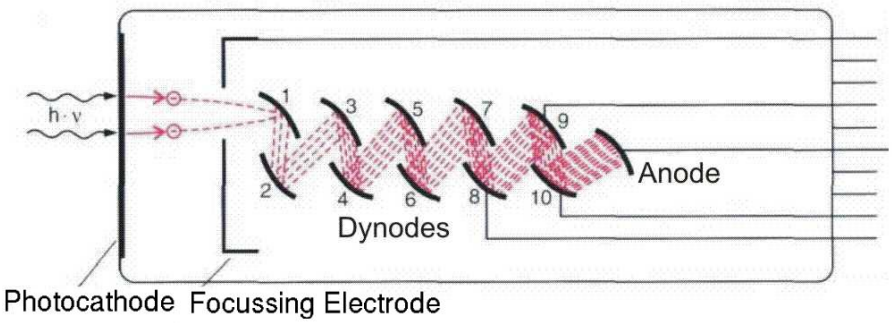

Figure 3.4: Schematic of the operation of a photo-multiplier tube. Electrons emitted at the cathode through the photoelectric effect cascade through the dynode chain to be absorbed at the anode, generating a current pulse.

narrow time span containing an image. In order to determine when a possibly interesting or useful event has taken place, a **trigger** system is used, which is an automated logical framework designed to generate a signal (trigger) indicating that the information captured by the camera should be recorded for later analysis.

3.2 VERITAS

Figure 3.5: The VERITAS array in its present configuration. Image credit — S. Criswell, Fred Lawrence Whipple Observatory.

The **Very Energetic Radiation Imaging Telescope Array System**

(VERITAS) is an array of four imaging AC telescopes, see Figure 3.5, situated at latitude 31.675, longitude −110.952 in southern Arizona, USA. It was constructed with the purpose of observing EAS in Earth's upper atmosphere allowing the detection of astrophysical sources of **Very High Energy** (VHE) gamma rays. The telescopes work together, co-pointing, to capture images of the same AC flash, allowing stereoscopic reconstruction of the associated EAS.

Each of the VERITAS telescopes [83] is of f-1.0 Davies-Cotton design [66] having a 12-m aperture tessellated reflector born upon a dish-shaped **Optical Support Structure** (OSS). The OSS is itself mounted on a positioner[15] which can rotate the OSS about a vertical axis to control its orientation in azimuth and tilt the OSS in a vertical plane to control the angle of elevation. Each telescope is equipped with a PMT camera supported at a distance of 12 m from the reflector in a housing (**focus-box**) mounted at the apex of a pyramidal frame of four beams (**quadropods**) which are attached to the structural frame of the OSS. The quadropods also serve as conduits for the co-axial cables which carry signals from the PMT pixels to an electronics trailer stationed next to each telescope. Inside these trailers portions of the PMT signals containing the images of EASs are recorded for later analysis.

3.2.1 Optics

The main benefit of the Davies-Cotton design is the use of many identical reflecting facets arranged upon a spherical surface. This is a very cost-effective way of creating a large collecting area: identical facets can be mass-produced and it is relatively simple to construct a spherical OSS. With facets having identical focal lengths, the best image will be formed (and consequently the camera located) at the centre of the sphere of which the OSS is a portion.

For observation of AC light there is a slight disadvantage in that this arrangement is not isochronous[16]: light arriving at the same instant, parallel to the optical axis will have different path lengths before reaching the reflector depending upon the perpendicular distance from the optical axis at which it is reflected. After reflection the paths are, of course, identical but the centre of the reflector dish is recessed with respect to the edges. Thus photons which were emitted at some distant point and at the same instant have differing

[15] A commercial model supplied by Rotating Precision Mechanisms (RPM-PSI model PG-4003).

[16] This is in contrast to a parabolic reflector.

travel times through the telescope's optics and although they will arrive at the same position on the camera they will not do so simultaneously. For the geometry used by VERITAS there is an intrinsic time-spread of ~ 5 ns [210] but this time-spread is manifested as an approximately square pulse such that the rise-time (the time to reach 90% of the peak) is only 1.7 ns which is on par with the time-spread of the AC flash from an EAS. Thus, the start-time of an AC flash is preserved with reasonable fidelity but the time-structure will be smoothed out on the scale of 5 ns.

Following the Davies-Cotton design principle, each of the VERITAS telescopes' reflectors comprises approximately 350 hexagonal glass facets [185], each of diameter 60 cm. These facets each have a spherical aluminium-coated reflecting surface with radius of curvature 24 m and they are supported (by the OSS) in a spherical arrangement having a radius of 12 m, the focus-box being located at the centre. Given that the opening angle from the centre of the reflector to its edge, as viewed from the focus-box, is 30°, mirrors towards the centre of the dish are almost normal to the optical axis while those near the edge must be tilted at up to 15°. Each mirror facet is mounted on the OSS with a triangular three-point suspension supplied by McGill.[17] At each vertex, a brass mounting gimbal and adjustment nut are installed on a stainless-steel threaded rod. The mirrors are held in place by the gimbals and the adjustment nut allows translation of the gimbal assembly along the axis of the threaded rod. Thus the gimabls allow a mirror to tilt with minimal stress and warping. Correct alignment of the facet can be achieved by turning two of these adjustment nuts[18]. The mirror-mount geometry and threaded-rod pitch are such that one full turn on a nut changes the mirror orientation by 0.1°.

Recall that the optical resolution may be judged by the PSF which for a system such as this consists of the superposition of all the images formed by the individual facets. Thus, the PSF consists a mixture of images from approximately on-axis (central) and significantly off-axis (edge) facets.

3.2.1.1 Factors Influencing the PSF

For light rays reflected through only a small angle, the focal length of a reflecting surface is half of its radius of curvature. The facets are sufficiently

[17] This system was based on that used by Whipple.

[18] The third nut provides additional freedom in adjusting the depth of a mirror, necessary given the close-packing of the facets.

small[19] that their individual spherical aberration is minimal: rays from the edge of a central facet converge less than 1 mm in front of the nominal focal plane, which is less than the precision to which either the camera or the facets can be placed. Mirrors near the centre of the reflector focus an image onto the camera limited only by the accuracy and precision of their curvature.

For reflections from a spherical surface at larger angles, astigmatism becomes important and two focus points can be identified (Hecht p. 226 [96]): one (the tangential focus) due to reflection from a locus in the plane of the angle of incidence (tangential focus) and another (the sagittal focus) due to reflection from a locus in the plane normal to the arrival direction. Fortunately the point mid-way between the two foci, which marks the 'circle of least confusion' (the smallest approximately-focussed image of a point), remains very close to the nominal focal length. So mirrors mounted near the edge of the reflector still contribute a best-possible image at the camera face.

Thus the telescope PSF is, in principal, limited by astigmatism from off-axis facets as well as defects in facet curvature [185]. The distribution of measured radii of curvature among the population of mirrors on one of the telescopes is shown in Figure 3.6(a). The on-axis PSF of a single facet at the nominal focal length of 12 m varies as a result of the deviation of the radius of curvature from the nominal 24 m and also non-uniformity of that curvature across the reflecting surface. This is the practical limit of a single mirror's ability to focus and corresponds to its performance if it was positioned near the centre of the reflector. It can be expressed as the spot-size created by focussing parallel rays to a plane 12 m distant from the mirror itself. The distribution of spot-sizes for the same telescope is seen in Figure 3.6(b). A typical mirror near the centre of the reflector will provide a PSF at least 6 mm across (0.03 °), but no more than $\sim$1 cm.

For off-axis facets, even with the nominal 12 -m focal length, the two astigmatic focal points are up to 42 cm in front of and behind the camera plane. However, this is not seriously problematic because the small angular size of each facet *vis-à-vis* a focal point limits the spread of rays: a facet at the edge of the reflector produces a hexagonal spot of $\sim$ 21 mm diameter. Thus, the contribution to spot-size due to astigmatism exceeds that due to imprecision in the individual facets: the facets are of adequate optical quality, given the intrinsic limitations of the telescopes' design.

If all of the image-spots from the individual facets are properly aligned,

[19] Each subtends less than 0.05 radians (3°) when viewed from the focus-box.

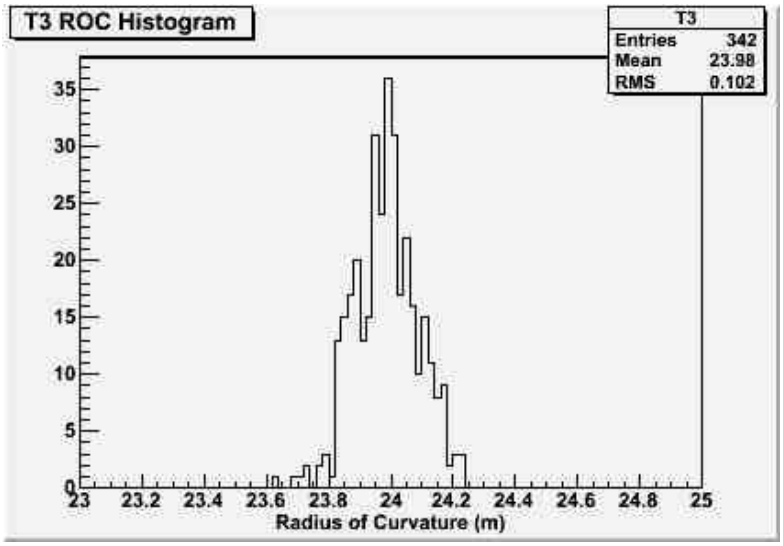

(a) Distribution of radii of curvature.

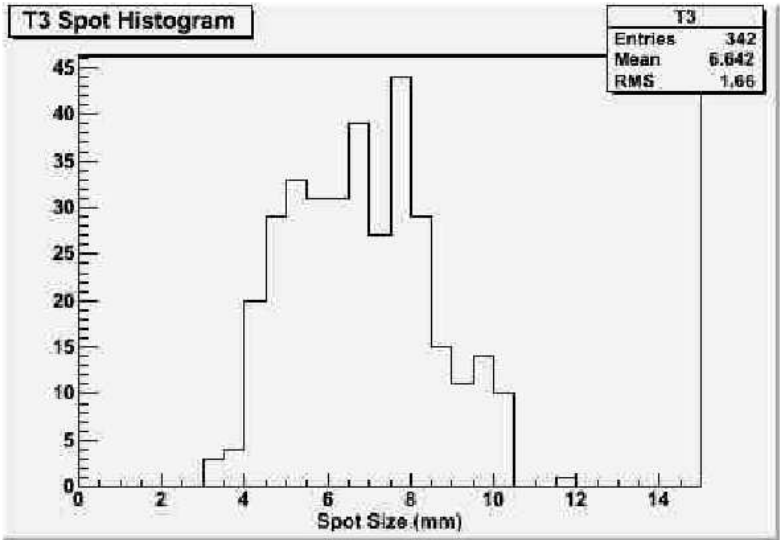

(b) Distribution of spot-sizes.

Figure 3.6: The distribution of optical characteristics for facets on telescope 3. The radii of curvature, (a), have a mean very close to the nominal 24 m; the worst outlier has a prime focus some 20 cm in front of the camera face. The spot-sizes, (b), have a mean ~ 7 mm; the worst outlier is less than 12 mm. Image credit — generated by `http://veritasm.sao.arizona.edu/DQM/mirrorHtmls/mirrorDatabase.html`.

the PSF will be no larger than ∼22mm, within the diameter of a single PMT pixel (see §3.2.2). Each facet thus contributes an approximately focussed image of a distant source at the focus-box and the optimal PSF is attained by aligning the individual facets so that these images are stacked-up, one upon another.

3.2.1.2 Alignment

All the individual facets must be correctly aligned so that the image-spots contribute to the total image. A simple, in concept, and extremely effective method to determine the correct alignment is to place a CCD camera at the focal point (the centre of the PMT camera) and observe the facets as the telescope points at a bright star: mirrors which appear illuminated in the CCD image are correctly aligned, they gather light from the star and reflect it to the focal point [31]. Furthermore, when pointing at a small angle away from a star, correctly aligned mirrors will appear dark but if a misaligned mirror appears bright the angle by which it is misaligned can be calculated. The implementation of this technique for VERITAS was developed by McGill: many pointings are tested in a raster scan of a grid of points around the direction of the star [157]. From the scan, a map of facet alignment corrections may be created which are applied by hand to the facet-mount adjustment nuts.

An image taken near the centre of such a scan, when the optical axis of the reflector is aligned with the chosen star, can be seen in Figure 3.7. Aligned facets near the centre of the reflector appear illuminated across their surface because the spot size is sufficiently small that rays reflected from the entire surface of a mirror are captured by the small aperture of the CCD camera. Aligned facets at the edge of the reflector are distinguished by a small bright patch near the centre of the mirror because the circle of least confusion is larger than the CCD camera's aperture which can thus only sample the centre of the solid cone of rays subtended by that facet.

The PSF produced by this reflector is shown in Figure 3.8(a) alongside its dependence with the elevation angle of the telescope. The OSS sags under the action of gravity and so its detailed geometry varies with the angle at which it is tilted, this affects the alignment of the facets and consequently alters the PSF. By performing the alignment raster scan at an elevation typical of gamma-ray observations (60–70°), the PSF is directly optimised for normal observing. The on-axis PSF is well contained by a single pixel at

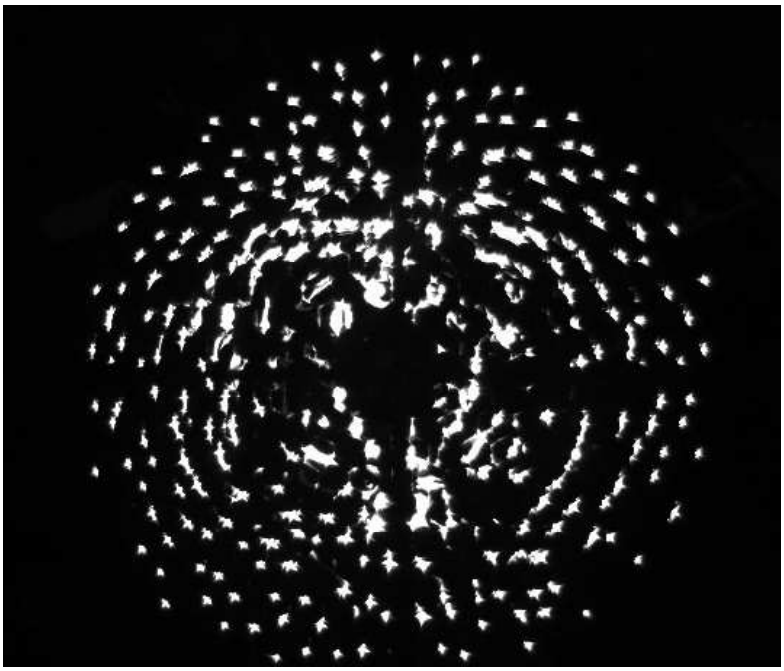

Figure 3.7: An image of the reflector of one of the VERITAS telescopes taken with a CCD camera placed at the focal point of the telescope. The telescope is pointing directly at a bright star. Individual aligned facets independently focus light from the star to the focal point. In the CCD image, starlight reflected by a facet appears to come from that facet. Image credit — Fig. 6(d) from [157].

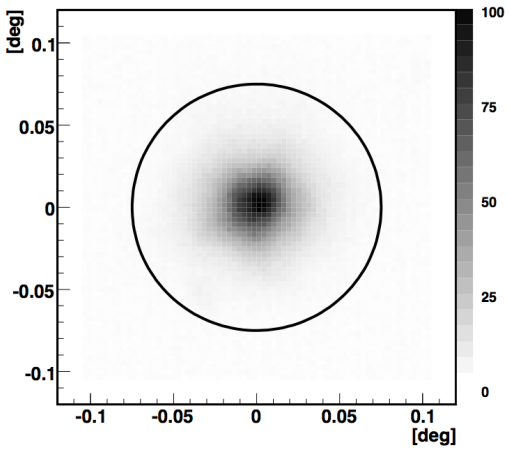

(a) PSF

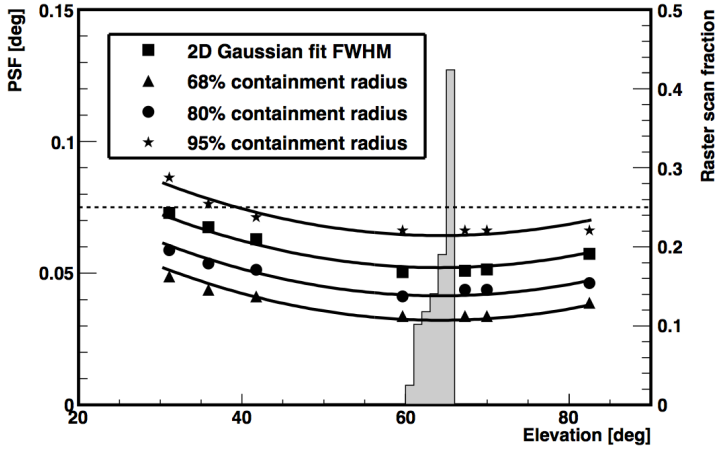

(b) Width dependence with elevation

Figure 3.8: The on-axis PSF due to a bright star, from [157]. An image of the smallest PSF is shown in (a). The intensity values (grey scale) are plotted in arbitrary units. A PSF image is made by mounting a white screen at a telescope's focal plane and photographing, (with a digital camera mounted on the OSS) the image formed by the telescope of a bright star being tracked by it. The dependence of the size of the on-axis PSF with elevation is shown in (b): the histogram indicates the number of raster-scan images taken at each elevation. The angular size of a single PMT pixel (see §3.2.2) is indicated by a circle in (a) and a dashed horizontal line in (b). Image credit — Fig. 6(b) and Fig. 7 from [157].

the level of 95% even to relatively low elevation.

3.2.1.3 Reflectivity

The aluminium reflecting surface of each facet is anodized[20] to help protect it from erosion and pitting by wind-borne dust (an inescapable hazard of the desert conditions of the telescopes' location) which over time degrades the reflectivity of the facets. To ensure that this modification of the surface does not hinder the light-collection efficiency of the reflectors, the process is carefully controlled so that the thickness of the aluminium oxide layer is especially favourable to the reflection of light near the peak of the atmospherically-absorbed AC radiation spectrum, see Figure 3.9, thus preserving the brightest component of any received AC flash. The surfacing and

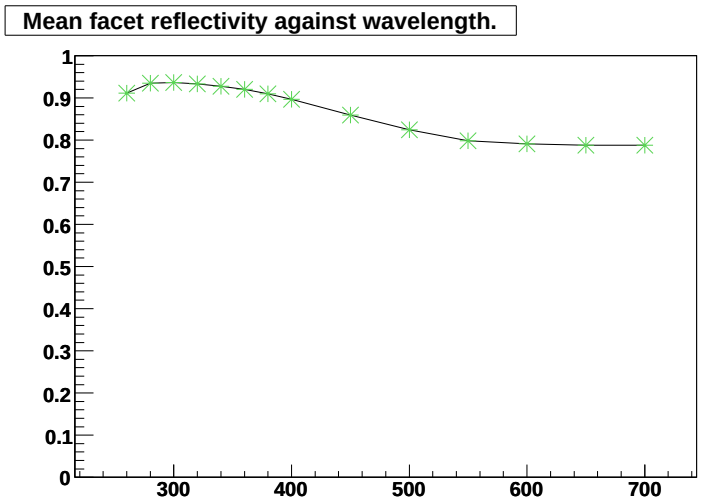

Figure 3.9: The facet reflectivity as a function of wavelength, being the fraction of incident photons reflected. Image credit — G. Maier.

anodisation of facets is carried out on-site and all the facets are in rotation to maintain reflectivity over the lifespan of the detector array. This program requires the regular removal and replacement of batches of facets which in

[20] The skin of the aluminium surface is electrolytically converted to aluminium oxide, which is harder than the base metal. Aluminium naturally develops a thin oxide layer due to the chemical action of the atmosphere, but the process of anodizing thickens it.

turn requires regular re-alignment of the reflectors by the process described above, together providing optimum reflectivity and PSF.

3.2.2 Camera

Each telescope is equipped with a camera of 499 29 -mm diameter PMTs, covering an approximately circular field of view having a diameter of 3.5°. To form the camera the cylindrical PMTs are hexagonal close-packed with a spacing corresponding to 0.15°. Close-packing of the circular faces of the PMTs leaves more than 10% dead-space where there is no photocathode to intercept photons arriving at the camera's surface. To mitigate this a faceplate of hybrid Winston cones [120, 168] (so-called **light-cones**), each having a hexagonal front aperture which evolves to a circular rear aperture (see Fig. 3.10), is used. The front apertures of the light-cones sit flush against

Figure 3.10: A sample of the hybrid Winston cones used to construct the light-concentrator faceplates. Image credit — Fig. 7 of [168].

each other providing near total coverage on a plane a short distance in front of the camera surface; the rear apertures are concentric with the circular faces of the PMTs at the camera surface; the reflective material from which the light-cones are constructed readily transmits and concentrates light received at the front aperture to the rear. The geometrical light collection efficiency of the camera's surface is increased from 55% to 75% [120] An additional

benefit of the cones is that they restrict the field of view of individual PMTs to admit only light reflected from the mirrors, thus reducing the incidence of NSB photons.

Each PMT is a Photonis XP 2970/02, having a quartz window over a bialkali photocathode followed by ten dynodes. The quartz window, unlike normal silica glass, is transparent to the UV light where the AC spectrum peaks (recall Figure 3.2). The bialkali photocathode has a quantum efficiency curve (as a function of photon wavelength) which is close to its maximum near the peak of the facet-reflected AC radiation spectrum, see Figure 3.11. These PMTs are operated at $\sim$1kV with the total voltage split evenly across

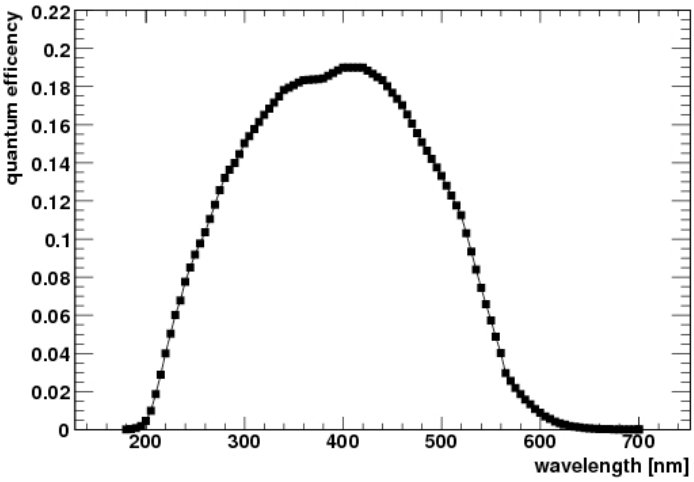

Figure 3.11: The effective quantum efficiency of PMTs used by VERITAS. The bialkali photocathode has broad sensitivity in the blue-UV range, overlapping with a large fraction of the received AC photons. This curve (constructed with input from measurements made at Purdue University) is averaged over the surface of the PMT and incorporates the collection efficiency of the PMT's first dynode ($\sim$87%): as such it represents the ratio of photoelectrons that may be registered by readout electronics to the total number incident on the PMT's face. Image credit — G. Maier, S. Fegan.

the photocathode, dynodes and anode.

The analogue signal from each PMT is transmitted, through 75 -Ω coaxial cables, to the readout electronics housed in a trailer stationed beside each telescope. This is not lossless: the signal will be subject to a certain level of dispersion and attenuation, broadening and diminishing the pulse. To mitigate the attenuation, the base of each PMT contains a preamplifier to magnify the pulse before it has passed far along the signal path. In this way the bulky readout electronics need not be supported in the camera housing.

3.2.3 Trigger & Readout

In the electronics trailer, each PMT signal is split between two paths: for the sake of discussion, we will denote them as the **control path** and the **readout path**, see Figure 3.12. The control path, being the entry point to the trigger system, determines when and also how the readout path should be used. The readout path has two entry points: high-gain and low-gain, suitable for small and large signals respectively, differing in the use of amplifiers with a relative gain of six and a small time-delay in the low-gain channel. The default for the readout path is high-gain but if the signal in the control path exceeds a set threshold the readout path is switched to low-gain while the low-gain time-delay allows the use of the same readout scale for both gain modes. In this way the dynamic range of the readout electronics (see §3.2.3.2 below) is effectively increased by a factor of ~ 6, although the resolution is coarsened for large-intensity signals.

Readout of the signal from a PMT occurs continuously: a **ring sample buffer** is used to store a 65.534-μs section of the waveform passing through the readout path by constantly overwriting the oldest portion of the waveform in its memory with the most recent[21]. It remains to identify which segment of the buffer contains useful or interesting information rather than noise. This determination must be made within the $\sim 65\,\mu$s that it takes for the sample buffer to be completely overwritten. Such a rapid decision requires a dedicated, electronic, logical framework based on simple criteria applied to the analogue signals from the PMT pixels. This is the purpose of the trigger system which takes the signals from the numerous individual control paths and uses three levels of coincidence to decide if information in the sample buffers should be recorded as an event. When the trigger system determines that an event has occurred, writing to the sample buffers is halted until the

[21] It's as if the buffer represents a window sliding along the PMT waveform.

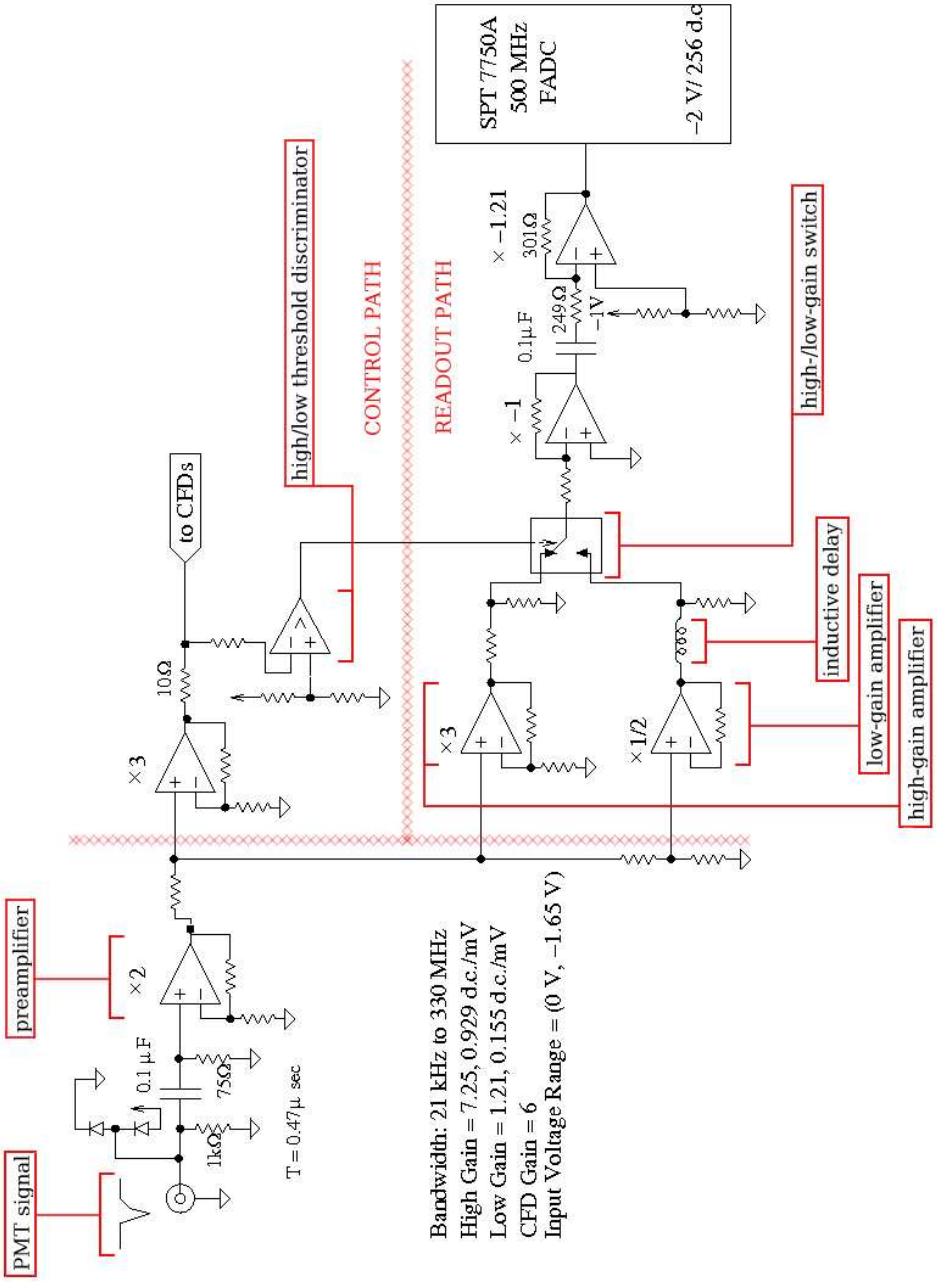

Figure 3.12: Signal path for a single data channel.

appropriate portion has been copied out for permanent storage. This pause constitutes a **deadtime** during which the array is not capable of recording further events. In fact, this is the principle motivation and design criterion for the trigger system: to allow the restriction of data-taking to only those events which may be useful, thereby reducing the deadtime and maintaining sensitivity.

3.2.3.1 Trigger System

As noted above (§3.1.1.2, §3.1.1.3), the vast majority of pulses generated by each PMT are due to NSB photons which arrive with random direction and timing. Thus, the trigger system is designed to determine when PMT pulses are a result of collecting coherent, coordinated Cherenkov photons instead of the continual, random NSB photons.

The trigger system makes use of the fact that Cherenkov radiation is coordinated by requiring agreement within a narrow time window, first between neighbouring pixels[22] (pattern trigger) and then between telescopes[23] (array trigger). The typical configuration of the trigger system is detailed in Table 3.1 and described below.

Trigger characteristic	Value
t_{L1} [mV]	50
R_{L1} [kHz]	16
n_{L2}	3
w_{L2} [ns]	6
R_{L2} [Hz]	600
n_{L3}	2
w_{L3} [ns]	50
R_{L3} [Hz]	210
d depth [ns]	40
f [%]	10

Table 3.1: Typical settings of the VERITAS three-level trigger system for astronomical observations. Explanation of the trigger characteristics can be found in the main text.

[22] An image with a significant angular size.
[23] A light pool on the scale of the telescope array.

ZCFD (Level 1). The control path of a PMT signal leads into the trigger system as it passes the analogue waveform to a **Zero-crossing Constant Fraction Discriminator** (ZCFD), whose role is to determine if its associated PMT has been subject to a pulse of light. This represents the first of three steps towards making a trigger decision: a **Level 1** (L1) trigger.

The ZCFD combines two functions: it generates a signal if the height of the input pulse exceeds a threshold (t_{L1}) but bases the timing of that signal upon a pulse-height-independent measure. This is important because the next level of the trigger system uses a narrow coincidence window to determine if neighbouring pixels have L1 triggers. The timing of the ZCFD works by adding an inverted, scaled and delayed copy of the waveform to itself. This imposes a particular form upon the signal such that, given the same pulse shape, it crosses zero at the same time relative to the position of the peak, regardless of the height of the peak. Thus pulses due to AC photons (which arrive with a characteristic time-spread) will have a particular position in the data-stream relative to the L1 trigger signal, and neighbouring pixels exposed to the same AC shower will have closely synchronised L1 triggers. The array will be most sensitive if t_{L1} is set such that any photoelectron generates a L1 trigger. The continuous hail of NSB photons is such that the L1 trigger rate (R_{L1}) is typically very large. It is left to the higher trigger levels to separate AC events from random triggers due to noise.

Pattern trigger (Level 2). The next step towards a trigger decision is the pattern trigger. L1 triggers from across the camera are passed to a topological logic module which determines if a certain number of contiguous pixels (n_{L2}) produce L1 triggers within a narrow time window (w_{L2}) appropriate for the timing response of the telescope optics. If this condition is met, a **Level 2** (L2) trigger is generated which occurs at a typical rate R_{L2}. There are very many possible configurations of a small number of contiguous channels given a circular array of 499. Thus, for practicality, the trigger condition is computed for all combinations of contiguous pixels within hexagonal patches of only nineteen pixels. The patches overlap in order to avoid edge effects, where a contiguous group of L1 triggers straddles the border of one of the patches, and achieve coverage of all but thirty-six pixels around the outskirts of the camera. If the trigger condition is met within any one of these patches, a L2 trigger is generated. Given the fact that R_{L1} may be very large, L2 triggers may be generated by random chance and the differences between

cameras[24] drive differences in R_{L2} from each telescope (see Figure 3.13). Also, AC events which trigger only a single telescope may be generated but they are not amenable to stereoscopic reconstruction and consequently are not useful.

Array trigger (Level 3). L2 triggers are passed to the central array-trigger computer. Here it is determined whether multiple telescopes have experienced a L2 trigger simultaneously. This requires allowing both for signal-cable propagation delays, which are fixed by the relative distances of the individual telescopes from the array-trigger system, and for delays in the light-transit time of the array, which changes continuously according to the pointing direction of the array. Thus, L2 trigger signals are passed through a programmable delay module[25], which is reprogrammed approximately once per second with delays appropriate to the contemporaneous elevation and azimuth, before being subject to the L3 trigger logic. If, after correction for delays, a certain number of L2 signals (n_{L3}) are within a given time window (w_{L3}) a **Level 3** (L3) trigger signal is generated: this is the final trigger decision and indicates that an event should be recorded. This occurs at a typical rate R_{L3}. When a L3 trigger is generated, a veto is placed on further L3 triggers until all the data from the readout sample buffers have been copied out at each telescope, resulting in a certain deadtime per event.

The effect of the trigger system in limiting the event rate, and consequently the deadtime, can be seen with a **bias curve**: data for the bias curve are accumulated by pointing at a patch of sky with the trigger settings in the configuration appropriate to astronomical observations except that t_{L1} is changed in small steps and the trigger rate is recorded at each level. The purpose of such a measurement is to determine at what level of t_{L1} the instrument is most sensitive to the dimmest showers without seriously impacting the exposure of the array through deadtime.

The bias curve indicates how trigger rates behave as a function of t_{L1}, see Figure 3.13. For small t_{L1}, R_{L2} and R_{L3} are dominated by random triggers due to chance coincidence in the very large rate of L1 triggers. As t_{L1} increases, a transition region is reached where a core of coordinated events

[24]Some PMTs are more sensitive to single photoelectrons, having larger R_{L1} for a given t_{L1}, which results in a greater incidence of chance coincidence with its neighbours. Thus, differences in L2 rates are driven by outliers in the population of PMTs in a camera.

[25]This unit is provided by McGill University, having previously been in use on the Solar Telescope Atmospheric Cherenkov Effect Experiment.

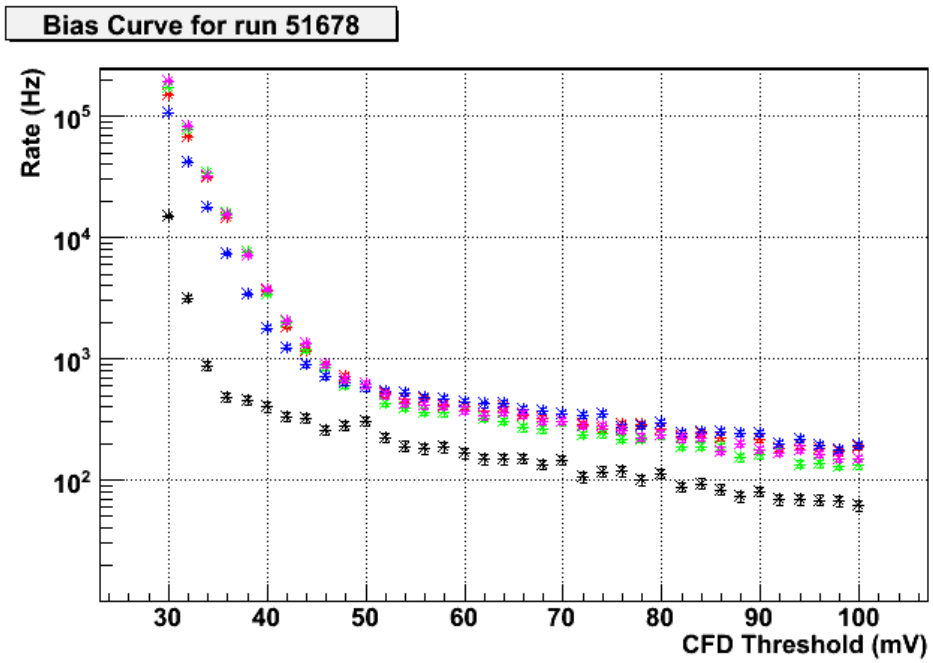

Figure 3.13: The rate of triggers at L2 for each of the telescopes 1-4 (red, green, blue, magenta) and at L3 (black). The trigger rate is dominated by NSB pulses for small CFD threshold (t_{L1}). The L3 rate is always lower than that of L2 and also reaches a plateau at a smaller threshold. Image credit — generated by `loggen` (see §5.1 for a description).

is revealed that shows a much weaker dependence upon t_{L1}: these are AC events[26]. For R_{L3} this plateau is reached at smaller values of t_{L1}, indicating the suppression of accidental L2 triggers and local AC events. Rates are capped by setting t_{L1} to be above the inflexion point of the R_{L3} curve, safely in the regime of AC events. This successfully limits fractional deadtime, f, to about 10% of the total observation time.

3.2.3.2 Readout

The readout of the analogue signal is effected via a **Flash Analogue-to-Digital Converter** FADC which continuously digitises the waveform from a single PMT in the camera. Each FADC has a dynamic range of 256 digital counts and operates at a rate of 0.5 -Giga-samples per second , meaning that every 2 ns an integer value between 0 and 255 is assigned according to the deviation of the waveform from a reference voltage, each value being a single 8 -bit (1 -byte) **sample** of the waveform. Recall that the intrinsic rise-time of the VERITAS optics is 1.7 ns : this is deliberately matched by the timing resolution of the FADCs.

Any signal that arrives has been subject to the 5 -ns time-spread of the optics and dispersion in the signal cables but can be reconstructed by integrating over a number of contiguous samples. A typical pulse as recorded by one of the FADC channels is shown in Figure 3.14. The sample buffer of the FADC can store up to 32767samples at a time, corresponding to 65.534 μs of the waveform from the PMT, as noted above.[27]

For every event during normal data-taking each FADC produces a trace with a depth of 20 samples. Given the 8-bit dynamic range and 500 channels, this results in some 10 kByte per telescope per event which must be copied out in preparation for permanent storage, before the array can be open to receiving further events. This data transfer leads to a deadtime of ~ 1 ms per event.

The waveform samples from an individual telescope are time stamped

[26] These events are due to cosmic rays which dominate the trigger rate because they cannot be distinguished from gamma-ray induced events at the trigger level. To do so would require a more advanced trigger system, known as a morphological trigger.

[27] Obviously the FADC's buffer is rapidly completely filled and, once this happens, the oldest byte in the buffer is always replaced by the newest sample: this looping over the available memory leads to the term 'ring buffer'. Thus the signal from the PMT is continuously digitised, as noted above.

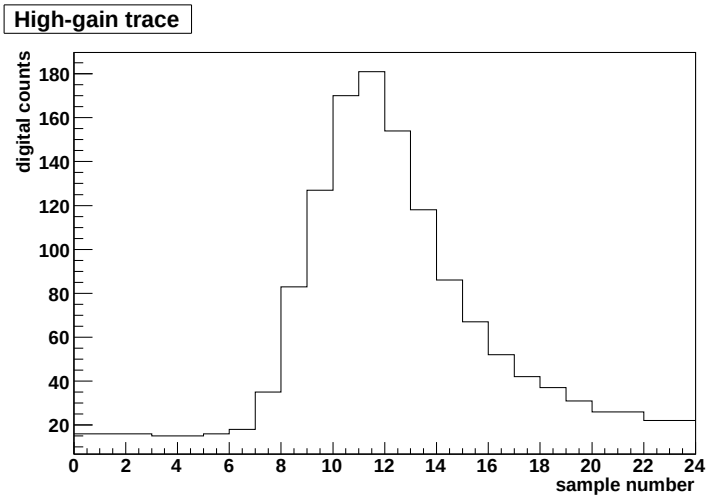

Figure 3.14: An FADC trace. Each sample is separated by two nanoseconds. Dispersion in the signal transmission reveals itself in the long tail of the pulse.

and transfered to a central data harvester where they are collated into array-wide events by an event builder. Events are packaged together as a specific run pertaining to a continuous period of exposure, to a particular source, in a particular mode. Each data run is permanently stored in a custom, compressed file format: the **compressed veritas bank format** (CVBF). These files, containing raw information from the cameras, may then be copied by interested parties within the collaboration and accessed for analysis as described in §4.1 and §5.2.1.

3.2.4 Calibration and Auxiliary Data

In order to correctly interpret signals captured by the cameras, it is necessary to also compile a certain amount of data regarding properties of the detector and its environment which may affect its response and thus require corrections to be applied to the raw observational data. Calibration data are gathered through regular monitoring of the performance of the sensitive part of the detector: the PMT cameras. They may be used to directly evaluate and adjust signals measured by individual PMTs. Additional, auxiliary data, which cannot generally be used directly in the analysis of raw PMT signals, are also useful as a means of estimating the quality of observational data and guarding against gross bias or offset in the results of image analysis.

3.2.4.1 Calibration

The most important calibration measurements are the baseline response and the flat-field. Firstly, to determine if a signal is actually present, we need to know how a pixel responds in the absence of AC light: any excess over this baseline or **pedestal** can be considered as a potential signal. Secondly, to ensure that the shape of an image is a genuine representation of the form of an EAS, we need to account for any inhomogeneity in the camera. For this we must know how each pixel responds relative to the rest of the camera when the latter is exposed to a 'flat-field', meaning uniform illumination: the relative response of a pixel is termed the **relative gain**. The application of these calibration measurements to observational data is described in §4.1.

Pedestal. The baseline signal is measured continually throughout data-taking via pedestal events which are recorded regularly at a rate of 1 Hz .[28] These events are collated and recorded alongside those created via L3 triggers in the same data run. Interpretation of pedestal events is built into the analysis framework of VERITAS data with the pedestal estimate being extracted from the same file as its associated observational data. Thus this estimate is always contemporaneous to the observations it influences.

Relative gain. The response to uniform illumination is measured, on average, once each night by pulsing a calibration light source (either a laser or a group of ganged LEDs [91]) through a diffuser to create a small Lambertian light source $\sim 4\,\mathrm{m}$ in front of the camera. The response of a given pixel over many ($\sim 10^3$) calibration pulses is measured and compared to an estimate of the mean response of the camera. Pixels which always show a signal larger (smaller) than the camera mean will need to have their signals scaled down (up) to compensate and make the camera's overall response flat. To this end, the ratio of an individual pixel's response to the camera's mean is computed and the mean of this ratio over many events used as a relative gain which is the appropriate scale factor, allowing the signals in different pixels to be properly matched during the analysis of observational data. Over time the ageing of PMTs causes their individual relative gains to drift and periodically the response of the whole camera is made more homogeneous by

[28] It is extremely unlikely that a pedestal event would accidentally coincide with AC light from an EAS.

using the relative gain measurements to estimate the required adjustment to the set voltage across each pixel: this process is known as **flat-fielding** because it makes the camera's response to uniform illumination more genuinely uniform.

3.2.4.2 Auxiliary

In addition to the output from the cameras, the status of the array is continuously monitored and logged in a database. In this way, the operating conditions under which data was acquired can later be retrieved to assist correct interpretation of that data and help assess its fidelity. Properties logged in this way include:

- pointing (azimuth and elevation) and pointing error.
- trigger scalars (a running total of signals generated) at all levels (L1, L2 and L3).
- sky conditions: far-infrared sky-temperature fluctuations indicate varying transparency (e.g. cloud cover).

A decision on the quality of data in a given run can be made on the basis of trigger rates and the sky-temperature readings (see §5.1 for a discussion of the criteria used in this thesis). If fluctuations in the sky-temperature are contemporaneous with a significant reduction in the L3 rate, that portion of data must be considered to be compromised and should be ignored. To that end, time cuts can be applied which ignore events within a user-defined period. The facility for time cuts in the analysis package used to generate the results presented in this thesis (see §5.2) was introduced by the author.

Whereas data recorded by the cameras are used in the determination of information directly for scientific ends (for which the processing required will be described in the next chapter, §4) this sort of meta-data ensures that the scientific analysis can be based upon observations made under optimum conditions. An example of this use is described in §5.1.

Chapter 4

Image Analysis & Shower Statistics

Simplistically, data from an imaging AC telescope array consist of many images of EASs. The images may be characterised in terms of their position and orientation in the camera's FOV, and also in terms of their shape and brightness. These image properties are functions of the EAS properties of spatial location and arrival direction, and also primary type and energy. In general, image position and orientation are geometrically related to shower location and arrival direction, (relative to telescope location and pointing direction, see Figures 4.4 and 4.5). In turn, image shape and brightness depend mainly upon primary identity and energy, but are also subtly affected by how a shower is viewed and therefore its geometry must be disentangled from the relationship. The underlying assumption of image analysis is that any gamma-ray-induced EAS produces an approximately elliptical image which encodes information about the shower and the primary and that this information can be unfolded from the properties of the image.

An individual EAS will be recorded in a single event as multiple images whose properties may be combined to reconstruct the essential parameters of the originating particle. From these images the pertinent properties of gamma-ray primaries that must be extracted are their arrival directions and energies. The former can be determined from the position and orientation of the approximately elliptical images and the latter from their overall brightness. In addition, the impact parameter (core location) and identity of the primary must be estimated in order to isolate and account for their contribution to the image parameters.

Image processing. Images captured by the telescope array must be alloyed with calibration data to ensure that light-levels from an air shower are correctly measured. The images from a single event can then be parametrised and combined to reconstruct the arrival direction and impact parameter of the particle that initiated the shower. Next they can be compared to the expected response of the array so as to estimate the energy and identity of the primary. The latter property (whether the primary was a gamma or cosmic ray) is of particular importance because the rate of gamma-ray events is typically $\sim 0.01\%$ of the rate of events due to cosmic rays: a flux of gamma rays could be easily masked (or mimicked) by statistical fluctuations in the much greater cosmic-ray flux.

It is essential to the success of the imaging AC technique that the background rate of cosmic rays be reduced to a level that allows any excess of detected gamma rays to be statistically meaningful. Much of the cosmic-ray flux can be rejected by limiting the region of interest in the sky to a particular direction where a gamma-ray source may be suspected to reside. Further background reduction is achieved by means of **gamma/hadron separation** which is the identification and rejection of showers likely due to hadronic primaries [72].

The principle of gamma/hadron separation. The means of distinguishing the nature of the primary is through the shape of the image of the EAS, as captured by each of the cameras during an event, see Figure 4.1. This approach was first proposed in 1983 [54] and later systematised and optimised by Hillas [106, 107] based on the observation that simulated images of gamma-ray-initiated EASs tended to be more compact and had a more obvious axis, in comparison to cosmic-ray-initiated EASs.

The differences between the images are driven by the physics of the shower's development. As noted in §3, a gamma-ray-induced shower consists of only electrons due to pair-production and gamma-rays due to *bremsstrahlung*, and the shower evolves via electromagnetic interactions alone. Due to this, the constituents of the shower have short interaction lengths and the majority of them remain close to the axis of the shower, forming an elongated core which corresponds closely to an extrapolation of the arrival direction of the original gamma-ray[1]. The resulting image of such an EAS is likewise

[1] This also leads to the uniformity of the Cherenkov light-pool which is one of the basic tenets of the air Cherenkov technique, as noted in §3.

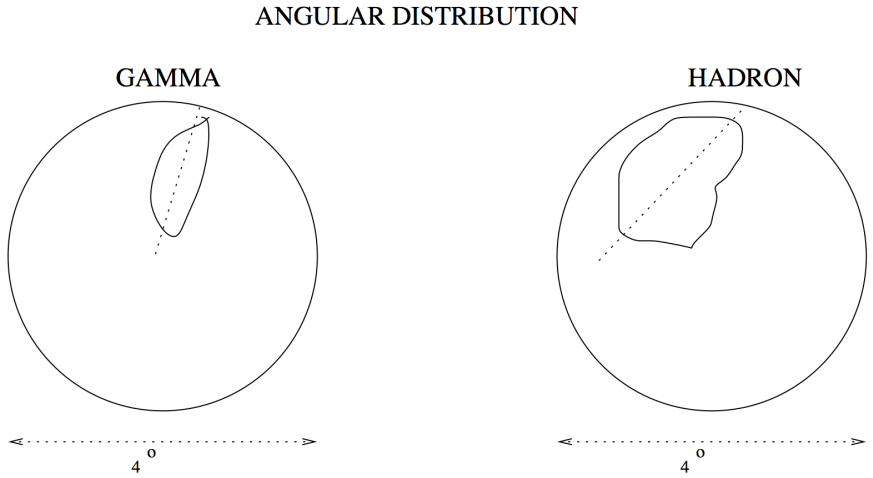

Figure 4.1: The camera of an imaging AC telescope samples the angular distribution of light from an EAS. A typical gamma-ray-induced EAS is more compact than that due to a hadronic cosmic-ray and this difference is reflected in the captured image. Image credit — from Fig. 2.8 of [207].

compact, with a well-defined axis.

In comparison, events of hadronic origin are often characterised by EASs composed of multiple sub-showers[2]. This sub-structure in the shower is due to the influence of strong nuclear interactions which impart significant transverse momentum to some constituents of the shower, originating from the large intrinsic momentum of quarks confined within mesons and baryons: hadronic products of these interactions may project a large fraction of the energy of the incident cosmic-ray into an angle significantly offset from the extrapolated trajectory of the primary. Thus for a hadronic shower, the image presents a more 'lumpy' and sprawling aspect.

So, in principle, there is a marked difference between gamma- and hadron-induced showers. However, the development of an EAS is governed by fluctuations: for any particle in the shower at any moment, what interaction occurs, what its outcome is and even whether an interaction occurs at all are all probabilistic processes. No two showers are identical and any two showers, even having identical primaries, may be quite dissimilar. To give a specific example, it is possible for the first interaction of a hadronic cosmic ray to

[2]Analogous to the phenomenon of jets in particle collider experiments.

deliver most of its energy to a neutral pion (π^0) which will decay to energetic gamma rays: in this way a hadronic primary can produce genuine gamma-ray-induced EASs but these should not be counted amongst any *astrophysical* flux of gamma rays!

Thus the imaging AC technique is afflicted by an irreducible background rate of **gamma-like hadronic events** for which fluctuations in the showers' development have rendered them essentially indistinguishable from showers due to gamma-rays of astrophysical origin. In addition, cosmic-ray electrons will also produce purely electromagnetic showers, evolving similarly to and appearing essentially indistinguishable from gamma-ray-induced showers, though the initial interaction will be the production of *bremsstrahlung* rather than pair-production.

Aside from these caveats, gamma/hadron separation based on the *tendency* for hadronic-event images to be to be more extensive than those of gamma-ray events can be very effective. What is done in practice is that simulations of gamma-ray-induced EASs (and the detector's response to them) are used to determine what form of image should be expected on average and with what range of variation. Events that do not conform to these expectations may be judged as likely being hadronic in origin and consequently rejected (cut) from further analysis. Specifically, the simulations are used to formulate a **cut**: a numerical value which represents the acceptable limit of a property for an event to be considered like one due to a gamma ray. Simulations indicate that such a cut (in combination with limiting the region of interest to a specific source direction) can reduce the contribution of hadronic events by more than 99% [107]. Figure 4.2 indicates the effectiveness of a gamma/hadron cut (see [136] for details). It is interesting to note that the rate of cosmic-ray electrons is little altered by the application of this cut: given that any rate of gamma rays would be affected similarly, this reassures us that few gamma rays are rejected by the cut, as intended. It should also be noted that gamma-like hadrons remain the largest component of the background after cuts: although the electron rate is little affected its initial value is negligible in comparison to the rate of hadrons and remains meagre against even a small fraction of that rate.

Statistical treatment of gamma-like events. Those events that survive the gamma/hadron separation cuts, by definition, have compact, well-defined images which are amenable to parametrisation. The images each have a

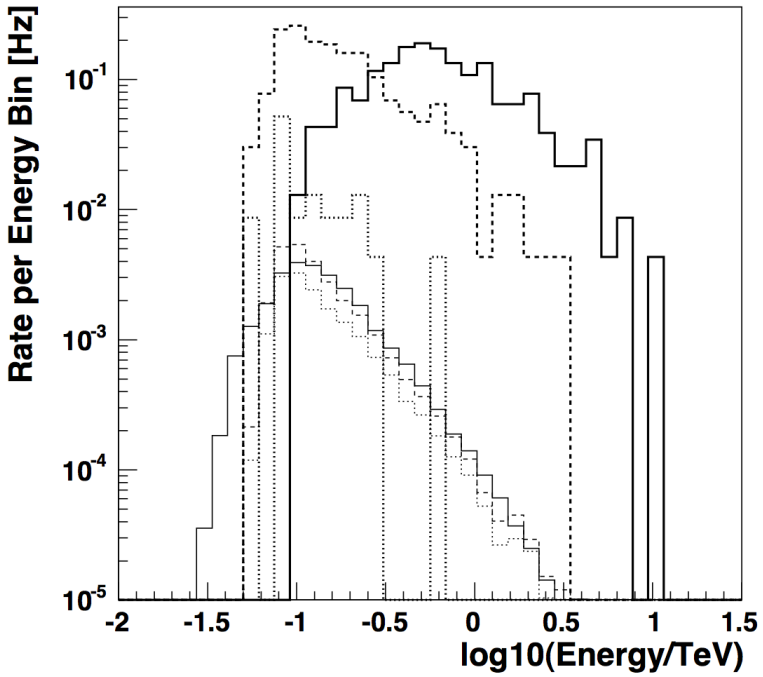

Figure 4.2: Rates of simulated cosmic-ray events detected by a simulated telescope array. The top three curves show the proton rate before application of the gamma/hadron separation cut, as a function of the true proton energy (solid line); before cut, as a function of the reconstructed energy (dashed line); and after cut, as a function of the reconstructed energy (dotted line). The lower three curves show the same for electrons rather than protons. One can see that the proton background dominates over the electron background, even after applying the gamma/hadron separation cut. Image credit — Fig. 10 from [136].

definite axis and, during stereoscopic reconstruction, extrapolation of these axes in the common FOV of the co-pointing cameras defines an intersection point which is the origin of the EAS[3]. In this way, each event is associated with a point on the sky, being the apparent arrival direction of a candidate gamma ray.

The next critical step is to use the fact that cosmic rays, being charged, are deflected by the Galactic magnetic field and that of the Earth such that their arrival directions are essentially randomised: they represent a uniform background. Due to this, the background rate of gamma-like hadrons expected to come from a given direction can be estimated by counting the rate from other directions under similar observing conditions. If we choose a particular direction that might contain a source (the **ON-region**) we can subtract a rate averaged over other directions (**OFF-regions**) to remove the contribution of the gamma-like hadron background. With this estimate of the background rate, it is possible to determine if an **excess** of candidate gamma-rays has been recorded in the ON-region and, more importantly, if that excess is statistically significant. In doing so, it is important to recognise that any signal is in relation to a large background rate, subject to large fluctuations, and therefore this must be one of the basic assumptions of the statistical analysis, such as that defined by Li & Ma [141].

Finally a counted excess of gamma-ray events must be related to some actual flux of gamma rays. To determine the relationship between observed excess and physical flux it is necessary to determine the sensitivity of the array and analysis chain. The efficiency with which astrophysical gamma rays are intercepted, detected and successfully reconstructed is embodied by the effective area.

4.1 Image Processing & Shower Reconstruction

Fundamentally, each event consists of a trace from every FADC monitoring each PMT of all cameras in the array: almost two thousand in all, an example may be seen in Figure 4.3. In a first pass over all the traces in a

[3] This is essentially a parallax phenomenon, analogous to the way in which parallel tracks of a railway line appear to converge at a point in the distance or a meteor shower appears to radiate from a particular point in the sky.

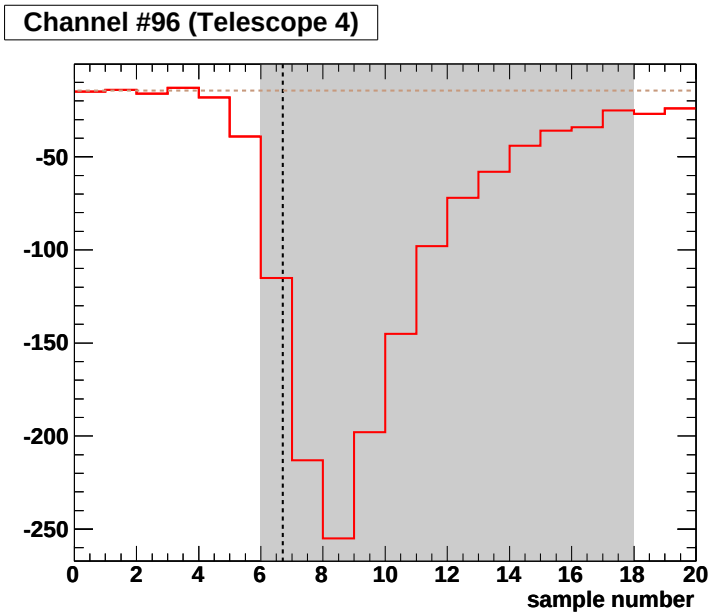

Figure 4.3: A typical FADC trace. The start of the pulse (indicated by the vertical dashed line) is first determined independently of the other channels as the first sample to reach half of the peak value; subsequently the timing gradient of the image may be used to refine this estimate. The integration window (shaded in grey) is placed according to the start of the pulse and the samples within it are totalled to yield the integrated charge. The signal from the pixel is calculated as the integrated charge less the pedestal integrated over a window of the same size. The pedestal is determined for each channel for various integration windows from pedestal events taken during the same run (see §3.2.4.1). Here, for reference, the run-averaged single-sample pedestal is indicated by the horizontal dashed line.

camera, the beginning of any pulse is determined as the earliest sample, t_0, that exceeds half the height of the inverted pulse and the location of the integration window is chosen according to this. Once the integration window has been placed the samples within it are totalled, yielding the **integrated charge**, Q. The integrated charge in each channel is then compared to the distribution of integrated charges (using the same-size window) from pedestal events[4], q, for that channel. The actual integrated charge has the mean of the pedestal distribution subtracted from it and this excess charge is taken to be the signal, Δ, in that channel :

$$\Delta = Q - \bar{q} \tag{4.1}$$

Now, the variance of the pedestal distribution, σ_q^2, constitutes a measure of the noise in this particular channel. Noise arises from the continual rain of NSB photons (see §3.1.1.2) and fluctuations in the readout electronics which, being uncoordinated and below the effective trigger threshold, are recorded equivalently in pedestal and other events. With this estimate, a **signal-to-noise ratio** (S/N) can be calculated :

$$R = \frac{\Delta}{\sigma_q} \tag{4.2}$$

which, being a measure of the likelihood that a pulse was detected in that channel, is used to discriminate between real pulses of light and noise. If the ratio exceeds 5 (*i.e.* the observed signal is more than five standard deviations above the pedestal mean) the pixel is defined as being part of the image. This allows elimination of channels with spurious signals, not associated with the real image of a shower, in what is termed **image cleaning**. The threshold of 5-σ S/N for image pixels is rather strict, however, and relevant information may be gleaned from weaker signals in the camera. To this end, so-called **picture/boundary cleaning** is employed to retain pixels bordering the core image of a shower: those channels passing the initial image-cleaning cut are 'picture' pixels; channels neighbouring the picture pixels are then considered and subject to a weaker cut of 2.5-σ S/N which, if passed, allows those channels to be included in the image as 'boundary' pixels. Channels failing both the criteria for picture and for boundary pixels are ignored in further analysis.

[4] See §3.2.4.1.

The pixels of which the image is composed are then gain-balanced. The signal in each channel is divided by the relative gain (see §3.2.4.1) appropriate to that channel :

$$\Delta' = \frac{\Delta}{g_{\text{rel}}} \tag{4.3}$$

If a channel produces more signal than the mean in a flat-field calibration run, it has a relative gain greater than one and systematically overestimates the amount of light, so the signal must be tempered; likewise, a relative gain less than one implies a systematic underestimate of the amount of light and the signal in that channel needs to be enhanced.

Image parametrisation. The resulting image, cleaned of noise and gain-balanced, may now reliably be parametrised, so as to estimate the position, orientation and spread of the distribution of light in the image. As prescribed by Hillas [106], moment analysis is used to construct the geometry of a two-dimensional (elliptical) Gaussian distribution :

$$\begin{aligned} f(x,y) \quad \propto \quad & \exp\left[-(x-\mu_x)^2/2\sigma_{x^2}^2\right] \\ & \times \exp\left[-(x-\mu_x)(y-\mu_y)/\sigma_{xy}^2\right] \\ & \times \exp\left[-(y-\mu_y)^2/2\sigma_{y^2}^2\right] \end{aligned} \tag{4.4}$$

which may approximate the form of the image. As the image geometry (Figure 4.4) is related to that of the event (Figure 4.5), these image parameters may eventually be used to construct a parametrisation of the shower geometry.

As detailed in [72], for all image pixels, with index j, the camera coordinates (x_j, y_j), weighted by the signal in each pixel (Δ'_j), are used to calculate the first moments :

$$\langle a \rangle \quad \text{for} \quad a = x, y \tag{4.5}$$

and second moments :

$$\langle ab \rangle \quad \text{for all combinations of} \quad a = x, y \quad \text{and} \quad b = x, y \tag{4.6}$$

of the image signal distribution, where :

$$\langle c \rangle = \sum_j (c)_j \Delta'_j / \sum_j \Delta'_j \tag{4.7}$$

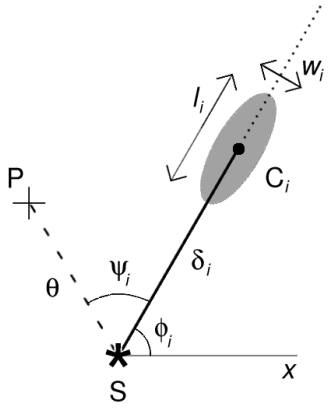

Figure 4.4: Single-telescope image geometry. In the FOV of a telescope (index i), a given direction is a point and a plane containing the telescope is projected onto a line. All telescopes share a common pointing direction, P (crosshair), and should agree on the source location, S (asterisk), and the angle θ whose plane is inclined to the image axis by the angle ψ_i. The shower maximum is viewed by each telescope as the centroid, C_i (spot), of an approximately elliptical image which is separated from the shower's arrival direction by an angle δ_i. The image may be parametrised equivalently relative to any location in the FOV common to all telescopes: here I have chosen the source location for simplicity of illustration, though this is obviously not known *a priori*. Typically it is most convenient, computationally, to use the pointing direction as the common origin: this introduces only an offset of the image centroids and does not affect the basic principles of the analysis. The FOV coordinates also must have a common axis: here the horizontal (x-) axis is indicated with the image axis inclined relative to it by the angle ϕ_i.

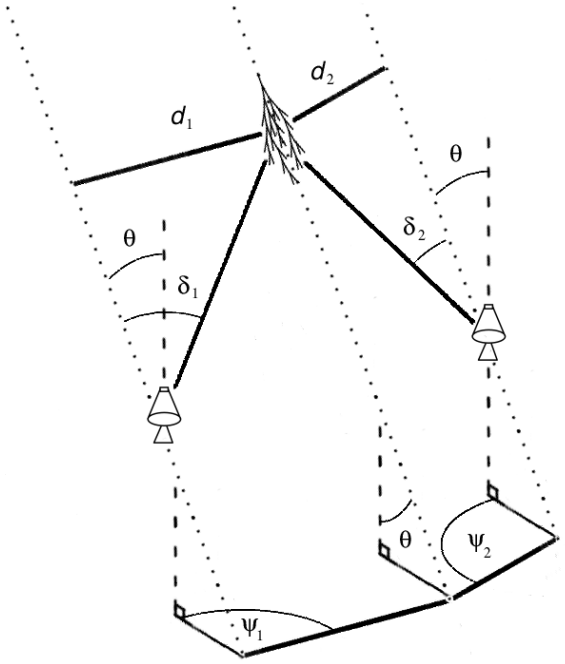

Figure 4.5: Spatial geometry of the stereoscopic observation of an EAS. Only two telescopes are shown and horizontal dimensions have been greatly exaggerated for clarity. Vertical dashed lines are parallel to the pointing direction. Slanted dotted lines are parallel to the arrival direction of the shower primary which is at an angle θ to the pointing direction. Thick lines indicate the impact parameter of the shower primary, d_i, and the direction of the shower maximum, δ_i, (relative to the arrival direction) as viewed from each of the telescope locations; $i = 1, 2$ is the telescope index. In the FOV of a telescope, a given direction is a point and a plane containing the telescope is projected onto a line. Spatial angles between planes are projected onto a plane perpendicular to the pointing direction. All telescopes share a common pointing direction and, consequently, the angle θ whose plane is inclined to that of the shower maximum direction by the angle ψ_i in the plane perpendicular to the pointing direction.

for $c = a$ or $c = ab$ as appropriate.

From these, the means :

$$\mu_x = \langle x \rangle \quad \text{and} \quad \mu_y = \langle y \rangle, \tag{4.8}$$

variances :

$$\sigma^2_{x^2} \quad \text{and} \quad \sigma^2_{y^2} \tag{4.9}$$

and covariance :

$$\sigma^2_{xy} \tag{4.10}$$

of the distribution may be calculated, where :

$$\sigma^2_{ab} = \langle ab \rangle - \langle a \rangle \cdot \langle b \rangle \tag{4.11}$$

Thus the images are parametrised as ellipses: *e.g.* Figure 4.6 and Figure 4.7. From these basic parameters of the distribution, the detailed geometrical parameters may be determined. Namely, image position :

$$\mathrm{C}_i(\mu_x, \mu_y) \tag{4.12}$$

and orientation of the major axis[5] :

$$\phi_i = \arctan\left[\frac{(t^2 + s^2)\mu_y + 2\sigma^2_{xy}\mu_x}{2\sigma^2_{xy}\mu_y - (t^2 - s^2)\mu_x}\right] \tag{4.13}$$

where $t^2 = \sigma^2_{y^2} - \sigma^2_{x^2}$ and $s^4 = t^4 + 4\sigma^4_{xy}$. As noted above, these are directly related to the geometry of the shower and may be used to reconstruct the shower axis by intersection of the multiple image ellipse axes.

Also of interest are the spread along the minor and major axes of the image ellipse, respectively known as the **width**, w, and **length**, l :

$$w = \sqrt{\frac{\sigma^2_{x^2} + \sigma^2_{y^2} - s}{2}} \tag{4.14}$$

$$l = \sqrt{\frac{\sigma^2_{x^2} + \sigma^2_{y^2} + s}{2}} \tag{4.15}$$

[5] Once the image axis has been defined, the gradient of t_0 along the shower is determined via a linear fit. This is used to refine the placement of the integration window of each channel in the image [110]. The revised t_0 is defined according to the value of the fit at a pixel's position along the major axis of the image, effectively averaging over nearby values of t_0. The new integration window is also narrower (12 instead of 18 samples) which helps to diminish noise due to NSB. The images are then re-parametrised using the improved integrated charges.

These parameters encapsulate the shape of the shower and will be used for gamma/hadron separation. For instance, compare Figure 4.6 and Figure 4.7: these two shower images are quite similar in most respects and, in particular, carry similar total signal (see 'size' below) but obviously differ considerably in terms of how this signal is distributed relative to the core of the image. The sprawling aspect of the image in Figure 4.7 and its concomitant large width mark it as the image of a hadronic shower.

The remaining image parameter of note is the **size** :

$$\varsigma = \sum_j \Delta'_j \tag{4.16}$$

which is simply the total signal in all of the image pixels. This property allows an estimate of the energy of the primary because it corresponds directly to the amount of light collected by the telescope to form the image which, in turn, is directly related to the number of relativistic particles created in the EAS and so to the energy deposited over the course of the event.

It should be noted that the size and spread of the image formed by a telescope depend not only upon the energy and type of the primary but also upon the distance of the EAS axis from the telescope. Eventually, we wish to unfold information concerning the energy and type of the primary from the location of the shower. Thus it is necessary to first reconstruct the location of the shower core relative to the telescopes, from which the required impact parameter follows. Given this information, the primary's energy and type may be estimated if the expected parameters for a shower with such a location are known. So, for a given event we must first reconstruct the arrival direction and core location of a shower and then estimate the energy and identity of the primary.

Image and reconstruction quality. Reconstruction of the axis and location of the shower is purely geometrical and is based on intersection of the image axes (see §4.1.1 and §4.1.2, below). To ensure that the intersection point is reliable, we may introduce quality cuts which ensure that there is proper and sufficient corroboration between images in this determination.

To begin with, we may ensure that the axes of images used are themselves reliable. **Image-quality cuts** ensure that an individual image is well-defined and therefore that its axis may be determined with reasonable accuracy. An image may be disregarded on the basis of a minimum number of pixels of

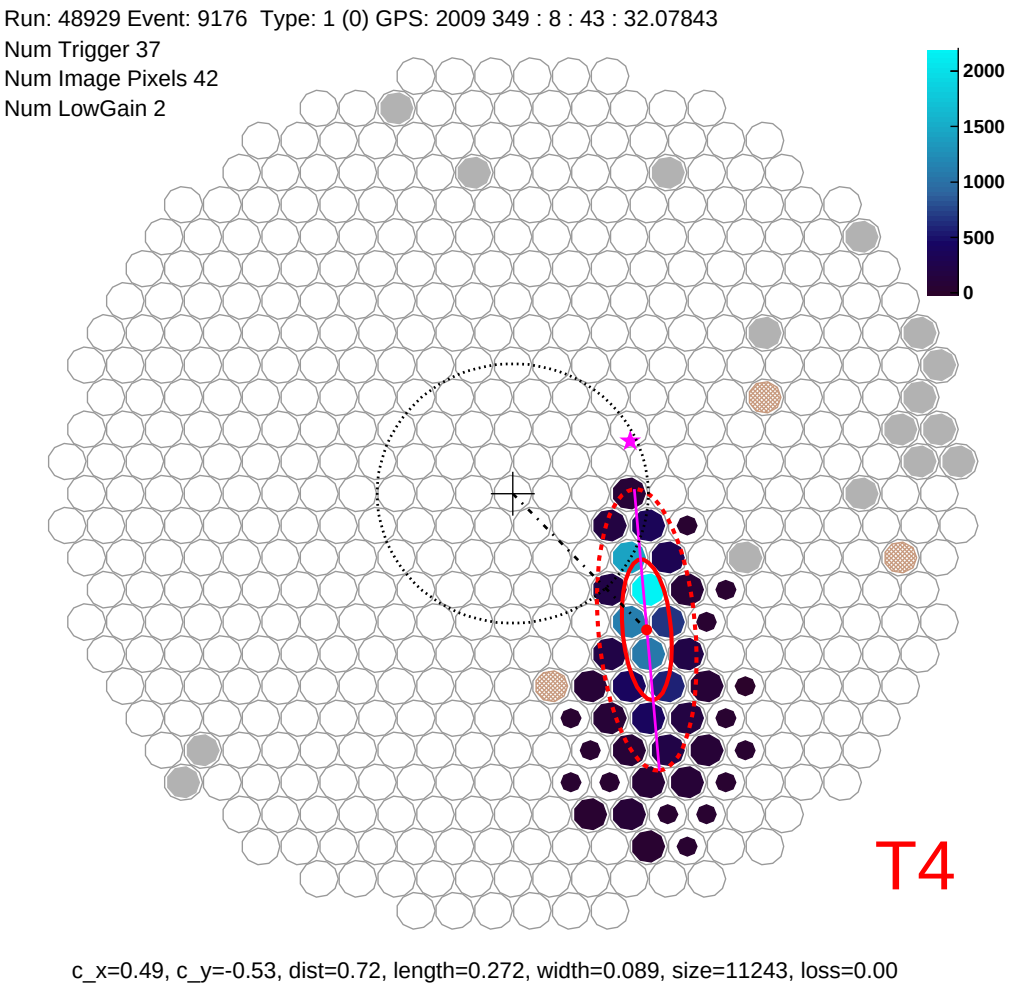

Figure 4.6: A parametrised image of a candidate gamma-ray-induced event. The colour code is of pedestal-subtracted integrated charge: pixels that are not filled according to the colour code are insensitive and not included in the image analysis. Larger colour-coded circles indicate picture pixels, smaller circles are boundary pixels: pixels below the boundary threshold are empty. The Gaussian approximation to the image charge distribution (the red ellipse is the 1-σ contour, whose major and minor axes correspond to the length and width, respectively) captures the form of the shower with reasonable accuracy. Image credit — captured by one of the telescopes of the VERITAS array during observation of the Crab; data processing and display due to `eventdisplay` (see §5.2.1).

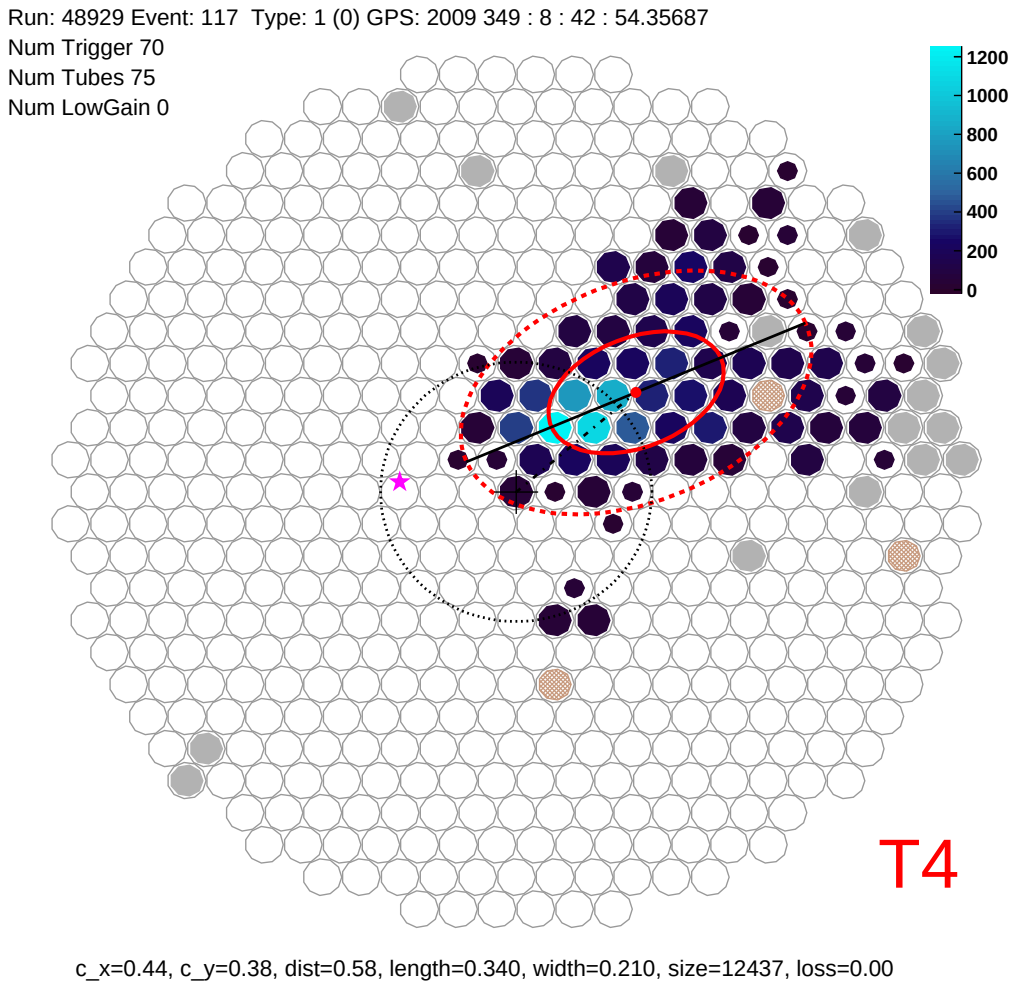

Figure 4.7: A parametrised image of a candidate hadronic cosmic-ray-induced event. The colour code is of pedestal-subtracted integrated charge: pixels that are not filled according to the colour code are insensitive and not included in the image analysis. Larger colour-coded circles indicate picture pixels, smaller circles are boundary pixels: pixels below the boundary threshold are empty. The Gaussian approximation to the image charge distribution (the red ellipse is the 1-σ contour, whose major and minor axes correspond to the length and width, respectively) does not accurately represent the sprawling form of the image but is notably broader than the candidate gamma-ray event in Figure 4.6, especially given the similarity between the images in terms of the other parameters. Image credit — captured by one of the telescopes of the VERITAS array during observation of the Crab; data processing and display due to `eventdisplay` (see §5.2.1).

which it must be composed, a minimum size or a maximum overlap of the camera edge. Firstly, if the image is not spread over enough pixels there will be insuffucient resolution in the moment analysis calculation of image distribution parameters: the intrinsic uncertainty will be too large. Secondly, an image with larger size constitutes a brighter image to which many photons contributed: fluctuations due to the distribution of photons across the image will be comparitvely less and the weighting of the image pixels will be far above noise. Finally, if an image abuts the edge of the camera, it is possible that it has, in fact, been truncated and that some of the image has been lost. To identify these cases each image is also assigned a **loss** value: this is the fraction of image size contained in pixels at the camera edge. If its loss is too large, an image is deemed to have excessive overlap of the camera edge. In this way not all images captured in an event may be used for detailed reconstruction.

Furthermore, an entire event may be deemed unusable if reconstruction itself cannot be performed reliably. This decision is based upon **(stereo-) reconstruction-quality cuts**. One such cut would simply be to require that an event have enough images of a sufficient quality for reliable stereoscopic reconstruction to proceed. The most relaxed form of this cut would require only two images (in order to have a single point of intersection between the two image axes) but, in order to avoid degeneracy when image axes are almost parallel, it is preferred that three images be present. Another criterion for the quality of reconstruction is that the image axes must not intersect at too shallow an angle because the location of the intersection point becomes strongly affected by even small deviations in image axis orientation. This occurs primarily when the core location is far from the array such that each telescope views the shower from a similar angle. Thus a maximum core distance may be used as a reconstruction quality cut.

These cuts are deliberately quite rudimentary and the cut values used (*e.g.* see Table 5.1) are quite loose, permitting a wide range of events to pass, in order to limit any bias they introduce. For example, it is typical to require at least four pixels in an image, requiring only one more than the hardware pattern trigger (see §3.2.3.1). These cuts are not intended to significantly reduce the number of events considered in analysis but serve only to ensure that reconstructed shower primary parameters are trustworthy.

4.1.1 Arrival Direction Reconstruction

The major axis of each image is taken as residing in a plane containing the shower, the telescope that imaged it and the primary's arrival direction. In Figure 4.5 these are each of the planes containing the angles δ_i. Each telescope has a different viewing location relative to the shower and this results in the differing centroid positions and image axis orientations between telescopes (see Figure 4.8). However, in any case, following an image axis corresponds to sweeping out the angle δ_i along the shower axis, leading inevitably to the source direction.

Multiple images of the same EAS are combined stereoscopically by superimposing them in their common angular coordinate system, that of their co-pointing FOV. To reconstruct a unique arrival direction the major axis of each image is extrapolated to a common intersection point, see Figure 4.9. This point defines the reconstructed position of the source of this shower in the sky.

In general the axes do not exactly overlap each other, all at the same point. So, in practice, a point which simultaneously minimizes the distance to all image axes is found [136]. Furthermore, as a brighter image may be presumed to be better defined and thus provide a more reliable determination of the major axis, image size is used as a weight for the squared perpendicular distance between an image axis and the candidate source location in the minimization. This idea is corollary to the principle of the size-based image-quality cut noted above.

The angular resolution of direction reconstruction is derived from the width of the distribution of reconstructed arrival directions of showers from a point-source, see Figure 4.10: for VERITAS, 68% of reconstructed gamma-rays are contained within a 0.1-degree radius of the true source location. This is sometimes termed the gamma-ray PSF, in analogy to the PSF describing the optical quality of a telescope. It is largely dominated by statistical fluctuations in the images. Higher resolution images of the showers themselves would not lead to a significantly more accurate determination of the images' axes, as would be required to improve the intersection point they provide. This is either due to a limited yield of Cherenkov photons from low energy showers or, at higher energies, intrinsic fluctuations in the EASs themselves.

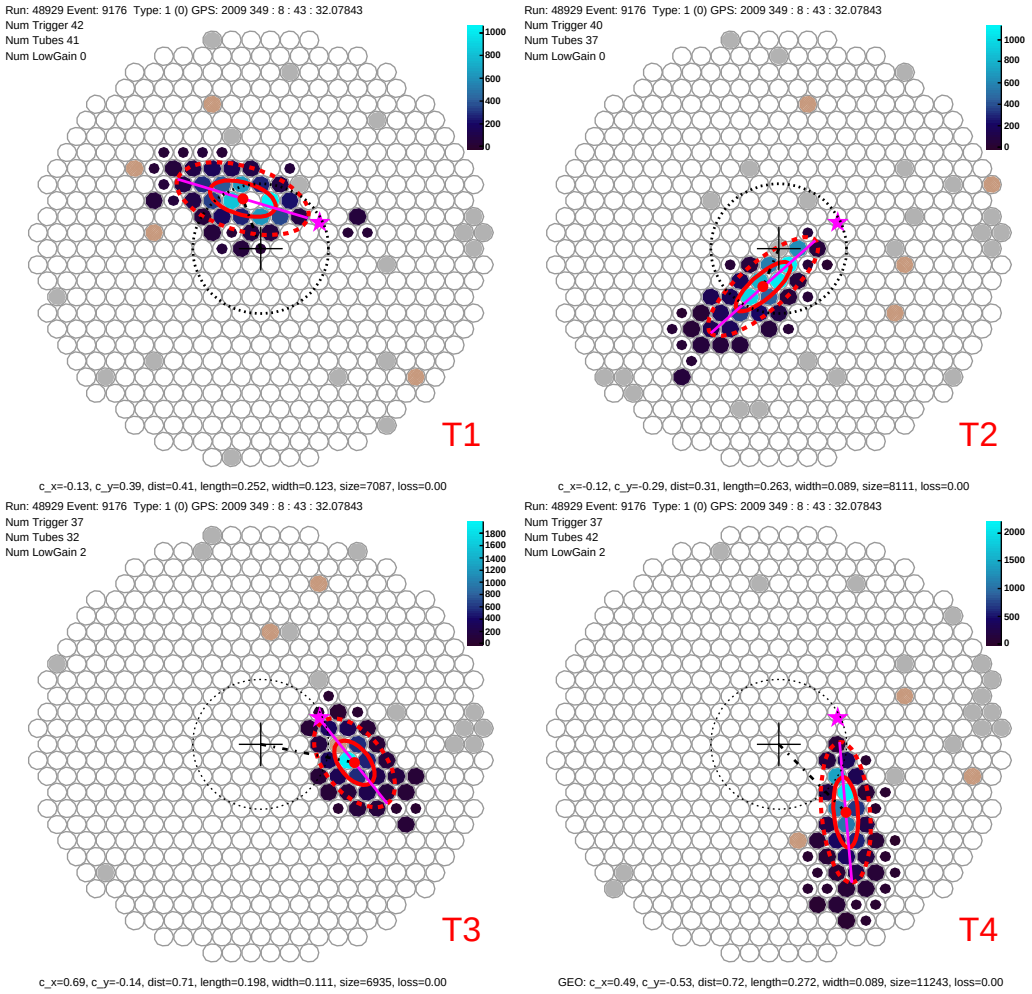

Figure 4.8: All of the images captured by the VERITAS array for a single gamma-ray candidate. Refer to Figure 4.4 for an explanation of the representation of the individual images. Recall that each image is a sample of the angular distribution of Cherenkov light from the observed EAS. The image axes are all oriented with respect to a single point/direction in the FOV shared by the co-pointing telescopes: this is the orientation of the observed EAS and the arrival direction of the primary that induced it. The magenta star indicates the reconstructed arrival direction (see Figure 4.9). Image credit — captured by the telescopes of the VERITAS array during observation of the Crab; data processing and display due to `eventdisplay` (see §5.2.1).

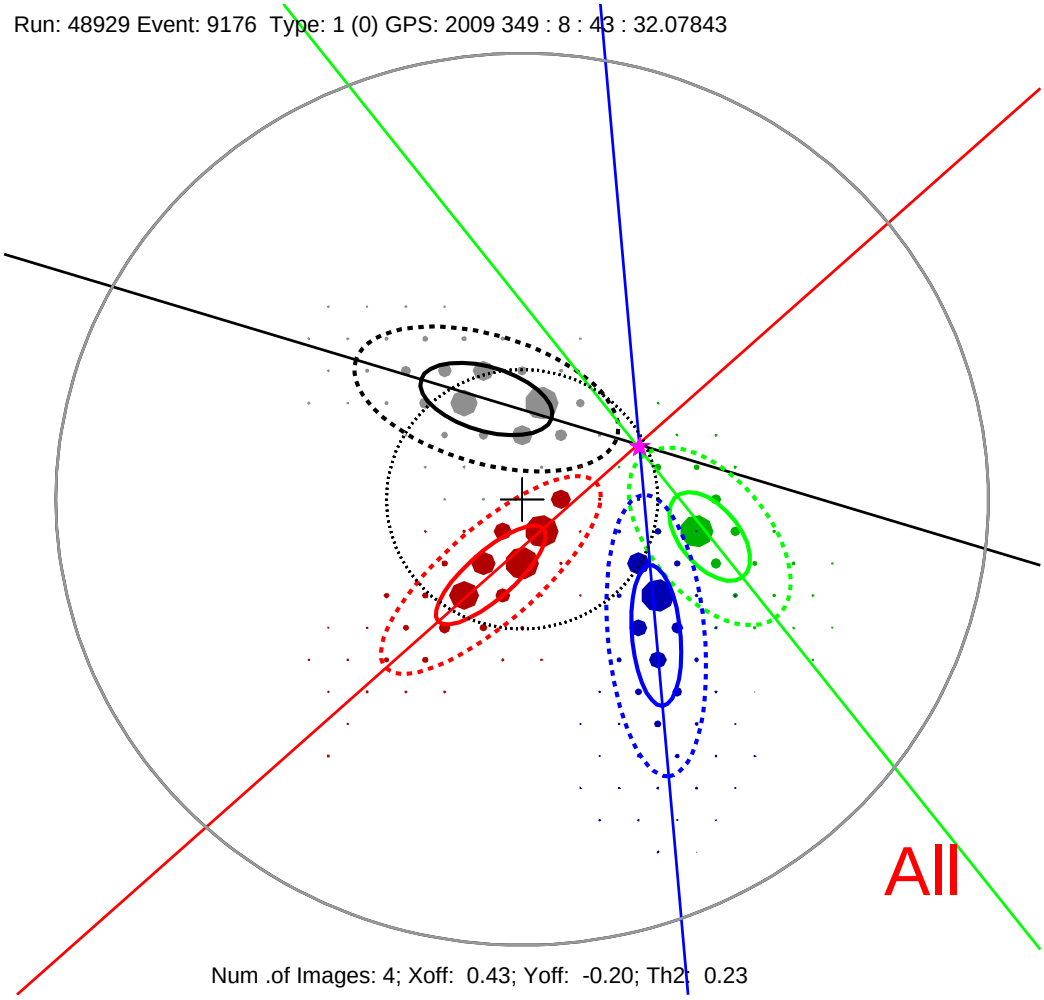

Figure 4.9: Arrival direction reconstruction for the event shown in Figure 4.8. The extrapolated major axes overlap at the position of the source in the common FOV of the co-pointing cameras. Image-parameter ellipses and axes from telescopes 1, 2, 3 and 4 are respectively black, red, green and blue. Pixels from the respective telescopes are colour-coded similarly; their areas are proportional to the signal in each. Image credit — captured by the telescopes of the VERITAS array during observation of the Crab; data processing and display due to `eventdisplay` (see §5.2.1).

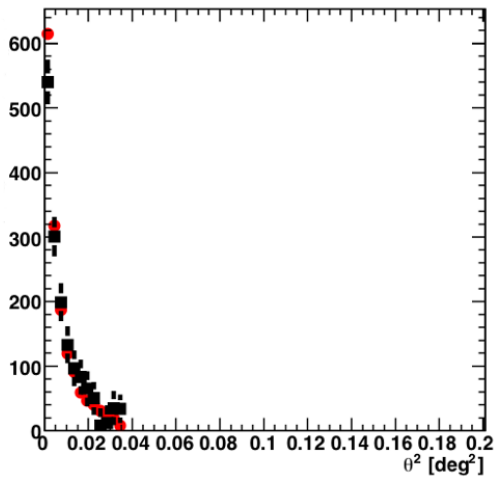

(a) Distribution of θ^2

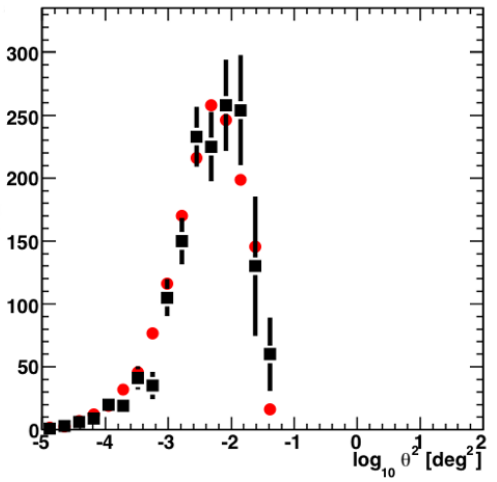

(b) Distribution of $\log_{10}\theta^2$

Figure 4.10: Distribution of reconstructed arrival direction for gamma-ray events: binned by the square of the angular offset from the source, (a), *i.e.* by θ^2; binned by $\log_{10}\theta^2$, (b). The black histograms were generated from background-subtracted Crab Nebula data: the vertical scale is the number of showers. The red histograms were generated using Monte-Carlo simulations: the vertical scale is arbitrary, chosen to give the same total content as the black histogram. The two data sets agree well. The angular resolution (68% containment) is 0.1°. This corresponds to a point (−2) near the peak of the distribution in $\log_{10}\theta^2$. Image credit — G. Maier.

4.1.2 Core Location Reconstruction

Further information is required to allow for gamma/hadron separation and energy estimation: the impact parameter of the shower core must also be determined. This can be achieved by considering, together, the orientation of the shower images and the locations of the telescopes in a plane perpendicular to the shower's arrival direction. A line from the reconstructed source, through the image centroid defines a plane containing the shower's axis and that particular telescope (again, this is the plane containing the angle δ_i in Figure 4.5).[6] If this plane, for each telescope, is extrapolated in the position coordinate system defined by the telescope's locations, the common line of intersection will be the unique axis of the EAS, see Figure 4.11.

In this way the impact parameter for each of the telescopes is effectively measured at the altitude of the shower maximum. This is the **core distance**, which represents the position of the telescope in the light-pool created by the shower. In general, the position in the light-pool subtly affects the amount and distribution of light received by the telescopes and thus the measured width, length and size (see §4.1.3 and §4.2.2).

4.1.3 Energy Estimation with Lookup Tables

The arrival direction of a primary (and consequently the core location) can, as indicated above, be determined purely by geometry but an estimate of the energy must take into account many absolute quantities of the detector response. The energy must be estimated from the amount of light received by the array and in order to relate this to the signal generated by a given telescope it is necessary to follow the complete throughput of each instrument including factors such as :

light-pool fluctuations — due to intrinsic shower fluctuations; atmospheric propagation effects, which vary with zenith angle and shower altitude; and shower viewing angle.

optical efficiency — including such effects as obscuration of mirrors by the camera housing; mirror reflectivity; the optical PSF; photon collection and conversion efficiencies on the PMTs at the camera face.

[6] Note that the reconstructed source is used and not the original image axis. Thus core location reconstruction benefits from an average over multiple images in the definition of the planes to be intersected.

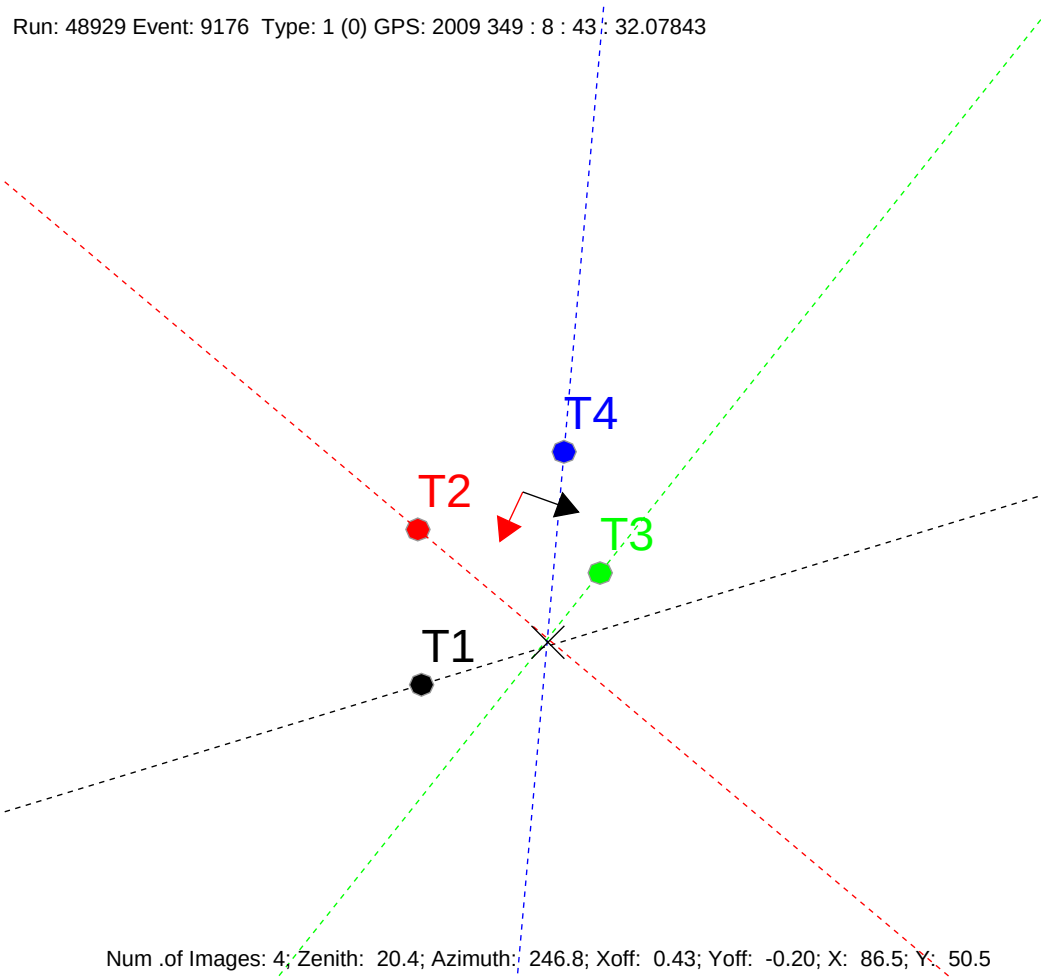

Figure 4.11: Each of the planes containing a telescope, the shower's core and the arrival direction intersects along the extrapolated path of the primary. Extrapolating the image orientations, in the coordinate space defined by the telescopes' positions perpendicular to the arrival direction, provides the core location as the intersection point. From this the impact parameter or core distance can be derived. The arrows indicate the ground plane of the array from the point of view of the arrival direction: the black (red) arrow indicates North (East). Image credit — captured by the telescopes of the VERITAS array during observation of the Crab; data processing and display due to `eventdisplay` (see §5.2.1).

electronic response — degradation of the absolute conversion of light to charge in any PMT occurs as the latter ages; the amount of pedestal noise (mainly due to NSB) will affect the number of image pixels determined by the analysis and directly interfere with the measured quantity of light.

Accounting for so many factors, many of which are described by purely empirical or *ad hoc* distributions, is a complex (if not intractable) task and so is consigned to the realm of simulation. EASs due to VHE gamma-ray primaries impinging on the upper atmosphere at a particular zenith angle are simulated using Monte Carlo methods to generate realistic fluctuations in the number of photons intercepted by the array. These photons are then passed through a simulation of the the telescope optics and electronics, operating at a particular noise level, in order to correctly calculate the number of photons collected and converted by each telescope and the PMT signals thereby generated. The simulated signals are processed and events reconstructed in exactly the same manner as genuine data. A histogram can then be constructed for the simulated energies required to produce a given image size from a given core distance.

By effectively inverting the process of filling such a histogram, it can be used as a **lookup table**: given a reconstructed size and a reconstructed core distance the mean intrinsic energy of gamma rays which produce those values can be retrieved. In fact, as events are observed at a given zenith angle and noise level, a set of lookup tables is required covering the possible ranges of these conditions and the correct lookup table must be used for any given event according to them. Also, for realistic events, light-pool fluctuations will result in differing estimates between telescopes so an average of individual estimated energies is used for the event as a whole.

Identification of the shower primary, as a gamma ray or hadronic cosmic ray, similarly uses lookup tables and is an important component of controlling background contamination of astrophysical gamma-ray signals. This will be addressed below.

4.2 Coping with Background

The background of hadronic cosmic-rays is isotropic whereas many gamma-ray sources are point-like, within the angular resolution of the arrival direction reconstruction. Thus, what might seem an overwhelming event rate due

to cosmic-ray-induced showers encroaching on the telescopes' FOV can be considerably alleviated by limiting the region of interest in the sky during analysis.

Beyond this, and as outlined above, the copious cosmic-ray rate can be substantially diminished by gamma/hadron separation. However, afterwards, there remains the irreducible component of that background and it must be accurately estimated and deducted from any observed event rate. Then we must appeal to a statistical treatment of any excess that explicitly accounts for the possibility of fluctuations in that remaining, appreciable background rate.

4.2.1 Source Region

The region of interest in analysis must be restricted to admit as little of the isotropic background as possible without greatly sacrificing exposure to any potential gamma-ray source. If we define θ to be the angular separation between a candidate source position[7] and the reconstructed arrival direction of an event, this restriction is defined by the θ^2 cut. Though θ corresponds to an angular radius the squared form is more convenient in that the area of the region defined (and so exposure to a uniform source) grows linearly with it.

This cut (a maximum allowed value of θ^2) ensures that the arrival direction of the primary is close to the sky position of the target of observations. The ideal value of the θ^2 cut is determined by the angular resolution of the direction reconstruction, seen in Figure 4.10(a). If the cut value is too small relative to the resolution, valid showers from the source region may be neglected and fail to be counted. If it is too large, extra background counts would be accumulated without a corresponding gain in exposure to a point source. The optimal region for this cut can be identified from the distribution due to a point source against $\log_{10}\theta^2$, *i.e.* Figure 4.10(b): considering that successive bins in $\log_{10}\theta^2$ represent ever greater angular area, it is apparent that near $\log_{10}\theta^2 \approx -2$ a law of diminishing returns sets in and the increasing bin area is not rewarded with an increase in collected events. The standard value for this cut is $\theta^2 < 0.010$–0.015 degrees-squared , depending upon the expected strength of the source.

[7] Above we took the candidate source position to be the pointing direction but this need not be the case and, indeed, in some cases it is desirable to deliberately introduce a pointing offset, as we shall see in §4.2.3.

4.2.2 Hadron Rejection

As with energy estimation, the expected response of the array must be catalogued in order to establish the link (albeit an approximate one) between a given image distribution and the identity of the shower primary. Thus, also in a similar manner to the determination of primary energy, lookup tables are constructed from simulations of gamma-ray events processed in exactly the same way as observational data. Showers are simulated at a given zenith angle and the median width and length of images are determined and recorded for a range of bins of characteristic image sizes and reconstructed core distances (*e.g.* Figure 4.12). Likewise the spread in the determined width and length of images in the same bins of size and distance are stored in another lookup table (*e.g.* Figure 4.13). With the observed size and reconstructed impact parameter of a real event the expected width and length and acceptable range of these parameters for a gamma-ray-induced shower may be recovered.

A given observed shower is compared to these expected distributions of width and length in the following way. Having measured the size, ς_i, width, w_i and length, l_i, of each of the images, i, and reconstructed the core distance to the respective telescopes, d_i, the event may be assigned a **mean scaled cut parameter** (MSCP). This is defined [62, 136] to be :[8]

$$\mathrm{MSCP} = \frac{1}{N_{\mathrm{tel}}} \sum_{i=1}^{N_{\mathrm{tel}}} \frac{p_i - m_p(s_i, d_i)}{\sigma_p(s_i, d_i)} \tag{4.17}$$

where N_{tel} is the number of telescopes having an image and the parameter, P (p), may be either width, W (w), or length, L (l): m_p is the median of the single-image parameter and σ_p^2 is its variance, as determined from the lookup tables.

The purpose of these parameters is to encapsulate to what extent the event deviates from the expected response of the array to a gamma-ray-induced shower. They account for both the expected extent of the image of a gamma-ray-induced EAS and the expected intrinsic variation between such showers. The definition also uses an average over all images in an event to improve the estimate.

The distribution of either MSCP (*i.e.* for both P = W and P = L) for gamma-ray events is centred on zero, corresponding to a shower that exactly

[8] Note that this is a dimensionless value, much like a signal-to-noise ratio.

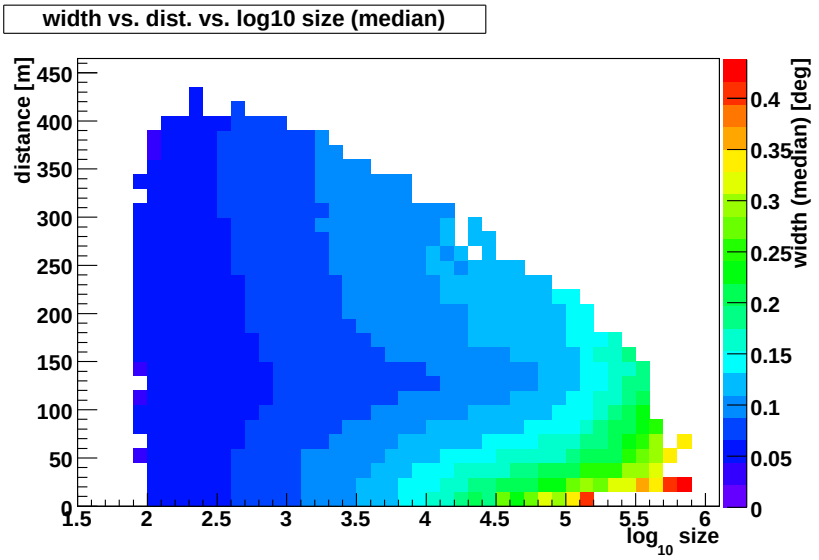

Figure 4.12: An example lookup table for median width. For given image size and core distance the expected width of the image (colour-coded: median width in degrees) due to a gamma-ray-induced EAS may be retrieved. It can be seen that brighter images (greater size) are generally larger (greater width) and that images of the most distant showers tend to be dimmer. Images may be formed of showers with impact parameter (distance) greater than the nominal light-pool radius (~ 120 m). This is possible because small-angle scattering of the light will diffuse it a little beyond this radius, accounting also for the dimness of distant showers. Inside the light-pool the image is dominated by Cherenkov light directly from the shower particles and so the image narrows with increasing distance as a telescope's aperture subtends a smaller angle relative to the shower. Also, the light-pool is actually somewhat more intense near the edge (where the direction to the shower as a whole is approximately the Cherenkov angle) so size migrates upwards with distance for a given shower, with a fixed physical extent.

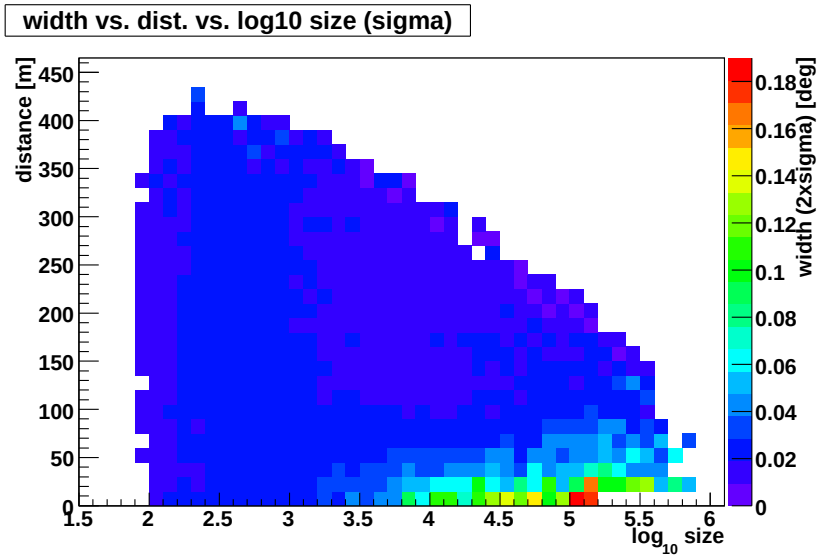

Figure 4.13: An example lookup table for the variation of the width. For given image size and core distance the spread in the measured width of the image (colour-coded: twice the square-root of the variance of the width) due to a gamma-ray-induced EAS may be retrieved. Note that the scale of the spread in the measured width (Figure 4.12) is less than half that of the median width. The variance is largest for images with small distance. This may be a consequence of these images being almost circular (the shower is viewed almost end-on) and shower fluctuations will drive determination of an image axis.

matches expectations, and spread symmetrically between ± 1. A hadronic shower is expected to generally produce more sprawling images than those due to a gamma-ray shower (*i.e.* MSCP > 0) but, as noted at the beginning of this chapter, they may also be quite similar in extent (MSCP $\simeq 0$)[9]. Thus, in order to adequately reduce background rates, it is necessary to assume that some events are not gamma-ray-induced even if their widths or lengths are within reasonable bounds of variability for just that sort of shower (MSCP $\lesssim 1$). On the other hand, images more compact than those expected from a gamma-ray shower (MSCP < 0) may safely be assumed to indeed be due to a gamma-ray-induced event. Thus, the acceptable range is deemed to be $-1.2 <$ MSCP < 0.5 (for both P = W and P = L) and events falling outside this domain are rejected.

We can see that these cuts have the intended effect by comparing simulated distributions of gamma-rays to observational data taken on a strong source such that the background introduces only minor fluctuations after estimation and subtraction (see §4.2.3): just such a strong source is the Crab Nebula. Figure 4.14 and Figure 4.15 demonstrate the agreement between simulations and background-subtracted Crab Nebula data. It is readily apparent that the MSCP cuts would become less efficient if they allowed values above 0.5.

For weaker sources (such as the majority of VHE targets and especially unknown ones) the principle remaining problem is estimation of the remaining background rate and accounting for its fluctuations in statistical analysis of any excess.

4.2.3 Estimation of Background

Due to the isotropic nature of the background of cosmic-ray events, the most straight-forward approach to background estimation is to count the rate of events in one or more regions of sky (OFF-regions) which should be identical to the candidate region (ON-region) except that the latter may be suspected to contain a gamma-ray source. This is the approach used by the **reflected region background model** [37] which has been used for the analysis results presented in this thesis.

The crux of this model is that observations are made in **wobble mode**:

[9] Ultimately, this is the origin of the irreducible background of gamma-like hadrons.

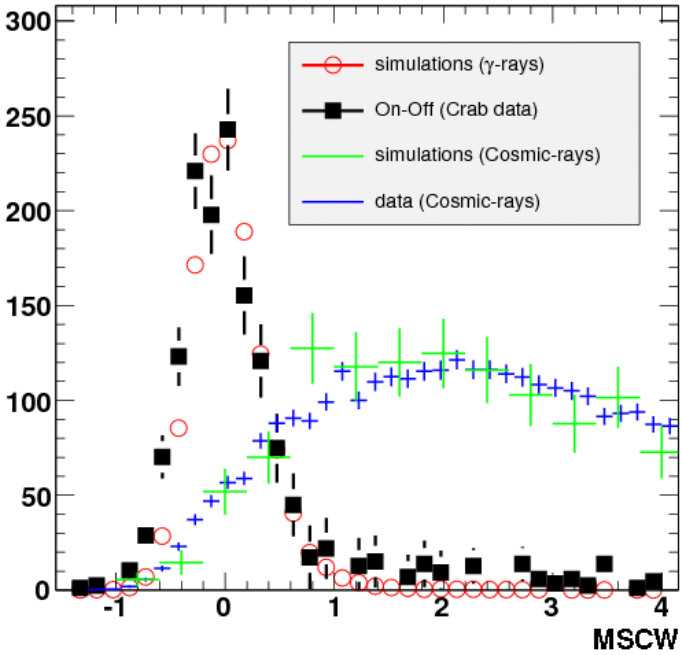

Figure 4.14: Distribution of a gamma/hadron separation parameter (MSCW, see main text for definition) for both types of primaries and comparing observations with simulations. Histograms of observational data have a vertical scale of the number of showers but cosmic ray rates have additionally been normalised to account for the different exposure in the ON- and OFF-regions (see §4.2.3). Histograms derived from Monte-Carlo simulations have an arbitrary vertical scale chosen to ensure the same normalisation as the observational data. Image credit — G. Maier.

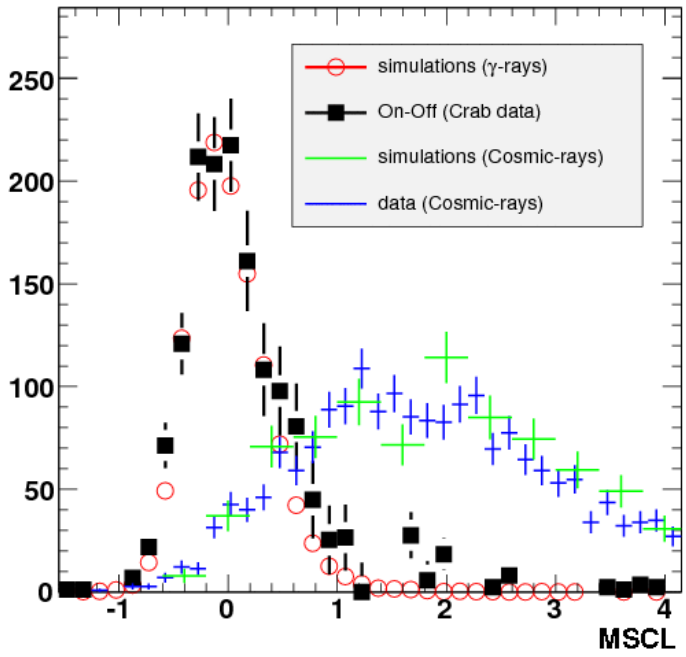

Figure 4.15: Distribution of a gamma/hadron separation parameter (MSCL, see main text for definition) for both types of primaries and comparing observations with simulations. Histograms of observational data have a vertical scale of the number of showers but cosmic ray rates have additionally been normalised to account for the different exposure in the ON- and OFF-regions (see §4.2.3). Histograms derived from Monte-Carlo simulations have an arbitrary vertical scale chosen to ensure the same normalisation as the observational data. Image credit — G. Maier.

that is, with a deliberate pointing offset from the suspected source.[10] This allows the definition of multiple OFF-regions placed symmetrically around the pointing direction. Each OFF-region has a distance from the centre of the FOV identical to that of the ON-region, see Figure 4.16. In this way

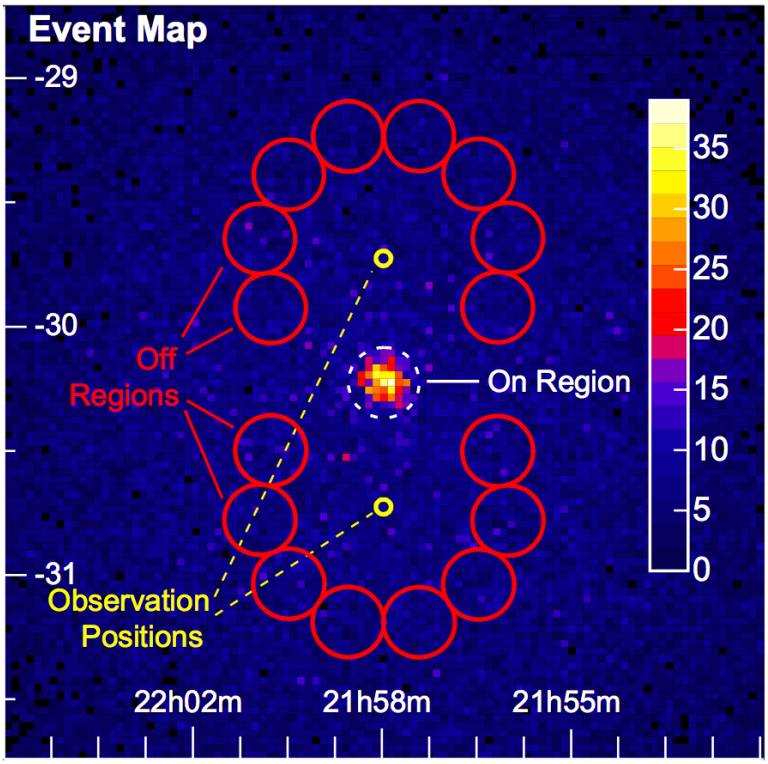

Figure 4.16: The ON-region is placed on the candidate source position, from which the observation positions (pointing directions) are deliberately offset. OFF-regions for background estimation are placed symmetrically about the pointing directions with respect to the ON-region. Background is estimated from equivalent regions (assuming rotational symmetry of the FOV) and under identical observing conditions. Image credit — from Fig. 4 of [37].

the exposure of the instrument for the purposes of background estimation is made simultaneously with observation and therefore under identical observing conditions. The only assumption made here is that the acceptance of the

[10] The name derives from the need to switch back and forth between several pointing directions around the target during successive data runs.

array is azimuthally symmetric. That is to say, a shower falling within the FOV has an equal probability of detection and reconstruction to any other whose arrival direction is offset by the same amount from the centre.

The critical parameters of this background model are the extent of the ON- and OFF-regions and the number of the latter. The size is defined by the θ^2 cut. There is only a single ON-region, of course ($n_{\mathrm{ON}} = 1$), and the number of OFF-regions (n_{OFF}) may be characterised by :

$$\frac{n_{\mathrm{ON}}}{n_{\mathrm{OFF}}} = \frac{1}{n_{\mathrm{OFF}}} = \alpha \tag{4.18}$$

for reasons which will become clear below. The total number of events collected in all the OFF-regions will be N_{OFF} and likewise N_{ON} for the ON-region.

The mean number of events in an average OFF-region can be used as an estimate of the number of events in the ON-region that are due to the irreducible background. Compared to this mean, an excess of events, $X = N_{\mathrm{ON}} - \alpha N_{\mathrm{OFF}}$, in the ON-region could indicate the presence of an additional source of gamma-ray-like showers. However, as the background level tends to be quite large and suffer correspondingly large fluctuations, it may also be that the ON-region has simply, by chance, collected more background counts than the mean. To determine success in the detection of a source, we must appeal to statistics to estimate the probability that any excess is significantly greater than the level of background fluctuations.

4.2.4 Statistical Treatment

The standard treatment of a small excess over a prominent background, was developed in the field of VHE gamma-ray astronomy by Li & Ma [141]. They introduced a statistical measure which assumes, in essence, the null hypothesis : that counts measured in the ON- and OFF-regions are due to background alone and therefore that they constitute independent measurements of the same background rate. This was expressed in Eq. 5 of [141] as :

$$S = \frac{N_{\mathrm{ON}} - \alpha N_{\mathrm{OFF}}}{\sqrt{N_{\mathrm{ON}} + \alpha^2 N_{\mathrm{OFF}}}} \tag{4.19}$$

where N_{ON} (N_{OFF}) is the number of counts in the ON-region (OFF-region) and α is the ratio of exposure between the ON- and OFF-regions which, in the context of the reflected region model, is simply the inverse of the number

of OFF-regions. The numerator is an estimate of the excess count rate in the ON-region and the denominator an estimate of the scale of fluctuations possible in any one region, including the ON-region as a measure of the background rate.

This statistic can be understood as a measure of the probability that any excess can be explained solely by background fluctuations. Values of S close to zero indicate that the ON-region is very much consistent with the background rate; values of S far from zero indicate that it is less probable that the count rate in the ON-region is due solely to a fluctuation in the background rate. Also, more OFF-regions (smaller α) evidently leads to a greater value of S for a given excess, corresponding to the improved estimation of the background rate.

With continuing exposure $N_{\rm ON}$ and $N_{\rm OFF}$ will both grow (on average) linearly with time, t. It can be seen that if a steady source is present, so that the excess also grows (on average) linearly with t, S will grow only as $\sqrt{t}$. In observing a source one tenth as strong as some nominal value, one hundred times the exposure is required to attain the same significance.

Although the interpretation of this statistic is straight-forward, this particular definition does not lead to a standard normal distribution[11] of S and, perhaps more importantly, the distribution of S is dependent upon α: values of S are not directly comparable if α is subject to change between two particular measurements.

By considering a likelihood ratio instead, but using the same basic assumptions, Li & Ma derived the following estimate (Eq. 17 of [141]) of the **statistical significance** of an ON-region excess count rate :

$$S = \sqrt{2}\frac{X}{|X|}\left\{N_{\rm ON}\ln\left[\frac{1+\alpha}{\alpha}\left(\frac{N_{\rm ON}}{N_{\rm ON}+N_{\rm OFF}}\right)\right] + N_{\rm OFF}\ln\left[(1+\alpha)\left(\frac{N_{\rm OFF}}{N_{\rm ON}+N_{\rm OFF}}\right)\right]\right\}^{1/2} \quad (4.20)$$

This definition *does* lead to a standard normal distribution of S (including negative values for negative excess, $X<0$) and this property is independent of α. Such a property can be used to formulate a test of the uniformity of a data set: many directions within the FOV of observations can be treated as ON-regions and the distribution of S over all these directions should, within error, form a Gaussian distribution with an RMS of 1.

[11] $P(S)=\frac{1}{\sqrt{2\pi}\sigma}e^{-(S-\mu)^2/2\sigma^2}$ having $\mu=0$ and variance $\sigma^2=1$.

The individual values of S for each of the directions tested can be displayed at the appropriate positions in angular coordinates to construct a **sky map**. The sky map indicates the probability that background fluctuations are not sufficient to explain the measured excess from a given direction. In particular, negative values of S are displayed in cases where the excess is negative and simply indicate that the event rate from that direction is almost certainly due to background alone which in that case had fluctuated below the estimated level. For a well-estimated background and in the absence of sources, half of the sky map's area should display negative significance and these regions indicate the normal scale of fluctuations in the data set. The sky map contains many independent measurements of S, or trials, and so apparently large values can appear which are due simply to statistical fluctuations in a large sample. With this in mind, the standard threshold for detection is a seemingly draconian 5 sigma, corresponding to about one chance in three million for random fluctuations to generate such a significance in *a particular randomly-chosen* independent direction in the FOV. Reaching this threshold accidentally *anywhere* in a sky map of one thousand bins (*e.g.* a one-degree radius and 0.05-degree bin width) corresponds to a significance, after accounting for trials ('post-trials significance'), of only 3.4 sigma.

4.3 Event Sensitivity and Physical Measurements

As discussed above, the array registers individual photons and the subsequent analysis estimates their energy and arrival direction. However, physical models of emission mechanisms are based on concepts such as energy balance and flux. To convert measurements of counted photons to photon flux we must estimate the sensitivity of the instrument to photons of any given energy. This is embodied in the **effective area** function, $A_{\text{eff}}(\varepsilon)$.

Given a certain flux, $F(\varepsilon) = \frac{\mathrm{d}N}{\mathrm{d}\epsilon\ \mathrm{d}A\ \mathrm{d}t}$, the number of events, n, which successfully pass through the analysis chain can be defined by :

$$n = \int F(\varepsilon) A_{\text{eff}}(\epsilon)\, \mathrm{d}\epsilon \cdot t \tag{4.21}$$

where t is the dead-time-corrected duration of observation (the effective exposure of the detector). The effective area converts the number of actual

events that arrive N into the number successfully observed by weighting the sensitive area of the detector appropriate to the probability that a shower of given energy will be successfully detected and correctly reconstructed: $A_{\text{eff}} = \frac{\mathrm{d}n}{\mathrm{d}N} A$. Thus, effective area is a function of energy whose form depends upon the observing conditions, specifically:

image noise — the mean pedestal variance, as determined from pedestal events accumulated during a data run, is a measure of the contamination of the images by NSB which may render small-size events unreliable or unusable.

zenith angle of observation — increasing zenith angle increases the depth of atmosphere Cherenkov photons must traverse, which decreases the probability of correctly reconstructing low-energy showers because they generate few photons; it also increases the sensitive area of the detector because EASs are occurring farther from the telescopes, casting larger light-pools, resulting in a greater chance of intercepting the relatively less-common high-energy showers.

arrival direction offset — if the source of gamma-rays is offset from the observing direction[12] there is a risk that large images will spill over the edge of the camera and be rendered less amenable to analysis: this effect is more pronounced for high energy showers.

In addition, the effective area curve is sensitive to the assumed slope of the spectrum being observed. This is due primarily to the finite resolution of energy estimation: events with a particular reconstructed energy may have, in fact, deposited more (less) energy but light-pool fluctuations or core-reconstruction errors may lead to their energies being under-(over-)estimated and mis-classified. If an observed spectrum is flat[13], mis-classification from higher to lower energies would cancel similar errors in the other sense. However, for a steep spectrum a given reconstructed energy bin may include a significant fraction of lower-energy events which have been mis-classified. It will contain far fewer events with under-estimated energies simply because there are far fewer high energy events to be misclassified. The effective area function accounts for this contamination by decreasing where the assumed

[12] For example, the wobble mode used to facilitate the reflected-region background model introduces a systematic offset of the target.

[13] Having equal flux at energies just above and just below a given point.

spectrum is steeply falling: the actual number of showers at a given energy is smaller than that observed due to the excess from lower energies

Again, as with energy estimation itself and the assignment of gamma/hadron separation parameters the complex behaviour of this multi-parameter function is handled *via* lookup tables. Simulations based on a range of the observational parameters are processed identically to observational data and the ratios between the simulated flux (which is a function of true energy, ε_{true}) and the number of reconstructed events (ordered into bins of reconstructed energy, ε_{rec}) are tabulated according to the assumed parameters. Thus we define :

$$A_{\mathrm{eff}} = \frac{\mathrm{d}n \,/\, \mathrm{d}\varepsilon_{\mathrm{rec}}}{t \cdot F(\epsilon_{\mathrm{true}})} \tag{4.22}$$

where we let $\varepsilon_{\mathrm{rec}} = \epsilon_{\mathrm{true}}$, within the resolution of the energy bins. Different spectral indices can be reproduced by weighting the contribution of an individual event according to its simulated energy.

With the effective area function computed, the final piece of the analysis puzzle is in place. It is possible to trace the pulses recorded in FADC channels back to an individual air shower and so to estimates of the intrinsic properties of its primary: arrival direction, identity and energy. By restricting analysis to a limited region of the sky and selecting events that are more likely due to gamma rays, it is possible to discern a count rate of astrophysical gamma rays against the ubiquitous but homogeneous background of cosmic rays. The effective area now allows any measured count rate, in excess of the estimated background, to be converted into a measurement of energy flux from a putative gamma ray source. I shall now use this probe of very energetic radiation to determine what possible flux of VHE gamma rays can be emitted from a globular cluster and thereby confront models of such emission with observations.

Part III

Results & Discussions

Chapter 5

Analysis Results

In light of the arguments for VHE gamma-ray emission from globulars (see §1.2.4) made by Bednarek & Sitareck [36] and Venter & de Jaeger [202], and, in particular, the predictions laid out in B&S07 (see §2.3), observations of M13 were made with VERITAS. Here I present the results of analysis of the viable data collected during 2010. Of thirty-two runs taken using the full array of four telescopes, twenty-one survive (at least in part) an examination of their trigger-rate stability (as a proxy for fidelity).

This analysis followed the sequence laid out in §4 and was performed using a software suite called *Eventdisplay* [62] (see §5.2). Most of the figures presented below were produced with customised and expanded versions of macros packaged with *Eventdisplay*. I use them to demonstrate the homogeneity of the data set and thus justify a statistical comparison of ON- and OFF-regions. This comparison allows the construction of upper limits on any count rate that could be due to a possible source. These are then converted to flux upper limits with the use of the mean effective area of the detector/analysis-chain. Finally the spectral flux upper limits are used to relate these observations, and the non-detection of M13, to the emission curves modelled in B&S07.

5.1 Data Selection

Between 22 May and 7 July 2010, thirty-one observation runs of twenty-minutes duration (and one of ten-minutes) were taken on M13 in wobble mode, with an offset of 0.5°, using all four telescopes of the array. Observers

(those personnel responsible for operating the array during data-taking) are required to attach comments to a run in the event of hardware or software glitches. One run was flagged with such a comment and was considered to be of suspect quality.

Array-trigger-rate stability. From the remaining data set, runs were selected based primarily on the stability and level of the array trigger (L3) rate (see 3.2.3.1). The L3 rate is a direct measure of the data recorded by the array during observations and is dominated by the stable and largely isotropic rate of cosmic-rays. Disruption to the operation of the array, including variation in its sensitivity due to vagaries of the atmosphere, typically affects the L3 rate and this makes it a useful diagnostic of data quality.

In examining the L3 rate it is instructive to compare these values to sky temperature, as measured by a far-infrared (FIR) pyrometer: this passive device essentially measures the average temperature of water vapour in the atmosphere by the infrared radiation it emits. Such a temperature reading is a proxy for the altitude of any clouds which may be present or, if they are not, the transparency of the atmosphere. In either case, fluctuation towards higher FIR sky temperature represents a possible degradation in observing conditions and if this coincides with a depression in the L3 rate it can be taken as a signature of atmospheric interference with detector sensitivity.

The examination of such meta-data is facilitated by `loggen` : a World-Wide-Web interface to the database tables detailing many of the facets of VERITAS's operation.[1] This portal has been maintained and expanded by the author between 2007 and the present. The `loggen` interface includes the ability to plot the trends of L3 and FIR readings together and this was used here in an initial visual inspection of data-taking quality, looking for coincident variations in the two properties. Five runs were flagged as being of suspect quality on this basis, see Figure 5.1 for an example.

A more systematic examination uses a statistical measure of L3 fluctuations within a run. Each measurement of the L3 rate consists a certain number of events over a given time period. Therefore, each measurement has

[1] Its name derives from its original function as a run list generator for use as a tool in the book-keeping associated with nightly data-taking. Its functionality has since expanded to the ability to recall most of the operating conditions of the array contemporaneous with any given data run and provide basic display of some engineering data, such as bias curves (recall Figure 3.13). It can also list runs according to a desired individual (or range of) source, date, elevation, duration, *etc.*

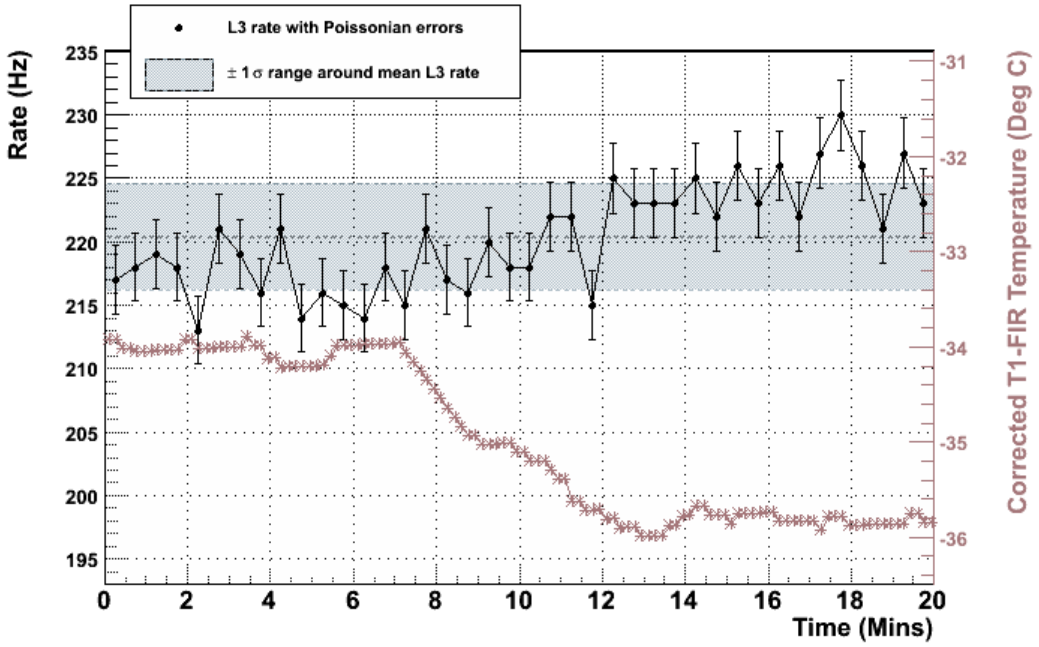

Figure 5.1: L3 rate (upper points) and sky temperature from an FIR pyrometer (lower points) versus time for a single data run (#51588). The non-statistical fluctuation of the rate is correlated with changes in the transparency of the atmosphere. Image credit — plotted by `loggen` (see main text for a description).

an intrinsic Poissonian error, ς, and these stochastic counting errors should, ideally, be the only source of variation of the rate measurements. Thus, the actual stability of the L3 rate can be estimated by comparing the standard deviation, σ, of measurements of the rate to the mean Poissonian error, $\bar{\varsigma}$, of the ensemble of measurements. The L3-rate stability may be defined as :

$$s = \frac{\sigma - \bar{\varsigma}}{\bar{\varsigma}} \tag{5.1}$$

where s has a distribution well-approximated as a Gaussian (see Figure 5.2) with mean $\mu_s = -0.02$ and standard deviation $\sigma_s = 0.11$ which have negligible dependence upon rate. This measure of the stability may be taken as an estimate of the probability that variations in the array event rate during a run are not only stochastic and therefore that the run may have not experienced stable conditions.

Runs demonstrating rate variation in excess of that expected for stochastic variation, i.e. $s > \mu_s + 2\sigma_s$, were considered to be of suspect quality. This threshold, of $+2\sigma$, rejects 2.5% of those runs whose rates are affected by only stochastic variation which allows us to expect that no more than one good run would be excluded by mistake in a data set of this size. A typical run which passed this test is shown in Figure 5.3. In all, four runs were identified as being of suspect quality on the basis of this statistic.

Finally, the mean L3 rates of runs at similar elevations were compared. If the rate for a given run seemed depressed relative to that of others by more than 5% it was rejected. Four runs (including the single 10-min run) failed this quality criterion.

Remedial action. Within runs of suspect quality, the variation of the L3 rate with time was examined closely, in combination with comments from observers. If there were periods where the rate had obviously departed from an otherwise stable mean, the stable portion of the run was recovered by placing a time cut around the period of aberrant rate, which effectively masks that period in the final analysis (see §5.2.3). This allowed 58 minutes to be recovered from three 20-minute runs. In all, the data after quality selection constitute 7 hours of observing time.

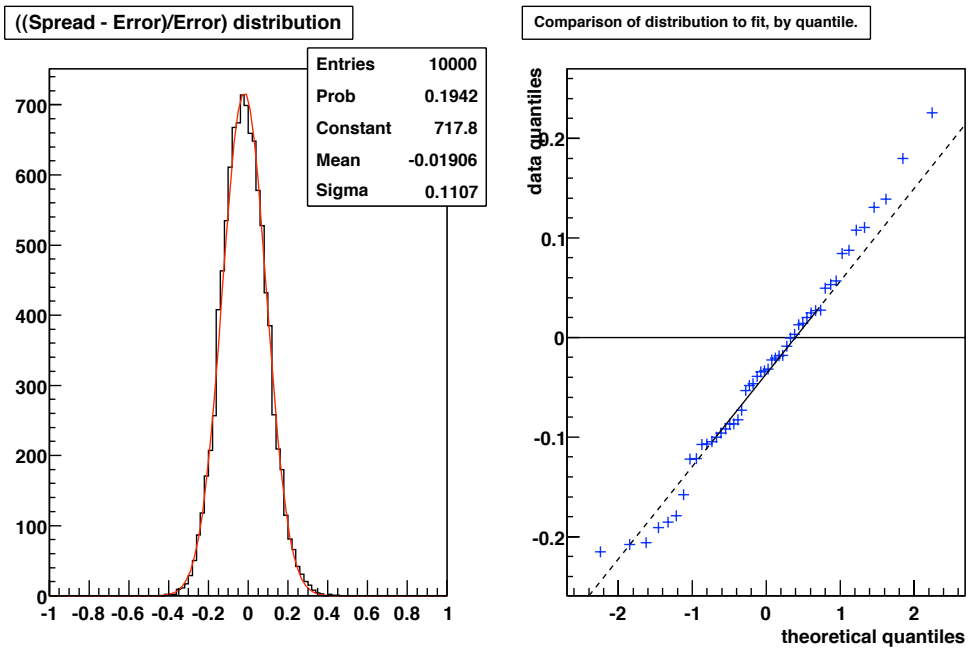

Figure 5.2: In the presence of only stochastic fluctuations the standard deviation, σ, of a set of measurements of the same quantity is similar to the mean Poissonian error of those measurements, $\bar{\varsigma}$. Here is shown the distribution of the statistic $s = \frac{\sigma - \bar{\varsigma}}{\bar{\varsigma}}$ from ten thousand Monte-Carlo trials of forty measurements of a Poisson event rate with a mean of six thousand. A typical 20-minute-long observing run has a mean rate of $\sim 200\,\mathrm{Hz}$ and the L3 rate is averaged over 30 seconds for clarity when plotting. The statistic is seen to be distributed about zero, as expected, and is well-approximated by a Gaussian fit function whose parameters are indicated in the box (left-hand-side plot). The quantile-versus-quantile plot (right-hand-side) shows that out to 2σ ('theoretical quartiles') the distribution of s ('data quartiles') is approximated by a Gaussian to around 10%; an exact Gaussian distribution would lay quantile-quantile points along the dashed diagonal line.

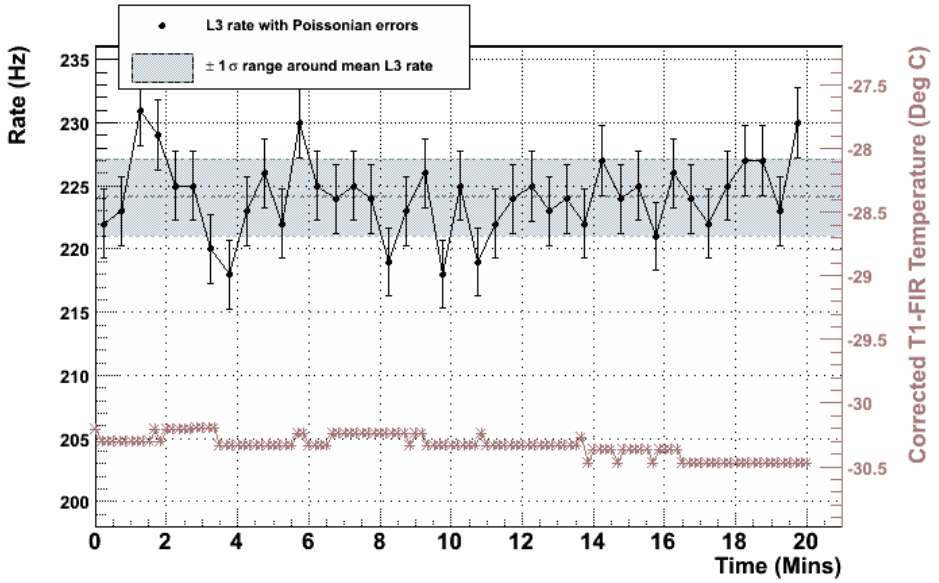

Figure 5.3: L3 rate (upper points) and sky temperature from an FIR pyrometer (lower points) versus time for a single data run (#51535). The fluctuations of the rate are not stochastic at the level of only 1.1σ and are therefore consistent with stability. Image credit — plotted by `loggen` (see main text for a description).

5.2 Analysis Software

The VERITAS collaboration supports several independent analysis packages. This work presents results produced using the package called *Eventdisplay*[2] [136, 62] which was initially developed at the University of Leeds, U.K., by Jamie Holder and Gernot Maier.[3] It comprises three main programs, detailed below. Together these programs constitute an analysis chain which follows the procedures described in §4 and the division of these tasks is as follows:

`eventdisplay` reads raw data files, performs data reduction by pulse summation and image parametrisation; reconstructs air-shower arrival direction and impact parameter.

[2] Version 3.46.

[3] Now based, respectively, at the Bartol Research Institute, University of Delaware, USA, and DESY, Germany, they continue to supervise its development.

`mscw_energy` estimates the gamma/hadron separation parameters and energy for each event using lookup tables.

`anasum` applies cuts; builds histograms for sky maps and energy spectra.

A given observing run is processed in sequence by each of the first two programs. Output from those two programs, for many individual runs, are collated by the third.

5.2.1 `eventdisplay`

Before analysis of a particular observing run can begin, a certain amount of groundwork is necessary in accumulating appropriate calibration information, see §3.2.4.1. A calibration run from the same night as the observing run is used to establish the response and timing of individual channels. This is performed using `eventdisplay`, as it ensures that the methods used for isolating and integrating calibration light pulses are identical to those used for Cherenkov light pulses.

With calibration information in hand, an observing run may enter the analysis chain. Raw data from observing runs are processed with `eventdisplay` which gathers pedestal information from the observing run itself and combines it with the calibration information to clean, construct and parametrise EAS images, as described in §4.1. Here image quality cuts are applied to help ensure that the parametrisation will be reliable. The geometrical event parameters (arrival direction and core location), derived using images that pass quality cuts, are stored in an output file, to be passed on to the next stage in the analysis chain. In fact, parameters are calculated using a range of standard image-quality-cut sets and stored as a vector. This is because the dominant factor in the computational speed of `eventdisplay` is the time to load data from the compressed raw data files. Thus it is expedient to calculate different versions of the parametrisation while the raw information is readily available in computing memory. The specific cuts used in this analysis are indicated in Table 5.1.

These early steps of the analysis, as outlined above, are well-defined and require little user input so, to reduce replicated effort, an archive of `eventdisplay` output files is maintained, created from the processing of observing runs with reliable calibration runs. The archive is generated by the University of Delaware group and accommodated by the University of California, Los Angeles, group, which provides data storage infrastructure for

the collaboration as a whole. This work used the data products from that archive.

5.2.2 `mscw_energy`

As noted in §4.1.3 and §4.2.2, lookup tables are required to allow the estimation of both the primary energy and identity for individual showers. The events that fill a given lookup table have been selected using one of the standard image-quality-cut sets, thus a specific lookup table must be chosen by a user depending upon the desired set of image-quality cuts.[4]

For improved precision at this stage of the analysis, `mscw_energy` performs interpolation between the lookup table bins nearest to each observed event's image parameters and the observing conditions in effect at that moment. The estimated shower energy, which is based upon the expected brightness of showers (*i.e.* image sizes), is the mean of the interpolated values of energy for each image in an event. The gamma/hadron separation variables (see §4.2.2), which are based upon the expected extent, p, of the images (*i.e.* width, $p = w$, and length, $p = l$), are calculated using interpolated median p and spread σ_p for each image These values are stored in an extended version of the input file, along with the parameters determined previously by `eventdisplay`. Once this is complete, it is possible to apply cuts to reject hadrons and accumulate counts collected during the run for the determination of source statistics.

5.2.3 `anasum`

Here gamma-ray-like events are selected (§4.2.2) and collated into directional (§4.2.1) and energy bins for the calculation of signal and background rates (see §4.2.3) and statistics pertaining to the significance of any excess (see §4.2.4).

As implied in §4.1, an accurately determined impact parameter for the shower is required for the effective use of lookup tables to estimate energy and the gamma/hadron separation parameters. To ensure that only those events are retained for which these values have been reliably estimated, a reconstruction-quality cut on the mean distance from the telescope to the core location is applied. As noted in §4.2.2, gamma/hadron selection is performed

[4] As lookup tables are by their nature very large, it is preferable that only those pertaining to a particular, utilised set of image-quality cuts need be handled by a user.

on the basis of the MSCP values (for both P = W and P = L) of each event. The specific cuts used in this analysis are indicated in Table 5.1.

To ensure that direction reconstruction was sufficiently reliable for a given event, at least three images (after image-quality cuts) are required to have been present. Then, remaining uncertainty in the reconstruction (*i.e.* the gamma-ray PSF) is accounted for by accepting only events falling within an angle θ of the suspected source direction.[5] This defines the ON-region used for determing source statistics and events collected here (and in equivalent OFF-regions) are sub-divided into bins of reconstructed energy for later spectral analysis.

At this point, time cuts may also be applied. This facility was implemented in `anasum` by the author. It operates as a mask which is defined for every second of the run. A user may define any number of seconds at any point in the run over which the mask is closed, `anasum` then verifies that the mask is open for the time during the run at which a given event arrived before filling any of the appropriate histograms. The exposure of the array during a run is calculated as the open portion of the mask.

During the selection of events, `anasum` also constructs an effective area curve to record the sensitivity of the array (see §4.3). For each selected event the effective area function is generated from a lookup table by interpolation between the bins nearest to the observational parameters (zenith angle and image pedestal variance) appropriate to that event. Fixed values of the wobble offset of the run, being the angular offset between the pointing direction and the source, and a user-selected, assumed spectral power-law index are also used for referencing the lookup table. The effective area functions are averaged across all of the selected events and this yields a mean effective area for a run.

The `anasum` output file contains the complete directional and spectral histograms of the data set and the mean effective area for the observations. Macros may then be used to manipulate these products for the purposes of visual presentation and detailed flux calculations.

[5] This is equivalent to assuming that the primary's true arrival direction is within an angle θ of the reconstructed direction.

Cut Type		Parameter	Condition
Quality	Image	N_{pix}	≥ 4
		ς	≥ 500
		Λ	< 0.20
	Reconstruction	N_{img}	≥ 3
		$\bar{d}$	< 250
Analysis		θ^2	< 0.010
		MSCP	> -1.2
			< 0.5

Table 5.1: Cuts used in this analysis. Image-quality cuts are based upon the number of pixels in an image, N_{pix}, image size, ς in digital counts, and loss Λ. Reconstruction-quality cuts are based upon the number of useful images in an event, N_{img}, and the mean distance from the array to the shower core, $\bar{d}$ in metres. Analysis cuts (for background reduction) are based upon the arrival direction offset, θ^2 in square-degrees, and the gamma/hadron separation parameters, MSCP for both P = W and P = L. The cut condition indicates the allowed range: if an observed parameter satisfies this condition it passes the cut.

5.3 Results for M13

There are many ways to present the data set. Probably the most general overview is provided by the sky maps of excess and significance indicating the likelihood of gamma-ray emission from a large set of directions near the target. As indicated in §4.2.4, the distribution of values in a sky map can be used to test the uniformity of the data set and ensure that no particular direction is subject to gross aberrations.

Ultimately only a single direction in the sky map corresponds to the target. I will compare the distributions of events associated with this direction to the distributions collated from otherwise equivalent background-estimation regions. Again, this is to be certain that results from the source direction are not aberrant.

With the assurance that any excess of events, or lack thereof, from the source direction is reliably measured I may calculate, with reference to the effective area (as defined in §4.3), a flux or flux upper limit.

5.3.1 Excess, Significance and Quality

The number of events within 0.1° of a candidate direction is compared to the number of background events in up to ten reflected regions, as detailed in §4.2.3. Many such candidate directions are examined within a 1 -degree radius of the target on a grid of spacing 0.05°. The excess from each candidate direction over the estimated background rate is determined: the grid of these values is shown in Figure 5.4. Note that, because the grid spacing is smaller than the radius over which events are counted for a given direction, there is some correlation between neighbouring bins as any given event is counted separately in many of them[6]. As a consequence the map has a certain smoothness, without large fluctuations between neighbouring bins, and exhibits 'islands' of large or small excess.

A significance is assigned to each candidate direction according to the prescription of Li & Ma (Eq. 17 in [141]) and this corresponds to a sky map of the likelihood of VHE gamma-ray emission. The sky map within 1° of M13 is shown in Figure 5.5. Furthermore, as noted in §4.2.4, measurements of the statistical significance (as defined by Li & Ma) should follow a standard normal distribution. The distribution of significances for all bins within a 1 -degree radius of the centre of the sky map is shown in Figure 5.6. A Gaussian function with mean and RMS fixed to 0 and 1 respectively but with free normalisation fits this distribution reasonably well (reduced-χ^2 of 1.2) indicating that the data set is uniform, having a distribution of significances within the field of view consistent with only statistical fluctuations.

The central pixel in the sky map corresponds to the direction of M13. The ON-region used in calculations of excess and significance (and ultimately of upper limits) is centred here and the OFF-regions were determined for each run individually, according to the wobble direction. Any VHE gamma rays emitted by M13 and subsequently detected by VERITAS and successfully reconstructed in this analysis would appear in the ON-region. VHE emission from M13, following the model I wish to test, should be predominantly from the core of the globular cluster. The angular radius of the core of M13 is 0.010° , an order of magnitude smaller than the ON-region radius. Also, the entire region considered in B&S07 for modelling emission from this globular is contained within 0.081° : any emission from M13 would be well contained. Were it a source, it would not be resolved and could be treated as a point

[6] A single event contributes to up to twelve bins for this combination of bin width and integration radius (θ^2 cut).

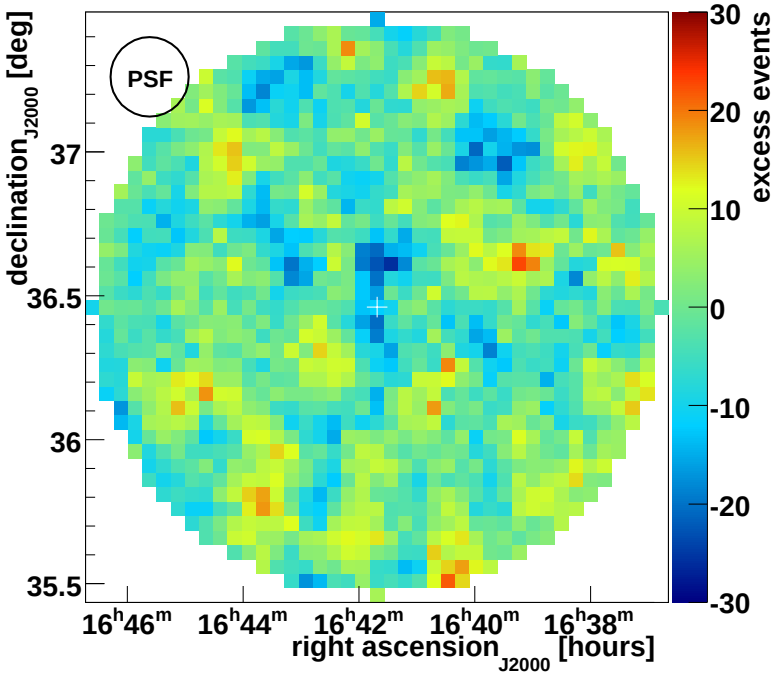

Figure 5.4: Excess events for a grid of directions within a 1° radius of the target. The grid spacing is 0.05°. Each bin in this sky map indicates the excess events which have passed the θ^2 cut with respect to the center of that bin and that have also passed the MSCW and MSCL cuts.

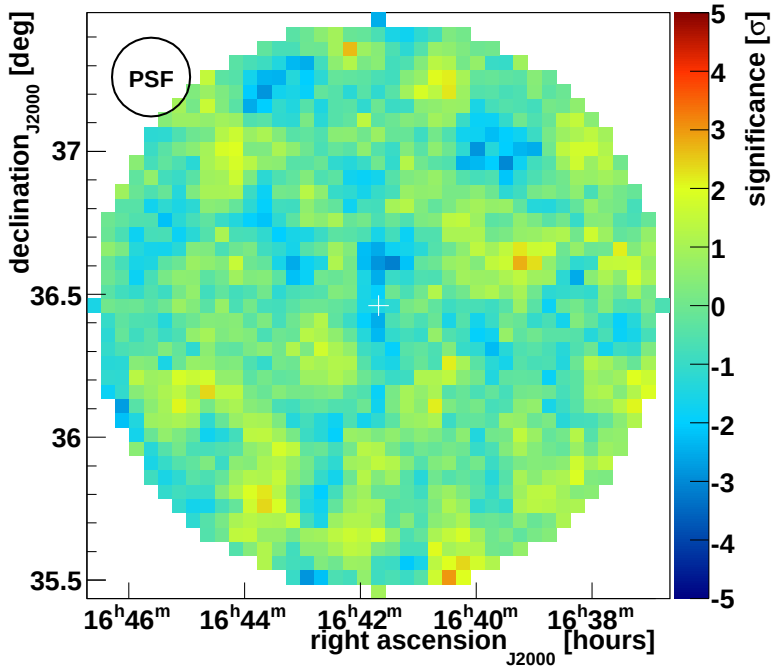

Figure 5.5: The statistical significance of the excess for a grid of directions within a 1° radius of the target. The grid spacing is 0.05°.

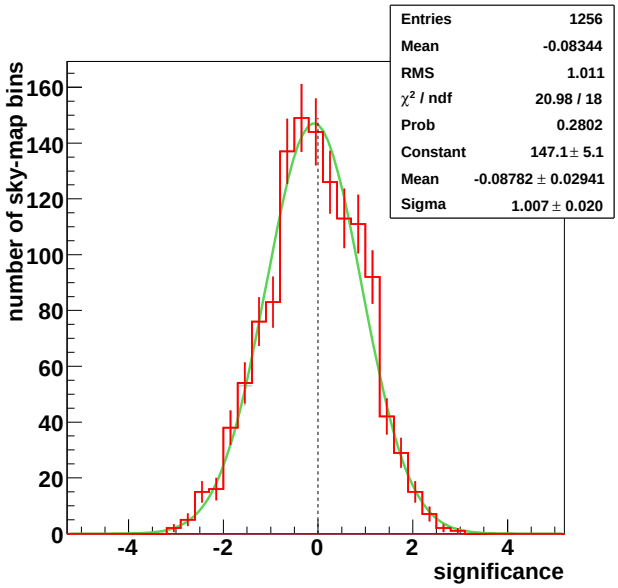

(a) Significance distribution.

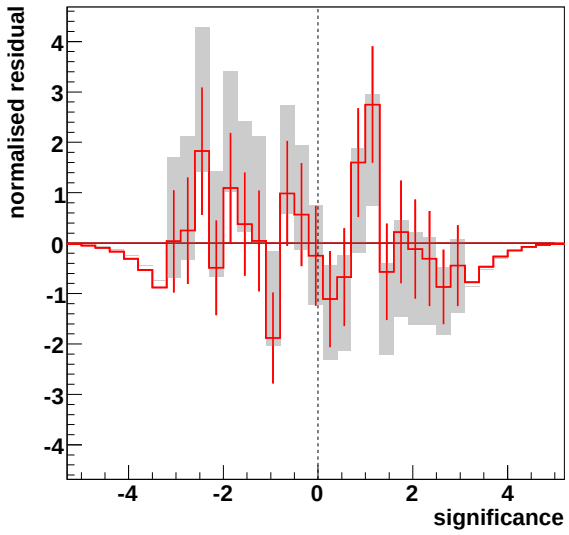

(b) Normalised residuals.

Figure 5.6: Distribution of sky-map significances within one degree of the target, 5.6a, and the normalised residuals of that distribution. Significance estimates calculated using Eq. 17 in [141] (Li & Ma) should obey a standard normal distribution. A standard normal Gaussian function (mean=0, RMS=1) fits the distribution with probability 7% (χ^2/d.o.f = 1.5). The fit function shown (green curve) is a Gaussian with floating mean and RMS; the fit parameters (shown in the box) are each within $3\,\sigma$ of a standard normal. The normalised residuals of the distribution with respect to both the standard normal (grey boxes) and the fit function (red histogram) are shown.

source as is done in this analysis. The excess from the direction of M13 is -12.0 and the significance -1.4σ. There is no evidence for VHE emission from this object.

The angular distributions of events around the centres of ON- and OFF-regions are shown in Figure 5.7. Events falling to the left of the vertical red line pass the θ^2 cut. For events passing the θ^2 cut, the distributions of the gamma/hadron separation parameters are shown in Figure 5.8. There appears to be acceptable agreement between the distributions of events in the ON- and OFF-regions. To verify this, the ON- and OFF-region distributions were compared in a fiducial zone separated from the portion passing cuts, *i.e.* $\theta^2 > 0.03$ and MSCP > 1.2. All distributions are found to be mutually consistent between the ON- and OFF-regions, with a probability of at least 20%, according to χ^2-test comparisons [81]. The χ^2 test determines if differences between corresponding bins of two histograms are consistent with statistical fluctuations between two measurements of the same rate. As it is an analysis of bin-by-bin fluctuations it is somewhat insensitive to the scale of the histograms compared, so the integrals of the distributions were also compared. The total contents in these fiducial zones were treated as measurements of the same background rate and found to be different with a significance within $-2.64\,\sigma$ (as calculated with Eq. 17 of [141]) and, therefore, the scales of the ON- and OFF-region distributions are consistent within symmetrical 99.2% confidence limits.

The set of all events passing cuts is summarised in Table 5.2. The distribution in energy of these events is shown in Figure 5.9: with increasing energy, it rises steeply to a peak and then settles into a power-law-like decline. It takes this form because it is the product of the mean effective area for this data set (shown in Figure 5.10) with the steeply-falling spectrum of gamma-like events provided by the cosmic-ray background. Below the

Region	Norm.	Counts	Energy [TeV]			Mean
			Min.	Peak	Max.	$[\log_{10}(\epsilon/\mathrm{TeV})]$
ON	1	55	0.105	0.200	1.32	-0.594 ± 0.029
OFF	0.1	670	0.085	0.204	5.22	-0.574 ± 0.009

Table 5.2: Characteristics of the sets of events passing cuts in the ON- and OFF-regions. The energy of the peak is estimated by the weighted mean of the centres of the three most populated bins (see Figure 5.9).

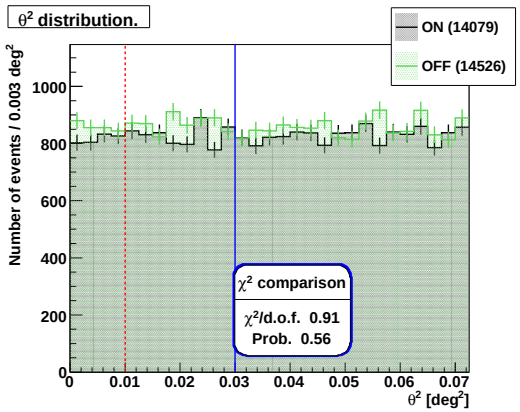

(a) Distribution in θ^2.

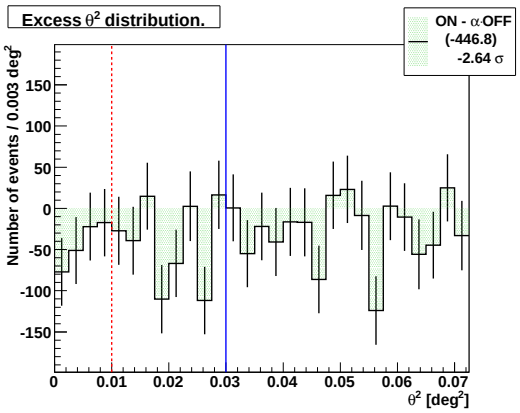

(b) Excess.

Figure 5.7: Distribution of event arrival directions relative to the centre of the target ON-region (black line) and a representative OFF-region (pale-green line), 5.7a. For the OFF histogram, the angular separation from a randomly chosen reflected region is determined for each event. The distribution of excess events ($n_{\mathrm{ON}} - n_{\mathrm{OFF}}$) in θ^2 is also shown, 5.7b. The vertical dashed, red line is the θ^2 cut: events to the left pass the cut. The vertical solid, blue line is the limit of the fiducial region: bins to the right are used in the comparison of ON- and OFF-regions, see text. The total contents shown in parentheses are for bins used in the comparison.

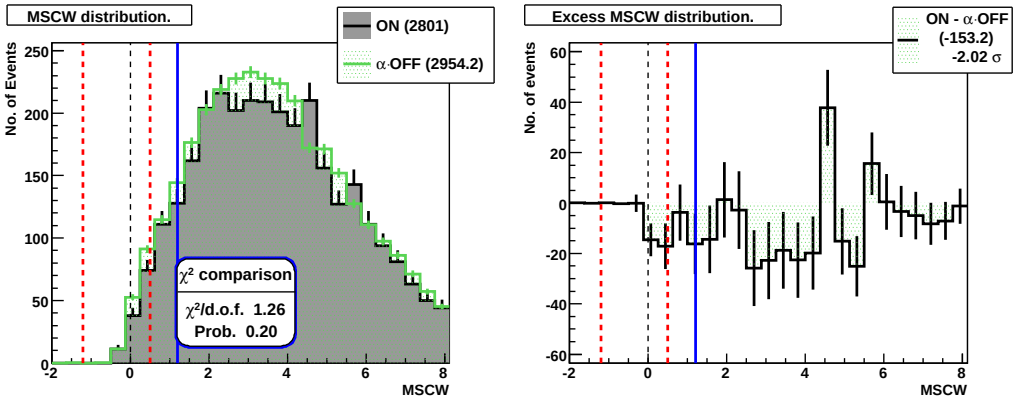

(a) Distribution in MSCW.

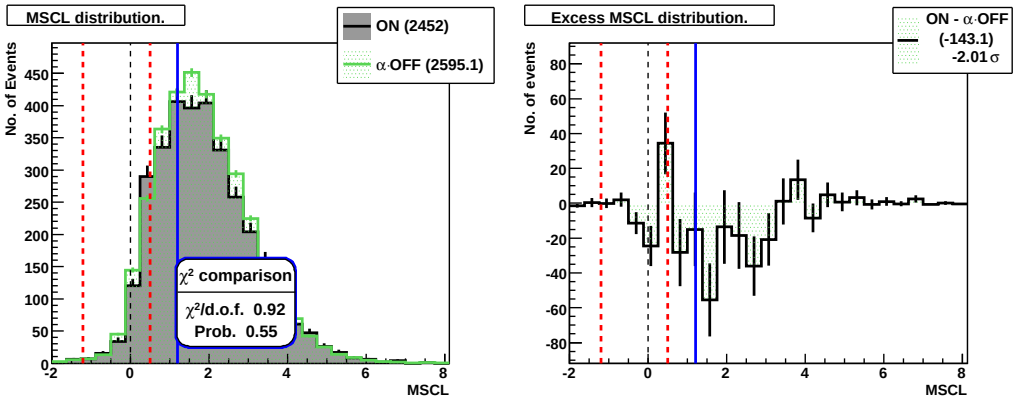

(b) Distribution in MSCL.

Figure 5.8: Distribution of events in the gamma/hadron separation parameters: MSCW (5.8a) and MSCL (5.8b), see §4.2.2 for details. In each case, the distribution of events in the target ON-region (black line) and the average distribution of events in all OFF-regions (green line) are shown on the left. The distributions of excess events ($n_{\mathrm{ON}} - \alpha \cdot n_{\mathrm{OFF}}$) are on the right. Events between the vertical dashed, red lines pass the gamma/hadron separation cut. Bins to the right of the solid, blue lines are used in the comparison of ON- and OFF-regions, see text. The total contents shown in parentheses are for bins used in the comparison.

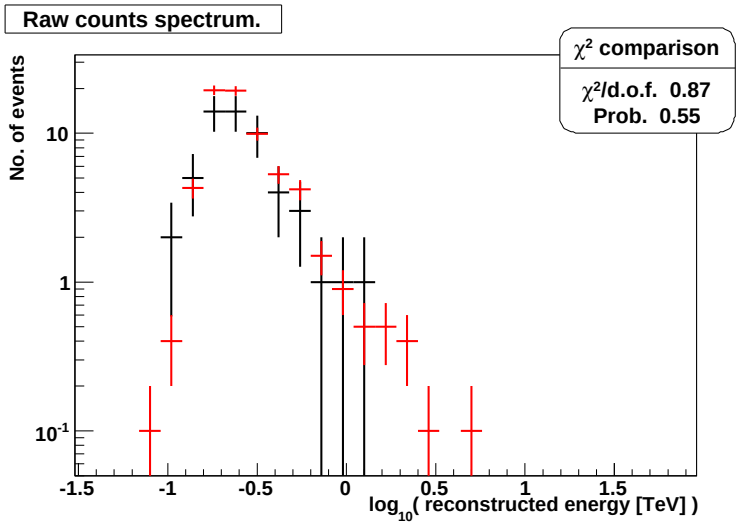

Figure 5.9: Energy distribution of events passing cuts from the direction of M13 shown with the normalised background counts. Black are ON; red are OFF, scaled by the normalisation factor $\alpha = 0.1$.

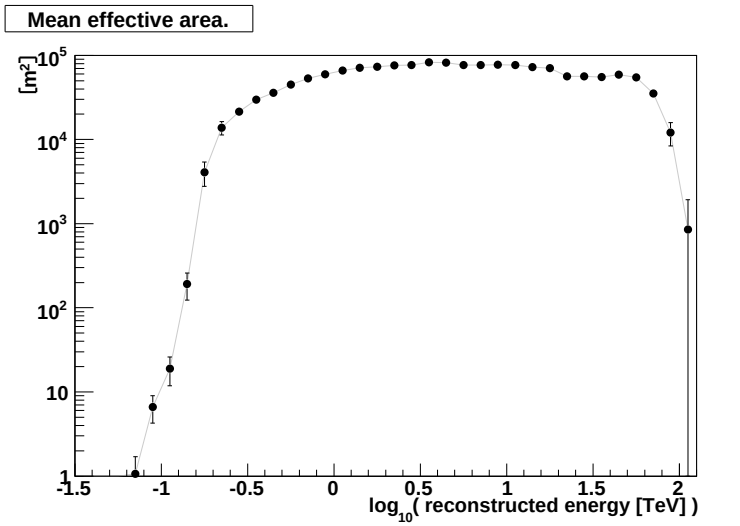

Figure 5.10: The mean effective area shown is the average of the run-wise effective area curves generated by `anasum`, weighted by the number of events over which each was computed. The errors indicate the range of variation of the effective area between runs: $\sim 30\%$ below the spectral peak and much smaller above it.

peak energy the spectral shape is dominated by the instrument, due to the rapidly rising effective area; above the peak energy, where the effective area varies less rapidly, it is dominated by the spectrum of detected events. The means of the ON- and OFF-region energy distributions are consistent and their peaks are very similar. The spectrum of counts accumulated in the OFF-regions covers a larger range of energies, as may be expected given the greater exposure (by a factor of ten).

We may conclude that, overall, the data set is homogeneous and the target direction is largely consistent with others. In particular, events collected near the source (close enough to the target so as to be indistinguishable from it) are distributed across various key parameters in a manner that conforms with the corresponding distributions of events collated from background-estimation regions: the background has been reasonably well-estimated and further statistical inference may be considered trustworthy.

5.3.2 Flux Upper Limits

In this data set no source has been detected at the location of M13. We may, however, derive the range of possible fluxes which could be due to a source sufficiently weak that it remains compatible with the non-detection of any excess in this analysis. Such a range of fluxes may be characterised by a single value having a large probability of being greater than any real flux: this value is a **flux upper limit**.

A given flux corresponds to a certain rate of detected events and *vice versa*, according to the sensitivity of the detector. By determining an upper limit on the number of events that could, in principle, be detected from a source concealed beneath the estimated background rate, it is possible to use the known sensitivity of the detector to calculate a corresponding flux upper limit.

5.3.2.1 Upper limit derivation

The upper limit on a number of source counts in the presence of background was derived using a Bayesian formalism by Helene [99]. The basic premise is that if the probability distribution function (p.d.f.) of the intrinsic count rate that may be due to a weak source can be derived, its cumulative distribution function (c.d.f.) defines upper limit confidence levels. That is, the c.d.f. allows

the estimation with a particular confidence that the count rate must be equal to or less than a given value.

To determine the probability that the source count rate, a, is below a certain level, $A_{\max}$, we must compute the c.d.f. :

$$P(a \leq A_{\max}) = \int_0^{A_{\max}} p(a)\,\mathrm{d}a \; = l \tag{5.2}$$

where $p(a)$ is the p.d.f. for the count rate due to the source. This yields the confidence level, l, for $A_{\max}$ to be the upper limit of counts due to the observation of gamma rays from a putative source.

Now, the p.d.f. for the intrinsic count rate can be derived from the observed count rates from the background-estimation region (consisting purely of background counts, B') and from the source region (including both source and background counts, $C = A + B$). Specifically, Eqn. 5 from [99] :

$$p(a) = \tau \int_0^{\infty} e^{-(a+b)}\,\frac{(a+b)^C}{C!} \cdot f(b)\,\mathrm{d}b \tag{5.3}$$

shows the means of deriving the probability distribution function for an intrinsic source rate, a, given measured source-region counts, C, and where uncertainty in the estimate of the actual background rate, b, is accounted for by performing an integral over all of its possible values, weighted by their prior probabilities, $f(b)$: this process is called **marginalisation**.[7] Here τ is a normalisation factor such that $\int_0^{\infty} p(a)\,\mathrm{d}a \; = 1$.

The probability distribution function for the actual background rate $f(b)$ in the source region may be estimated as a Gaussian distribution on the condition that the observed number of background counts, B', is large enough ($B' \gtrsim 10$). This can be thought of as the fact that the error on an estimate of the mean of any distribution is itself distributed normally[8]. The Gaussian background rate p.d.f. has mean equal to the normalised observed background count rate $\mu = \alpha B'$ and variance $\sigma^2 = \mu$, such that the number of background counts contributing to C should be $B \simeq \alpha B'$. This corresponds to Eqn. 6 from [99] which is commonly used in this field, under the additional assumption that $C \gg 1$. However, I will not be able to make this

[7] In the case that the background rate is known to be $b = \bar{B}$ exactly (or with negligible uncertainty), its p.d.f. may be defined as a Dirac delta-function $f(b) = \delta(b - \bar{B})$ such that Eqn. 2 from [99] is recovered.

[8] This is simply the well-known **central limit theorem** (see *e.g.* [180]).

final assumption as we shall see below (specifically Table 5.3 and Figure 5.14) and Eqn. 5.3, is required.

Here it is adequate to use a Gaussian distribution for $f(b)$ because the background rate is estimated over ten times as many regions as the source-region rate. However, as an aside, I note that a complete p.d.f. for the actual background rate, regardless of the number of observed counts, may be constructed in a manner similar to the derivation of Eqn. 5.3, but related to the number of counts in the background estimation region, giving :

$$f(b) = e^{-(b')} \frac{(b')^{B'}}{B'!} = e^{-(b/\alpha)} \frac{(b/\alpha)^{B'}}{B'!} \tag{5.4}$$

where B' counts were collected in total over the background-estimation regions which had an exposure relative to the source region of $1/\alpha$ so that the actual background rates in the ON- and OFF-regions are related by $b = \alpha b'$.[9]

With the p.d.f. for the background rate defined, the p.d.f. for the source rate (Eqn. 5.3) may be evaluated and the c.d.f. (Eqn. 5.2) can be solved numerically to obtain $A_{\max}$ at a desired confidence level.[10] For the sake of comparison with the results of observations of M13 by MAGIC [24], I will use (as they did) a confidence level of 95% ($l = 0.95$ in Eqn. 5.2) such that this process yields the upper limit on the range of event rates that can account for 95% of the probable cases where the observed number of counts were detected in the presence of a background with the mean rate as that estimated. There is only a 5% probability that the actual count rate due to a source (or a flux of gamma rays that would cause it) exceeds the values quoted below.

Flux calculation. In order to compare observations to physical models of emission, we need to relate any possible count rate of successfully reconstructed events to a possible physical flux of gamma rays. As indicated in §4.3, any count rate, $\frac{\mathrm{d}n}{\mathrm{d}t}$, due to a source (be that a measured excess or

[9] This is related to the gamma distribution for x given k and θ: $p(x|k,\theta) = e^{-x/\theta} \frac{x^{k-1}}{\Gamma(k)\theta^k}$ where, in this case, $k = B' + 1$ and $\theta = 1$ for $x = b'$. Note that the gamma distribution for the actual rate, given a certain number of observed counts, is continuous, in contrast to the discrete Poisson distribution of counts, given an intrinsic rate: $p(C|\lambda) = e^{-\lambda} \frac{\lambda^C}{C!}$.

[10] Note that the integral over $p(a)$ requires an integral over $f(b)$ at every sample point and so this can be quite computationally intensive. For that reason, Eqn. 10 from [99] (which follows directly from Eq. 6 of that paper) is normally used to evaluate the confidence level directly via the error function. The numerical solution for a required confidence level is then greatly hastened.

an estimated upper limit) would be the result of a flux, $F(\epsilon) = \frac{\mathrm{d}N}{\mathrm{d}\epsilon\ \mathrm{d}A\ \mathrm{d}t}$, of gamma-rays from the source impinging upon the effective area of the detector, A_{eff}. Thus we may state :

$$n = \int F(\epsilon) A_{\mathrm{eff}}(\epsilon)\,\mathrm{d}\epsilon \cdot t \tag{5.5}$$

or, equally :

$$\frac{\mathrm{d}n}{\mathrm{d}\epsilon} = F(\epsilon) t A_{\mathrm{eff}}(\epsilon) \tag{5.6}$$

Eqn. 5.5 defines an integral relation for the flux, accounting for observed events over a broad range of energies and Eqn. 5.6 defines a differential one, examining the event rate near a particular energy only.

A complete definition of the integral flux requires an assumption about the shape of the spectrum. It is common to assume a power-law spectrum, $F(\epsilon) = F_0(\epsilon/\epsilon_0)^{-\delta}$, as this is the simplest form valid in this energy domain. With this, the integral flux from a source, being the number of gamma rays arriving at the detector within its sensitive range, may be defined as :

$$\begin{aligned} I(\epsilon > \epsilon_{\mathrm{thresh}}) &= \frac{\int \mathrm{d}N(\epsilon > \epsilon_{\mathrm{thresh}})}{tA} && (5.7)\\ &= \int_{\epsilon_{\mathrm{thresh}}}^{\infty} F(\epsilon)\,\mathrm{d}\epsilon && (5.8)\\ &= F_0 \int_{\epsilon_{\mathrm{thresh}}}^{\infty} \left(\frac{\epsilon}{\epsilon_0}\right)^{-\delta} \mathrm{d}\epsilon && (5.9) \end{aligned}$$

where the last integral over epsilon is a well-defined numerical factor depending upon the spectral index δ, the normalisation energy ϵ_0 and the chosen energy threshold $\epsilon_{\mathrm{thresh}}$. The **flux normalisation** is the power-law spectrum evaluated at the normalisation energy: $F_0 = F(\epsilon = \epsilon_0)$.

However, we must work with the number of *observed events* :

$$\begin{aligned} \frac{\int \mathrm{d}n(\epsilon > \epsilon_{\mathrm{thresh}})}{t} &= \int_{\epsilon_{\mathrm{thresh}}}^{\infty} F(\epsilon) \cdot A_{\mathrm{eff}}(\epsilon)\,\mathrm{d}\epsilon && (5.10)\\ &= F_0 \int_{\epsilon_{\mathrm{thresh}}}^{\infty} A_{\mathrm{eff},\delta}(\epsilon) \cdot \left(\frac{\epsilon}{\epsilon_0}\right)^{-\delta} \mathrm{d}\epsilon && (5.11)\\ &= F_0 \hat{A}_{\mathrm{eff},\delta} && (5.12) \end{aligned}$$

where $\hat{A}_{\mathrm{eff},\delta}$ is the spectrally weighted effective area[11] and the original effective area has been chosen to match the assumed spectral index. Thus :

$$F_0 = \frac{n(\epsilon > \epsilon_{\mathrm{thresh}})}{t \cdot \hat{A}_{\mathrm{eff},\delta}} \tag{5.13}$$

defines the scale of the spectrum with an assumed power-law shape and allows us to evaluate the integral flux, $I(\epsilon > \epsilon_{\mathrm{thresh}})$. The integral flux calculation itself is relatively free of systematic error, making few demands on accurate energy resolution and allowing the choice of an appropriate effective area, but it does require an assumption concerning the spectral index. We will see below that the effect of this assumption may be minimised by a judicious choice of $\epsilon_{\mathrm{thresh}}$.

Meanwhile, the differential flux is derived rather more directly from Eqn. 5.6 :

$$F(\epsilon) = \frac{\mathrm{d}n \,/\, \mathrm{d}\epsilon}{tA_{\mathrm{eff}}(\epsilon)} \tag{5.14}$$

However, when collating events, we must work with finite bin widths such that, for a bin i with lower edge ϵ_i :

$$n_i = \int_{\epsilon_i}^{\epsilon_{i+1}} \frac{\mathrm{d}n}{\mathrm{d}\epsilon}\,\mathrm{d}\epsilon \tag{5.15}$$

$$= \int_{\epsilon_i}^{\epsilon_{i+1}} F(\epsilon)A_{\mathrm{eff}}(\epsilon)\,\mathrm{d}\epsilon \cdot t \tag{5.16}$$

$$\frac{n_i}{\epsilon_{i+1} - \epsilon_i} = \bar{F}_i t \bar{A}_{\mathrm{eff},i} \tag{5.17}$$

$$\bar{F}_i = \frac{n_i/\Delta\epsilon_i}{t\bar{A}_{\mathrm{eff},i}} \tag{5.18}$$

where $\Delta\epsilon_i$ is the width of the energy bin, n_i is the number of source counts estimated for the bin, $\bar{A}_{\mathrm{eff},i}$ and $\bar{F}_i$ are, respectively, the mean effective area and flux over the width of the energy bin.

In principle this derivation makes no assumption about the shape of the source flux, nevertheless the effective area at a given energy does depend

[11] In practice the integral is not up to infinity but rather a maximum energy where event reconstruction becomes unreliable but, because of the power-law decline in the spectral weight, this upper bound introduces an error of only $\sim$1%.

somewhat upon the slope of the spectrum and so there is a systematic error in this calculation due to the necessity of choosing an effective area function.

Both of these approaches to flux calculation have their strengths and will be used below to derive flux upper limits from counts upper limits. The integral upper limit is the more transferable, in that it is based upon clear assumptions, and is the more sensitive, taking into account all of the data simultaneously. The differential upper limit has the advantage that it is not tied to simple assumptions concerning the source flux which are not, in fact, realised by the physical models under examination.

5.3.2.2 Integral Flux Upper Limits and Decorrelation

The integral flux upper limit seeks to answer the question—what credible level of source flux can exist within the entire sensitive range of the detector? It is derived from Eqn. 5.9 and Eqn. 5.13 setting $n(\epsilon > \epsilon_{\mathrm{thresh}})$ to be the upper limit on counts above the threshold energy. The latter is derived from Eqn. 5.2 with Eqn. 5.3 where the source-region counts are taken to be all ON-counts above the energy threshold ($C = n_{\mathrm{ON}}(\epsilon > \epsilon_{\mathrm{thresh}})$); the background is estimated through Eqn. 5.4 using all OFF-counts above the energy threshold ($B' = n_{\mathrm{OFF}}(\epsilon > \epsilon_{\mathrm{thresh}})$). The valid range of the effective area function is limited, by the statistical accuracy of simulations used to generate it, to energies below 30 TeV : the range of the power-law (in Eqn. 5.9) and the summation of counts (for C and B) is correspondingly limited.

Recall that this process uses an assumed spectral index and evidently a sensible threshold energy must also be chosen. We could in principle choose any threshold within the observed domain of counts. However, it so happens that a judicious choice of the energy threshold can render the integral upper limit relatively insensitive to the value of the spectral index. This is worth exploiting because it is preferable for a derived limit to be stable with respect to assumptions about the properties of any presumed source, including its spectrum.

We may investigate the stability of derived upper limits against uncertainty in the spectral index for many thresholds and adopt that threshold which provides the most general result. This is achieved by calculating the integral flux upper limit, above a particular threshold, over a uniformly sampled range of spectral indices. The range of spectral indices encapsulates that known for VHE PWNe ($\sim$2.0 to $\sim$2.7) and is centred on 2.6 as this is the index used in [24], to which I would like to directly compare the integral

flux upper limit calculated below.

As I am interested in the variation across spectral index, rather than that across threshold energy, I standardise each set of integral flux upper limits determined using a particular threshold by dividing them by the mean value obtained with that threshold. The resulting surface is shown in Figure 5.11: the trend at any given threshold energy may be understood as the evolution of the spectrally weighted effective area (see Eqn. 5.12) with the spectral slope.[12] It may be seen that for a threshold energy near 0.8 TeV the derived upper limit does not deviate far from the mean, regardless of the value of the assumed spectral index (within the range shown). A threshold energy chosen in this way may be termed the **decorrelation threshold energy** because the flux upper limit becomes largely independent of index, when this threshold is chosen.

To be more quantitative we may compute the RMS, s, and the mean, μ, of the set of integral flux upper limit values determined for each particular threshold. Then the ratio s/μ will be a measure of how close the values stay to the mean on average: *i.e.* the stability of the integral flux upper limit above this threshold energy when subject to an arbitrary assumption about the spectral index. It may be seen in Figure 5.12 that this ratio is indeed least for a threshold energy of 0.8 TeV . However, it is also clear that a threshold energy of 0.9 TeV may also be consistent with the same level of stability within the range of spectral indices examined. I have successfully reduced to a minimum ($\sim$0.3%) the systematic error on the integral flux upper limit due to uncertainty in the assumed spectral index but I am left with $\sim$10% systematic error from uncertainty in the choice of the best threshold energy.

With this caveat, I estimate the integral flux upper limit, above the decorrelation energy threshold of 0.8 TeV , at a confidence level of 95% to be $0.306 \times 10^{-12}\,\mathrm{cm}^{-2}\,\mathrm{s}^{-1}$ (see Table 5.3 for details). This upper limit is shown in Figure 5.15 with a spectral index of 2.6 for direct comparison with the integral upper limit (95% C.L.) obtained by MAGIC through their own observations of M13 [24]. Also shown in Figure 5.15 are the same integral upper limit for the extreme spectral indices considered above: namely 2.0 (shallow dotted line) and 3.2 (steep dotted line).

This upper limit is the most stable in terms of future comparison, in that

[12] This evolution involves both the change in spectral slope and the subtle variation in the scale and form of the effective area curve which itself is sensitive to the assumed spectral slope (*e.g.* see 5.13).

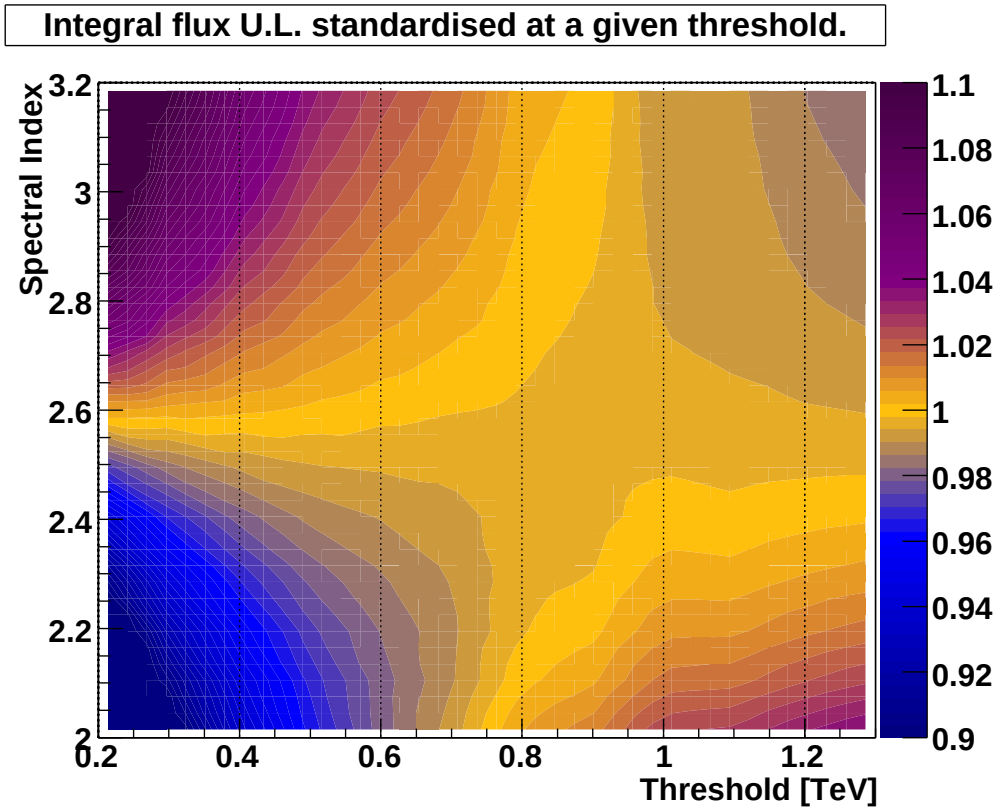

Figure 5.11: Surface of integral flux upper limits, standardised to the mean at a given threshold energy, against threshold energy and assumed spectral index. The colour-code was chosen to highlight the region around the mean.

it is valid across a reasonably wide range of power-law spectra and thus may be compared directly to other measurements, if they too are analysed assuming a power-law spectrum. Also, this limit is largely independent of model assumptions, insofar as those models predict simple power-law spectra. However, its comparison to the model motivating these observations (B&S07) is not clear (see §C for a discussion). That model presents a diversity of possible spectra covering a variety of energy ranges and with spectral indices that evolve with energy. It may be argued that, for this purpose, it is preferable to determine upper limits within relatively narrow energy bands so that they can be reasonably treated as upper limits on the average flux within their respective bands. Thus, these upper limits could be individually compared

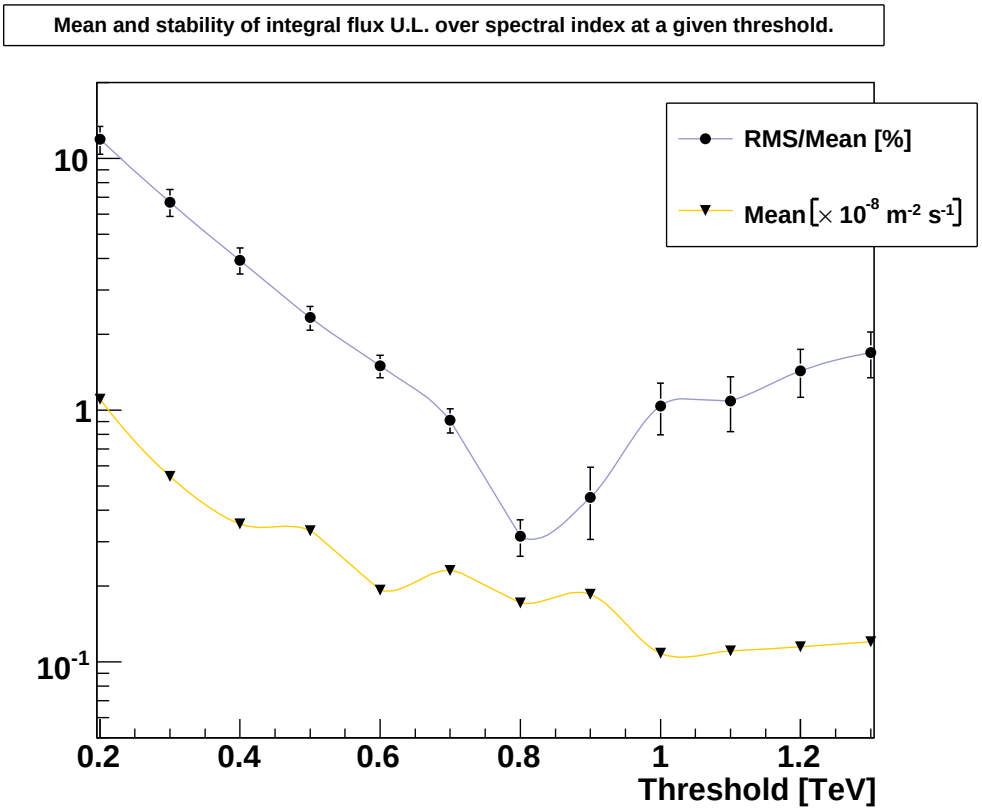

Figure 5.12: Stability and mean of the integral flux upper limit, across a range of assumed spectral index, against threshold energy. The stability is defined as the (RMS/Mean) of a set of integral flux upper limits created by sampling uniformly over a range of spectral index. The smooth curves are provided by the plotter and serve only to guide the eye.

to any of the modelled spectra.

5.3.2.3 Spectral Upper Limits

To allow comparison with the broad selection of emission curves presented in B&S07, which do not generally have simple spectral forms, I adopt an approach similar to that used in [24] which confronted the same emission curves with VHE observations of M13 using the MAGIC detector. That is to say, I derive differential flux upper limits in a range of spectral bins. To achieve this I subdivide the set of events in the ON- and OFF-regions according to

Energy [TeV]		Sig.	Counts				Flux UL
Thresh.	Max.	$[\sigma]$	ON	OFF	Excess	UL	$[\times 10^{-12}\,\mathrm{cm}^{-2}\,\mathrm{s}^{-1}]$
0.8	30	-0.4	2	26	-0.6	4.6	0.306

Table 5.3: Integral flux upper limit details. There are only two ON-counts above the decorrelation energy threshold so a fully Poissonian treatment of these counts is required when deriving upper limits from them (recall §5.3.2.1). The background count rate in the ON-region is estimated from the count rate in the OFF-regions with a normalisation of 0.1 (there are 10 OFF-regions). The integral flux upper limit is at 95% CL and is independent of spectral index to within $\sim 1\%$ for the stated threshold energy. The flux normalisation of $0.342 \times 10^{-12}\,\mathrm{cm}^{-2}\ \mathrm{s}^{-1}\ \mathrm{TeV}^{-1}$ (at 1.0 TeV) is specific to an assumed spectral index of 2.6; it has a systematic error of $\sim 15\%$ due to uncertainty in the index.

reconstructed/estimated energy and derive differential flux upper limits for individual energy bins.

To ensure that these upper limits are constructed only from the most sensitive portion of the array's response and that portion which is less susceptible to fluctuations, events are selected for inclusion in the upper limit calculation only if they lie in the energy regime where the mean effective area for that run is above 25% of its maximum for that run. The variation of the effective area curve between individual runs in this regime is around 5% and not greater than the uncertainty due to the unknown spectral index, as may be seen in Figure 5.13. With this requirement, the lower limit of the energy range of admitted events varies over 0.26–0.34 TeV .

The resulting spectra of ON- and OFF-events are shown in Figure 5.14. There are fewer than ten ON-events in total, so it is clear that I am not free to make any large-number-limit approximation in constructing upper limits for any of these spectral bins, as noted in §5.3.2.1.

Weighting the upper-limit number of events in each energy bin by the effective area averaged over each bin yields an average flux upper limit for each bin according to Eqn. 5.18. In this analysis the bin average effective area is constructed event-by-event and interpolation in $\log_{10}\epsilon_{rec}$ is used to establish an accurate effective area for the particular reconstructed energy ϵ_{rec} of each event individually. The mean of the effective area curves used to construct these bin-wise averages is shown in Figure 5.13. A spectral index

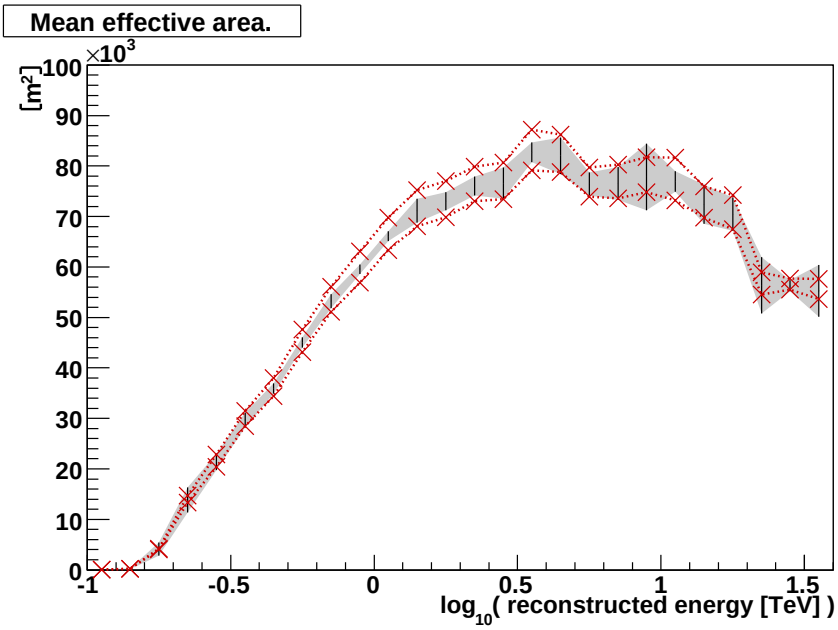

Figure 5.13: The grey band indicates the range of variation of the effective area between individual data runs using an assumed spectral index of 2.6. Red markers indicate mean effective area values due to using assumed spectral indices of 2.0 (lower) and 3.2 (upper). Systematic error in estimation of the flux due to uncertainty in the effective area is around 5%.

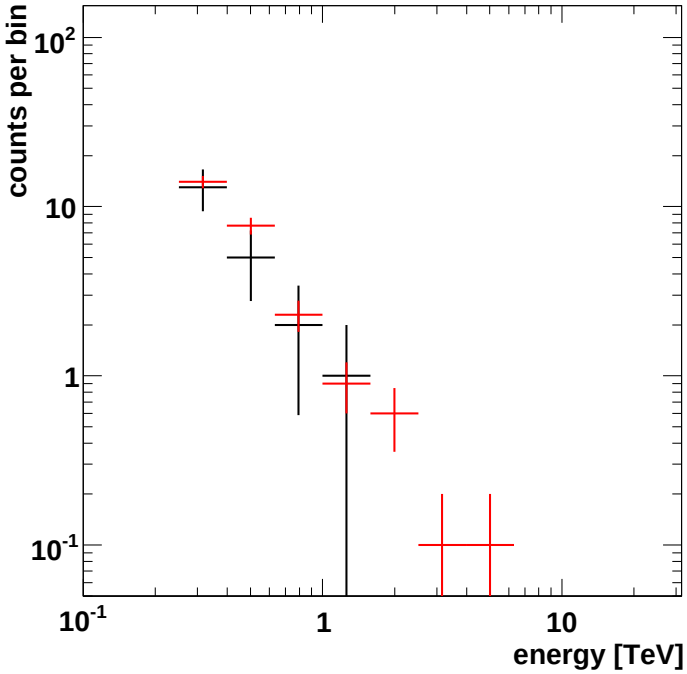

Figure 5.14: Energy distribution of events within the regime of large effective area. Black are ON; red are OFF scaled by the normalisation factor $\alpha = 0.1$. Note that the effective exposure is less in the first bin due to the fluctuation of the threshold energy between runs. There are fewer than ten ON-counts in all but one of the spectral bins so a fully Poissonian treatment of these counts is required when deriving upper limits from them (recall §5.3.2.1).

Bin centre	Sig.	Counts				Flux UL
[TeV]	[σ]	ON	OFF	Excess	UL	[$\times 10^{-12}\,\mathrm{cm}^{-2}\,\mathrm{s}^{-1}\,\mathrm{TeV}^{-1}$]
0.316	-0.26	13	140	-1.0	8.61	36.5
0.501	-1.12	5	77	-2.7	5.37	2.43
0.794	-0.20	2	23	-0.3	4.72	1.27
1.26	0.10	1	9	0.1	4.15	0.344
2.00	-2.45	0	6	-0.6	3.00	0.190
3.16	-1.00	0	1	-0.1	3.00	0.120
5.01	-1.00	0	1	-0.1	3.00	0.0733

Table 5.4: Spectral bin statistics. The bins have equal widths in $\log_{10}\epsilon$ of 0.2. The first bin has only partial exposure (360 min as opposed to 419 min in the others) due to the analysis threshold fluctuating between runs. The normalisation of OFF-counts is 0.1, as there are ten reflected OFF-regions for each-ON region. The counts upper limits (ULs) were calculated using Eqn. 5 from [99], (see §5.3.2.1). The flux upper limits were derived using the mean effective area constructed with an assumed spectral index of 2.6. It may be seen that each of the three highest-energy bins represents a counts upper limit of three; the variation between the flux upper limits there represents the evolution of the effective area with energy.

of 2.6 was used to define the mean effective area curve but this choice is somewhat arbitrary, so the mean curves resulting from two other extreme spectral indices (2.0 and 3.2) are also indicated in Figure 5.13. This allows us to estimate the systematic error in the differential flux upper limits, due to ill-adapted effective area curves, to be $\sim$5%.

The resulting spectral upper limits, and the bin-wise statistics used to generate them, are summarised in Table 5.4. These upper limits are shown in Figure 5.15, along with the integral upper limit calculated above and the upper limits due to observations by MAGIC [24]. I will confront emission curves constructed for M13 with these upper limits in the same manner as [24]: I will demand that the curve should be scaled such that the predicted flux is entirely below each and all of the spectral upper limits.

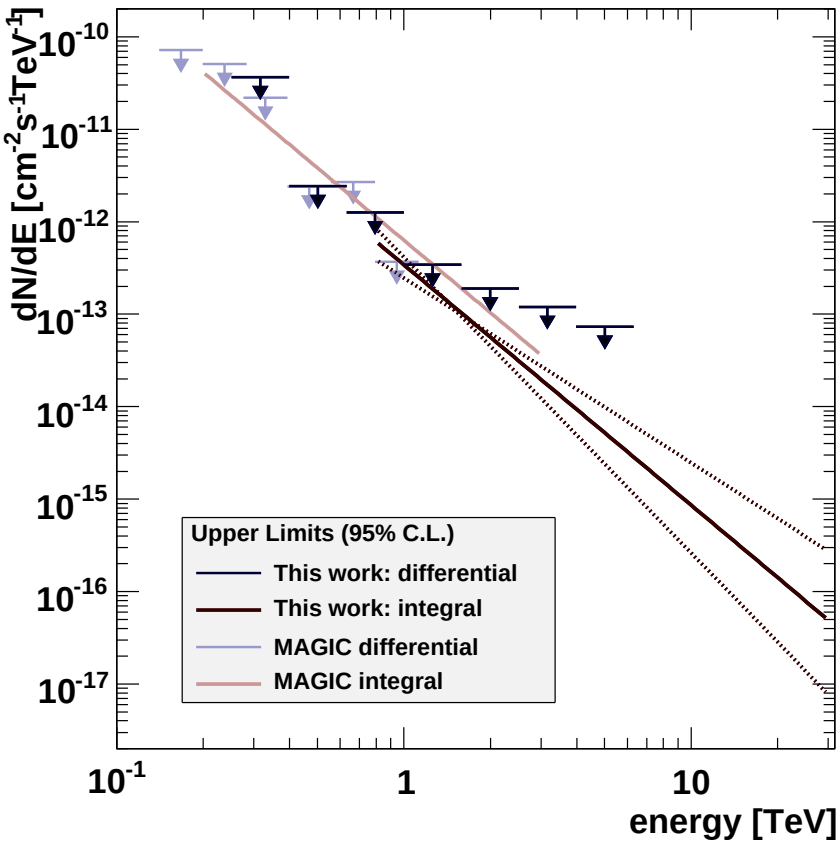

Figure 5.15: Differential and integral flux upper limits on VHE emission from M13 at the 95% confidence level. I have plotted the MAGIC upper limit up to a maximum energy of 3 TeV though no upper bound was noted in the publication [24]. This matches their published sensitivity range reasonably well and introduces only a $\sim$1% correction relative to an infinite upper bound. The integral upper limit from this work is shown covering the entire range over which it was calculated, 0.8–30 TeV: note that it is dominated by the count rate near the lower bound of this range, where it is seen to agree most closely with the spectral limits. Equivalent curves for the integral upper limit, corresponding to the extrema of the range of spectral indicies considered in the derivation of the decorrelation threshold energy (see 5.3.2.2), are also shown: the limits are at their most flexible at high energies, where few events would be collected. Likewise, the spectral upper limits are softest (relative to the integral upper limit curve) at higher energies: the highest energy bin corresponds to a counts upper limit that is thirty times the estimated background rate (see Table 5.4).

5.4 Comparison to Modelled Emission

The model of B&S07 predicts a variety of possible emission curves. Below I compare each emission curve to all of the spectral upper limits and determine the smallest scale factor required for a given curve to be placed below them. A visual comparison of the upper limits from this work and [24] with the predicted flux is shown for the case of a mono-energetic injection spectrum in Figure 5.16 and that of a power-law injection spectrum in Figure 5.17.

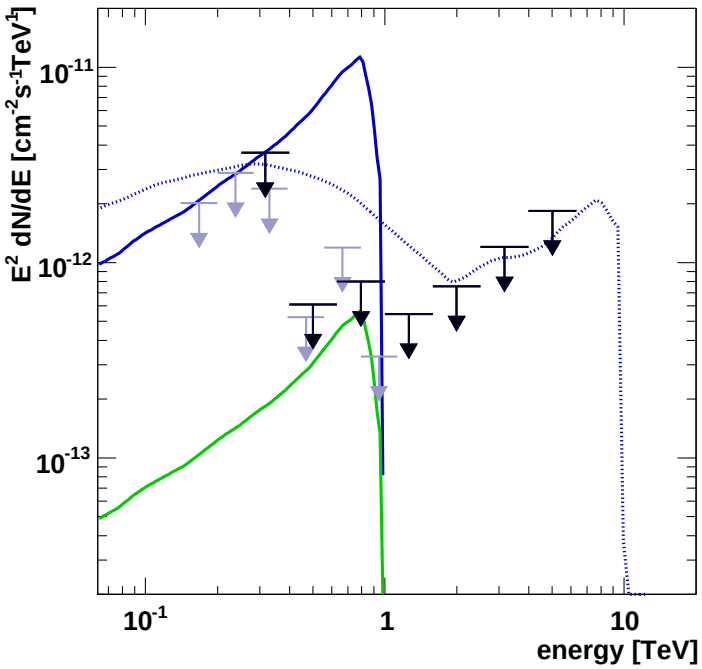

Figure 5.16: Upper limits from this work (black arrows) plotted with the B&S07prediction for injection of mono-energetic electrons. The width of the horizontal bar indicates the bin width. The solid emission curve is for the case of 1 -TeV electrons; the dotted curve for 10 TeV . The emission curves were extracted from the published plots using the online implementation of Dexter [70] (available at `http://dc.zah.uni-heidelberg.de/sdexter`). The 1 -TeV curve is also shown scaled down to the known population of 5 pulsars for $\eta = 0.01$ (green curve). The pale upper limits are due to observations by MAGIC [24].

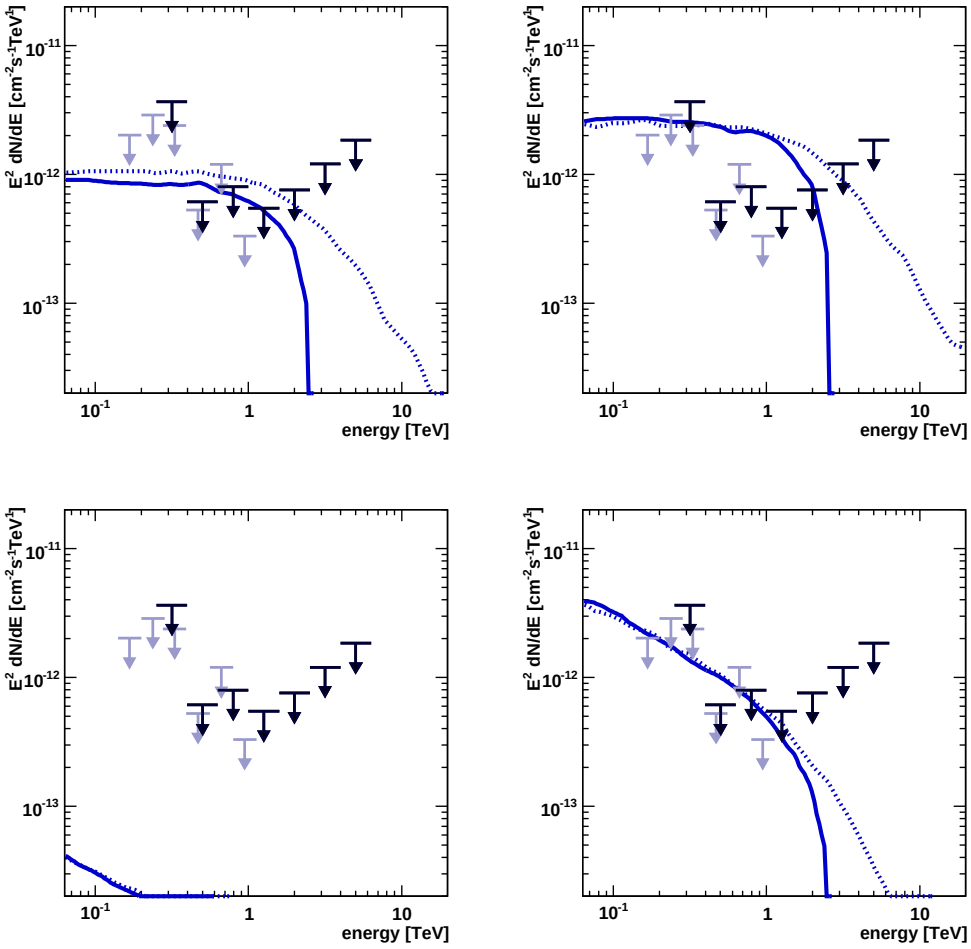

Figure 5.17: Upper limits from this work (black arrows) plotted with the B&S07 prediction for injection of power-law-distributed electrons. The top row corresponds to an injected spectrum with index 2 and the bottom row to index 3; the left column corresponds to a minimum injection energy of 1 GeV and the right column to a minimum injection energy of 100 GeV . Solid curves are for a maximum injection energy of 3 TeV and dotted curves for 30 TeV . The emission curves were extracted from the published plots using the online implementation of Dexter [70] (available at `http://dc.zah.uni-heidelberg.de/sdexter`). The pale upper limits are due to observations by MAGIC [24].

Each emission curve, j, has been defined in terms of energy flux, $\Phi_j(\epsilon)$. An individual spectral upper limit, $\bar{F}_i$, is compared to an emission curve by first integrating the photon flux implied by that curve, $\epsilon^{-2}\Phi(\epsilon)$, across the energy bin, i, for which that upper limit was defined. Then the average photon flux for that bin multiplied by a scale factor, f_{ij}, is set equal to the upper limit :

$$\bar{F}_i = f_{ij} \frac{\int_{\epsilon_i}^{\epsilon_{i+1}} \epsilon^{-2}\Phi_j(\epsilon)\,\mathrm{d}\epsilon}{\Delta\epsilon_i} \tag{5.19}$$

where $\Delta\epsilon_i$ is the width of the energy bin. The scale factor, f_{ij}, between the model and the upper limit must then be the ratio of the upper limit to the average photon flux :

$$f_{ij} = \frac{\bar{F}_i \Delta\epsilon_i}{\int_{\epsilon_i}^{\epsilon_{i+1}} \epsilon^{-2}\Phi_j(\epsilon)\,\mathrm{d}\epsilon} \tag{5.20}$$

The smallest scale factor for a given emission curve ensures that the curve is below all of the upper limits and this is the required value for that curve :

$$f_j = \min(\{f_{ij} | i = 1, \ldots, 6\}) \tag{5.21}$$

Thus f_j may be taken as an upper limit on the scale of the emission curve: the emission curve normalisation is required to be below this scale factor for that curve to be consistent with observations at the appropriate confidence level.

Recalling §2.3.3 and in particular Eqn. 2.20 we see that upper limits in terms of f_j may be applied directly to the parameters of the model :

$$\Phi_j(E) \quad \propto \quad f_j \bar{L}_{\text{s-d}} \eta_{\pm} N_{\text{P}} \tag{5.22}$$

In particular B&S07 assumed a particular mean pulsar spin-down luminosity, $\bar{L}_{\text{s-d}}$ and set $\eta_{\pm} N_{\text{P}} = 1$ to construct the emission curves, where N_{P} is the number of pulsars in the globular cluster and $\eta_{\pm}$ is the efficiency with which a pulsar converts spin-down power to relativistic electrons. We can thus compare the upper limits in terms of f_j directly to limits on $\eta_{\pm} N_{\text{P}}$, under the assumption that the mean spin-down luminosity has been properly estimated, as presented in [24]. Upper limits of the scale factor on each of the emission curves, due to this work, are presented in Table 5.5. Overall, these limits are more constraining than those quoted in [24] by as much as 50% and approximately 30% on average: this is unexpected as the flux upper limits themselves are not, in general, any lower (recall Figure 5.15). Presumably

the root of this discrepancy lies in the method of comparison between the binned flux upper limits and the continuous modelled emission curves: the exact means by which this comparison was conducted in [24] is not described there, so this remains speculation.[13] However, across certain key bins, the modelled flux does vary by as much as a factor of two so that, if comparison was made at some specific point (*e.g.* one of the bin limits) instead of through a bin-wise average (as is done in this work), the scaling could fluctuate by such a degree.

Power	$E_{\pm,\mathrm{min}}$ [GeV]	1		100		**Mono-energetic**	
Law	$E_{\pm,\mathrm{max}}$ [TeV]	3	30	3	30	1	10
Spectral	2.1	0.74	0.60	0.26	0.26	0.098	0.22
Index	3.0	59	56	0.61	0.58		

Table 5.5: Scaling factors to the most constraining upper limit for the emission curves due to the model of Bednarek & Sitareck [36]. These may be considered to be limits on the product of model parameters $\eta_{\pm} N_{\mathrm{P}}$, if the mean spin-down luminosity is assumed to be correct. The emission curves are categorised by the type of electron injection spectrum (power-law or mono-energetic) and the detailed properties assumed within those types: *i.e.* electron energy (range), $E_{\pm,(\mathrm{min,max})}$, and spectral index (for power-law only).

The emission curves associated with those scenarios of power-law injected-electron spectra where the minimum injection energy is only 1 GeV are not very amenable to interpretation in terms of VHE observations. They are better suited to examination by HE observatories such as *Fermi* (recall Figure 1.10) and I will not consider them further.[14] The other scenarios indicate a median value of the scale factor to be $\tilde{f} \simeq 0.26$ and I will carry this representative value forward to the following discussion of the implications of these limits. It must be born in mind, however, that this value carries with

[13] In this regard, I note that in certain cases (*e.g.* $E_{\pm,\mathrm{min}} = 100\,\mathrm{GeV}$; $E_{\pm,\mathrm{max}} = 3\,\mathrm{TeV}$; spectral index 3.0; Figure 5.17 lower-right, solid) a scale factor of 1.0 is indicated by [24] (identical to the level of modelled emission) yet there are upper limits clearly completely below the modelled emission curve, contrary to the stated criterion for comparison.

[14] This mechanism was briefly considered as a possible source of HE emission from 47 Tucanae in [6] though consideration of the spectral shape ruled out a strong contribution to the detected flux. The entire flux could be explained by direct, unresolved emission from up to sixty pulsars.

it an error of a factor of two due to the wide variation between the different scenarios.

Chapter 6

Discussions & Conclusions

Recall that, in the models of B&S07 (see §2.3), the energy flux, $\Phi(\epsilon)$, from a globular cluster in VHE gamma rays is directly related to the total power of the population of MSPs in relativistic electrons, $L_{\pm}$: in turn, this is linearly related to three parameters of the population of millisecond pulsars :

$$\Phi(\epsilon) \propto L_{\pm} \quad = \quad \eta_{\pm} \bar{L}_{\text{s-d}} N_{\text{P}} \tag{6.1}$$

where N_{P} is the number of pulsars in the cluster, $\bar{L}_{\text{s-d}}$ is their mean spin-down luminosity and $\eta_{\pm}$ the efficiency with which this power is transmitted to relativistic electrons. Now, we may summarise the observational limits, $\bar{F}_i$, established above (see §5.4) in terms of a scale factor, $\tilde{f}$:

$$\bar{F}_i \quad \propto \quad \tilde{f} \Phi(\epsilon) \tag{6.2}$$

$$\propto \quad \tilde{f} \eta_{\pm} \bar{L}_{\text{s-d}} N_{\text{P}} \tag{6.3}$$

Thus, the limit determined in the previous chapter can be applied to any of these three parameters, given assumptions about the other two. Below, we estimate two of the three parameters at a time and apply $\tilde{f} = 0.26$ to the remaining one. Let us first consider the range of values expected for these parameters.

6.1 Feasible Ranges of the Model Parameters

I will review possible ranges for each of the parameters in turn and select three representative values for each. The major obstacles to estimating the three parameters are :

total population — existing pulsar surveys are sensitivity limited such that many more pulsars may exist than are currently observed.

mean power — the mean energy-loss rate of pulsars is not generally well known and direct estimates require measurement of the spin-down rate, which is unknown for all of the detected MSPs in M13.

particle efficiency — the total energy budget of pulsars is unclear, though it is apparent that a relatively small fraction of their power is emitted directly so that most of it must be lost to a wind, the composition of which is not well constrained.

I will discuss, and attempt to circumvent, these difficulties below.

For this I will rely upon the interpretation of observations in other domains (radio, X-ray and HE gamma rays) of pulsars (particularly MSPs), their wind-nebulae and globular clusters. In particular, one of the most intensively-studied[1] globulars, due to its proximity and size, 47 Tucanae (47 Tuc) will figure prominently in what follows, affording estimates of pulsar content and spin-down luminosity. It is expected that the primary difference between globulars, in terms of their pulsar populations, is due to their stellar interaction rates which drive the peculiar richness of these objects (recall §1.2) and the difference between M13 and 47 Tuc, in this respect, will be accounted for in what follows. Nonetheless, it should be noted that the major sub-division of the population of Galactic globulars is into two groups according to their metallicity (the ratio of Iron to Hydrogen abundance, [Fe/H]) [214, 215] and 47 Tuc and M13 reside unequivocally in differing subpopulations. However, the abundance of close binary systems in globulars seems to be adequately described with reference only to stellar interaction rate, across a diverse group of clusters with differing metallicities (including 47 Tuc and M13) [177, 176]. It remains an open (and intriguing) question as to whether cluster metallicity affects the spin-down luminosity of the pulsar population it hosts. The information available for 47 Tuc is singularly detailed amongst the Galactic globulars and, for this reason, it is the point of comparison for other clusters.

As we shall see, interpretation of observations of all globular clusters is complicated by their distance ($D > 2\,\mathrm{kpc}$). Thus, we will have cause to refer also to observations of local ($D < 2\,\mathrm{kpc}$) pulsars, and in particular local MSPs, in the Galactic plane.

[1] Radio studies: [50, 76, 75]; X-ray studies: [88, 98, 44]; HE gamma-ray studies: [6].

6.1.1 Pulsar Population

Pulsars in globulars are usually discovered in targeted radio surveys and the five MSPs known to exist in M13 were discovered in this way [137, 25, 68, 103]. Currently, 143 pulsars are known in 27 globular clusters[2] thanks to radio surveys. However, these successes are in spite of several selection effects, all of which discriminate particularly against the detection of short-period MSPs such as those found in globulars [144]. In essence, these effects are related to the fact that pulsars will be more difficult to detect if the pulses become smeared while accumulating the signal [181].

Such smearing of the pulsar signal can happen for a number of reasons. Primarily, it is caused by propagation of the pulses through the ionised **InterStellar Medium** (ISM) causing a pulse to arrive with a slightly different lag depending upon the radio frequency at which it is observed: this effect is called dispersion.[3] The column depth of the ISM, also called the **dispersion measure**, between the source and Earth must be accounted for to allow summation of the signal across different frequencies.[4] This becomes particularly important if successive pulses have small separation, *i.e.* the pulse-period is short. Another possibility is that if the pulsar is accelerating, its period appears to fluctuate as the Doppler shift due to its motion evolves. The majority of globular MSPs[5] are in binary systems due to their evolutionary path (see §1.2.2) so, again, this particularly hinders their detection.

In addition to these difficulties, radio surveys must contend with the fact that MSPs are objects with intrinsically low radio luminosity. For instance, in the most recent survey of M13 [103] the four brightest pulsars observed (for which luminosity could be determined with an error of no more than $\sim 50\%$) had luminosities in the range 1.3–8.3 mJy kpc^2 (measured at 1.4 GHz), the brightest being less than five times the nominal sensitivity of the survey for this cluster (1.7 mJy kpc^2). Thus, due to the low radio luminosity of these objects, existing radio pulsar surveys are sensitivity limited [181]. This constitutes an observational bias because only those objects with the greatest

[2] See http://www.naic.edu/~pfreire/GCpsr.html for an up-to-date listing.

[3] Other propagation effects are also important to pulsar survey bias; see [144] for an overview.

[4] In fact, once a pulsar has been discovered, its dispersion measure will be known exactly and this can be converted to an estimate of the distance to the pulsar. However, this estimate is based upon models of the ionised gas distribution in and around the galactic plane [60] and is subject to fairly large errors [39, 103].

[5] Almost 60% of those *observed*, despite this bias.[181]

luminosities will be reliably detected. Overall, there may be many pulsars that remain unseen for each one detected in a radio survey [51].

Under these conditions, in order to estimate the actual total pulsar population it is necessary to extrapolate the perceived population of pulsars (having large luminosities) to objects with lower luminosities which presently evade direct detection. This may be done by appealing either to radio or X-ray observations.

6.1.1.1 Radio Luminosity Distribution Function

To extrapolate radio observations to lower luminosities, I follow the example of [50] by using the **luminosity distribution function** (l.d.f.): a power-law which describes the intrinsic radio brightness of the pulsar population. This distribution allows us to estimate how much of the population is hidden by the limitations of radio surveys because a certain number of pulsars observed at large luminosities implies a definite quantity of others that are dimmer. How many low-radio-luminosity pulsars are hidden depends upon the slope, λ, and the lower limit, L', of the l.d.f.

The logarithmic form of the l.d.f.has been determined for globular MSPs [103] to be :

$$\lambda = \frac{\mathrm{d}(\log N)}{\mathrm{d}(\log L)} = -0.9 \pm 0.07 \tag{6.4}$$

This study compiled results across many surveys, but remained relatively free of bias because the distances to most globulars are reasonably well known; they are generally out of the galactic plane, which limits the dispersion measure; and isolated pulsars were used specifically to avoid selection effects against binary ones. Nonetheless, this l.d.f. was derived above $1.5\,\mathrm{mJy\,kpc^2}$ (at $1.4\,\mathrm{GHz}$) because, below this level, the observational bias against dim sources at great distance comes into play in surveys of globulars. So, the total number of pulsars actually detected in a survey, N_0, will depend upon the sensitivity of the survey which can be described in terms of the threshold luminosity for a pulsar to be visible, L_0. That is, $N_0 = N(L > L_0)$, the total number of pulsars in the population having a luminosity greater than the threshold. Now, those pulsars not detected in the survey must have a luminosity between the lower limit of the population, L', and the threshold for

detection, L_0. Thus, in terms of the **cumulative luminosity distribution** :

$$\log N(L > L_0) = \int_{L_0}^{\infty} \lambda \ \mathrm{d}(\log L) \tag{6.5}$$

$$= \int_{L'}^{\infty} \lambda \ \mathrm{d}(\log L) - \int_{L'}^{L_0} \lambda \ \mathrm{d}(\log L) \tag{6.6}$$

$$\simeq \log N' - 0.9 \log\left(\frac{L_0}{L'}\right) \tag{6.7}$$

where $N' = N(L > L')$ is the total pulsar population. Thus, if L' can be determined, the total population can be estimated from the number observed and the luminosity of the dimmest pulsar seen, the latter being taken as an estimate of the threshold luminosity.

To glean an estimate of L' we may appeal to observations of local pulsars, for which even the dimmest may be visible.[6] In [150] the then-known sample of twenty-one local MSPs was examined, carefully accounting for observational bias. It was determined that these pulsars were consistent with a l.d.f. of the form $\mathrm{d}(\log N) = -\mathrm{d}(\log L)$ down to luminosities below $1\,\mathrm{mJy\ kpc^2}$ from observations at $\nu = 0.4\,\mathrm{GHz}$.[7] We may convert the lower limit of that distribution, $L'_{0.4}$, to a limit at $1.4\,\mathrm{GHz}$, $L'_{1.4}$, by reference to the mean spectral index of pulsars derived in [155], namely -1.8 ± 0.2; note that this is the same manner by which surveys at different frequencies were compared in [103].

$$L_\nu \propto \nu^{-1.8\pm0.2} \tag{6.8}$$

$$\frac{L'_{1.4}}{L'_{0.4}} = \left(\frac{1.4}{0.4}\right)^{-1.8\pm0.2} \tag{6.9}$$

$$L'_{1.4} = 1.0 \times \left(\frac{0.4}{1.4}\right)^{1.8\mp0.2} = 0.1^{+0.03}_{-0.02} \tag{6.10}$$

[6] It is important to note that other sources of bias are exacerbated in just such surveys as observations in the Galactic plane inevitably encounter much greater dispersion measures and the distances of many pulsars may be estimated only from the dispersion measure, implying, because of the inverse-square law, potentially very large errors in the derived radio luminosity. Thus, these surveys must estimate and account for observing bias.

[7] Note that [114] aimed to update the study of [150] by drawing MSPs in the Galactic field from the ATNF pulsar catalogue [154] but apparently neglected to account for the bias due to poor distance estimation and ISM effects, which can be particularly important for nearby pulsars [144]. Consequently [114] derives much flatter distributions than all previous studies and concludes that there is a marked difference between globular-cluster and galactic-plane pulsars.

This lower limit is in agreement with that of a more modern study, conducted at 1.4 GHz, of non-recycled, isolated pulsars in the galactic plane [146] which also found a l.d.f. having a slope just compatible with that derived in [103].

I assert, therefore, that the l.d.f. for radio MSPs in globulars is as described in [103] but extending, unbroken, in the manner of the similar distributions of galactic pulsars, to a lower limit of 0.1 mJy kpc^2 . This implies the presence of many more pulsars just out of reach of the current sensitivity of radio telescopes, as may be the case in other globulars such as 47 Tuc [50, 51].

I now use this to estimate the total pulsar population of M13. Basing this calculation on those pulsars with reasonably well-known luminosities (*i.e.* taking $N(L > 1.3) = 4$)[8]and recalling Eq. 6.7, I calculate :

$$\log N(L > L_0) \simeq \log N' - 0.9 \log\left(\frac{L_0}{L'}\right) \tag{6.11}$$

$$N(L > L_0) \propto L_0^{-0.9} \tag{6.12}$$

$$\frac{N(L > 0.1)}{N(L > 1.3)} = \left(\frac{0.1}{1.3}\right)^{-0.9} \tag{6.13}$$

$$N(L > 0.1) = N(L > 1.3)\left(\frac{0.1}{1.3}\right)^{-0.9} = 40 \tag{6.14}$$

Thus, by extrapolating from existing radio observations, I estimate that there could be around forty pulsars in M13 in total.

However, there is some evidence that the l.d.f. for globular MSPs does not extend to such low luminosities. For 47 Tuc the cumulative luminosity distribution has been derived with pulsars observed in this cluster alone [158]; again it is seen to be consistent with $\mathrm{d}(\log N) = -\mathrm{d}(\log L)$. This study goes further, using measurements of the integrated radio emission from 47 Tuc at 1.4 GHz along with that cumulative luminosity distribution to demonstrate that the low-luminosity limit of the distribution is likely no less than 0.4 mJy kpc^2 . Assuming the same l.d.f. and limiting luminosity for M13 implies, by a similar calculation to that above (Eq. 6.14)[9], thirteen pulsars in total.

[8] The lowest luminosity pulsar was detected in only two out of sixty-seven observations during the survey [103] and evidently represents the type of object which the survey was strongly biased against.

[9] $N(L > 0.4) = N(L > 1.3)\left(\frac{0.4}{1.3}\right)^{-1} = 13$

Note that these estimates do not account for beaming of radio emission, *i.e.* that the radio beams may sweep out only a small solid angle. In this case the correct orientation, by chance, of a pulsar's spin-axis, magnetic-axis inclination and the Earth's position is required to make the detection of any individual, active pulsar possible. This would imply a still larger population of pulsars including a fraction rendered invisible to radio telescopes by the simple matter of the directed radio emission never sweeping over the Earth. As noted in [144], such geometrical factors are subject to widely varying interpretations [149, 40] and may require an order of magnitude correction [197] to survey populations. However, in general, short-period pulsars seem to have broader beams [197] and so require a smaller correction. I have ignored beaming factors in these estimates.

6.1.1.2 X-Ray Source Counts and Stellar Interaction Rates

Another avenue is open to us to estimate the intrinsic pulsar population. X-ray observations of globulars suggest that the abundance of sources, of which MSPs are an important component, is directly related to those properties of the cluster that contribute to a large stellar encounter rate. Using this relationship, we can relate the estimated pulsar content of 47 Tuc to the specific case of M13.

MSPs are commonly X-ray sources, most often exhibiting only thermal emission[10] and observable for all combinations of obliquity and viewing angle [43]. For instance, deep *Chandra* observations of 47 Tuc [98] detect all MSPs having precisely known positions [44]; they are scattered amongst approximately 230 sources within the half-mass radius and associated with the cluster. Furthermore, by consideration of the spectral properties of unidentified X-ray sources, it is estimated that this globular contains approximately twenty-five pulsars and less than sixty with 95% confidence.[11] In the case of M13, X-ray observations reveal approximately twenty sources within the half-mass radius and associated with the cluster [188]. However, only one MSP has a well-known position and it is seemingly not detected in these observations [35]. [12]

[10] Occasionally a non-thermal component is also present due to appropriate alignment of beamed magnetospheric emission or due to interaction of the pulsar wind with a binary companion.

[11] *Fermi* observations of 47 Tuc also indicate a population of up to sixty pulsars [6].

[12] It is stated in [103] that, in the same *Chandra* data set, there are no obvious coun-

This profusion of X-ray sources in globulars is composed primarily of compact binary systems [204]: cataclysmic variables and other such systems containing a main sequence star with a degenerate companion (*i.e.* a white dwarf or neutron star). Such systems may be precursors to MSPs and certainly act as tracers for the sort of exchange interactions that are believed to be necessary to the enrichment of globulars with MSPs [115]. Hence, the number of X-ray sources per unit mass, $N_{\rm X}/m = n$, is seen (in a study combining X-ray observations of 23 globulars) [176] to scale with the **specific stellar encounter rate**[13], ξ, according to the relation :

$$n = C + A\xi^{\alpha} \tag{6.15}$$

where the first term represents a primordial contribution to this population and the second term the contribution due to stellar interactions. Here, the mass of the cluster may be taken as being proportional to its luminosity, $L \propto 10^{-0.4M_{\rm V}}$, where $M_{\rm V}$ is the absolute visual magnitude.

Now, the relationship between source counts and ξ may differ for different sub-populations of X-ray sources. For instance, [176] defines four sub-populations: population III contains most of the identified MSPs (but also many other sources) and has a best-fit relation of $n_{\rm III}$ to ξ with $C = -12$, $\alpha = 0.27$ and $A = 9.23$.[14] I will now make the assumption that the quantity, $N_{\rm X,III} = n_{\rm III}m$, of this sub-population of X-ray sources may be treated as a proxy for the MSP population, $N_{\rm P}$: *i.e.* I assume MSPs form a constant fraction of this sub-population ($N_{\rm P}/N_{\rm X,III}$) across all globular clusters.

Given this, I can state :

$$N_{\rm P} \propto N_{\rm X,III} = (C + A\xi^{\alpha})m \tag{6.16}$$

and use this scaling relation and the detailed estimates for the total MSP

terparts for another three of the pulsars in M13 but their exact locations are not recorded in the ATNF pulsar catalogue [154].

[13] The specific stellar encounter rate is simply the stellar encounter rate, Ξ, per unit mass. The stellar encounter rate itself is related to the density profile of stars (*i.e.* a King model [126]), their velocity distribution and the mass of the cluster [176] : $\Xi = \int_0^h 4\pi r^2 \rho^2/\sigma_v \, {\rm d}r$ where h is the half-mass radius and ρ and σ_v are, respectively, the density and velocity dispersion as functions of radius.

[14] The value of A is not listed in [176] but may be derived from Fig. 2c where $n(\xi = 100) = 20$. Note that [176] uses γ for the specific stellar encounter rate but I have used ξ to avoid confusion with the Lorentz factor.

population of 47 Tuc to calculate the total pulsar population for M13 :

$$N_{\mathrm{P(M13)}} = N_{\mathrm{X(M13),III}} \frac{N_{\mathrm{P(47Tuc)}}}{N_{\mathrm{X(47Tuc),III}}} \tag{6.17}$$

where, as noted above, $N_{\mathrm{P(47Tuc)}}$ is likely 25 but may be as large as 60 (see Table 6.1). It is notable that this scaling relationship almost exactly reproduces the relative abundance of currently known pulsars in these two globulars. The implied upper limit on the number of pulsars in M13 is eleven.

Name		M_{V}	m	ξ	n_{III}	$N_{\mathrm{P}}/N_{\mathrm{X,III}}$	N_{P}
NGC#	Other		$[M_\odot \times 10^6]$				
104	47 Tuc	-9.37	1.41	273.8	30.01	0.59 (1.43)	25 (60)
6205	M13	-8.5	0.63	40.86	13.13		5 (11)

Table 6.1: Globular cluster parameters related to stellar encounter rate and scaling for the number of MSPs. Absolute magnitude, M_{V}, taken from the 2003 edition of the catalogue due to Harris [94] for consistency with [176]. Mass, m, is assumed to scale with the total luminosity, as derived from the absolute magnitude. Specific stellar encounter rate, ξ, has been extracted from Fig. 2c of [176] using the online implementation of Dexter [70] (available at http://dc.zah.uni-heidelberg.de/sdexter). The specific source count, n_{III}, has been calculated using the best-fit for population III as defined in [176]. $N_{\mathrm{X,III}}$ is the number of sources in population III of [176] whose definition does not extend below $4 \times 10^{30}\,\mathrm{erg\ s^{-1}}$ because some of the clusters in the study did not have sufficient exposure for lower luminosities. There are, however, identified MSPs with lower luminosities and the study of X-ray sources in 47 Tuc extended below this level, hence $N_{\mathrm{P}} > N_{\mathrm{X,III}}$ is not unexpected. The number of pulsars for 47 Tuc are those suggested by X-ray source counts, with the 95% C.L. value in parenthesis [44]; for M13 they are those derived assuming the 47 Tuc MSP population will scale to other globulars as population III of [176].

6.1.1.3 Feasible Values for the Pulsar Population

In summary, I claim that reasonable values for the total pulsar population of M13, $\langle N_{\mathrm{P}} \rangle$, may be derived from the radio luminosity distribution functions observed for globular cluster pulsars and local MSPs (RadioLDF); or be

derived from the radio luminosity distribution function observed in 47 Tuc; or be derived from the observed relationship between stellar encounter rates and X-ray source abundance in globulars (X-RAYUL). The latter two estimates (both derived relative to 47 Tuc) provide very similar upper limits, and the most probable value of the last one agrees with the currently known population (KNOWN). I will define a feasible set of values to be :

$$\langle N_{\rm P} \rangle \equiv \{\text{KNOWN, X-RAYUL, RADIOLDF}\} \quad (6.18)$$
$$= \{5, 11, 40\} \quad (6.19)$$

with the middle value being preferred by consistency between radio and X-ray studies of another globular cluster (47 Tuc).

6.1.2 Spin-Down Luminosity

The strong magnetic field of a pulsar extracts energy from its rotation. Thus, the pulsar's rotation rate decreases while it releases energy (as radiation and as a particle wind) to its surroundings. This phenomenon is quantified by the spin-down luminosity which is often expressed approximately as the energy lost by an orthogonally-rotating magnetic dipole in a vacuum[15] : $L_{\rm s\text{-}d} \propto B^2 P^{-4}$. In the model of B&S07, the typical surface magnetic field and period of MSPs in globulars were taken to be $10^9\,{\rm G}$ and $4\,{\rm ms}$, respectively, which implied a spin-down luminosity of $1.2 \times 10^{35}\,{\rm erg\ s^{-1}}$. They used this value for all four of the clusters they considered, including M13 and 47 Tuc.

Somewhat more empirically, the energy of a pulsar is stored in its rotational motion and so its rate of energy loss, $\dot{E}$, is related to its changing rotation rate, $\Omega = 2\pi/P$, as follows :

$$\dot{E} = \frac{{\rm d}E}{{\rm d}t} = \frac{\rm d}{{\rm d}t}\left(\frac{I}{2}\Omega^2\right) = -4\pi^2 I \frac{\dot{P}}{P^3} \quad (6.20)$$

where I is the moment of inertia. Thus, the spin-down luminosity of a pulsar may be estimated directly from knowledge of its period, P, and period derivative (also called the **spin-down rate**), $\dot{P}$, and assumptions concerning

[15] For the reasons outlined by Goldreich & Julian (recall §2.1.2) it cannot be in a vacuum locally. More modern treatments (see Eqn. 2.1) [192] include something very like the orthogonal rotator relation as a special case. The apparent accuracy of the orthogonal rotator model can be accounted for by imagining that the long-wavelength dipole-radiation is absorbed in and energises the surrounding plasma.

its moment of inertia[16]. However, for pulsars in globulars, measurement of their spin-down rates is complicated by the gravitational field of the cluster within which they are bound. Their motion due to orbiting about the centre of the cluster introduces a persistent Doppler-shift. This must be accounted for to attain the intrinsic period derivative and hence the correct spin-down luminosity.

The spin-down rate has not been measured for any of the pulsars in M13, and consequently their spin-down luminosities have not been estimated. However, we may estimate a reasonable value for the energy loss rate of pulsars in M13 by considering the known (or derived) properties of others like those in M13.

6.1.2.1 Globular-Cluster MSPs

The intrinsic spin-down rates of a sub-set of the pulsars of 47 Tuc have been estimated [44]. This was done by estimating the three-dimensional position of the individual pulsars relative to the centre of the globular assuming a constant gas density in the cluster to account for differences in their dispersion measures. A King model [126, 127, 128] for the stellar distribution was then used to determine the gravitational effect of the globular on each pulsar. With the caveat that the assumption of a constant gas density may be an over-simplification, the mean spin-down luminosity was estimated to be $2.1 \times 10^{34}\,\mathrm{erg\ s^{-1}}$.[17]

If we assume that the pulsars of all globular clusters are similar[18], we may use this sample as an estimate of the mean spin-down luminosity for the population of pulsars in M13. The pulsars of M13 may be compared to those of 47 Tuc used in this estimate in Figure 6.1, where their periods are seen to occupy a similar range. Those two pulsars with periods shorter than the fastest pulsar of M13 have spin-down luminosities estimated to be similar to the others and do not significantly bias the mean spin-down luminosity of this population.

[16] $I = 10^{38}\,\mathrm{kg\ m^2} = 10^{45}\,\mathrm{g\ cm^2}$ with approximately 70% error (§3.1.2 of [147]).

[17] This is almost an order of magnitude below the value adopted in B&S07. That choice was critiqued for the specific case of 47 Tuc in a paper detailing observations of that globular by the H.E.S.S. collaboration [17].

[18] In the sense that their properties are similarly distributed.

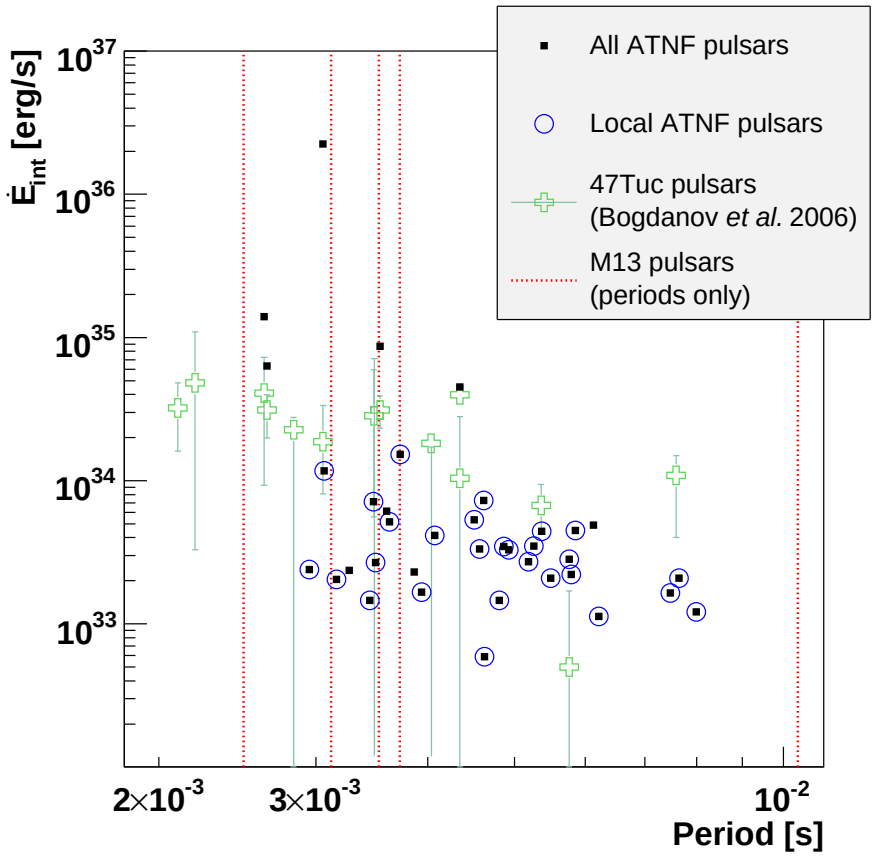

Figure 6.1: The intrinsic spin-down luminosity, of pulsars for which it has been estimated, against pulsar period. The ATNF pulsar properties were retrieved from the ATNF Pulsar Catalogue [154] (available at `http://www.atnf.csiro.au/research/pulsar/psrcat`). The local pulsars are within 2 kpc of Earth. It may be seen that pulsars observed at greater distances often have much larger spin-down luminosity, which is likely a selection effect. The ATNF database accounts only for proper motion in deriving the intrinsic spin-down luminosity. The four pulsars of 47 Tuc from the ATNF database (near $\dot{E} \approx 10^{35}\,\mathrm{erg\ s^{-1}}$) have over-estimated spin-down luminosity relative to the values derived in [44] in which the effect of motion in the gravitational field of the cluster was accounted for. For comparison, the periods of M13 pulsars are indicated by vertical dotted red lines: their spin-down luminosities are unknown.

6.1.2.2 Pulsar Population Statistics

Additionally, if we assume that all MSPs are similar we may examine all known pulsars with periods similar to those of the M13 MSPs. In particular, we may use the subset of those pulsars which have an estimated intrinsic period derivative:, *i.e.* a spin-down rate that has been corrected for the proper motion of the pulsar. These pulsars will have a corresponding intrinsic spin-down luminosity which may be used to estimate the mean spin-down luminosity of the pulsar population of M13.

The **Australia Telescope National Facility** (ATNF) pulsar catalogue [154] is a database that makes these properties readily accessible. Here I draw from this database the intrinsic spin-down luminosities for pulsars having periods in the range 2.487 – 10.378 ms and with existing estimates of the intrinsic period derivative, providing a sample of thirty-seven pulsars[19] (see Figure 6.1). All of these pulsars are within 6kpc, less than the distance to M13 (7.5 kpc). The distribution of their spin-down luminosities is summarised in Table 6.2 and plotted in Figure 6.2. The mean spin-down luminosity of all these pulsars is $7.3 \times 10^{34}\,\mathrm{erg\ s^{-1}}$.

However, this estimate includes nine pulsars located very far ($D > 2\,\mathrm{kpc}$) from the Earth (six of which reside in three globular clusters)[20] and their observation is likely aided principally by their high luminosities. This would constitute a bias in the measured distribution relative to the actual one because there likely exist other pulsars at such distances, having less extreme properties, which we are currently unable to observe. A less-biased sample might be constructed by examining only nearby pulsars ($D < 2\,\mathrm{kpc}$). The distribution of the spin-down luminosities of this reduced sample is also summarised in Table 6.2 and plotted in Figure 6.2. Considering only these local pulsars we arrive at a mean spin-down luminosity of $0.38 \times 10^{34}\,\mathrm{erg\ s^{-1}}$.

6.1.2.3 Feasible Values for the Mean Spin-Down Luminosity

Thus, I claim that representative values of the typical mean spin-down luminosity of millisecond pulsars, $\langle \bar{L}_{\text{s-d}} \rangle$, may be derived from a database sample

[19] Nine of these pulsars have been directly detected by *Fermi*. In addition, a further four of them are associated with 47 Tuc and the most powerful one (the first globular-cluster pulsar to have ever been detected [148]) resides in M28: both of these globular clusters have also been detected by *Fermi* [9].

[20] Namely M28, 47 Tuc and NGC6752.

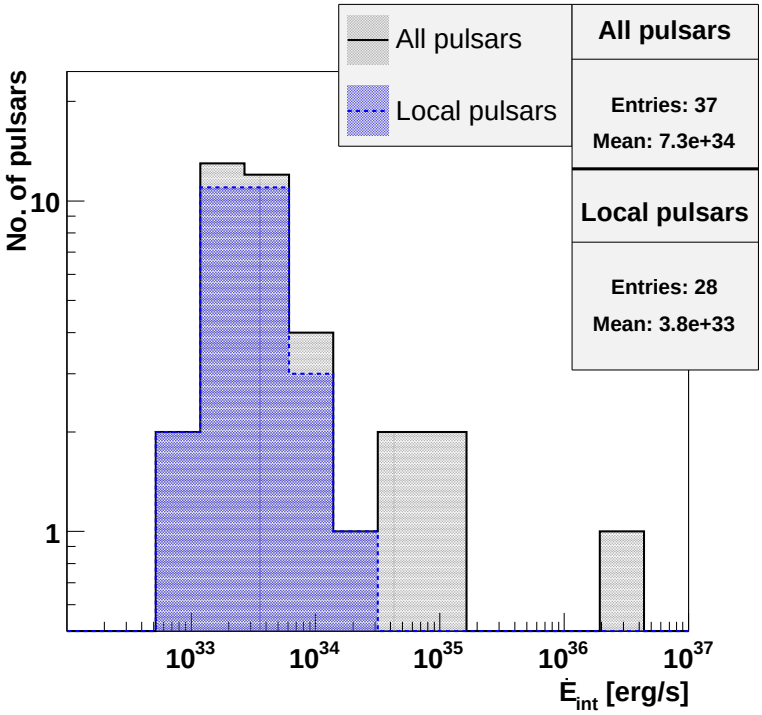

Figure 6.2: The distribution of the spin-down luminosity for pulsars having periods similar to those of M13. The pulsar power featured in this distribution has been determined using the 'intrinsic' spin-down rate (compensated for the proper motion of the pulsar), where available and non-negative. The distribution for all pulsars fulfilling these criteria is shown along with that of pulsars which are also closer than 2 kpc . The latter distribution (of local pulsars) is likely less biased than that including the most distant pulsars which may be visible only because they are exceptionally luminous. These data were retrieved from the ATNF Pulsar Catalogue [154] (available at http://www.atnf.csiro.au/research/pulsar/psrcat).

Pulsar population	Total	Spin-down range			$\bar{L}_{\text{s-d}}$ $[\times 10^{33}\,\text{erg s}^{-1}]$
		Limit	Rate $[\times 10^{-20}\,\text{s s}^{-1}]$	Power $[\times 10^{33}\,\text{erg s}^{-1}]$	
All	37	min	0.148	0.589	73
		max	162.0	2240.0	
Local	28	min	0.148	0.589	3.8
		max	2.35	20.8	

Table 6.2: Pulsar population statistics for pulsars with spin periods in the same range as those known in M13. Local pulsars are within 2 kpc .

of local pulsars (DB-LOCAL); or be equivalent to that estimated for 47 Tuc (47 TUC); or be derived from a database sample of all pulsars (DB-ALL) :

$$\langle \bar{L}_{\text{s-d}} \rangle \equiv \{\text{DB-LOCAL, 47 TUC, DB-ALL}\} \quad (6.21)$$
$$= \{3.8,\, 22,\, 73\} \times 10^{33}\,\text{erg s}^{-1} \quad (6.22)$$

The lowest of these estimates is likely the least biased but may not correspond well to the MSP population of a globular. It is notable that these values are all distinctly less than that assumed in B&S07.

6.1.3 Conversion Efficiency to Relativistic Electrons

The power taken up by electrons as they are accelerated above a pulsar polar cap, as a fraction of the spin-down power of the pulsar, has been calculated [164] to be 4–19 % for MSPs[21]. This estimate ignores the effects of pair production which can reduce the efficiency of the acceleration. B&S07 used this to motivate $\eta_{\pm} = 0.01$ and the MAGIC collaboration [24] used the same model to claim $\eta_{\pm} = 0.1$.

However, recent *Fermi* data [203] rule out the possibility of pair-starved polar cap emission, which had previously been assumed the correct model for MSPs. This may indicate that copious pair-production occurs over the poles of MSPs: such high pair-multiplicity[22], $\kappa_{\pm}$, is thought to set up the higher-altitude acceleration/emission gaps apparently necessary to satisfy these new

[21] This range is due to inclination between the magnetic moment and the rotation axis.
[22] The mean number of electron-positron pairs produced per primary electron accelerated from the pulsar's surface.

observations [203]. These slot-gap or outer-gap emission mechanisms (outlined in §2.1.3.2 and §2.1.3.3), and the attendant abundance of pair-plasma, were previously thought to be restricted to younger pulsars, having larger magnetic fields, but could be explained by distortion of a MSP's magnetic field [93, 34].

Regardless, in all these models, HE emission is considered as being curvature emission from electrons accelerated to a large, radiation-reaction limited Lorentz factor. Thus, observations of HE pulsed emission [4, 5] indicate that young pulsars and recycled pulsars share similar emission mechanisms and also represent strong evidence for the presence of TeV electrons within the magnetospheres of these pulsars.

However, the emission mechanism for globular clusters considered here (B&S07) requires that these electrons escape from the vicinity of a pulsar as a wind of plasma. How much of a pulsar's spin-down luminosity is delivered to TeV electrons *in the wind* depends upon the energy budget of the pulsar and the composition and energy-balance of the wind itself.

Energy budget. The, apparently un-biased, sample of eight nearby MSPs detected by Fermi [3] indicates that the pulsed emission (which is dominated energetically by HE gamma-rays [199]) accounts for between five and fifteen percent of the rotational energy losses of these objects. In particular, taking values for the efficiency of gamma-ray production from the First *Fermi*-LAT Pulsar Catalog [4], those four MSPs with accurate distances[23] and having error in the efficiency less than 100%, exhibit gamma-ray efficiencies ranging between 2 and 17% and with a mean of 9% of the spin-down luminosity.

Furthermore, the efficiency with which the pulsar population of 47 Tuc produces HE gamma rays has been estimated as less than $\sim$12% [6], assuming that the flux detected by *Fermi* is due solely to unresolved pulsed emission and that there may be more pulsars there than are currently known. Thus, the pulsed HE gamma-ray emission does not account for the majority of the rotational energy loss of a pulsar and the power that is not radiated directly by the pulsar in this fashion (in excess of ninety percent of the spin-down luminosity) must be carried away by the pulsar wind.

Composition of the pulsar wind. The relativistic wind which carries this power [184, 27] is, initially, a synergy of a tightly-wound, strong magnetic

[23] Determined via parallax measurements rather than relying on dispersion measure.

field and a plasma of ions, electrons and positrons. The wind carries energy both as an electromagnetic (Poynting) flux and as the kinetic energy of the particles. Near the pulsar, and its intense magnetic field, the wind is believed to be dominated by the magnetic flux such that the charged particles of the plasma are effectively prohibited from moving other than along a magnetic field line. This magnetic dominance can be quantified by the magnetisation parameter, σ, which is simply the ratio of the electromagnetic flux, $L_{\rm B}$, to the kinetic energy flux, $L_{\rm KE}$ [122, 27] :

$$\sigma = \frac{L_{\rm B}}{L_{\rm KE}} = \frac{B^2}{4\pi n \gamma^2 m_{\rm eff} c^2} \tag{6.23}$$

where $\gamma \gg 1$ is the bulk Lorentz factor of the relativistic wind n is the proper density[24] and $m_{eff} = m_{\rm ion} + m_{\rm e}(1 + 2\kappa_{\pm})$ is the effective mass-loading of the wind. Close to the star, the magnetic field, B, is sufficient that $\sigma \gg 1$ when the wind is 'launched' [130], despite the wind already being relativistic[25].

A consequence of this magnetic dominance is that the pulsar wind should be well described by ideal **MagnetoHydroDynamics** (MHD), a description which entails particle acceleration [47, 48, 59, 130].

Acceleration and magnetic dissipation. Support is leant to this picture in the case of the Crab pulsar by considering that the majority of electrons leaving a pulsar's inner magnetosphere should have Lorentz factors [105] of $\sim 10^2$ yet, to avoid suppression of the Crab's radio pulses by induced Compton scattering on its pulsar wind [211],the Lorentz factor of the wind must exceed 10^4 at a distance from the pulsar of 100 times the light-cylinder radius [130]. Presumably the bulk Lorentz factor has increased and this must be at the expense of the Poynting flux: σ must have decreased.

Furthermore, the properties of the wind at its termination shock, where it interacts with the nebula (see Figure 6.3), have been studied in detail [122, 123]: essentially, that the Crab Nebula exhibits powerful synchrotron emission, accounting for a large fraction of the PWN's energy budget [26],

[24] At the star this corresponds to the Goldreich-Julian charge density §2.1.2.

[25] Strong acceleration in a pulsar's magnetosphere ensures the existence of electrons with radiation-reaction limited Lorentz factors up to $\sim 10^7$ (as noted in §2.1.3) but the high-energy curvature emission from these particles, in the intense magnetic field, should support copious pair-production [93] which dominates the population with less energetic, though still relativistic, electrons [105]: the median Lorentz factor of pair-produced particles leaving a pulsar's inner magnetosphere is thought to be $\sim$200.

[26] 10–20 % of the spin-down luminosity [122].

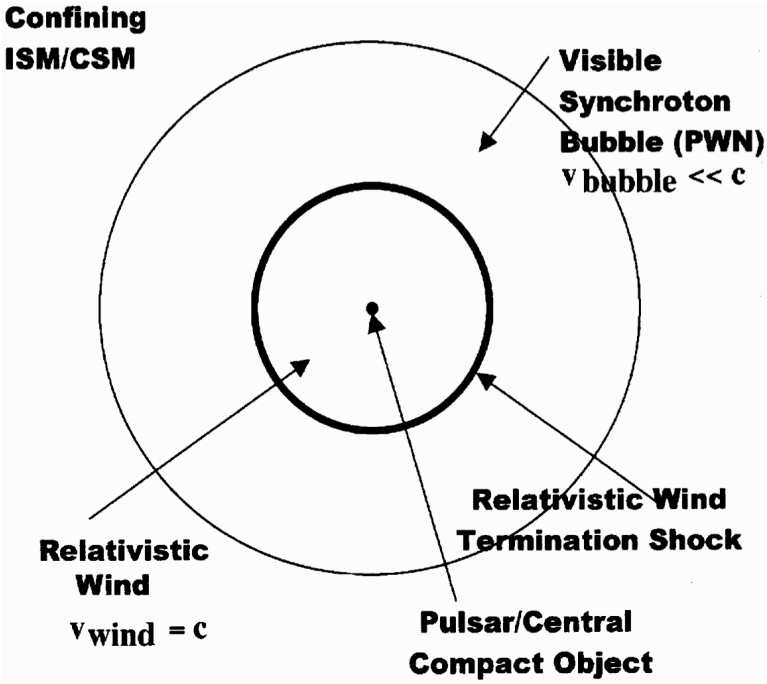

Figure 6.3: Schemtaic of a PWN. Image credit — Fig. 2 from [27].

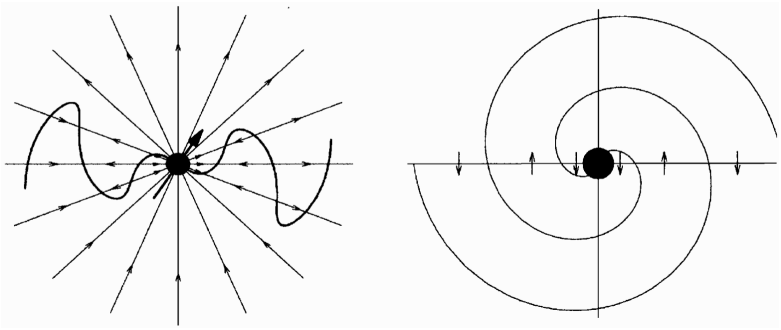

Figure 6.4: Schematic of the striped wind. On the left is the poloidal field structure (approximated asymptotically by a split monopole), demonstrating the undulating current sheet near the equator instigated by the periodic field reversals due to the rotation of the inclined dipole of the pulsar. On the right, an equatorial cross-section indicates the zones of alternating field direction, interleaved with the current sheet (spirals). Image credit — Fig. 5 of [27].

suggests that the wind power of the pulsar has been almost completely converted to kinetic energy by the point the wind's progress is checked by the shockfront and the flow rate of material from the wind is slowed to match its expansion into the surrounding interstellar medium. This study also determined the effective terminal wind Lorentz factor to be $\Gamma \sim 10^6$ [123] which seems to have become the canonical value for most subsequent pulsar wind studies [27].

More recently, it has been found [69, 133] that the detailed X-ray morphology of the Crab Nebula is well-described by MHD simulations only if the wind is kinetic-energy dominated ($\sigma \ll 1$). Between leaving the magnetosphere of the pulsar and colliding with the enclosing medium the electromagnetic energy carried by the wind has apparently been dissipated and transfered to the particles: this is sometimes termed the 'σ paradox' [129].

Some mechanism is required for this conversion of the wind from magnetic to kinetic-energy dominance but the intrinsic MHD acceleration mentioned above does not seem to be adequate, as it must cease before the magnetisation parameter becomes small [130]. The paradox is likely resolved by a peculiar trait of pulsar winds: that they are described by two asymptotically monopole magnetic hemispheres separated by an equatorial current sheet which is warped by spiral corrugations due to the inclination of the pulsar's magnetic moment [61, 130] (see Figure 6.4). Such a configuration

(a so-called **striped wind**) may result in the dissipation of these stripes, due to current instabilities acting between neighbouring ripples [131], and an associated transformation of magnetic flux into kinetic energy. Indeed, this mechanism may operate more effectively for MSPs than young pulsars [151]. Outside the equatorial plane other mechanisms may operate [152], but most of the energy in a pulsar wind is carried in the equatorial plane [130].

6.1.3.1 Conversion Efficiency via Energy Balance

If these mechanisms are indeed realised, the power transferred to relativistic electrons may be limited only by the energy budget of the pulsar wind. We may express the efficiency with which spin-down power is transferred to relativistic electrons, $\eta_{\pm} = L_{\pm}/L_{\text{s-d}}$, in terms of the fraction of lost rotational energy delivered to the pulsar wind, η_{W}, the fraction of that wind power carried by the kinetic energy of particles[27], η_{KE}, and the fraction of that kinetic energy carried by electrons, η_{e}; thus :

$$\eta_{\text{W}} = \frac{L_{\text{W}}}{L_{\text{s-d}}} \ , \quad \eta_{\text{KE}} = \frac{L_{\text{KE}}}{L_{\text{W}}} \text{ and } \quad \eta_{\text{e}} = \frac{L_{\pm}}{L_{\text{KE}}}$$
$$\therefore \eta_{\pm} = \eta_{\text{e}}\,\eta_{\text{KE}}\,\eta_{\text{W}}$$

We have already noted that the pulsar wind should carry all the power, L_{W}, that remains having accounted for directly emitted radiation (especially HE emission), $L_{\text{rad}} \simeq L_{\text{HE}}$, thus :

$$\eta_{\text{W}} = \frac{L_{\text{W}}}{L_{\text{s-d}}} \tag{6.24}$$
$$= 1 - \frac{L_{\text{HE}}}{L_{\text{s-d}}} \tag{6.25}$$

and $L_{\text{HE}}/L_{\text{s-d}} = 5\text{–}10\,\%$. Furthermore, as the wind power is divided between electromagnetic flux, L_{B}, and kinetic energy, L_{KE} :

$$L_{\text{W}} = L_{\text{B}} + L_{\text{KE}} \tag{6.26}$$
$$\frac{L_{\text{KE}}}{L_{\text{W}}} = \left[\frac{L_{\text{B}}}{L_{\text{KE}}} + 1\right]^{-1} \tag{6.27}$$
$$\eta_{\text{KE}} = \frac{1}{\sigma + 1} \tag{6.28}$$

[27] This should be the asymptotic value, far from the pulsar to correspond to the case of MSPs in globular clusters.

and the division of the kinetic energy between electrons and protons implies :

$$L_{\rm KE} = L_{\pm} + L_{\rm p} \tag{6.29}$$

$$\frac{L_{\pm}}{L_{\rm KE}} = \left[\frac{L_{\rm p}}{L_{\pm}} + 1\right]^{-1} \tag{6.30}$$

$$\eta_{\rm e} = \frac{U_{\pm}/U_{\rm ions}}{(U_{\pm}/U_{\rm ions}) + 1} \tag{6.31}$$

where $U_{\pm}$ and $U_{\rm ions}$ are the energy density of electrons and ions (protons) in the pulsar wind; their ratio is related to the relative abundance of the particle species[28] , $(1 + 2\kappa_{\pm})/1$, and the species' relativistic energies [28] :

$$\frac{U_{\pm}}{U_{\rm ions}} = (1 + 2\kappa_{\pm})\frac{\gamma_{\pm} m_{\rm e}}{\gamma_{\rm ions} m_{\rm p}} \tag{6.32}$$

$$= \frac{(1 + 2\kappa_{\pm})}{\varrho} \tag{6.33}$$

where in the last step we have assumed that all species in the wind move at the same bulk velocity ($\gamma_{\pm} = \gamma_{\rm ions} = \Gamma$) and $\varrho = m_{\rm p}/m_{\rm e} = 1.83 \times 10^3$. Thus, in terms of the wind composition :

$$\eta_{\pm} = 0.9 \times \frac{1}{\sigma + 1} \times \frac{1 + 2\kappa_{\pm}}{(2\kappa_{\pm} + 1) + \varrho} \tag{6.34}$$

$$\approx \frac{0.9}{(\sigma + 1)} \left(\frac{\kappa_{\pm}}{\kappa_{\pm} + 1000}\right) \tag{6.35}$$

where we have assumed $\kappa_{\pm} \gg 1$ which is reasonable given that pair-starved polar caps have been ruled out.

As mentioned above, the composition of the pulsar wind powering the Crab Nebula may be gleaned from the properties of the Nebula. Modelling of the synchrotron X-ray spectrum emitted by the Nebula can be most successfully modelled as being energised by an MHD shock terminating the pulsar wind [122, 123] if the wind has $\sigma \approx 0.003$ and $\kappa_{\pm} \approx 10^4$. More modern studies [69] incorporating the morphology require $\sigma \approx 0.02$ and $\kappa_{\pm} \approx 10^4$. Either way $\eta_{\pm}$ is about 80%. Given that young and recycled pulsars appear

[28] The number of primary electrons is equal to that of ions (protons) in order to keep the pulsar's surface neutral and is set by the so-called Goldreich-Julian current: the current required to maintain at least the Goldreich-Julian charge density.

to exhibit similar magnetospheric conditions[29] and that the description of a pulsar wind outlined above seems generic, we may accept this as a feasible estimate of the efficiency of conversion of spin-down luminosity to relativistic electrons.

Note, however, that much of the modelling work that has been carried out in relation to pulsar winds has been in the context of young pulsars and especially the Crab Pulsar and Nebula which form the prototypical PWN. This bias against recycled pulsars is related to young pulsars' intrinsic greater luminosity and more dense environments which afford much better opportunities for observation. Nonetheless, as noted in §2.1.1, there is direct evidence for relativistic pulsar winds from MSPs, such as the X-ray tail detected [193] in association with the luminous MSP PSR 1957+20. In fact, this object was re-examined in a study of non-pulsed, non-thermal X-ray emission around five MSPs [57]. It was concluded that in most cases this emission could be modelled as synchrotron radiation from the pulsars' winds terminating on the inter-stellar medium or close companions. To model the shock fronts they assumed the wind Lorentz factor to be $\Gamma \sim 10^6$ and equipartition between electrons and ions in the winds: for our purposes this would reduce Eq. 6.33 to $\frac{U_\pm}{U_{\rm ions}} = 1$ and so Eq. 6.35 becomes :

$$\eta_\pm = \frac{0.9}{\sigma + 1} 0.5 = \frac{0.45}{\sigma + 1} \tag{6.36}$$

For most of the sources examined, it was found that the model used was largely insensitive to σ, but for the specific case of PSR 1957+20 the model favoured $\sigma < 0.02$, implying that $\eta_\pm$ should be 45% or more for this MSP.

The above estimates are based on fairly specific assumptions, particularly concerning $\kappa_\pm$ and Γ, that must be made without concrete evidence. A more conservative approach considers just the pulsed emission which we can presume probes directly the population of energetic electrons for which a pulsar is directly responsible.

6.1.3.2 Minimal Conversion Efficiency via Radiation-Reaction Limited Luminosity

If magnetic dissipation is not, in fact, realised in the winds of MSPs or pulsar HE emission is constrained to high altitudes for reasons other than high

[29] In particular a modern pair-creation cascade model [93], based on a distorted magnetic field, implies that $\kappa_\pm$ may indeed be as large as 10^4.

multiplicity (e.g. emission from a return-current sheet beside the last open field line [29], [34]) HE gamma emission may trace the only acceleration of electrons in the vicinity of a MSP. In addition, the recent discovery of VHE emission from the Crab pulsar [205] (likely representing an inverse-Compton scattering component to the pulsed emission) may be regarded as additional evidence of TeV electrons at relatively high altitudes in pulsar magnetospheres. Assuming that these TeV electrons do indeed escape unfettered across the light cylinder they would represent the minimal contribution of the pulsar to a wind of TeV particles.

Pulsar models typically describe pulsed emission as being due to curvature radiation from electrons maintained at high energies ($\gamma \sim 10^7$) against radiation reaction [3]. This implies that the power carried by this population of particles should be less than the observed emission because, as a particle approaches its terminal energy, additional energy gain is lost to radiation, by definition.[30] So, radiation-reaction limited HE emission at $\sim$10% of the spin-down luminosity may indicate that up to 5% of the spin-down power is delivered to highly relativistic electrons regardless of the wind's characteristics.

6.1.3.3 Feasible Values of Conversion Efficiency

Though HE emission dominates the energy *radiated* by a pulsar, most of the spin-down power is released by some other mechanism. There is consensus that the bulk of a pulsar's spin-down luminosity goes into a relativistic plasma wind but much uncertainty surrounds the composition of this wind. I have found that reasonable arguments can justify values of the conversion efficiency of spin-down power to relativistic electrons across almost the entire range physically allowed. I have argued that MSP winds should be similar to those of young pulsars that power PWNe (Crab-PWN); or be similar to that of a local MSP that powers a PWN (MSP-PWN); or be populated by very-energetic particles sourced only from the magnetosphere of the pulsar (MSP-mag) :

$$\langle \eta_{\pm} \rangle \equiv \{\text{MSP-mag, MSP-PWN, Crab-PWN}\} \quad (6.37)$$

$$= \{0.05, 0.45, 0.80\} \quad (6.38)$$

[30] It would be a remarkable coincidence if it so happened that particles typically escaped the region that induces curvature radiation only shortly after attaining their maximum energy.

The lowest of these values is the most conservative, but is still by no means certain. The middle value has been estimated in relation to a study specifically targeting MSP winds but (as with the largest estimate) its validity rests on the assumption that MSP winds typically achieve a terminal Lorentz factor of 10^6: although standard practice, this remains to be proven.

6.2 Limits on Physical Parameters

We have inherited, from the analysis in the preceeding chapter (§5.4), an upper limit as a scale factor: $\tilde{f} = 0.26$. The models of Bednarek & Sitareck were constructed assuming $\bar{L}_{\text{s-d}} = 12 \times 10^{34} \text{erg s}^{-1}$, $N_{\text{P}} = 100$ and $\eta_{\pm} = 0.01$. Now we have estimates for each of these parameters: $\langle N_{\text{P}} \rangle$, $\langle \bar{L}_{\text{s-d}} \rangle$ and $\langle \eta_{\pm} \rangle$. Assigning two of these (*e.g.* $\langle \eta_{\pm} \rangle$ and $\langle N_{\text{P}} \rangle$) and leaving the other free allows us to hypothesise a model that matches the experimental limits :

$$\tilde{f} \bar{L}_{\text{s-d}} \eta_{\pm} N_{\text{P}} = \langle \bar{L}_{\text{s-d}} \rangle \underbrace{\langle \eta_{\pm} \rangle \langle N_{\text{P}} \rangle}_{\text{estimated}} \tag{6.39}$$

where the underbrace indicates that these quantities are a fixed estimate and the remaining parameter on the right-hand-side is free to allow equality. We can then invert this relation, effectively absorbing the scale factor into the original, assumed, value of the parameter of interest, to derive a limit on the free parameter (in this case $\langle L_{\text{s-d}} \rangle$) :

$$\langle \bar{L}_{\text{s-d}} \rangle = \tilde{f} \bar{L}_{\text{s-d}} \underbrace{\frac{\eta_{\pm} N_{\text{P}}}{\langle \eta_{\pm} \rangle \langle N_{\text{P}} \rangle}}_{\text{estimated}} \tag{6.40}$$

Below, I estimate each of the three parameters in turn, using all nine combinations of the other two. The results are presented in Table 6.3, Table 6.4 and Table 6.5. I will identify those combinations of parameters which lead to unphysical limits on the free parameter or limits that seem to contradict the estimated values of the free parameter as I have derived above. In this way I will establish which portions of the parameter space are mutually inconsistent.

6.2.1 Upper Limits on Pulsar Population

The pulsar population limits in Table 6.3 are widely varied. Nevertheless, the existing number of known pulsars rules out the possibility of efficient

$\langle L_{\text{s-d}} \rangle$ \ $\langle \eta_\pm \rangle$		MSP-MAG 0.05	MSP-PWN 0.45	CRAB-PWN 0.8
DB-LOCAL	3.8	164	18.2	10.3
47 TUC	22.	28.4	3.15	1.77
DB-ALL	73.	8.55	0.950	0.534

Table 6.3: Upper limits for pulsar population, given estimates for spin-down luminosity [10^{33} erg s^{-1}] and particle conversion efficiency. Recall that I have estimated that the pulsar population can feasibly be: {KNOWN, X-RAYUL, RADIOLDF} = {5, 11, 40}. The upper limit must be greater than five to be consistent with the known number of pulsars.

acceleration of electrons in pulsar winds to TeV energies if the pulsars of M13 have luminosities at least similar to those of 47 Tuc. On the other hand, unless pulsars in M13 have very low luminosities compared to those in 47 Tuc, they are less numerous than suggested by extrapolation of the radio luminosity distribution to the lowest limit (as suggested by observation of local pulsars).

6.2.2 Upper Limits on Mean Spin-Down Luminosity

$\langle \eta_\pm \rangle$ \ $\langle N_{\text{P}} \rangle$		KNOWN 5	X-RAYUL 11	RADIOLDF 40
MSP-MAG	0.05	125	56.7	15.6
MSP-PWN	0.45	13.9	6.30	1.73
CRAB-PWN	0.8	7.80	3.55	0.975

Table 6.4: Upper limits for mean spin-down luminosity [10^{33} erg s^{-1}], given estimates for particle conversion efficiency and pulsar population. Recall that I have estimated that the mean spin-down luminosity can feasibly be: {DB-LOCAL, 47 TUC, DB-ALL} = {3.8, 22, 73}$\times 10^{33}$ erg s^{-1} .

The mean spin-down luminosity in M13 is here constrained to be less than the value assumed in B&S07 for all but one of the combinations of other parameters of the model, as indicated in Table 6.4. Only in the case that there are no more pulsars in M13 than have been detected to date and that the efficiency with which those pulsars generate TeV electrons is consistent

with the minimal assumption that they correspond with models of pulsar gamma-ray emission can the spin-down luminosity assumed in B&S07 be accommodated. For the most part, these limits are compatible with the range of values I have estimated for MSPs (§6.1.2). However, if there remain more pulsars to be found in M13 (as would seem reasonable given the sensitivity-limited nature of radio surveys) we can infer that the acceleration of electrons in globular cluster pulsar winds is incompatible with M13 having pulsars with luminosities at least similar to those in 47 Tuc. In particular, the largest pulsar population (derived assuming similarity with the local population of MSPs) cannot coexist with acceleration of electrons in those pulsars' winds, unless the luminosities of pulsars in M13 are actually less than those of the local MSPs.

6.2.3 Upper Limits on Conversion Efficiency

$\langle L_{\text{s-d}} \rangle$ \ $\langle N_{\text{P}} \rangle$		KNOWN	X-RAYUL	RADIOLDF
		5	11	40
DB-LOCAL	3.8	1.64	0.746	0.205
47 TUC	22.	0.284	0.129	0.0355
DB-ALL	73.	0.0855	0.0389	0.0107

Table 6.5: Upper limits for the particle conversion efficiency, given estimates for spin-down luminosity [10^{33} erg s^{-1}] and pulsar population. Recall that I have estimated that the particle conversion efficiency can feasibly be: {MSP-MAG, MSP-PWN, CRAB-PWN} = {0.05, 0.45, 0.80}. As efficiency cannot exceed 100% (except in professional sports) an upper limit in excess of 1 provides no physical constraint.

The conversion efficiency limits in Table 6.5 have a wide range but most are below the maximum possible according to the pulsar wind's energy budget ($\sim$90% of the spin-down luminosity). Note that all efficiency upper limits are in excess of 1%, which was the value assumed to derive emission curves in B&S07: *i.e.* by using realistic estimates of the spin-down luminosity and pulsar population, the model presented in B&S07 is rendered entirely consistent with these observations.

On the other hand, in light of the discussion presented above concerning models of pulsar winds, I can set interesting limits under certain self-consistent conditions. If the pulsars in M13 have luminosities at least similar

to those in 47 Tuc, we can infer that the acceleration of electrons in globular cluster pulsar winds occurs with much less efficiency than might be expected from studies of nearby pulsar wind nebulae, especially if there are more pulsars yet to be discovered (as is likely the case in most globular clusters). Similarly, if the pulsars in M13 are like local MSPs (being part of a distribution that extends to low spin-down and radio luminosities), we may again conclude that electrons are accelerated in pulsar winds to TeV energies with much less efficiency than is typically assumed.

6.2.4 Discussion of Limits to Physical Parameters

If we make reasonable assumptions concerning MSPs in M13 (*i.e.* that they are fairly luminous, like those of 47 Tuc, or they are less luminous but numerous, like local MSPs) the observational limits contradict the assumption of efficient acceleration of electrons to TeV energies in pulsar winds. The converse is that to support the idea that electrons are accelerated in the winds of MSPs in M13 requires us to assume that those pulsars are unusually few or unusually dim.

It may be that confinement of the wind by the interstellar medium is a necessary spur for magnetic dissipation [153, 189] whereas the sparse gas in the cores of globulars [77] offers little resistance to a streaming pulsar wind.

It is also quite possible that the terminal energies of electrons, having evolved through the pulsar wind, are not in the TeV range. Recall that in the wind models examined above, the canonical terminal wind Lorentz factor of $\gamma \sim 10^6$ was assumed. However, considering the lower initial magnetisation that the winds of MSPs must have, when compared to those of young pulsars, and the recent evidence for large multiplicities in MSP magnetospheres, which may dilute the energy available in the wind, a diminished Lorentz factor does not seem implausible.

6.3 Limits on the VHE Emission Efficiency of the Pulsar Population of M13

For completeness sake, I will here derive upper limits on the VHE gamma-ray emission efficiency, $\eta_{\rm VHE} = L_{\rm VHE}/L_{\rm s\text{-}d}$ of the pulsar population of M13. Again, I will have to assume the feasible values of the number of pulsars and mean spin-down luminosity derived above; the product of these provides

the total luminosity of the pulsar population, $L_{\text{s-d}} = N_{\text{P}} \bar{L}_{\text{s-d}}$. The upper limit on the VHE gamma-ray luminosity, L_{VHE}, of M13 will be constructed from the integral flux upper limit derived in §5.3.2.2. For a flux of gamma rays, $F(\epsilon) = \frac{\mathrm{d}N}{\mathrm{d}\epsilon\ \mathrm{d}A\ \mathrm{d}t} = F_0(\epsilon/\epsilon_0)^{-\delta}$, the luminosity of the source, located at a distance, d, in an energy range between ϵ_{min} and ϵ_{max}, is given by:

$$L_{\text{min–max}} = 4\pi d^2 \int_{\epsilon_{\text{min}}}^{\epsilon_{\text{max}}} \epsilon F(\epsilon)\, \mathrm{d}\epsilon \tag{6.41}$$

$$= 4\pi d^2 F_0 \int_{\epsilon_{\text{min}}}^{\epsilon_{\text{max}}} \epsilon \left(\frac{\epsilon}{\epsilon_0}\right)^{-\delta} \mathrm{d}\epsilon \tag{6.42}$$

For consistency with [101] (which lists the VHE-efficiencies of seventeen PWNe), I will use the energy range 1–10 TeV, thus $L_{\text{VHE}} \equiv L_{1\text{–}10}$. and $\eta_{\text{VHE}} \equiv \eta_{1\text{–}10} = L_{1\text{–}10}/L_{\text{s-d}}$.

In particular, for the nominal spectral index of 2.6 adopted in §5.3.2.2 $L_{1\text{–}10} = 4.1 \times 10^{33}\,\text{erg s}^{-1}$ but this result is dependent upon the spectral index: for the extreme values considered in §5.3.2.2, index 2.0 (3.2) corresponds to $5.5 \times 10^{33}\,\text{erg s}^{-1}$ ($3.1 \times 10^{33}\,\text{erg s}^{-1}$). For all these cases the distance to M13 is taken to be 7.1 kpc . Using the nominal spectral index, Table 6.6 displays the efficiency of spin-down power to VHE emission for each combination of estimated $\bar{L}_{\text{s-d}}$ and N_{P}. These are all compatible with the range of VHE efficiencies of individual PWNe calculated in [101], namely 0.01–1 % (for objects with well-defined[31] distance estimates).

In comparison, H.E.S.S. set an upper limit for this quantity of 3.0 % in the context of observations of 47 Tuc, using an assumed spectral index of 2.0 and only the population of known pulsars [17]. Assuming the pulsars of M13 have similar mean spin-down luminosity to those of 47 Tuc (and likewise using an assumed spectral index of 2.0 and only the population of known pulsars) I derive an upper limit of 5.0 % which is compatible.

[31] Not dependent upon dispersion measure.

$\langle L_{\text{s-d}} \rangle$ \ $\langle N_{\text{P}} \rangle$		KNOWN	X-RAYUL	RADIOLDF
		5	11	40
DB-LOCAL	3.8	22.	9.9	2.7
47 TUC	22.	3.7	1.7	0.47
DB-ALL	73.	1.1	0.51	0.14

Table 6.6: Upper limits for VHE (1–10 TeV) emission efficiency [%] given estimates for spin-down luminosity [10^{33} erg s^{-1}] and pulsar population. The upper limit on VHE luminosity used here was calculated from the decorrelated integral flux upper limit assuming a spectral index of 2.6. The VHE emission efficiency for individual PWNe seems to lie in the range 0.008–5 % , as determined in [101], though the distances to the majority of these PWNe were estimated only from dispersion measure.

6.4 Conclusions

I have analysed data acquired during observations of the globular cluster M13 with VERITAS, an instrument sensitive to VHE gamma rays. No evidence for a flux of VHE gamma rays was found and rigorously derived upper limits on this flux, within the sensitive range of this instrument, were calculated. The observational upper limits were used to confront emission curves predicted for this object in B&S07, which were calculated according to a model concerning highly relativistic winds of electrons powered by a large population of MSPs. I found, through a discussion of pertinent literature and my own derivations, that the original implementation of this model was over-optimistic in terms of the number and power of pulsars present within this globular cluster. Nonetheless, through attempting to relate this model to existing literature pertaining to pulsar winds, I have been able to exclude efficient acceleration of electrons to TeV energies in the pulsar wind itself (*outside* pulsar light-cylinders); this is under the condition that the pulsars of M13 are either like the pulsars of other globular clusters (fairly powerful) or self-consistently like local MSPs (not so powerful, but plentiful). In addition I estimated upper limits on the efficiency with which VHE gamma rays are produced by the pulsar population of M13. These were found to be compatible with the known range of such efficiencies found in PWNe in the Galactic Plane.

Part IV

Appendicies

Appendix A

Globular Cluster Properties

Name		RA	Dec.	R_{GC}	[Fe/H]	ISC	M_V
NGC#	Other			[kpc]			
6205	M13	16 41 41.24	36 27 35.5	8.4	-1.53	F6	-8.55
7078	M15	21 29 58.33	12 10 01.2	10.4	-2.37	F3/4	-9.19
104	47 Tuc	00 24 05.67	-72 04 52.6	7.4	-0.72	G4	-9.42
-	Ter 5	17 48 04.80	-24 46 45	1.2	-0.23	-	-7.42
6342	-	17 21 10.08	-19 35 14.7	1.7	-0.55	G3/4	-6.42
6440	-	17 48 52.70	-20 21 36.9	1.3	-0.36	G4	-8.75
6624	-	18 23 40.51	-30 21 39.7	1.2	-0.44	G4/5	-7.49

Table A.1: Properties of globular clusters mentioned in this thesis. RA and Dec. are J2000 values. R_{GC} is the distance from the Galactic Centre. [Fe/H] is the metallicity. ISC is the Integrated Spectral Class of all light from the cluster. M_V is the absolute visual magnitude. These values are reproduced from the catalogue due to Harris [95] (2010 edition).

Name		$R_{\rm Sol}$	$r_{\rm c}$	$r_{\rm h}$	c	$\mu_{\rm V}$	ρ_0	# PSR
NGC#	Other	[kpc]	[pc]	[pc]			$\log([L_\odot/{\rm pc}^3])$	
6205	M13	7.1	1.28	6.09	1.53	16.59	3.55	5
7078	M15	10.4	0.42	4.83	2.29	14.21	5.05	8
104	47 Tuc	4.5	0.47	4.17	2.07	14.38	4.88	23
-	Ter 5	6.9	0.32	1.69	1.62	21.08	5.14	34
6342	-	8.5	0.12	1.80	2.5	16.97	4.97	1
6440	-	8.5	0.35	1.82	1.62	17.06	5.24	6
6624	-	7.9	0.14	2.00	2.5	15.32	5.3	6

Table A.2: Properties of globular clusters mentioned in this thesis. $c = \log(r_{\rm t}/r_{\rm c})$ is the King-model concentration where $r_{\rm t}$ is the tidal radius. $\mu_{\rm V}$ is the central surface brightness in visual magnitudes per square-arcsecond. ρ_0 is the logarithm of the central luminosity density. These values are reproduced from the catalogue due to Harris [95] (2010 edition) with the following exceptions: the core radius, $r_{\rm c}$, has been computed from the angular radius and distance given in the Harris catalogue; the half-mass radius has been computed as $r_{\rm h} = \sqrt{2 r_{\rm c} r_{\rm t}/3}$ according to the relation stated in B&S07; the number of known pulsars, # PSR, is the total of those listed by Friere at http://www.naic.edu/~pfreire/GCpsr.html.

Appendix B

VHE Emission due to a Young Pulsar Associated with Terzan 5

Detailed stellar evolution modelling, with stellar populations comparable to the content of globulars and taking into account stellar dynamics/interactions in the dense environments which typify these clusters, indicates that an object like Terzan 5, having a very compact core, should currently produce young (i.e. non-recycled) pulsars at the rate of $20-40\ \mathrm{Gyr}^{-1}$ [116] via electron-capture supernovae in O-Ne-Mg white dwarfs that have accreted matter from a companion acquired during exchange interactions. This is in line with observations of other globular clusters: up to four young pulsars may be associated with up to three globular clusters, namely NGC 6624, 6440 and 6342 [46], which all have large metallicities ([Fe/H] $\gtrsim -0.55$) and large central densities ($\rho_0 \gtrsim 10^5\,\mathrm{L}_\odot\ \mathrm{pc}^{-3}$).[1] I note here that Terzan 5 has a greater metallicity (-0.23, third-largest of all Galactic globulars) and a comparable central density ($1.4 \times 10^5\,\mathrm{L}_\odot\ \mathrm{pc}^{-3}$) with respect to these three clusters.

In addition, the same simulations (amongst others, *e.g.* [139]) indicate that many of the pulsars born in a typical globular are ejected from the cluster and that an object like Terzan 5 will retain little more than half. Pulsars are shed in this way because their births, in supernovae, tend to impart a large

[1] The association of a young pulsar in a close binary system with NGC 6342 is uncertain, partly because its position would be in the outskirts of the cluster.

velocity [108], a **natal kick**, which can be sufficient to exceed the escape velocity of the cluster. A recent statistical study of the measured proper motions of 233 pulsars [108] indicates that the distribution of transverse velocities of these objects has a mean of $\sim 211\,\mathrm{km\ s^{-1}}$ and extends up to $\sim 1600\,\mathrm{km\ s^{-1}}$; in comparison, the estimated escape velocity from the core of Terzan 5 is $49.4\,\mathrm{km\ s^{-1}}$ [206]. In fact this distribution is likely composed entirely of pulsars created in core-collapse supernovae instead of the less-powerful ECSe [132] which must be the source of young pulsars in globulars. For this reason, the afore-mentioned simulations [116] adopted natal kicks for ECSe one-tenth of those for core-collapse supernovae; I note here that this led to a retention of neutron stars in excess of observations and that [132] claimed compatibility between the results of their simulations and observations of the Crab SNR, the pulsar of which has a transverse velocity of $140\,\mathrm{km\ s^{-1}}$ [108].

Thus, it is a distinct possibility that a young pulsar may have been created recently within Terzan 5 but was promptly ejected with a transverse velocity of $\sim 100\,\mathrm{km\ s^{-1}}$. Here I entertain the possibility that the VHE emission observed from the direction of Terzan 5 is due to such a pulsar which has encountered the dense ISM near the galactic core and formed a powerful PWN. Thus the pulsar is associated with Terzan 5 but is not bound to it. This may alleviate the difficulty of an unassociated young pulsar being accidentally superimposed upon Terzan 5 (demonstrated in [100] to have a probability of chance coincidence of only $\sim 10^{-4}$) while simultaneously allowing for the offset in the emission maximum relative to the core of Terzan 5.

There are previous instances of PWNe having been discovered as TeV sources before the identification of the pulsar itself. For example, the first unidentified TeV source was found by HEGRA (TeV J2032+4130) [13, 14] and could not be identified through X-ray observations [49], but it was later associated with a *Fermi*-detected pulsar (PSR J2032+4127) [2] which itself was finally detected in the radio and characterized as the power source of the TeV object [52]. Also, an extended Milagro source (MGRO J1908+06) [11], confirmed by H.E.S.S. (HESS J1908+063) [16], was later revealed to contain a radio-quiet gamma-ray pulsar (PSR J1907+0602) [8].

Age and luminosity. If we consider this hypothetical young pulsar to have been created in the core of Terzan 5 with a transverse velocity of $v_{\mathrm{T}} \simeq 100\,\mathrm{km\ s^{-1}}$, we may estimate its age by its current position. Assuming the

pulsar is near the centroid of the TeV emission[2], which is offset from the centre of Terzan 5 by $\delta = 4'.0$, at the distance[3] of Terzan 5, $d = 5.9\,\mathrm{kpc}$, it must have travelled some $\delta d = 6.9\,\mathrm{pc} = 2.1 \times 10^{14}\,\mathrm{km}$. Thus the age of the pulsar is given by $\delta d / v_{\mathrm{T}} = 6.7 \times 10^3$ years. Given that Terzan 5 may be expected to generate pulsars of this sort at the rate of 20–40 Gyr^{-1}, the probability of one no older than this existing may be estimated as the product of this age and the rate, yielding $1\text{–}2 \times 10^{-4}$. Thus this object is no less probable than the chance coincidence of a PWN associated with the galactic plane.

The H.E.S.S. detection of Terzan 5 identifies a power-law spectrum from the source with index 2.5 and normalization at 1 TeV of $5.2 \times 10^{-13}\,\mathrm{cm}^{-2}\ \mathrm{s}^{-1}\ \mathrm{TeV}^{-1}$. This result corresponds to a VHE gamma-ray luminosity (in the range 1–10 TeV) of $4.7 \times 10^{33}\,\mathrm{erg\,s}^{-1}$. The efficiency with which H.E.S.S.-detected PWNe convert pulsar spin-down power to VHE gamma rays has been summarised to be in the range 0.08–5 % [101]. Thus I can claim that the spin-down luminosity of this hypothetical pulsar should be in the range $0.095\text{–}5.9 \times 10^{36}\,\mathrm{erg\ s}^{-1}$.

Period and spin-down rate. The characteristic age of a pulsar, τ_c, assumes that the spin-down rate, $\dot{P}$, is proportional to the rotation rate, $1/P$, and that the pulsar's period, P, is initially very small, compared to its present value :

$$\tau_c = \frac{P}{2\dot{P}} \quad . \tag{B.1}$$

In addition, the characteristic spin-down luminosity of a pulsar, $\dot{E}$, is related to its period and spin-down rate with an assumption of the moment of inertia [147], $I \simeq 10^{45}\,\mathrm{g\,cm}^2$:

$$\dot{E} = -4\pi^2 I \frac{\dot{P}}{P^3} \quad . \tag{B.2}$$

Insofar as these assumptions are valid and the characteristic values are representative of actual physical properties, I may set the age estimate from the travel time of the pulsar equal to the characteristic age and the spin-down

[2] Generally the TeV component of a PWN is offset from the powering pulsar's position; it is not understood if this is due to the pulsar drifting away from a cocoon of energetic electrons emitted soon after its birth (here implying a faster or older pulsar), or the pulsar wind impinging upon an asymmetric medium (here implying a slower or younger pulsar). In any case, the offset of the pulsar from the cluster core would presumably be of the same order as that of the nebula.

[3] The value used here is that quoted in the H.E.S.S. paper, due to [74].

luminosity, estimated from the gamma-ray flux, equal to the characteristic spin-down luminosity. I can then solve these two equations to arrive at estimates of the period and period derivative.

$$P = \pi\sqrt{I}\sqrt{\frac{2\tau_c}{\tau_c^2 \dot{E}}} \tag{B.3}$$

$$\dot{P} = \pi\sqrt{I}\sqrt{\frac{1/(2\tau_c)}{\tau_c^2 \dot{E}}} \tag{B.4}$$

The resulting values are indicated in Table B.1 and the general region of the P-$\dot{P}$ plane implied is indicated in Figure B.1.

τ_c	$\dot{E}$		P	$\dot{P}$
[kyr]	[$\times 10^{36}$ erg s^{-1}]		[s]	[$\times 10^{-15}$ s s^{-1}]
6.7	min	0.095	0.31	0.74
	max	5.9	0.040	9.4

Table B.1: Estimated properties of a hypothetical pulsar powering VHE gamma-ray emission near Terzan 5.

The estimated pulsar properties are quite feasible, especially for the smaller spin-down luminosities, *i.e.* for larger assumed VHE efficiencies (a smaller spin-down loss is required to account for the same measured gamma-ray luminosity). This tallies with the estimated age of the pulsar given that PWN VHE efficiency seems to increase with age.[4] At the very least, that the estimated age and spin-down luminosity of this hypothetical pulsar can correspond to a feasible set of pulsar characteristics is an intriguing coincidence.

[4] Dividing the sample of seventeen PWNe which may be associated with H.E.S.S. sources and are listed in [101] into roughly equal halves, according to characteristic age, nine have $\tau_c \leq 16\,\mathrm{kyr}$ and eight have $\tau_c > 16\,\mathrm{kyr}$ (the youngest of these has $\tau_c = 21\,\mathrm{kyr}$). The mean VHE efficiency of the younger portion is 0.9% whereas that of the older portion is 1.9%.

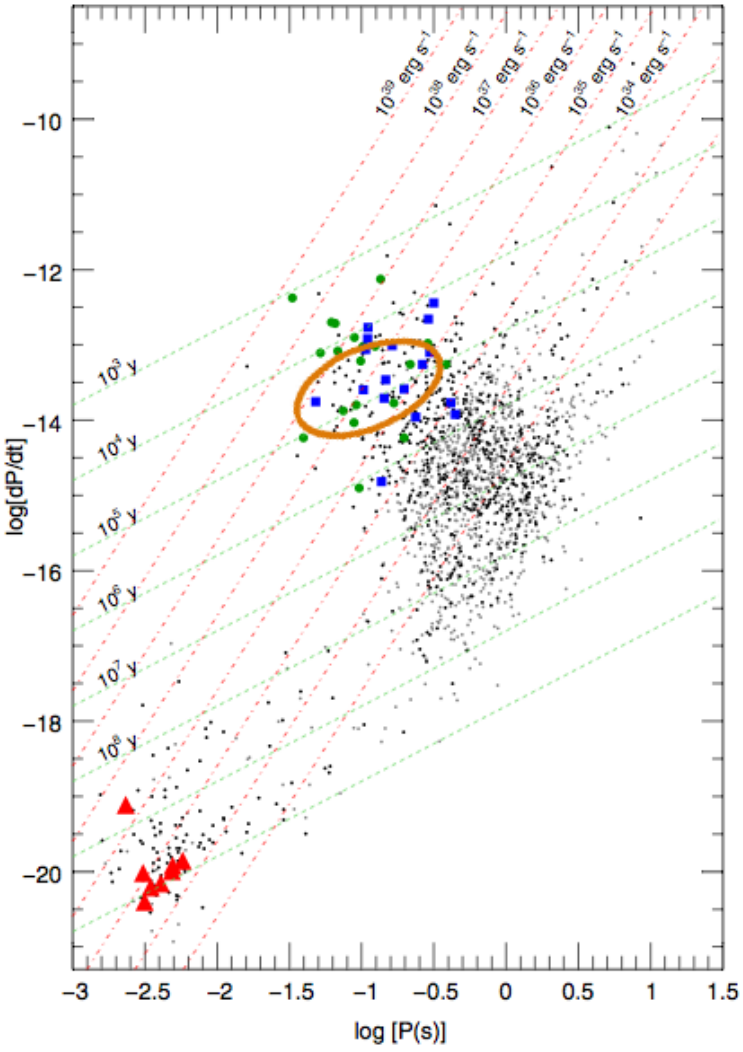

Figure B.1: The P-$\dot{P}$ diagram from the First *Fermi* Pulsar Catalog with the approximate region indicated (orange ellipse) where a hypothetical young pulsar powering VHE emission near Terzan 5 would be situated. Image credit — adapted from Fig. 2 of [4].

Appendix C

Comparison of Integral Upper Limits to Non-Power-Law Modelled Flux

To compare an integral upper limit, based upon the assumption of a source spectrum with a fixed power-law index, with a modelled spectrum, that generally does not obey that assumption, there are essentially two possible paths. Firstly, one could try to equate the total flux from the derived upper-limit power-law spectrum with that of the modelled spectrum. Secondly one could use the upper-limit flux normalisation at a particular spectral point as a direct comparison to the modelled flux-level at that point. Both are frustrated by the assumptions made in deriving the integral flux upper limit.

Total flux. Given a power-law above a certain threshold and up to a limiting energy, one might wish to claim that it approximates an arbitrary model if the total flux of gamma rays in that energy range from power-law and model are equal. However, an upper limit calculation is based upon an excess count rate (or lack thereof), so to properly compare the two curves it may be necessary to account for variation of the effective area: the model curve and the power-law do not necessarily yield the same count rate because the energy distribution of photons is (by construction) different between the two and, thus, the mean effective area per photon may differ.

To estimate the scale of uncertainty, I took a typical power-law spectrum (red curve in plots: index 2.5; 0.219–30 TeV; normalisation $1.37 \times 10^{-8}\,\mathrm{m}^{-2}\ \mathrm{s}^{-1}\ \mathrm{TeV}^{-1}$ at the decorrelated spectral point, 0.464 TeV) as an example and compared

it to each of the M13 models (blue curves). Several examples are shown in Figures C.1, C.2, C.3 and C.4. I scaled the model curve to give the same integral flux as the power-law within the latter's range (the resulting curve is the green one). I then multiplied the scaled model curve and the power-law by an example effective area function (each resulting function is a dotted line) and integrated across the energy range to give a count rate. The ratio of the count rate from the power-law to that from the model curve I termed the 'correction factor': the scaled model curve would need to be multiplied by this factor to recover the count rate implied by the integral upper limit. The correction always requires that the model be scaled upwards and ranges from a few percent to almost thirty percent.

It should be noted, that the count rate for the model has been calculated using an effective area curve that was not derived assuming that spectrum, so these 'correction' factors only indicate the range of uncertainty in scaling the model to the power-law and don't allow accurate reconstruction of the count rate (upper limit) due to a given model.

Spectral point. The scale of an integral flux may be stated as the flux normalisation at a particular normalisation energy. If one examines the integral upper limit shown in Figure 5.15 it is readily apparent that, for a range of spectral indicies, there is a particular energy (near 1.5 TeV in that case) at which the flux normalisation is insensitive to the assumed spectral index. This is another approach to constructing a decorrelated integral flux upper limit and yields a decorrelated spectral point at this 'special' normalisation energy which may be termed the **decorrelation energy**. To be clear, this differential flux limit at the decorrelation energy is a point on a power-law function that describes an integral upper limit. Thus it remains sensitive to assumptions about the spectral shape (beyond a simple power law) across the range covered by the integral upper limit.

If the goal is to compare this single spectral point to the level of an emission curve at the same energy it is worthwhile to estimate how much error is introduced for an actual flux that provides the same flux of gamma rays as implied by the integral upper limit. To this end, I also calculated the relative error of the differential flux point at the decorrelation energy between the flux-scaled model curve and the power-law: This can be large ($\sim$ 20%) and depends critically upon the relative slope of the model curve and power-law near the decorrelation energy.

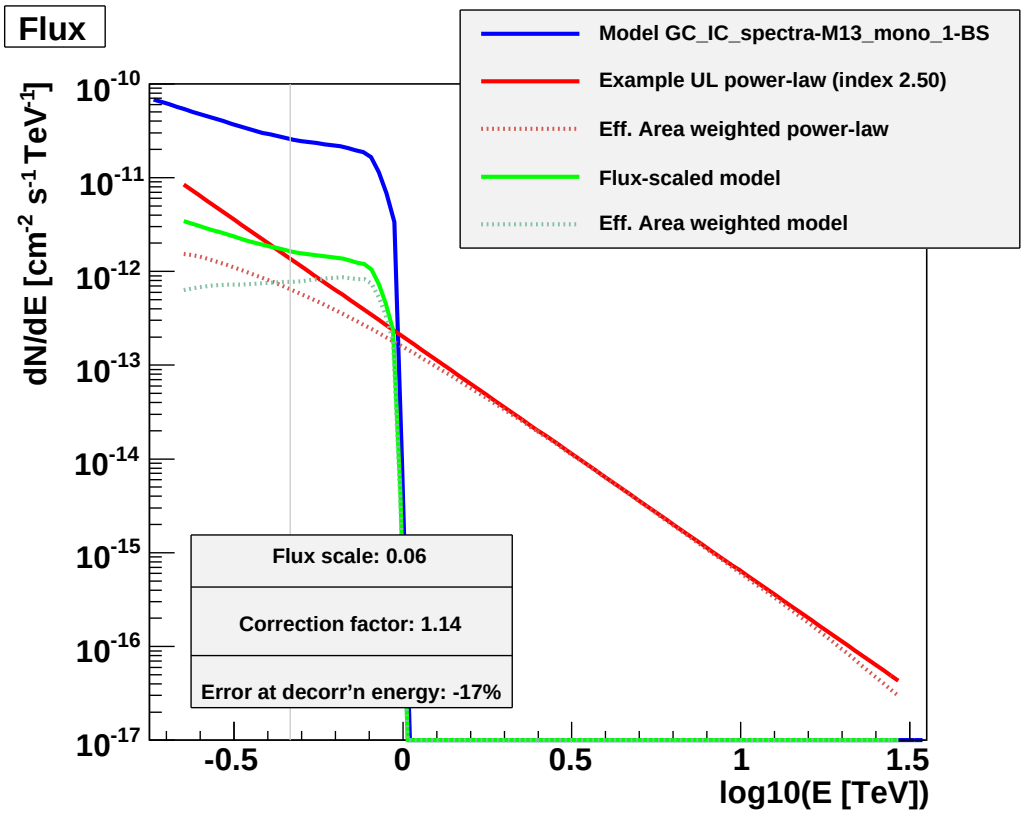

Figure C.1: Example integral upper limit scaling to the emission curve for a globular cluster injection spectrum of mono-energetic (1 TeV) electrons.

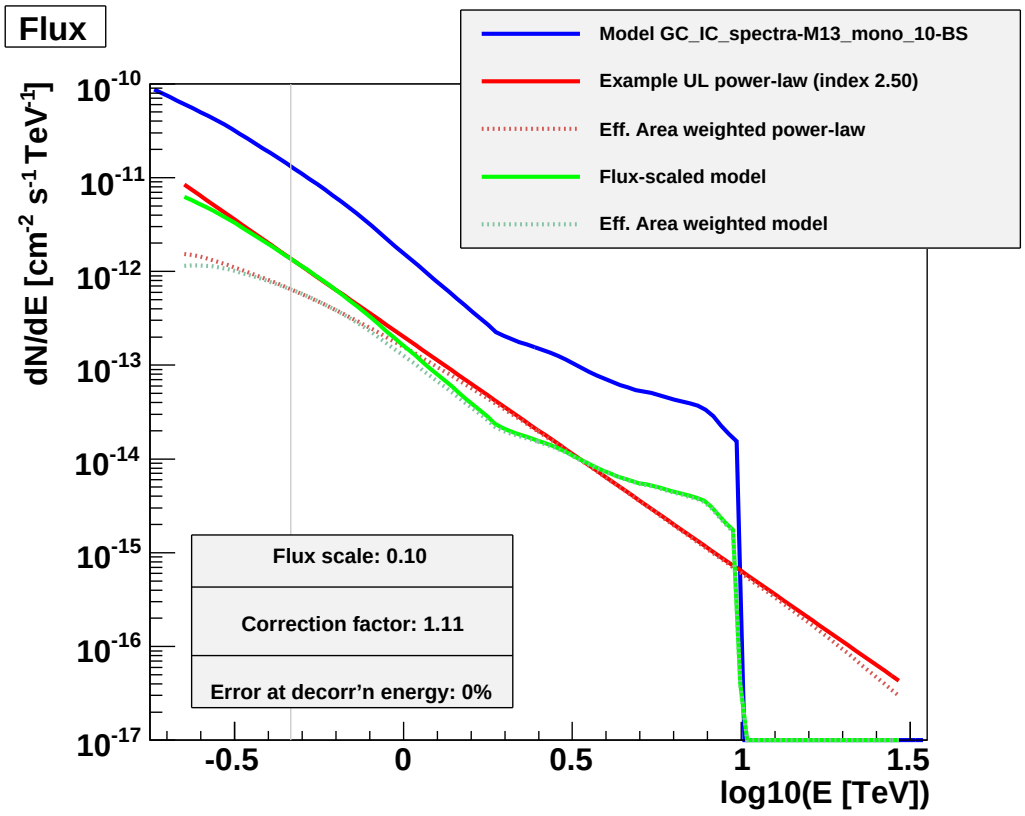

Figure C.2: Example integral upper limit scaling to the emission curve for a globular cluster injection spectrum of mono-energetic (10 TeV) electrons.

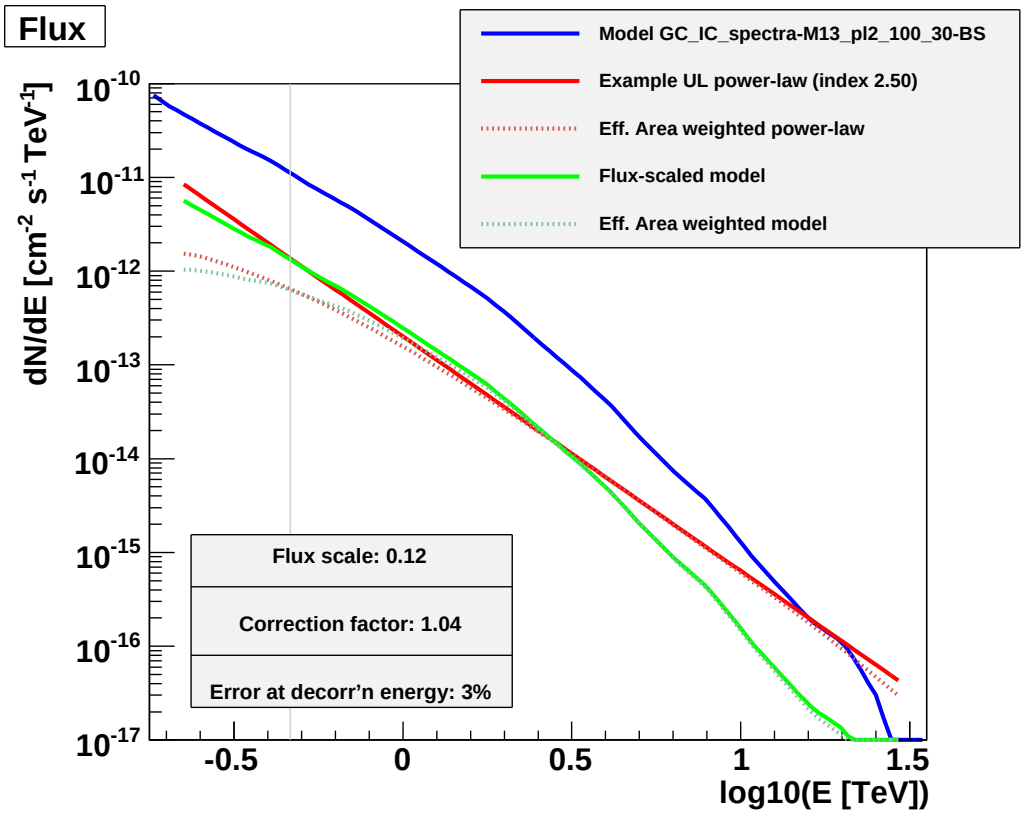

Figure C.3: Example integral upper limit scaling to the emission curve for a globular cluster injection spectrum of power-law distributed (0.1–30 TeV , index 2.1) electrons.

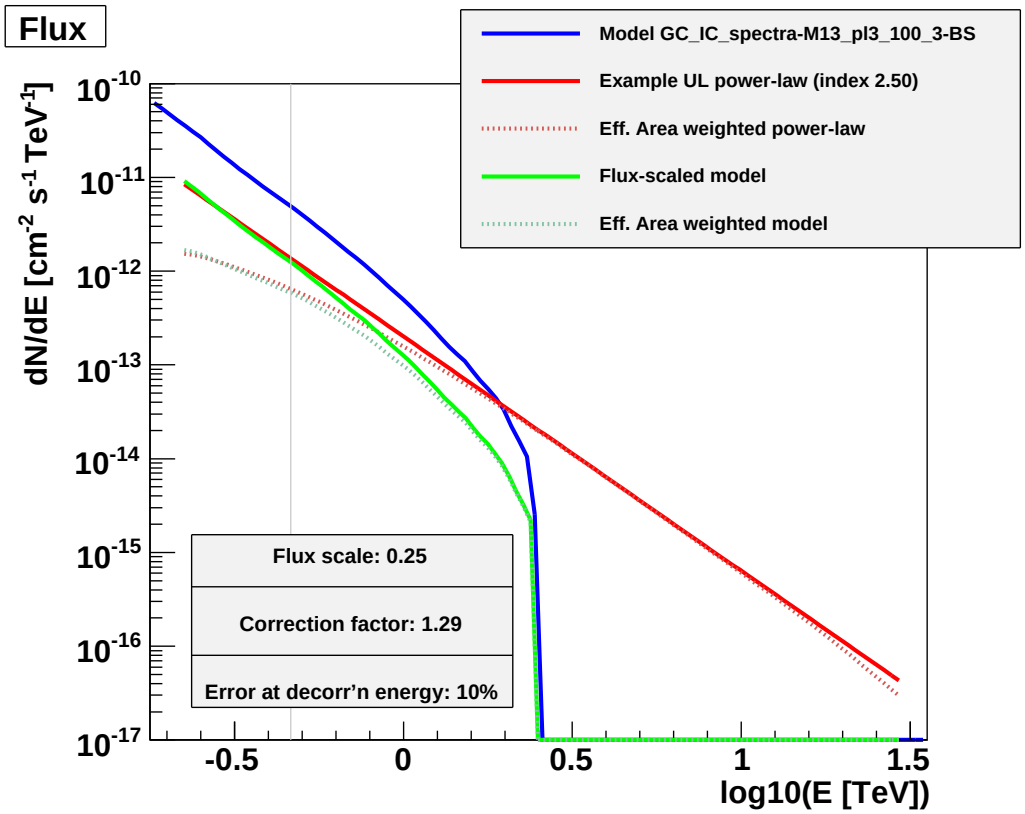

Figure C.4: Example integral upper limit scaling to the emission curve for a globular cluster injection spectrum of power-law distributed (0.1–3 TeV , index 3.0) electrons.

Summary. The correction factor for the integral upper limit and the relative error of the decorrelated spectral point are minimised when the model curve's slope and energy range are similar to the power-law's. This suggests that uncertainties in the comparison of these curves may be kept under control if integral upper limits are derived that have been deliberately tailored in both range and spectral index to approximate each of the model curves individually. However, this somewhat defeats one of the primary goals of constructing an integral upper limit, namely its generality.

Appendix D

Glossary of Acronyms

ACT Atmospheric Cherenkov. Relating to the emission of Cherenkov radiation by the Earth's atmosphere.

ACT Atmospheric Cherenkov Telescope. A telescope system designed to detect and reconstruct EASs by gathering the photons they emit *via* Cherenkov radiation.

AGN Active Galactic Nucleus. The luminous core of a galaxy powered by active accretion of matter onto the super-massive black hole at its centre.

ATNF Australia Telescope National Facility. The umbrella organisation that coordinates Australia's radio observatories for the national government body for scientific research in Australia. It maintains a database of the properties of known pulsars.

CANGAROO Collaboration between Australia and Nippon for a Gamma Ray Observatory in the Outback. An imaging ACT array which operated in southern Australia between 2004 and 2010.

Chandra A very successful X-ray observatory which was launched in 1999 and remains operational. It has the best angular resolution of any astronomical X-ray instrument.

CGRO Compton Gamma-Ray Observatory. A large satellite which operated from 1991–2000 and carried EGRET, a pair-production telescope. The predecessor to GLAST.

CMB Cosmic Microwave Background.[1] The strongly red-shifted relic photons from the surface of last-scattering, when the Universe first became transparent.

CV Cataclysmic Variable. A binary system containing a white dwarf and a normal (*i.e.* thermonuclear-powered) star. The system is powered by accretion onto the white dwarf upon whose surface hydrogen accumulates and is heated until a cataclysmic outburst of thermonuclear fusion occurs.

EAS Extensive Air Shower. The shower of particles initiated by the impact of a very energetic particle upon the upper atmosphere. Such particles are mostly charged cosmic rays, which themselves are mostly protons (hydrogen nuclei).

EGRET Energetic Gamma-Ray Experiment Telescope. See CGRO.

FADC Flash Analogue-to-Digital Converter. An analogue-to-digital converter which continuously digitises an analogue signal allowing fine time-resolution in the recording of the waveform. For their use in VERITAS see §3.2.3.2.

Fermi See GLAST.

GLAST Gamma-ray Large Area Space Telescope. Renamed *Fermi* after its launch in 2008, the principle instrument on this satellite is the LAT, a pair-production telescope (see §1.1).

HE High Energy. Refering to gamma-ray radiation in the range 0.03–100 GeV. This can be thought of as an operational definition: it is the energy range in which the use of pair-production telescopes is effective (see §1.1).

HEGRA High-Energy Gamma-Ray Astronomy array. The first imaging ACT to apply the stereoscopic reconstruction method.

H.E.S.S. High Energy Stereoscopic System. A very successful imaging ACT array which operates in Namibia.

[1] a.k.a. 'cosmic microwave backround' because it's behind everything and all around.

HMXB High-Mass X-ray Binary. An X-ray luminous binary system containing a normal (*i.e.* thermonuclear-powered) star which is more massive than its degenerate companion. The companion is usually thought to be a neutron star or black hole and the system is powered by accretion onto this object.

IC Inverse Compton. Refers to the scattering of a photon by a charged particle which results in a transfer of energy to the photon (see §2.2.1).

ISM InterStellar Medium. The haze of gases, dust and a weak magnetic field that permeates the galaxy between individual stellar systems. The main component is ionised hydrogen.

L1 Level 1. Relating to the VERITAS trigger system, this is the pixel-level trigger, determining if an individual pixel has been subject to a pulse of light.

L2 Level 2. Relating to the VERITAS trigger system, this is the telescope-level trigger, determining if multiple neighbouring pixels have been subject to a pulse of light and consequently that the telescope may have intercepted light from an extended object such as an EAS.

L3 Level 3. Relating to the VERITAS trigger system, this is the array-level trigger, determining if multiple telescopes have been subject to a pulse of light and consequently that the array has likely intercepted the coordinated light-front from an EAS.

LAT Large Area Telescope. See GLAST.

LMXB Low-Mass X-ray Binary. An X-ray luminous binary system containing a normal (*i.e.* thermonuclear-powered) star which is less massive than its degenerate companion. The companion is usually thought to be a neutron star and the system is powered by accretion onto this object.

MAGIC Major Atmospheric Gamma-ray Imaging Cherenkov Telescopes. An imaging ACT array with a low energy threshold which operates in the Canary Islands.

MHD MagnetoHydroDynamics. The physical description of electrically conducting fluids. In such a medium, it is necessary to describe the

flow of matter with reference also to any electromagnetic fields present. In the extreme case, the kinetic energy and inertia of the fluid is negligible and the behaviour of the magnetic field governs any flow.

MSCL Mean Scaled Cut Length. See MSCP.

MSCP Mean Scaled Cut Parameter. The Parameter in question can be either Width (giving MSCW) or Length (giving MSCL). These are the principle gamma/hadron separation cuts used in the analysis of VERITAS data (see §4) and are based on the expected shape of images of gamma-ray induced EASs.

MSCW Mean Scaled Cut Width. See MSCP.

MSP Milli-Second Pulsar. A pulsar whose period is less than $\sim 100\,\mathrm{ms}$. This usually implies a recycled pulsar, whose spin-down rate is small and period will, therefore, remain short for many millions of years. For example, the Crab pulsar has a period of 33 ms but is not usually referred to as a MSP because it is a young pulsar, slowing rapidly.

NSB Night-Sky Background. The stochastic flux of photons from the night sky (see §3.1.1.2).

OSS Optical Support Structure. In relation to VERITAS this is the space frame which defines the spherical surface upon which individual mirror facets are mounted.

PMT Photo-Multiplier Tube. A highly photo-sensitive analogue electronic device with very fine time resolution. It relies on the photo-electric effect and has the capacity to detect individual photons.

PSF Point-Spread Function. A characteristic of an image forming device (*e.g.* a telescope). The distribution of light formed at the imaging surface / focal plane due to a distant point source. For such an object, light rays enter the device uniformly and parallel. This represents the smallest image that can be formed and the limit of angular resolution.

PWN Pulsar-Wind Nebula. The energised, luminous medium surrounding and powered-by a pulsar.

SNR SuperNova Remnant. The ejected material and associated shockwaves due to a historical supernova.

UL Upper Limit. Relating to the strength of a potential signal which is below the threshold of detection, it is a level which has a large probability of being greater than any possible signal.

VERITAS Very Energetic Radiation Imaging Telescope Array System. An imaging ACT array which operates in Arizona, USA. Currently the most sensitive VHE detector in operation.

VHE Very High Energy. Refering to gamma-ray radiation in the range 0.1–30 TeV . This can be thought of as an operational definition: it is the energy range in which the use of ACTs is effective (see §1.1).

Whipple 10 -m ACT at the Fred Lawrence Whipple Observatory. The pioneering imaging ACT which detected the first astrophysical source of VHE gamma rays.

ZCFD Zero-crossing Constant Fraction Discriminator. An electronic device which determines the time at which a waveform exceeds a set threshold. In addition, for a fixed pulse shape, the time offset relative to the peak of the waveform is fixed regardless of the pulse height.

Bibliography

[1] A. A. Abdo, M. Ackermann, M. Ajello, A. Allafort, E. Antolini, W. B. Atwood, M. Axelsson, L. Baldini, J. Ballet, G. Barbiellini, and et al. Fermi Large Area Telescope First Source Catalog. ApJS, 188:405–436, June 2010. 11, 12

[2] A. A. Abdo, M. Ackermann, M. Ajello, B. Anderson, W. B. Atwood, M. Axelsson, L. Baldini, J. Ballet, G. Barbiellini, M. G. Baring, D. Bastieri, B. M. Baughman, K. Bechtol, R. Bellazzini, B. Berenji, G. F. Bignami, R. D. Blandford, E. D. Bloom, E. Bonamente, A. W. Borgland, J. Bregeon, A. Brez, M. Brigida, P. Bruel, T. H. Burnett, G. A. Caliandro, R. A. Cameron, P. A. Caraveo, J. M. Casandjian, C. Cecchi, Ö. Çelik, A. Chekhtman, C. C. Cheung, J. Chiang, S. Ciprini, R. Claus, J. Cohen-Tanugi, J. Conrad, S. Cutini, C. D. Dermer, A. de Angelis, A. de Luca, F. de Palma, S. W. Digel, M. Dormody, E. do Couto e Silva, P. S. Drell, R. Dubois, D. Dumora, C. Farnier, C. Favuzzi, S. J. Fegan, Y. Fukazawa, S. Funk, P. Fusco, F. Gargano, D. Gasparrini, N. Gehrels, S. Germani, B. Giebels, N. Giglietto, P. Giommi, F. Giordano, T. Glanzman, G. Godfrey, I. A. Grenier, M.-H. Grondin, J. E. Grove, L. Guillemot, S. Guiriec, C. Gwon, Y. Hanabata, A. K. Harding, M. Hayashida, E. Hays, R. E. Hughes, G. Jóhannesson, R. P. Johnson, T. J. Johnson, W. N. Johnson, T. Kamae, H. Katagiri, J. Kataoka, N. Kawai, M. Kerr, J. Knödlseder, M. L. Kocian, M. Kuss, J. Lande, L. Latronico, M. Lemoine-Goumard, F. Longo, F. Loparco, B. Lott, M. N. Lovellette, P. Lubrano, G. M. Madejski, A. Makeev, M. Marelli, M. N. Mazziotta, W. McConville, J. E. McEnery, C. Meurer, P. F. Michelson, W. Mitthumsiri, T. Mizuno, C. Monte, M. E. Monzani, A. Morselli, I. V. Moskalenko, S. Murgia,

P. L. Nolan, J. P. Norris, E. Nuss, T. Ohsugi, N. Omodei, E. Orlando, J. F. Ormes, D. Paneque, D. Parent, V. Pelassa, M. Pepe, M. Pesce-Rollins, M. Pierbattista, F. Piron, T. A. Porter, J. R. Primack, S. Rainò, R. Rando, P. S. Ray, M. Razzano, N. Rea, A. Reimer, O. Reimer, T. Reposeur, S. Ritz, L. S. Rochester, A. Y. Rodriguez, R. W. Romani, F. Ryde, H. F.-W. Sadrozinski, D. Sanchez, A. Sander, P. M. S. Parkinson, J. D. Scargle, C. Sgrò, E. J. Siskind, D. A. Smith, P. D. Smith, G. Spandre, P. Spinelli, J.-L. Starck, M. S. Strickman, D. J. Suson, H. Tajima, H. Takahashi, T. Takahashi, T. Tanaka, J. G. Thayer, D. J. Thompson, L. Tibaldo, O. Tibolla, D. F. Torres, G. Tosti, A. Tramacere, Y. Uchiyama, T. L. Usher, A. Van Etten, V. Vasileiou, N. Vilchez, V. Vitale, A. P. Waite, P. Wang, K. Watters, B. L. Winer, M. T. Wolff, K. S. Wood, T. Ylinen, M. Ziegler, and Fermi-LAT Collaboration.

Detection of 16 Gamma-Ray Pulsars Through Blind Frequency Searches Using the Fermi LAT.

Science, 325:840–, August 2009.

15, 206

[3] A. A. Abdo, M. Ackermann, M. Ajello, W. B. Atwood, M. Axelsson, L. Baldini, J. Ballet, G. Barbiellini, M. G. Baring, D. Bastieri, B. M. Baughman, K. Bechtol, R. Bellazzini, B. Berenji, G. F. Bignami, R. D. Blandford, E. D. Bloom, E. Bonamente, A. W. Borgland, J. Bregeon, A. Brez, M. Brigida, P. Bruel, T. H. Burnett, G. A. Caliandro, R. A. Cameron, F. Camilo, P. A. Caraveo, P. Carlson, J. M. Casandjian, C. Cecchi, Ö. Çelik, E. Charles, A. Chekhtman, C. C. Cheung, J. Chiang, S. Ciprini, R. Claus, I. Cognard, J. Cohen-Tanugi, L. R. Cominsky, J. Conrad, R. Corbet, S. Cutini, C. D. Dermer, G. Desvignes, A. de Angelis, A. de Luca, F. de Palma, S. W. Digel, M. Dormody, E. do Couto e Silva, P. S. Drell, R. Dubois, D. Dumora, Y. Edmonds, C. Farnier, C. Favuzzi, S. J. Fegan, W. B. Focke, M. Frailis, P. C. C. Freire, Y. Fukazawa, S. Funk, P. Fusco, F. Gargano, D. Gasparrini, N. Gehrels, S. Germani, B. Giebels, N. Giglietto, F. Giordano, T. Glanzman, G. Godfrey, I. A. Grenier, M. H. Grondin, J. E. Grove, L. Guillemot, S. Guiriec, Y. Hanabata, A. K. Harding, M. Hayashida, E. Hays, G. Hobbs, R. E. Hughes, G. Jóhannesson, A. S. Johnson, R. P.

Johnson, T. J. Johnson, W. N. Johnson, S. Johnston, T. Kamae, H. Katagiri, J. Kataoka, N. Kawai, M. Kerr, J. Knödlseder, M. L. Kocian, M. Kramer, M. Kuss, J. Lande, L. Latronico, M. Lemoine-Goumard, F. Longo, F. Loparco, B. Lott, M. N. Lovellette, P. Lubrano, G. M. Madejski, A. Makeev, R. N. Manchester, M. Marelli, M. N. Mazziotta, W. McConville, J. E. McEnery, M. A. McLaughlin, C. Meurer, P. F. Michelson, W. Mitthumsiri, T. Mizuno, A. A. Moiseev, C. Monte, M. E. Monzani, A. Morselli, I. V. Moskalenko, S. Murgia, P. L. Nolan, J. P. Norris, E. Nuss, T. Ohsugi, N. Omodei, E. Orlando, J. F. Ormes, D. Paneque, J. H. Panetta, D. Parent, V. Pelassa, M. Pepe, M. Pesce-Rollins, F. Piron, T. A. Porter, S. Rainò, R. Rando, S. M. Ransom, P. S. Ray, M. Razzano, N. Rea, A. Reimer, O. Reimer, T. Reposeur, S. Ritz, L. S. Rochester, A. Y. Rodriguez, R. W. Romani, M. Roth, F. Ryde, H. F. W. Sadrozinski, D. Sanchez, A. Sander, P. M. Saz Parkinson, J. D. Scargle, T. L. Schalk, C. Sgrò, E. J. Siskind, D. A. Smith, P. D. Smith, G. Spandre, P. Spinelli, B. W. Stappers, J. L. Starck, E. Striani, M. S. Strickman, D. J. Suson, H. Tajima, H. Takahashi, T. Tanaka, J. B. Thayer, J. G. Thayer, G. Theureau, D. J. Thompson, S. E. Thorsett, L. Tibaldo, D. F. Torres, G. Tosti, A. Tramacere, Y. Uchiyama, T. L. Usher, A. Van Etten, V. Vasileiou, C. Venter, N. Vilchez, V. Vitale, A. P. Waite, E. Wallace, P. Wang, K. Watters, N. Webb, P. Weltevrede, B. L. Winer, K. S. Wood, T. Ylinen, and M. Ziegler.

A Population of Gamma-Ray Millisecond Pulsars Seen with the Fermi Large Area Telescope.

Science, 325:848–, August 2009.

31, 39, 40, 186, 193

[4] A. A. Abdo, M. Ackermann, M. Ajello, W. B. Atwood, M. Axelsson, L. Baldini, J. Ballet, G. Barbiellini, M. G. Baring, D. Bastieri, and et al.

The First Fermi Large Area Telescope Catalog of Gamma-ray Pulsars.

ApJS, 187:460–494, April 2010.

186, 209

[5] A. A. Abdo, M. Ackermann, M. Ajello, W. B. Atwood, M. Axelsson, L. Baldini, J. Ballet, G. Barbiellini, M. G. Baring, D. Bastieri, and et al.

Erratum: "The First Fermi Large Area Telescope Catalog of Gamma-Ray Pulsars" ¡A href="/abs/2010ApJS..187..460A"¿(2010, ApJS, 187, 460)¡/A¿.
ApJS, 193:22–+, March 2011.
186

[6] A. A. Abdo, M. Ackermann, M. Ajello, W. B. Atwood, M. Axelsson, L. Baldini, J. Ballet, G. Barbiellini, D. Bastieri, B. M. Baughman, K. Bechtol, R. Bellazzini, B. Berenji, R. D. Blandford, E. D. Bloom, E. Bonamente, A. W. Borgland, J. Bregeon, A. Brez, M. Brigida, P. Bruel, T. H. Burnett, G. A. Caliandro, R. A. Cameron, P. A. Caraveo, J. M. Casandjian, C. Cecchi, Ö. Çelik, E. Charles, S. Chaty, A. Chekhtman, C. C. Cheung, J. Chiang, S. Ciprini, R. Claus, J. Cohen-Tanugi, J. Conrad, S. Cutini, C. D. Dermer, F. de Palma, S. W. Digel, M. Dormody, E. do Couto e Silva, P. S. Drell, R. Dubois, D. Dumora, C. Farnier, C. Favuzzi, S. J. Fegan, W. B. Focke, M. Frailis, Y. Fukazawa, P. Fusco, F. Gargano, D. Gasparrini, N. Gehrels, S. Germani, B. Giebels, N. Giglietto, F. Giordano, T. Glanzman, G. Godfrey, I. A. Grenier, J. E. Grove, L. Guillemot, S. Guiriec, Y. Hanabata, A. K. Harding, M. Hayashida, E. Hays, D. Horan, R. E. Hughes, G. Jóhannesson, A. S. Johnson, R. P. Johnson, T. J. Johnson, W. N. Johnson, T. Kamae, H. Katagiri, N. Kawai, M. Kerr, J. Knödlseder, F. Kuehn, M. Kuss, J. Lande, L. Latronico, M. Lemoine-Goumard, F. Longo, F. Loparco, B. Lott, M. N. Lovellette, P. Lubrano, A. Makeev, M. N. Mazziotta, W. McConville, J. E. McEnery, C. Meurer, P. F. Michelson, W. Mitthumsiri, T. Mizuno, A. A. Moiseev, C. Monte, M. E. Monzani, A. Morselli, I. V. Moskalenko, S. Murgia, P. L. Nolan, J. P. Norris, E. Nuss, T. Ohsugi, N. Omodei, E. Orlando, J. F. Ormes, D. Paneque, J. H. Panetta, D. Parent, V. Pelassa, M. Pepe, M. Pierbattista, F. Piron, T. A. Porter, S. Rainò, R. Rando, M. Razzano, N. Rea, A. Reimer, O. Reimer, T. Reposeur, S. Ritz, L. S. Rochester, A. Y. Rodriguez, R. W. Romani, M. Roth, F. Ryde, H. F.-W. Sadrozinski, D. Sanchez, A. Sander, P. M. Saz Parkinson, C. Sgrò, D. A. Smith, P. D. Smith, G. Spandre, P. Spinelli, J.-L. Starck, M. S. Strickman, D. J. Suson, H. Tajima, H. Takahashi, T. Tanaka, J. B. Thayer, J. G. Thayer, D. J. Thompson, L. Tibaldo, D. F. Torres, G. Tosti, A. Tramacere, Y. Uchiyama, T. L. Usher,

V. Vasileiou, N. Vilchez, V. Vitale, P. Wang, N. Webb, B. L. Winer, K. S. Wood, T. Ylinen, and M. Ziegler.
Detection of High-Energy Gamma-Ray Emission from the Globular Cluster 47 Tucanae with Fermi.
Science, 325:845–, August 2009.
168, 172, 177, 186

[7] A. A. Abdo, M. Ackermann, M. Ajello, W. B. Atwood, M. Axelsson, L. Baldini, J. Ballet, G. Barbiellini, D. Bastieri, B. M. Baughman, K. Bechtol, R. Bellazzini, B. Berenji, E. D. Bloom, E. Bonamente, A. W. Borgland, J. Bregeon, A. Brez, M. Brigida, P. Bruel, T. H. Burnett, G. A. Caliandro, R. A. Cameron, P. A. Caraveo, P. Carlson, J. M. Casandjian, C. Cecchi, Ö. Çelik, A. Chekhtman, C. C. Cheung, S. Ciprini, R. Claus, J. Cohen-Tanugi, J. Conrad, S. Cutini, C. D. Dermer, A. de Angelis, F. de Palma, S. W. Digel, E. d. C. e. Silva, P. S. Drell, R. Dubois, D. Dumora, C. Farnier, C. Favuzzi, S. J. Fegan, W. B. Focke, M. Frailis, Y. Fukazawa, S. Funk, P. Fusco, F. Gargano, D. Gasparrini, N. Gehrels, S. Germani, B. Giebels, N. Giglietto, F. Giordano, T. Glanzman, G. Godfrey, I. A. Grenier, M.-H. Grondin, J. E. Grove, L. Guillemot, S. Guiriec, Y. Hanabata, A. K. Harding, M. Hayashida, E. Hays, R. E. Hughes, G. Jóhannesson, A. S. Johnson, R. P. Johnson, W. N. Johnson, T. Kamae, H. Katagiri, N. Kawai, M. Kerr, J. Knödlseder, M. L. Kocian, F. Kuehn, M. Kuss, J. Lande, L. Latronico, M. Lemoine-Goumard, F. Longo, F. Loparco, B. Lott, M. N. Lovellette, P. Lubrano, A. Makeev, M. N. Mazziotta, J. E. McEnery, C. Meurer, P. F. Michelson, W. Mitthumsiri, T. Mizuno, A. A. Moiseev, C. Monte, M. E. Monzani, A. Morselli, I. V. Moskalenko, S. Murgia, P. L. Nolan, J. P. Norris, E. Nuss, T. Ohsugi, A. Okumura, N. Omodei, E. Orlando, J. F. Ormes, M. Ozaki, D. Paneque, J. H. Panetta, D. Parent, M. Pepe, M. Pesce-Rollins, F. Piron, M. Pohl, T. A. Porter, S. Rainò, R. Rando, M. Razzano, A. Reimer, O. Reimer, T. Reposeur, S. Ritz, L. S. Rochester, A. Y. Rodriguez, F. Ryde, H. F.-W. Sadrozinski, D. Sanchez, A. Sander, P. M. Saz Parkinson, T. L. Schalk, A. Sellerholm, C. Sgrò, D. A. Smith, P. D. Smith, G. Spandre, P. Spinelli, J.-L. Starck, F. W. Stecker, M. S. Strickman, A. W. Strong, D. J. Suson, H. Tajima, H. Takahashi, T. Takahashi, T. Tanaka, J. B. Thayer, J. G. Thayer, D. J. Thomp-

son, L. Tibaldo, D. F. Torres, G. Tosti, A. Tramacere, Y. Uchiyama, T. L. Usher, V. Vasileiou, N. Vilchez, V. Vitale, A. P. Waite, P. Wang, B. L. Winer, K. S. Wood, T. Ylinen, and M. Ziegler.
Fermi LAT Observation of Diffuse Gamma Rays Produced Through Interactions Between Local Interstellar Matter and High-energy Cosmic Rays.
ApJ, 703:1249–1256, October 2009.
11

[8] A. A. Abdo, M. Ackermann, M. Ajello, L. Baldini, J. Ballet, G. Barbiellini, D. Bastieri, B. M. Baughman, K. Bechtol, R. Bellazzini, B. Berenji, R. D. Blandford, E. D. Bloom, E. Bonamente, A. W. Borgland, J. Bregeon, A. Brez, M. Brigida, P. Bruel, T. H. Burnett, S. Buson, G. A. Caliandro, R. A. Cameron, F. Camilo, P. A. Caraveo, J. M. Casandjian, C. Cecchi, Ö. Çelik, A. Chekhtman, C. C. Cheung, J. Chiang, S. Ciprini, R. Claus, I. Cognard, J. Cohen-Tanugi, L. R. Cominsky, J. Conrad, S. Cutini, A. de Angelis, F. de Palma, S. W. Digel, B. L. Dingus, M. Dormody, E. d. C. e. Silva, P. S. Drell, R. Dubois, D. Dumora, C. Farnier, C. Favuzzi, S. J. Fegan, W. B. Focke, P. Fortin, M. Frailis, P. C. C. Freire, Y. Fukazawa, S. Funk, P. Fusco, F. Gargano, D. Gasparrini, N. Gehrels, S. Germani, G. Giavitto, B. Giebels, N. Giglietto, F. Giordano, T. Glanzman, G. Godfrey, I. A. Grenier, M.-H. Grondin, J. E. Grove, L. Guillemot, S. Guiriec, Y. Hanabata, A. K. Harding, E. Hays, R. E. Hughes, M. S. Jackson, G. Jóhannesson, A. S. Johnson, T. J. Johnson, W. N. Johnson, S. Johnston, T. Kamae, H. Katagiri, J. Kataoka, N. Kawai, M. Kerr, J. Knödlseder, M. L. Kocian, M. Kuss, J. Lande, L. Latronico, M. Lemoine-Goumard, F. Longo, F. Loparco, B. Lott, M. N. Lovellette, P. Lubrano, A. Makeev, M. Marelli, M. N. Mazziotta, J. E. McEnery, C. Meurer, P. F. Michelson, W. Mitthumsiri, T. Mizuno, A. A. Moiseev, C. Monte, M. E. Monzani, A. Morselli, I. V. Moskalenko, S. Murgia, P. L. Nolan, J. P. Norris, E. Nuss, T. Ohsugi, N. Omodei, E. Orlando, J. F. Ormes, D. Paneque, D. Parent, V. Pelassa, M. Pepe, M. Pesce-Rollins, F. Piron, T. A. Porter, S. Rainò, R. Rando, P. S. Ray, M. Razzano, A. Reimer, O. Reimer, T. Reposeur, S. Ritz, M. S. E. Roberts, L. S. Rochester, A. Y. Rodriguez, R. W. Ro'mani, M. Roth, F. Ryde, H. F.-W. Sadrozinski, D. Sanchez, A. Sander,

P. M. Saz Parkinson, J. D. Scargle, C. Sgrò, E. J. Siskind, D. A. Smith, P. D. Smith, G. Spandre, P. Spinelli, M. S. Strickman, D. J. Suson, H. Tajima, H. Takahashi, T. Tanaka, J. B. Thayer, J. G. Thayer, G. Theureau, D. J. Thompson, L. Tibaldo, O. Tibolla, D. F. Torres, G. Tosti, A. Tramacere, Y. Uchiyama, T. L. Usher, A. Van Etten, V. Vasileiou, C. Venter, N. Vilchez, V. Vitale, A. P. Waite, P. Wang, K. Watters, B. L. Winer, M. T. Wolff, K. S. Wood, T. Ylinen, and M. Ziegler.

PSR J1907+0602: A Radio-Faint Gamma-Ray Pulsar Powering a Bright TeV Pulsar Wind Nebula.

ApJ, 711:64–74, March 2010.

206

[9] A. A. Abdo, M. Ackermann, M. Ajello, L. Baldini, J. Ballet, G. Barbiellini, D. Bastieri, R. Bellazzini, R. D. Blandford, E. D. Bloom, E. Bonamente, A. W. Borgland, A. Bouvier, T. J. Brandt, J. Bregeon, M. Brigida, P. Bruel, R. Buehler, S. Buson, G. A. Caliandro, R. A. Cameron, P. A. Caraveo, S. Carrigan, J. M. Casandjian, E. Charles, S. Chaty, A. Chekhtman, C. C. Cheung, J. Chiang, S. Ciprini, R. Claus, J. Cohen-Tanugi, J. Conrad, M. E. Decesar, C. D. Dermer, F. de Palma, S. W. Digel, E. D. C. E. Silva, P. S. Drell, R. Dubois, D. Dumora, C. Favuzzi, P. Fortin, M. Frailis, Y. Fukazawa, P. Fusco, F. Gargano, D. Gasparrini, N. Gehrels, S. Germani, N. Giglietto, F. Giordano, T. Glanzman, G. Godfrey, I. Grenier, M.-H. Grondin, J. E. Grove, L. Guillemot, S. Guiriec, D. Hadasch, A. K. Harding, E. Hays, P. Jean, G. Jóhannesson, T. J. Johnson, W. N. Johnson, T. Kamae, H. Katagiri, J. Kataoka, M. Kerr, J. Knödlseder, M. Kuss, J. Lande, L. Latronico, S.-H. Lee, M. Lemoine-Goumard, M. Llena Garde, F. Longo, F. Loparco, M. N. Lovellette, P. Lubrano, A. Makeev, M. N. Mazziotta, P. F. Michelson, W. Mitthumsiri, T. Mizuno, C. Monte, M. E. Monzani, A. Morselli, I. V. Moskalenko, S. Murgia, M. Naumann-Godo, P. L. Nolan, J. P. Norris, E. Nuss, T. Ohsugi, N. Omodei, E. Orlando, J. F. Ormes, B. Pancrazi, D. Parent, M. Pepe, M. Pesce-Rollins, F. Piron, T. A. Porter, S. Rainò, R. Rando, A. Reimer, O. Reimer, T. Reposeur, J. Ripken, R. W. Romani, M. Roth, H. F.-W. Sadrozinski, P. M. Saz Parkinson, C. Sgrò, E. J. Siskind, D. A. Smith, P. Spinelli, M. S. Strickman, D. J. Suson, H. Takahashi,

T. Takahashi, T. Tanaka, J. B. Thayer, J. G. Thayer, L. Tibaldo, D. F. Torres, G. Tosti, A. Tramacere, Y. Uchiyama, T. L. Usher, V. Vasileiou, C. Venter, N. Vilchez, V. Vitale, A. P. Waite, P. Wang, N. Webb, B. L. Winer, Z. Yang, T. Ylinen, and M. Ziegler.

A population of gamma-ray emitting globular clusters seen with the Fermi Large Area Telescope.

A&A, 524:A75+, December 2010.

13, 32, 183

[10] A. A. Abdo, B. Allen, D. Berley, E. Blaufuss, S. Casanova, C. Chen, D. G. Coyne, R. S. Delay, B. L. Dingus, R. W. Ellsworth, L. Fleysher, R. Fleysher, I. Gebauer, M. M. Gonzalez, J. A. Goodman, E. Hays, C. M. Hoffman, B. E. Kolterman, L. A. Kelley, C. P. Lansdell, J. T. Linnemann, J. E. McEnery, A. I. Mincer, I. V. Moskalenko, P. Nemethy, D. Noyes, J. M. Ryan, F. W. Samuelson, P. M. Saz Parkinson, M. Schneider, A. Shoup, G. Sinnis, A. J. Smith, A. W. Strong, G. W. Sullivan, V. Vasileiou, G. P. Walker, D. A. Williams, X. W. Xu, and G. B. Yodh.

Discovery of TeV Gamma-Ray Emission from the Cygnus Region of the Galaxy.

ApJ, 658:L33–L36, March 2007.

6

[11] A. A. Abdo, B. Allen, D. Berley, S. Casanova, C. Chen, D. G. Coyne, B. L. Dingus, R. W. Ellsworth, L. Fleysher, R. Fleysher, M. M. Gonzalez, J. A. Goodman, E. Hays, C. M. Hoffman, B. Hopper, P. H. Hüntemeyer, B. E. Kolterman, C. P. Lansdell, J. T. Linnemann, J. E. McEnery, A. I. Mincer, P. Nemethy, D. Noyes, J. M. Ryan, P. M. Saz Parkinson, A. Shoup, G. Sinnis, A. J. Smith, G. W. Sullivan, V. Vasileiou, G. P. Walker, D. A. Williams, X. W. Xu, and G. B. Yodh.

TeV Gamma-Ray Sources from a Survey of the Galactic Plane with Milagro.

ApJ, 664:L91–L94, August 2007.

6, 206

[12] F. Aharonian, A. Akhperjanian, J. Barrio, K. Bernlöhr, H. Börst, H. Bojahr, O. Bolz, J. Contreras, J. Cortina, S. Denninghoff, V. Fonseca, J. Gonzalez, N. Götting, G. Heinzelmann, G. Hermann, A. Heusler, W. Hofmann, D. Horns, A. Ibarra, C. Iser-

lohe, I. Jung, R. Kankanyan, M. Kestel, J. Kettler, A. Kohnle, A. Konopelko, H. Kornmeyer, D. Kranich, H. Krawczynski, H. Lampeitl, M. Lopez, E. Lorenz, F. Lucarelli, N. Magnussen, O. Mang, H. Meyer, R. Mirzoyan, A. Moralejo, E. Ona, L. Padilla, M. Panter, R. Plaga, A. Plyasheshnikov, J. Prahl, G. Pühlhofer, G. Rauterberg, A. Röhring, W. Rhode, G. P. Rowell, V. Sahakian, M. Samorski, M. Schilling, F. Schröder, M. Siems, W. Stamm, M. Tluczykont, H. J. Völk, C. A. Wiedner, and W. Wittek.

Evidence for TeV gamma ray emission from Cassiopeia A.
A&A, 370:112–120, April 2001.
15

[13] F. Aharonian, A. Akhperjanian, M. Beilicke, K. Bernlöhr, H. Börst, H. Bojahr, O. Bolz, T. Coarasa, J. Contreras, J. Cortina, S. Denninghoff, V. Fonseca, M. Girma, N. Götting, G. Heinzelmann, G. Hermann, A. Heusler, W. Hofmann, D. Horns, I. Jung, R. Kankanyan, M. Kestel, J. Kettler, A. Kohnle, A. Konopelko, H. Kornmeyer, D. Kranich, H. Krawczynski, H. Lampeitl, M. Lopez, E. Lorenz, F. Lucarelli, N. Magnussen, O. Mang, H. Meyer, M. Milite, R. Mirzoyan, A. Moralejo, E. Ona, M. Panter, A. Plyasheshnikov, J. Prahl, G. Pühlhofer, G. Rauterberg, R. Reyes, W. Rhode, J. Ripken, A. Röhring, G. P. Rowell, V. Sahakian, M. Samorski, M. Schilling, F. Schröder, M. Siems, D. Sobzynska, W. Stamm, M. Tluczykont, H. J. Völk, C. A. Wiedner, W. Wittek, Y. Uchiyama, T. Takahashi, and HEGRA Collaboration.

An unidentified TeV source in the vicinity of Cygnus OB2.
A&A, 393:L37–L40, October 2002.
15, 206

[14] F. Aharonian, A. Akhperjanian, M. Beilicke, K. Bernlöhr, H.-G. Börst, H. Bojahr, O. Bolz, T. Coarasa, J. Contreras, J. Cortina, S. Denninghoff, V. Fonseca, M. Girma, N. Götting, G. Heinzelmann, G. Hermann, A. Heusler, W. Hofmann, D. Horns, I. Jung, R. Kankanyan, M. Kestel, A. Kohnle, A. Konopelko, D. Kranich, H. Lampeitl, M. Lopez, E. Lorenz, F. Lucarelli, O. Mang, D. Mazin, H. Meyer, R. Mirzoyan, A. Moralejo, E. Oña-Wilhelmi, M. Panter, A. Plyasheshnikov, G. Pühlhofer, R. de los Reyes, W. Rhode, J. Ripken, G. P. Rowell, V. Sahakian, M. Samorski, M. Schilling,

M. Siems, D. Sobzynska, W. Stamm, M. Tluczykont, V. Vitale, H. J. Völk, C. A. Wiedner, and W. Wittek.
The unidentified TeV source (TeV J2032+4130) and surrounding field: Final HEGRA IACT-System results.
A&A, 431:197–202, February 2005.
15, 206

[15] F. Aharonian, A. Akhperjanian, M. Beilicke, K. Bernlöhr, H.-G. Börst, H. Bojahr, O. Bolz, T. Coarasa, J. L. Contreras, J. Cortina, S. Denninghoff, M. V. Fonseca, M. Girma, N. Götting, G. Heinzelmann, G. Hermann, A. Heusler, W. Hofmann, D. Horns, I. Jung, R. Kankanyan, M. Kestel, A. Kohnle, A. Konopelko, H. Kornmeyer, D. Kranich, H. Lampeitl, M. Lopez, E. Lorenz, F. Lucarelli, O. Mang, H. Meyer, R. Mirzoyan, A. Moralejo, E. Ona-Wilhelmi, M. Panter, A. Plyasheshnikov, G. Pühlhofer, R. de los Reyes, W. Rhode, J. Ripken, G. Rowell, V. Sahakian, M. Samorski, M. Schilling, M. Siems, D. Sobzynska, W. Stamm, M. Tluczykont, V. Vitale, H. J. Völk, C. A. Wiedner, and W. Wittek.
Is the giant radio galaxy M 87 a TeV gamma-ray emitter?
A&A, 403:L1–L5, May 2003.
15

[16] F. Aharonian, A. G. Akhperjanian, G. Anton, U. Barres de Almeida, A. R. Bazer-Bachi, Y. Becherini, B. Behera, W. Benbow, K. Bernlöhr, C. Boisson, A. Bochow, V. Borrel, I. Braun, E. Brion, J. Brucker, P. Brun, R. Bühler, T. Bulik, I. Büsching, T. Boutelier, S. Carrigan, P. M. Chadwick, A. Charbonnier, R. C. G. Chaves, A. Cheesebrough, L.-M. Chounet, A. C. Clapson, G. Coignet, M. Dalton, M. K. Daniel, B. Degrange, C. Deil, H. J. Dickinson, A. Djannati-Ataï, W. Domainko, L. O'C. Drury, F. Dubois, G. Dubus, J. Dyks, M. Dyrda, K. Egberts, D. Emmanoulopoulos, P. Espigat, C. Farnier, F. Feinstein, A. Fiasson, A. Förster, G. Fontaine, M. Füßling, S. Gabici, Y. A. Gallant, L. Gérard, B. Giebels, J. F. Glicenstein, B. Glück, P. Goret, D. Hauser, M. Hauser, S. Heinz, G. Heinzelmann, G. Henri, G. Hermann, J. A. Hinton, A. Hoffmann, W. Hofmann, M. Holleran, S. Hoppe, D. Horns, A. Jacholkowska, O. C. de Jager, I. Jung, K. Katarzyński, U. Katz, S. Kaufmann, E. Kendziorra, M. Kerschhaggl, D. Khangulyan, B. Khélifi, D. Keogh, N. Komin, K. Ko-

sack, G. Lamanna, J.-P. Lenain, T. Lohse, V. Marandon, J. M. Martin, O. Martineau-Huynh, A. Marcowith, D. Maurin, T. J. L. McComb, M. C. Medina, R. Moderski, E. Moulin, M. Naumann-Godo, M. de Naurois, D. Nedbal, D. Nekrassov, J. Niemiec, S. J. Nolan, S. Ohm, J.-F. Olive, E. de Oña Wilhelmi, K. J. Orford, M. Ostrowski, M. Panter, M. Paz Arribas, G. Pedaletti, G. Pelletier, P.-O. Petrucci, S. Pita, G. Pühlhofer, M. Punch, A. Quirrenbach, B. C. Raubenheimer, M. Raue, S. M. Rayner, M. Renaud, O. Reimer, F. Rieger, J. Ripken, L. Rob, S. Rosier-Lees, G. Rowell, B. Rudak, C. B. Rulten, J. Ruppel, V. Sahakian, A. Santangelo, R. Schlickeiser, F. M. Schöck, R. Schröder, U. Schwanke, S. Schwarzburg, S. Schwemmer, A. Shalchi, J. L. Skilton, H. Sol, D. Spangler, Ł. Stawarz, R. Steenkamp, C. Stegmann, G. Superina, P. H. Tam, J.-P. Tavernet, R. Terrier, O. Tibolla, C. van Eldik, G. Vasileiadis, C. Venter, L. Venter, J. P. Vialle, P. Vincent, M. Vivier, H. J. Völk, F. Volpe, S. J. Wagner, M. Ward, A. A. Zdziarski, and A. Zech.

Detection of very high energy radiation from HESS J1908+063 confirms the Milagro unidentified source MGRO J1908+06.

A&A, 499:723–728, June 2009.

206

[17] F. Aharonian, A. G. Akhperjanian, G. Anton, U. Barres de Almeida, A. R. Bazer-Bachi, Y. Becherini, B. Behera, K. Bernlöhr, C. Boisson, A. Bochow, V. Borrel, I. Braun, E. Brion, J. Brucker, P. Brun, R. Bühler, T. Bulik, I. Büsching, T. Boutelier, P. M. Chadwick, A. Charbonnier, R. C. G. Chaves, A. Cheesebrough, L.-M. Chounet, A. C. Clapson, G. Coignet, M. Dalton, M. K. Daniel, I. D. Davids, B. Degrange, C. Deil, H. J. Dickinson, A. Djannati-Ataï, W. Domainko, L. O'C. Drury, F. Dubois, G. Dubus, J. Dyks, M. Dyrda, K. Egberts, D. Emmanoulopoulos, P. Espigat, C. Farnier, F. Feinstein, A. Fiasson, A. Förster, G. Fontaine, M. Füßling, S. Gabici, Y. A. Gallant, L. Gérard, B. Giebels, J. F. Glicenstein, B. Glück, P. Goret, D. Hauser, M. Hauser, S. Heinz, G. Heinzelmann, G. Henri, G. Hermann, J. A. Hinton, A. Hoffmann, W. Hofmann, M. Holleran, S. Hoppe, D. Horns, A. Jacholkowska, O. C. de Jager, I. Jung, K. Katarzyński, U. Katz, S. Kaufmann, E. Kendziorra, M. Kerschhaggl, D. Khangulyan, B. Khélifi, D. Keogh, N. Komin,

K. Kosack, G. Lamanna, J.-P. Lenain, T. Lohse, V. Marandon, J. M. Martin, O. Martineau-Huynh, A. Marcowith, D. Maurin, T. J. L. McComb, M. C. Medina, R. Moderski, E. Moulin, M. Naumann-Godo, M. de Naurois, D. Nedbal, D. Nekrassov, J. Niemiec, S. J. Nolan, S. Ohm, J.-F. Olive, E. de Oña Wilhelmi, K. J. Orford, M. Ostrowski, M. Panter, M. Paz Arribas, G. Pedaletti, G. Pelletier, P.-O. Petrucci, S. Pita, G. Pühlhofer, M. Punch, A. Quirrenbach, B. C. Raubenheimer, M. Raue, S. M. Rayner, O. Reimer, M. Renaud, F. Rieger, J. Ripken, L. Rob, S. Rosier-Lees, G. Rowell, B. Rudak, C. B. Rulten, J. Ruppel, V. Sahakian, A. Santangelo, R. Schlickeiser, F. M. Schöck, R. Schröder, U. Schwanke, S. Schwarzburg, S. Schwemmer, A. Shalchi, J. L. Skilton, H. Sol, D. Spangler, Ł. Stawarz, R. Steenkamp, C. Stegmann, G. Superina, A. Szostek, P. H. Tam, J.-P. Tavernet, R. Terrier, O. Tibolla, C. van Eldik, G. Vasileiadis, C. Venter, L. Venter, J. P. Vialle, P. Vincent, M. Vivier, H. J. Völk, F. Volpe, S. J. Wagner, M. Ward, A. A. Zdziarski, and A. Zech.

HESS upper limit on the very high energy γ-ray emission from the globular cluster 47 Tucanae.

A&A, 499:273–277, May 2009.

26, 181, 198

[18] F. Aharonian, A. G. Akhperjanian, U. Barres de Almeida, A. R. Bazer-Bachi, B. Behera, M. Beilicke, W. Benbow, K. Bernlöhr, C. Boisson, O. Bolz, V. Borrel, I. Braun, E. Brion, A. M. Brown, R. Bühler, T. Bulik, I. Büsching, T. Boutelier, S. Carrigan, P. M. Chadwick, L.-M. Chounet, A. C. Clapson, G. Coignet, R. Cornils, L. Costamante, M. Dalton, B. Degrange, H. J. Dickinson, A. Djannati-Ataï, W. Domainko, L. O. Drury, F. Dubois, G. Dubus, J. Dyks, K. Egberts, D. Emmanoulopoulos, P. Espigat, C. Farnier, F. Feinstein, A. Fiasson, A. Förster, G. Fontaine, S. Funk, M. Füßling, Y. A. Gallant, B. Giebels, J. F. Glicenstein, B. Glück, P. Goret, C. Hadjichristidis, D. Hauser, M. Hauser, G. Heinzelmann, G. Henri, G. Hermann, J. A. Hinton, A. Hoffmann, W. Hofmann, M. Holleran, S. Hoppe, D. Horns, A. Jacholkowska, O. C. de Jager, I. Jung, K. Katarzyński, E. Kendziorra, M. Kerschhaggl, B. Khélifi, D. Keogh, N. Komin, K. Kosack, G. Lamanna, I. J. Latham, A. Lemière, M. Lemoine-Goumard, J.-P. Lenain, T. Lohse, J. M. Martin, O. Martineau-

Huynh, A. Marcowith, C. Masterson, D. Maurin, G. Maurin, T. J. L. McComb, R. Moderski, E. Moulin, M. de Naurois, D. Nedbal, S. J. Nolan, S. Ohm, J.-P. Olive, E. de Oña Wilhelmi, K. J. Orford, J. L. Osborne, M. Ostrowski, M. Panter, G. Pedaletti, G. Pelletier, P.-O. Petrucci, S. Pita, G. Pühlhofer, M. Punch, S. Ranchon, B. C. Raubenheimer, M. Raue, S. M. Rayner, M. Renaud, J. Ripken, L. Rob, L. Rolland, S. Rosier-Lees, G. Rowell, B. Rudak, J. Ruppel, V. Sahakian, A. Santangelo, R. Schlickeiser, F. Schöck, R. Schröder, U. Schwanke, S. Schwarzburg, S. Schwemmer, A. Shalchi, H. Sol, D. Spangler, Ł. Stawarz, R. Steenkamp, C. Stegmann, G. Superina, P. H. Tam, J.-P. Tavernet, R. Terrier, C. van Eldik, G. Vasileiadis, C. Venter, J. P. Vialle, P. Vincent, M. Vivier, H. J. Völk, F. Volpe, S. J. Wagner, M. Ward, A. A. Zdziarski, and A. Zech.

HESS very-high-energy gamma-ray sources without identified counterparts.

A&A, 477:353–363, January 2008.

15

[19] F. Aharonian, A. G. Akhperjanian, A. R. Bazer-Bachi, M. Beilicke, W. Benbow, D. Berge, K. Bernlöhr, C. Boisson, O. Bolz, V. Borrel, I. Braun, F. Breitling, A. M. Brown, P. M. Chadwick, L.-M. Chounet, R. Cornils, L. Costamante, B. Degrange, H. J. Dickinson, A. Djannati-Ataï, L. O. Drury, G. Dubus, D. Emmanoulopoulos, P. Espigat, F. Feinstein, G. Fontaine, Y. Fuchs, S. Funk, Y. A. Gallant, B. Giebels, S. Gillessen, J. F. Glicenstein, P. Goret, C. Hadjichristidis, M. Hauser, G. Heinzelmann, G. Henri, G. Hermann, J. A. Hinton, W. Hofmann, M. Holleran, D. Horns, A. Jacholkowska, O. C. de Jager, B. Khélifi, N. Komin, A. Konopelko, I. J. Latham, R. Le Gallou, A. Lemière, M. Lemoine-Goumard, N. Leroy, T. Lohse, J. M. Martin, O. Martineau-Huynh, A. Marcowith, C. Masterson, T. J. L. McComb, M. de Naurois, S. J. Nolan, A. Noutsos, K. J. Orford, J. L. Osborne, M. Ouchrif, M. Panter, G. Pelletier, S. Pita, G. Pühlhofer, M. Punch, B. C. Raubenheimer, M. Raue, J. Raux, S. M. Rayner, A. Reimer, O. Reimer, J. Ripken, L. Rob, L. Rolland, G. Rowell, V. Sahakian, L. Saugé, S. Schlenker, R. Schlickeiser, C. Schuster, U. Schwanke, M. Siewert, H. Sol, D. Spangler, R. Steenkamp, C. Stegmann, J.-P. Tavernet,

R. Terrier, C. G. Théoret, M. Tluczykont, G. Vasileiadis, C. Venter, P. Vincent, H. J. Völk, and S. J. Wagner.
The H.E.S.S. Survey of the Inner Galaxy in Very High Energy Gamma Rays.
ApJ, 636:777–797, January 2006.
15

[20] E. Aliu, H. Anderhub, L. A. Antonelli, P. Antoranz, M. Backes, C. Baixeras, J. A. Barrio, H. Bartko, D. Bastieri, J. K. Becker, W. Bednarek, K. Berger, E. Bernardini, C. Bigongiari, A. Biland, R. K. Bock, G. Bonnoli, P. Bordas, V. Bosch-Ramon, T. Bretz, I. Britvitch, M. Camara, E. Carmona, A. Chilingarian, S. Commichau, J. L. Contreras, J. Cortina, M. T. Costado, S. Covino, V. Curtef, F. Dazzi, A. De Angelis, E. De Cea del Pozo, R. de los Reyes, B. De Lotto, M. De Maria, F. De Sabata, C. Delgado Mendez, A. Dominguez, D. Dorner, M. Doro, D. Elsässer, M. Errando, M. Fagiolini, D. Ferenc, E. Fernandez, R. Firpo, M. V. Fonseca, L. Font, N. Galante, R. J. Garcia Lopez, M. Garczarczyk, M. Gaug, F. Goebel, D. Hadasch, M. Hayashida, A. Herrero, D. Höhne, J. Hose, C. C. Hsu, S. Huber, T. Jogler, D. Kranich, A. La Barbera, A. Laille, E. Leonardo, E. Lindfors, S. Lombardi, F. Longo, M. Lopez, E. Lorenz, P. Majumdar, G. Maneva, N. Mankuzhiyil, K. Mannheim, L. Maraschi, M. Mariotti, M. Martinez, D. Mazin, M. Meucci, M. Meyer, J. M. Miranda, R. Mirzoyan, M. Moles, A. Moralejo, D. Nieto, K. Nilsson, J. Ninkovic, N. Otte, I. Oya, R. Paoletti, J. M. Paredes, M. Pasanen, D. Pascoli, F. Pauss, R. G. Pegna, M. A. Perez-Torres, M. Persic, L. Peruzzo, A. Piccioli, F. Prada, E. Prandini, N. Puchades, A. Raymers, W. Rhode, M. Ribó, J. Rico, M. Rissi, A. Robert, S. Rügamer, A. Saggion, T. Y. Saito, M. Salvati, M. Sanchez-Conde, P. Sartori, K. Satalecka, V. Scalzotto, V. Scapin, T. Schweizer, M. Shayduk, K. Shinozaki, S. N. Shore, N. Sidro, A. Sierpowska-Bartosik, A. Sillanpää, D. Sobczynska, F. Spanier, A. Stamerra, L. S. Stark, L. Takalo, F. Tavecchio, P. Temnikov, D. Tescaro, M. Teshima, M. Tluczykont, D. F. Torres, N. Turini, H. Vankov, A. Venturini, V. Vitale, R. M. Wagner, W. Wittek, V. Zabalza, F. Zandanel, R. Zanin, J. Zapatero, O. C. de Jager, E. de Ona Wilhelmi, and MAGIC Collaboration.

Observation of Pulsed γ-Rays Above 25 GeV from the Crab Pulsar with MAGIC.
Science, 322:1221–, November 2008.
16, 30

[21] M. A. Alpar, A. F. Cheng, M. A. Ruderman, and J. Shaham.
A new class of radio pulsars.
Nature, 300:728–730, December 1982.
22

[22] M. Amenomori, S. Ayabe, P. Y. Cao, Danzengluobu, L. K. Ding, Z. Y. Fen, Y. Fu, H. W. Guo, M. He, K. Hibino, N. Hotta, Q. Huang, A. X. Huo, K. Izu, H. Y. Jia, F. Kajino, K. Kasahara, Y. Katayose, Labaciren, J. Y. Li, H. Lu, S. L. Lu, G. X. Luo, X. R. Meng, K. Mizutani, J. Mu, H. Nanjo, M. Nishizawa, M. Ohnishi, I. Ohta, T. Ouchi, J. R. Ren, T. Saito, M. Sakata, T. Sasaki, Z. Z. Shi, M. Shibata, A. Shiomi, T. Shirai, H. Sugimoto, K. Taira, Y. H. Tan, N. Tateyama, S. Torii, T. Utsugi, C. R. Wang, H. Wang, X. W. Xu, Y. Yamamoto, G. C. Yu, A. F. Yuan, T. Yuda, C. S. Zhang, H. M. Zhang, J. L. Zhang, N. J. Zhang, X. Y. Zhang, Zhaxisangzhu, Zhaxiciren, and W. D. Zhou.
Detection of TeV gamma rays from Mrk 501 at high flaring state of activity in 1997 with the Tibet air shower array.
In B. L. Dingus, M. H. Salamon, & D. B. Kieda, editor, *American Institute of Physics Conference Series*, volume 515 of *American Institute of Physics Conference Series*, pages 139–143, June 2000.
6

[23] M. Amenomori, S. Ayabe, P. Y. Cao, Danzengluobu, L. K. Ding, Z. Y. Feng, Y. Fu, H. W. Guo, M. He, K. Hibino, N. Hotta, Q. Huang, A. X. Huo, K. Izu, H. Y. Jia, F. Kajino, K. Kasahara, Y. Katayose, Labaciren, J. Y. Li, H. Lu, S. L. Lu, G. X. Luo, X. R. Meng, K. Mizutani, J. Mu, H. Nanjo, M. Nishizawa, M. Ohnishi, I. Ohta, T. Ouchi, J. R. Ren, T. Saito, M. Sakata, T. Sasaki, Z. Z. Shi, M. Shibata, A. Shiomi, T. Shirai, H. Sugimoto, K. Taira, Y. H. Tan, N. Tateyama, S. Torii, T. Utsugi, C. R. Wang, H. Wang, X. W. Xu, Y. Yamamoto, G. C. Yu, A. F. Yuan, T. Yuda, C. S. Zhang, H. M. Zhang, J. L. Zhang, N. J. Zhang, X. Y. Zhang, Zhaxisangzhu, Zhaxiciren, W. D. Zhou, and The Tibet As Γ Collaboration.

Observation of Multi-TEV Gamma Rays from the Crab Nebula using the Tibet Air Shower Array.
ApJ, 525:L93–L96, November 1999.
6

[24] H. Anderhub, L. A. Antonelli, P. Antoranz, M. Backes, C. Baixeras, S. Balestra, J. A. Barrio, D. Bastieri, J. Becerra González, J. K. Becker, W. Bednarek, K. Berger, E. Bernardini, A. Biland, R. K. Bock, G. Bonnoli, P. Bordas, D. Borla Tridon, V. Bosch-Ramon, D. Bose, I. Braun, T. Bretz, I. Britvitch, M. Camara, E. Carmona, S. Commichau, J. L. Contreras, J. Cortina, M. T. Costado, S. Covino, V. Curtef, F. Dazzi, A. DeAngelis, E. DeCea del Pozo, R. de los Reyes, B. DeLotto, M. DeMaria, F. DeSabata, C. Delgado Mendez, A. Dominguez, D. Dorner, M. Doro, D. Elsaesser, M. Errando, D. Ferenc, E. Fernández, R. Firpo, M. V. Fonseca, L. Font, N. Galante, R. J. García López, M. Garczarczyk, M. Gaug, F. Goebel, D. Hadasch, M. Hayashida, A. Herrero, D. Hildebrand, D. Höhne-Mönch, J. Hose, C. C. Hsu, T. Jogler, D. Kranich, A. La Barbera, A. Laille, E. Leonardo, E. Lindfors, S. Lombardi, F. Longo, M. López, E. Lorenz, P. Majumdar, G. Maneva, N. Mankuzhiyil, K. Mannheim, L. Maraschi, M. Mariotti, M. Martínez, D. Mazin, M. Meucci, M. Meyer, J. M. Miranda, R. Mirzoyan, H. Miyamoto, J. Moldón, M. Moles, A. Moralejo, D. Nieto, K. Nilsson, J. Ninkovic, N. Otte, I. Oya, R. Paoletti, J. M. Paredes, M. Pasanen, D. Pascoli, F. Pauss, R. G. Pegna, M. A. Perez-Torres, M. Persic, L. Peruzzo, F. Prada, E. Prandini, N. Puchades, I. Reichardt, W. Rhode, M. Ribó, J. Rico, M. Rissi, A. Robert, S. Rügamer, A. Saggion, T. Y. Saito, M. Salvati, M. Sanchez-Conde, K. Satalecka, V. Scalzotto, V. Scapin, T. Schweizer, M. Shayduk, S. N. Shore, N. Sidro, A. Sierpowska-Bartosik, A. Sillanpää, J. Sitarek, D. Sobczynska, F. Spanier, A. Stamerra, L. S. Stark, L. Takalo, F. Tavecchio, P. Temnikov, D. Tescaro, M. Teshima, M. Tluczykont, D. F. Torres, N. Turini, H. Vankov, R. M. Wagner, W. Wittek, V. Zabalza, F. Zandanel, R. Zanin, and J. Zapatero.
Search for VHE γ-ray Emission from the Globular Cluster M13 with the Magic Telescope.
ApJ, 702:266–269, September 2009.

26, 153, 156, 157, 159, 163, 164, 165, 166, 167, 168, 185

[25] S. B. Anderson.
A study of recycled pulsars in globular clusters.
PhD thesis, California Institute of Technology, Pasadena., 1993.
173

[26] A. M. Archibald, I. H. Stairs, S. M. Ransom, V. M. Kaspi, V. I. Kondratiev, D. R. Lorimer, M. A. McLaughlin, J. Boyles, J. W. T. Hessels, R. Lynch, J. van Leeuwen, M. S. E. Roberts, F. Jenet, D. J. Champion, R. Rosen, B. N. Barlow, B. H. Dunlap, and R. A. Remillard.
A Radio Pulsar/X-ray Binary Link.
Science, 324:1411–, June 2009.
22

[27] J. Arons.
Theory of pulsar winds.
Advances in Space Research, 33:466–474, 2004.
36, 186, 187, 188, 189

[28] J. Arons.
Pulsar Emission: Where to Go.
In W. Becker, editor, *Astrophysics and Space Science Library*, volume 357 of *Astrophysics and Space Science Library*, pages 373–+, 2009.
36, 191

[29] J. Arons.
A Tale of Two Current Sheets.
In D. F. Torres & N. Rea, editor, *High-Energy Emission from Pulsars and their Systems, Astrophysics and Space Science Proceedings, ISBN 978-3-642-17250-2. Springer-Verlag Berlin Heidelberg, 2011, p. 165*, pages 165–+, 2011.
192

[30] J. Arons, D. C. Backer, A. Spitkovsky, and V. M. Kaspi.
Probing Relativistic Winds: The Case of PSR J0737-3039 A and B.
In F. A. Rasio & I. H. Stairs, editor, *Binary Radio Pulsars*, volume 328 of *Astronomical Society of the Pacific Conference Series*, page 95, July 2005.
62

[31] F. Arqueros, G. Ros, G. R. Elorza, and D. García-Pinto.
A technique for the optical characterization of imaging air-Cherenkov telescopes.
Astroparticle Physics, 24:137–145, September 2005.
79

[32] R. Atkins, W. Benbow, D. Berley, M.-L. Chen, D. G. Coyne, R. S. Delay, B. L. Dingus, D. E. Dorfan, R. W. Ellsworth, C. Espinoza, D. Evans, A. Falcone, L. Fleysher, R. Fleysher, G. Gisler, J. A. Goodman, T. J. Haines, C. M. Hoffman, S. Hugenberger, L. A. Kelley, S. Klein, I. Leonor, J. Macri, M. McConnell, J. F. McCullough, J. E. McEnery, R. S. Miller, A. I. Mincer, M. F. Morales, M. M. Murray, P. Nemethy, G. Paliaga, J. M. Ryan, M. Schneider, B. Shen, A. Shoup, G. Sinnis, A. J. Smith, G. W. Sullivan, T. N. Thompson, O. T. Tumer, K. Wang, M. O. Wascko, S. Westerhoff, D. A. Williams, T. Yang, and G. B. Yodh.
Milagrito, a TeV air-shower array.
Nuclear Instruments and Methods in Physics Research A, 449:478–499, July 2000.

[33] W. B. Atwood, A. A. Abdo, M. Ackermann, W. Althouse, B. Anderson, M. Axelsson, L. Baldini, J. Ballet, D. L. Band, G. Barbiellini, and et al.
The Large Area Telescope on the Fermi Gamma-Ray Space Telescope Mission.
ApJ, 697:1071–1102, June 2009.
11

[34] X.-N. Bai and A. Spitkovsky.
Modeling of Gamma-ray Pulsar Light Curves Using the Force-free Magnetic Field.
ApJ, 715:1282–1301, June 2010.
61, 185, 192

[35] W. Becker, H. H. Huang, and T. Prinz.
X-ray Counterparts of Millisecond Pulsars in Globular Clusters.
ArXiv e-prints, June 2010.
177

[36] W. Bednarek and J. Sitarek.
High-energy γ-rays from globular clusters.

MNRAS, 377:920–930, May 2007.
iii, v, xix, 24, 39, 133, 168

[37] D. Berge, S. Funk, and J. Hinton.
Background modelling in very-high-energy γ-ray astronomy.
A&A, 466:1219–1229, May 2007.
122, 125

[38] B. Bertotti.
Rotating Neutron Stars and Pulsar Emission.
Nature, 221:624–626, February 1969.
30

[39] N. D. R. Bhat, J. M. Cordes, F. Camilo, D. J. Nice, and D. R. Lorimer.
Multifrequency Observations of Radio Pulse Broadening and Constraints on Interstellar Electron Density Microstructure.
ApJ, 605:759–783, April 2004.
173

[40] J. D. Biggs.
Meridional Compression of Radio Pulsar Beams.
MNRAS, 245:514–+, July 1990.
177

[41] P. M. S. Blackett.
A possible contribution to the night sky from the Cerenkov radiation emitted by cosmic rays.
In *The Emission Spectra of the Night Sky and Aurorae*, page 34, 1948.
72

[42] G. R. Blumenthal and R. J. Gould.
Bremsstrahlung, Synchrotron Radiation, and Compton Scattering of High-Energy Electrons Traversing Dilute Gases.
Reviews of Modern Physics, 42:237–271, 1970.
42, 44, 47, 50, 60

[43] S. Bogdanov and J. E. Grindlay.
An X-ray View of Radio Millisecond Pulsars.
In C. Bassa, Z. Wang, A. Cumming, & V. M. Kaspi, editor, *40 Years of Pulsars: Millisecond Pulsars, Magnetars and More*, volume 983 of *American Institute of Physics Conference Series*, pages 64–68, February 2008.

177

[44] S. Bogdanov, J. E. Grindlay, C. O. Heinke, F. Camilo, P. C. C. Freire, and W. Becker.
Chandra X-Ray Observations of 19 Millisecond Pulsars in the Globular Cluster 47 Tucanae.
ApJ, 646:1104–1115, August 2006.
31, 172, 177, 179, 181, 182

[45] A. Borione, M. Catanese, C. E. Covault, J. W. Cronin, B. E. Fick, K. G. Gibbs, K. D. Green, D. Kieda, T. A. McKay, J. Matthews, B. J. Newport, D. Nitz, R. A. Ong, L. J. Rosenberg, D. Sinclair, and J. C. van der Velde.
A Search for 100 TeV Gamma-Ray Emission from Cygnus X-3 and Hercules X-1 with CASA-MIA.
In *International Cosmic Ray Conference*, volume 1 of *International Cosmic Ray Conference*, pages 385–+, 1993.
6

[46] J. Boyles, D. R. Lorimer, P. J. Turk, R. Mnatsakanov, R. S. Lynch, S. M. Ransom, P. C. Freire, and K. Belczynski.
Young Radio Pulsars in Galactic Globular Clusters.
ApJ, 742:51, November 2011.
22, 205

[47] R. Buckley.
Acceleration of Charged Particles to Extremely High-Energies in Pulsar Far Fields.
Nature, 266:37–38, 1977.
187

[48] R. Buckley.
Pulsar magnetospheres with arbitrary geometry in the force-free approximation.
MNRAS, 180:125–140, July 1977.
187

[49] Y. M. Butt, J. Drake, P. Benaglia, J. A. Combi, T. Dame, F. Miniati, and G. E. Romero.
Deeper Chandra Follow-up of Cygnus TeV Source Perpetuates Mystery.
ApJ, 643:238–244, May 2006.

15, 206

[50] F. Camilo, D. R. Lorimer, P. Freire, A. G. Lyne, and R. N. Manchester.
Observations of 20 Millisecond Pulsars in 47 Tucanae at 20 Centimeters.
ApJ, 535:975–990, June 2000.
172, 174, 176

[51] F. Camilo and F. A. Rasio.
Pulsars in Globular Clusters.
In F. A. Rasio & I. H. Stairs, editor, *Binary Radio Pulsars*, volume 328 of *Astronomical Society of the Pacific Conference Series*, pages 147–+, July 2005.
174, 176

[52] F. Camilo, P. S. Ray, S. M. Ransom, M. Burgay, T. J. Johnson, M. Kerr, E. V. Gotthelf, J. P. Halpern, J. Reynolds, R. W. Romani, P. Demorest, S. Johnston, W. van Straten, P. M. Saz Parkinson, M. Ziegler, M. Dormody, D. J. Thompson, D. A. Smith, A. K. Harding, A. A. Abdo, F. Crawford, P. C. C. Freire, M. Keith, M. Kramer, M. S. E. Roberts, P. Weltevrede, and K. S. Wood.
Radio Detection of LAT PSRs J1741-2054 and J2032+4127: No Longer Just Gamma-ray Pulsars.
ApJ, 705:1–13, November 2009.
15, 206

[53] M. Catanese, A. Borione, C. E. Covault, J. W. Cronin, B. E. Fick, L. F. Fortson, K. G. Gibbs, M. A. K. Glasmacher, K. D. Green, D. Kieda, J. Matthews, B. J. Newport, D. Nitz, R. A. Ong, D. Sinclair, and J. C. van der Velde.
A Search for Ultrahigh-Energy Gamma Rays from EGRET-detected Active Galactic Nuclei Using CASA-MIA.
ApJ, 469:572–+, October 1996.
6

[54] M. F. Cawley, J. Clear, D. J. Fegan, N. A. Porter, K. Gibbs, P. Gorham, V. S. Stenger, R. C. Lamb, I. Macrae, and P. K. MacKeown.
Application of two dimensional imaging of atmospheric Cerenkov light to very high energy gamma ray astronomy.
In N. Durgaprasad, S. Ramadurai, P. V. Ramana Murthy, M. V. S. Rao, & K. Sivaprasad, editor, *International Cosmic Ray Conference*, vol-

ume 1 of *International Cosmic Ray Conference*, pages 118–121, August 1983.
96

[55] R. C. G. Chaves, E. de Oña Wilhemi, and S. Hoppe.
The H.E.S.S. Galactic Plane Survey.
In F. A. Aharonian, W. Hofmann, & F. Rieger, editor, *American Institute of Physics Conference Series*, volume 1085 of *American Institute of Physics Conference Series*, pages 219–222, December 2008.
15

[56] A. Cheng, M. Ruderman, and P. Sutherland.
Current flow in pulsar magnetospheres.
ApJ, 203:209–212, January 1976.
40

[57] K. S. Cheng, R. E. Taam, and W. Wang.
Pulsar Wind Nebulae and the Nonthermal X-Ray Emission of Millisecond Pulsars.
ApJ, 641:427–437, April 2006.
192

[58] G. W. Clark.
X-ray binaries in globular clusters.
ApJ, 199:L143–L145, August 1975.
23

[59] I. Contopoulos and D. Kazanas.
Toward Resolving the Crab σ-Problem: A Linear Accelerator?
ApJ, 566:336–342, February 2002.
187

[60] J. M. Cordes and T. J. W. Lazio.
NE2001.I. A New Model for the Galactic Distribution of Free Electrons and its Fluctuations.
ArXiv Astrophysics e-prints, July 2002.
173

[61] F. V. Coroniti.
Magnetically striped relativistic magnetohydrodynamic winds - The Crab Nebula revisited.
ApJ, 349:538–545, February 1990.

189

[62] M. K. Daniel.
The VERITAS standard data analysis.
In *International Cosmic Ray Conference*, volume 3 of *International Cosmic Ray Conference*, pages 1325–1328, 2008.
119, 133, 138

[63] F. D'Antona and V. Caloi.
The fraction of second generation stars in globular clusters from the analysis of the horizontal branch.
MNRAS, 390:693–705, October 2008.

[64] F. D'Antona, P. Ventura, V. Caloi, A. D'Ercole, E. Vesperini, R. Carini, and M. Di Criscienzo.
Terzan 5: An Alternative Interpretation for the Split Horizontal Branch.
ApJ, 715:L63–L67, June 2010.
27

[65] A. Daum, G. Hermann, M. Hess, W. Hofmann, H. Lampeitl, G. Pühlhofer, F. Aharonian, A. G. Akhperjanian, J. A. Barrio, A. S. Beglarian, K. Bernlöhr, J. J. G. Beteta, S. M. Bradbury, J. L. Contreras, J. Cortina, T. Deckers, E. Feigl, J. Fernandez, V. Fonseca, A. Frass, B. Funk, J. C. Gonzalez, G. Heinzelmann, M. Hemberger, A. Heusler, I. Holl, D. Horns, R. Kankanyan, O. Kirstein, C. Köhler, A. Konopelko, D. Kranich, H. Krawczynski, H. Kornmayer, A. Lindner, E. Lorenz, N. Magnussen, H. Meyer, R. Mirzoyan, H. Möller, A. Moralejo, L. Padilla, M. Panter, D. Petry, R. Plaga, J. Prahl, C. Prosch, G. Rauterberg, W. Rhode, A. Röhring, V. Sahakian, M. Samorski, J. A. Sanchez, D. Schmele, W. Stamm, M. Ulrich, H. J. Völk, S. Westerhoff, B. Wiebel-Sooth, C. A. Wiedner, M. Willmer, and H. Wirth.
First results on the performance of the HEGRA IACT array.
Astroparticle Physics, 8:1–11, December 1997.
15

[66] John M. Davies and Eugene S. Cotton.
Design of the quartermaster solar furnace.
Solar Energy, 1(2-3):16 – 22, 1957.
The Proceedings of the Solar Furnace Symposium.

75

[67] O. C. de Jager and A. K. Harding.
The expected high-energy to ultra-high-energy gamma-ray spectrum of the Crab Nebula.
ApJ, 396:161–172, September 1992.
17

[68] W. T. S. Deich, S. B. Anderson, S. R. Kulkarni, T. A. Prince, and A. Wolszczan.
Orbital Parameters and Timing Results for Pulsars in the Globular Clusters NGC6760, M13, and M53.
In *American Astronomical Society Meeting Abstracts*, volume 24 of *Bulletin of the American Astronomical Society*, pages 1229–+, December 1992.
173

[69] L. Del Zanna, E. Amato, and N. Bucciantini.
Axially symmetric relativistic MHD simulations of Pulsar Wind Nebulae in Supernova Remnants. On the origin of torus and jet-like features.
A&A, 421:1063–1073, July 2004.
189, 191

[70] M. Demleitner, A. Accomazzi, G. Eichhorn, C. S. Grant, M. J. Kurtz, and S. S. Murray.
ADS's Dexter Data Extraction Applet.
In F. R. Harnden Jr., F. A. Primini, & H. E. Payne, editor, *Astronomical Data Analysis Software and Systems X*, volume 238 of *Astronomical Society of the Pacific Conference Series*, pages 321–+, 2001.
57, 58, 165, 166, 179

[71] A. D'Ercole, E. Vesperini, F. D'Antona, S. L. W. McMillan, and S. Recchi.
Formation and dynamical evolution of multiple stellar generations in globular clusters.
MNRAS, 391:825–843, December 2008.

[72] D. J. Fegan.
TOPICAL REVIEW: γ/hadron separation at TeV energies.
Journal of Physics G Nuclear Physics, 23:1013–1060, September 1997.

96, 103

[73] F. R. Ferraro.
The true nature of Terzan 5: the most efficient "furnace" of MSPs in the Galaxy.
In *American Institute of Physics Conference Series*, volume 1357 of *American Institute of Physics Conference Series*, pages 147–150, August 2011.
27

[74] F. R. Ferraro, E. Dalessandro, A. Mucciarelli, G. Beccari, R. M. Rich, L. Origlia, B. Lanzoni, R. T. Rood, E. Valenti, M. Bellazzini, S. M. Ransom, and G. Cocozza.
The cluster Terzan 5 as a remnant of a primordial building block of the Galactic bulge.
Nature, 462:483–486, November 2009.
27, 207

[75] P. C. Freire, F. Camilo, M. Kramer, D. R. Lorimer, A. G. Lyne, R. N. Manchester, and N. D'Amico.
Further results from the timing of the millisecond pulsars in 47 Tucanae.
MNRAS, 340:1359–1374, April 2003.
172

[76] P. C. Freire, F. Camilo, D. R. Lorimer, A. G. Lyne, R. N. Manchester, and N. D'Amico.
Timing the millisecond pulsars in 47 Tucanae.
MNRAS, 326:901–915, September 2001.
172

[77] P. C. Freire, M. Kramer, A. G. Lyne, F. Camilo, R. N. Manchester, and N. D'Amico.
Detection of Ionized Gas in the Globular Cluster 47 Tucanae.
ApJ, 557:L105–L108, August 2001.
197

[78] A. S. Fruchter, G. Berman, G. Bower, M. Convery, W. M. Goss, T. H. Hankins, J. R. Klein, D. J. Nice, M. F. Ryba, D. R. Stinebring, J. H. Taylor, S. E. Thorsett, and J. M. Weisberg.
The eclipsing millisecond pulsar PSR 1957 + 20.
ApJ, 351:642–650, March 1990.

31

[79] A. S. Fruchter and W. M. Goss.
The integrated flux density of pulsars in globular clusters.
ApJ, 365:L63–L66, December 1990.
23

[80] A. S. Fruchter, D. R. Stinebring, and J. H. Taylor.
A millisecond pulsar in an eclipsing binary.
Nature, 333:237–239, May 1988.
31

[81] N. D. Gagunashvili.
Comparison of weighted and unweighted histograms.
ArXiv Physics e-prints, May 2006.
147

[82] W. Galbraith and J. V. Jelley.
Light Pulses from the Night Sky associated with Cosmic Rays.
Nature, 171:349–350, February 1953.
14

[83] K. Gibbs, S. Criswell, A. Falcone, J. Gaidos, K. Harris, D. Horan, M. Schroedter, T. C. Weekes, and J. T. Williams.
The VERITAS Atmospheric Cerenkov Telescopes: Positioner, Optics and Associated Components.
In *International Cosmic Ray Conference*, volume 5 of *International Cosmic Ray Conference*, pages 2823–+, July 2003.
75

[84] T. Gold.
Rotating Neutron Stars as the Origin of the Pulsating Radio Sources.
Nature, 218:731–732, May 1968.
30

[85] P. Goldreich and W. H. Julian.
Pulsar Electrodynamics.
ApJ, 157:869–+, August 1969.
30, 33, 34

[86] J. Goodman and P. Hut.
Primordial binaries and globular cluster evolution.
Nature, 339:40–42, May 1989.

20

[87] J. E. Grindlay, F. Camilo, C. O. Heinke, P. D. Edmonds, H. Cohn, and P. Lugger.
Chandra Study of a Complete Sample of Millisecond Pulsars in 47 Tucanae and NGC 6397.
ApJ, 581:470–484, December 2002.
20

[88] J. E. Grindlay, C. O. Heinke, P. D. Edmonds, S. S. Murray, and F. Camilo.
Deepest Globular Cluster X-ray Survey: Chandra on 47Tuc.
In *American Astronomical Society Meeting Abstracts*, volume 32 of *Bulletin of the American Astronomical Society*, pages 126.06–+, December 2000.
172

[89] G. M. H. J. Habets and J. R. W. Heintze.
Empirical bolometric corrections for the main-sequence.
A&AS, 46:193–237, November 1981.
59

[90] T. A. Hall, I. H. Bond, S. M. Bradbury, J. H. Buckley, M. J. Carson, D. A. Carter-Lewis, M. Catanese, S. Dunlea, M. D'Vali, D. J. Fegan, S. J. Fegan, J. P. Finley, J. A. Gaidos, G. H. Gillanders, A. M. Hillas, D. Horan, M. Kertzman, D. Kieda, J. Kildea, J. Knapp, F. Krennrich, M. J. Lang, S. LeBohec, R. Lessard, J. Lloyd-Evans, B. McKernan, P. Moriarty, D. Muller, R. Ong, J. Quinn, P. T. Reynolds, H. J. Rose, G. H. Sembroski, S. P. Swordy, V. V. Vassiliev, and T. C. Weekes.
Search for TeV Emissions from Pulsars in Binary Systems.
ApJ, 583:853–860, February 2003.
24

[91] D. Hanna, A. McCann, M. McCutcheon, and L. Nikkinen.
An LED-based flasher system for VERITAS.
Nuclear Instruments and Methods in Physics Research A, 612:278–287, January 2010.
xxii, 93

[92] A. K. Harding and A. G. Muslimov.

Particle Acceleration Zones above Pulsar Polar Caps: Electron and Positron Pair Formation Fronts.
ApJ, 508:328–346, November 1998.
37, 39

[93] A. K. Harding and A. G. Muslimov.
Pulsar Pair Cascades in a Distorted Magnetic Dipole Field.
ApJ, 726:L10+, January 2011.
185, 187, 191

[94] W. E. Harris.
A Catalog of Parameters for Globular Clusters in the Milky Way.
AJ, 112:1487–+, October 1996.
59, 179

[95] W. E. Harris.
A New Catalog of Globular Clusters in the Milky Way.
ArXiv e-prints, December 2010.
19, 54, 203, 204

[96] E. Hecht.
Optics.
Addison-Wesley, 2002.
77

[97] D. C. Heggie.
Binary evolution in stellar dynamics.
MNRAS, 173:729–787, December 1975.
20

[98] C. O. Heinke, J. E. Grindlay, P. D. Edmonds, H. N. Cohn, P. M. Lugger, F. Camilo, S. Bogdanov, and P. C. Freire.
A Deep Chandra Survey of the Globular Cluster 47 Tucanae: Catalog of Point Sources.
ApJ, 625:796–824, June 2005.
172, 177

[99] O. Helene.
Upper limit of peak area.
Nuclear Instruments and Methods in Physics Research, 212:319–322, July 1983.
151, 152, 153, 163

[100] H.E.S.S. Collaboration, A. Abramowski, F. Acero, F. Aharonian, A. G. Akhperjanian, G. Anton, A. Balzer, A. Barnacka, U. Barres de Almeida, Y. Becherini, J. Becker, B. Behera, K. Bernlöhr, A. Bochow, C. Boisson, J. Bolmont, P. Bordas, J. Brucker, F. Brun, P. Brun, T. Bulik, I. Büsching, S. Carrigan, S. Casanova, M. Cerruti, P. M. Chadwick, A. Charbonnier, R. C. G. Chaves, A. Cheesebrough, L.-M. Chounet, A. C. Clapson, G. Coignet, G. Cologna, J. Conrad, M. Dalton, M. K. Daniel, I. D. Davids, B. Degrange, C. Deil, H. J. Dickinson, A. Djannati-Ataï, W. Domainko, L. O. Drury, F. Dubois, G. Dubus, K. Dutson, J. Dyks, M. Dyrda, K. Egberts, P. Eger, P. Espigat, L. Fallon, C. Farnier, S. Fegan, F. Feinstein, M. V. Fernandes, A. Fiasson, G. Fontaine, A. Förster, M. Füßling, Y. A. Gallant, H. Gast, L. Gérard, D. Gerbig, B. Giebels, J. F. Glicenstein, B. Glück, P. Goret, D. Göring, S. Häffner, J. D. Hague, D. Hampf, M. Hauser, S. Heinz, G. Heinzelmann, G. Henri, G. Hermann, J. A. Hinton, A. Hoffmann, W. Hofmann, P. Hofverberg, M. Holler, D. Horns, A. Jacholkowska, O. C. de Jager, C. Jahn, M. Jamrozy, I. Jung, M. A. Kastendieck, K. Katarzyński, U. Katz, S. Kaufmann, D. Keogh, D. Khangulyan, B. Khélifi, D. Klochkov, W. Kluźniak, T. Kneiske, N. Komin, K. Kosack, R. Kossakowski, H. Laffon, G. Lamanna, D. Lennarz, T. Lohse, A. Lopatin, C.-C. Lu, V. Marandon, A. Marcowith, J. Masbou, D. Maurin, N. Maxted, T. J. L. McComb, M. C. Medina, J. Méhault, R. Moderski, E. Moulin, C. L. Naumann, M. Naumann-Godo, M. de Naurois, D. Nedbal, D. Nekrassov, N. Nguyen, B. Nicholas, J. Niemiec, S. J. Nolan, S. Ohm, D. de Oña Wilhelmi, B. Opitz, M. Ostrowski, I. Oya, M. Panter, M. Paz Arribas, G. Pedaletti, G. Pelletier, P.-O. Petrucci, S. Pita, G. Pühlhofer, M. Punch, A. Quirrenbach, M. Raue, S. M. Rayner, A. Reimer, O. Reimer, M. Renaud, R. de los Reyes, F. Rieger, J. Ripken, L. Rob, S. Rosier-Lees, G. Rowell, B. Rudak, C. B. Rulten, J. Ruppel, F. Ryde, V. Sahakian, A. Santangelo, R. Schlickeiser, F. M. Schöck, A. Schulz, U. Schwanke, S. Schwarzburg, S. Schwemmer, M. Sikora, J. L. Skilton, H. Sol, G. Spengler, Ł. Stawarz, R. Steenkamp, C. Stegmann, F. Stinzing, K. Stycz, I. Sushch, A. Szostek, J.-P. Tavernet, R. Terrier, M. Tluczykont, K. Valerius, C. van Eldik, G. Vasileiadis, C. Venter, J. P. Vialle, A. Viana, P. Vincent, H. J. Völk, F. Volpe, S. Vorobiov, M. Vorster, S. J.

Wagner, M. Ward, R. White, A. Wierzcholska, M. Zacharias, A. Zajczyk, A. A. Zdziarski, A. Zech, and H.-S. Zechlin.
Very-high-energy gamma-ray emission from the direction of the Galactic globular cluster Terzan 5.
A&A, 531:L18+, July 2011.
26, 206

[101] J. W. T. Hessels, D. J. Nice, B. M. Gaensler, V. M. Kaspi, D. R. Lorimer, D. J. Champion, A. G. Lyne, M. Kramer, J. M. Cordes, P. C. C. Freire, F. Camilo, S. M. Ransom, J. S. Deneva, N. D. R. Bhat, I. Cognard, F. Crawford, F. A. Jenet, L. Kasian, P. Lazarus, J. van Leeuwen, M. A. McLaughlin, I. H. Stairs, B. W. Stappers, and A. Venkataraman.
PSR J1856+0245: Arecibo Discovery of a Young, Energetic Pulsar Coincident with the TeV γ-Ray Source HESS J1857+026.
ApJ, 682:L41–L44, July 2008.
198, 207, 208

[102] J. W. T. Hessels, S. M. Ransom, I. H. Stairs, P. C. C. Freire, V. M. Kaspi, and F. Camilo.
A Radio Pulsar Spinning at 716 Hz.
Science, 311:1901–1904, March 2006.
22, 26

[103] J. W. T. Hessels, S. M. Ransom, I. H. Stairs, V. M. Kaspi, and P. C. C. Freire.
A 1.4 GHz Arecibo Survey for Pulsars in Globular Clusters.
ApJ, 670:363–378, November 2007.
173, 174, 175, 176, 177

[104] A. Hewish, S. J. Bell, J. D. H. Pilkington, P. F. Scott, and R. A. Collins.
Observation of a Rapidly Pulsating Radio Source.
Nature, 217:709–713, February 1968.
30

[105] J. A. Hibschman and J. Arons.
Pair Production Multiplicities in Rotation-powered Pulsars.
ApJ, 560:871–884, October 2001.
37, 187

[106] A. M. Hillas.
Cerenkov light images of EAS produced by primary gamma.

In F. C. Jones, editor, *International Cosmic Ray Conference*, volume 3 of *International Cosmic Ray Conference*, pages 445–448, August 1985.
96, 103

[107] A. M. Hillas.
Differences between Gamma-Ray and Hadronic Showers.
Space Sci. Rev., 75:17–30, January 1996.
96, 98

[108] G. Hobbs, D. R. Lorimer, A. G. Lyne, and M. Kramer.
A statistical study of 233 pulsar proper motions.
MNRAS, 360:974–992, July 2005.
205, 206

[109] W. Hofmann.
The Very High Energy Gamma Ray Sky Viewed with H.E.S.S.
In *American Astronomical Society Meeting Abstracts #217*, volume 43 of *Bulletin of the American Astronomical Society*, page 330.01, January 2011.
15

[110] J. Holder.
Exploiting VERITAS Timing Information.
In *International Cosmic Ray Conference*, volume 5 of *International Cosmic Ray Conference*, pages 383–+, 2005.
106

[111] J. Holder, I. H. Bond, P. J. Boyle, S. M. Bradbury, J. H. Buckley, D. A. Carter-Lewis, W. Cui, C. Dowdall, C. Duke, I. de la Calle Perez, A. Falcone, D. J. Fegan, S. J. Fegan, J. P. Finley, L. Fortson, J. A. Gaidos, K. Gibbs, S. Gammell, J. Hall, T. A. Hall, A. M. Hillas, D. Horan, M. Jordan, M. Kertzman, D. Kieda, J. Kildea, J. Knapp, K. Kosack, H. Krawczynski, F. Krennrich, S. LeBohec, E. T. Linton, J. Lloyd-Evans, P. Moriarty, D. Müller, T. N. Nagai, R. Ong, M. Page, R. Pallassini, D. Petry, B. Power-Mooney, J. Quinn, P. Rebillot, P. T. Reynolds, H. J. Rose, M. Schroedter, G. H. Sembroski, S. P. Swordy, V. V. Vassiliev, S. P. Wakely, G. Walker, and T. C. Weekes.
Detection of TeV Gamma Rays from the BL Lacertae Object 1ES 1959+650 with the Whipple 10 Meter Telescope.

ApJ, 583:L9–L12, January 2003.
14

[112] N. J. Holloway.
Pulsars-p-n junctions in pulsar magnetospheres.
Nature, 246:6–+, November 1973.
40

[113] N. J. Holloway and M. H. L. Pryce.
Properties of gaps in pulsar magnetospheres.
MNRAS, 194:95–110, January 1981.
40

[114] C. Y. Hui, K. S. Cheng, and R. E. Taam.
Dynamical Formation of Millisecond Pulsars in Globular Clusters.
ApJ, 714:1149–1154, May 2010.
175

[115] P. Hut, S. McMillan, J. Goodman, M. Mateo, E. S. Phinney, C. Pryor, H. B. Richer, F. Verbunt, and M. Weinberg.
Binaries in globular clusters.
PASP, 104:981–1034, November 1992.
178

[116] N. Ivanova, C. O. Heinke, F. A. Rasio, K. Belczynski, and J. M. Fregeau.
Formation and evolution of compact binaries in globular clusters - II. Binaries with neutron stars.
MNRAS, 386:553–576, May 2008.
21, 22, 23, 205, 206

[117] N. Ivanova, C. O. Heinke, F. A. Rasio, R. E. Taam, K. Belczynski, and J. Fregeau.
Formation and evolution of compact binaries in globular clusters - I. Binaries with white dwarfs.
MNRAS, 372:1043–1059, November 2006.
21

[118] J. V. Jelley.
The atmospheric Cherenkov technique in gamma-ray astronomy - The early days.
Royal Society of London Philosophical Transactions Series A, 301:611–614, June 1981.

70, 72

[119] F. C. Jones.
Calculated Spectrum of Inverse-Compton-Scattered Photons.
Physical Review, 167:1159–1169, March 1968.
47

[120] Patrick Jordan and Frank Krennrich.
The design of light concentrators for a 12 m cherenkov telescope.
Design, 2004.
83

[121] J. I. Katz.
Two kinds of stellar collapse.
Nature, 253:698–+, February 1975.
23

[122] C. F. Kennel and F. V. Coroniti.
Confinement of the Crab pulsar's wind by its supernova remnant.
ApJ, 283:694–709, August 1984.
56, 187, 191

[123] C. F. Kennel and F. V. Coroniti.
Magnetohydrodynamic model of Crab nebula radiation.
ApJ, 283:710–730, August 1984.
187, 191

[124] J. Kildea, R. W. Atkins, H. M. Badran, G. Blaylock, I. H. Bond, S. M. Bradbury, J. H. Buckley, D. A. Carter-Lewis, O. Celik, Y. C. K. Chow, W. Cui, P. Cogan, M. K. Daniel, I. de La Calle Perez, C. Dowdall, C. Duke, A. D. Falcone, D. J. Fegan, S. J. Fegan, J. P. Finley, L. F. Fortson, D. Gall, G. H. Gillanders, J. Grube, K. J. Gutierrez, J. Hall, T. A. Hall, J. Holder, D. Horan, S. B. Hughes, M. Jordan, I. Jung, G. E. Kenny, M. Kertzman, J. Knapp, A. Konopelko, K. Kosack, H. Krawczynski, F. Krennrich, M. J. Lang, S. Lebohec, J. Lloyd-Evans, J. Millis, P. Moriarty, T. Nagai, P. A. Ogden, R. A. Ong, J. S. Perkins, D. Petry, F. Pizlo, M. Pohl, J. Quinn, M. Quinn, P. F. Rebillot, H. J. Rose, M. Schroedter, G. H. Sembroski, A. W. Smith, A. Syson, J. A. Toner, L. Valcarcel, V. V. Vassiliev, S. P. Wakely, T. C. Weekes, and R. J. White.
The Whipple Observatory 10 m gamma-ray telescope, 1997 2006.
Astroparticle Physics, 28:182–195, October 2007.

14

[125] A. R. King, M. E. Beer, D. J. Rolfe, K. Schenker, and J. M. Skipp.
The population of black widow pulsars.
MNRAS, 358:1501–1504, April 2005.

[126] I. King.
The structure of star clusters. I. an empirical density law.
AJ, 67:471–+, October 1962.
52, 53, 54, 178, 181

[127] I. R. King.
The structure of star clusters. III. Some simple dynamical models.
AJ, 71:64–+, February 1966.
20, 52, 54, 181

[128] I. R. King, E. Hedemann, Jr., S. M. Hodge, and R. E. White.
The Structure of Star Clusters. V. Star Counts in 54 Globular Clusters.
AJ, 73:456–+, August 1968.
52, 181

[129] J. G. Kirk.
Dissipation in pulsar winds.
Advances in Space Research, 37:1970–1974, 2006.
189

[130] J. G. Kirk, Y. Lyubarsky, and J. Petri.
The Theory of Pulsar Winds and Nebulae.
In W. Becker, editor, *Astrophysics and Space Science Library*, volume 357 of *Astrophysics and Space Science Library*, pages 421–+, 2009.
187, 189

[131] J. G. Kirk and O. Skjæraasen.
Dissipation in Poynting-Flux-dominated Flows: The σ-Problem of the Crab Pulsar Wind.
ApJ, 591:366–379, July 2003.
189

[132] F. S. Kitaura, H.-T. Janka, and W. Hillebrandt.
Explosions of O-Ne-Mg cores, the Crab supernova, and subluminous type II-P supernovae.
A&A, 450:345–350, April 2006.
206

[133] S. S. Komissarov and Y. E. Lyubarsky.
Synchrotron nebulae created by anisotropic magnetized pulsar winds.
MNRAS, 349:779–792, April 2004.
189

[134] K. Kosack, H. M. Badran, I. H. Bond, P. J. Boyle, S. M. Bradbury, J. H. Buckley, D. A. Carter-Lewis, O. Celik, V. Connaughton, W. Cui, M. Daniel, M. D'Vali, I. de la Calle Perez, C. Duke, A. Falcone, D. J. Fegan, S. J. Fegan, J. P. Finley, L. F. Fortson, J. A. Gaidos, S. Gammell, K. Gibbs, G. H. Gillanders, J. Grube, K. Gutierrez, J. Hall, T. A. Hall, D. Hanna, A. M. Hillas, J. Holder, D. Horan, A. Jarvis, M. Jordan, G. E. Kenny, M. Kertzman, D. Kieda, J. Kildea, J. Knapp, H. Krawczynski, F. Krennrich, M. J. Lang, S. Le Bohec, E. Linton, J. Lloyd-Evans, A. Milovanovic, J. McEnery, P. Moriarty, D. Muller, T. Nagai, S. Nolan, R. A. Ong, R. Pallassini, D. Petry, B. Power-Mooney, J. Quinn, M. Quinn, K. Ragan, P. Rebillot, P. T. Reynolds, H. J. Rose, M. Schroedter, G. H. Sembroski, S. P. Swordy, A. Syson, V. V. Vassiliev, S. P. Wakely, G. Walker, T. C. Weekes, and J. Zweerink.
TeV Gamma-Ray Observations of the Galactic Center.
ApJ, 608:L97–L100, June 2004.
14

[135] L. M. Krauss.
The End of the Age Problem, and the Case for a Cosmological Constant Revisited.
ApJ, 501:461–+, July 1998.
18

[136] H. Krawczynski, D. A. Carter-Lewis, C. Duke, J. Holder, G. Maier, S. Le Bohec, and G. Sembroski.
Gamma hadron separation methods for the VERITAS array of four imaging atmospheric Cherenkov telescopes.
Astroparticle Physics, 25:380–390, July 2006.
98, 99, 111, 119, 138

[137] S. R. Kulkarni, S. B. Anderson, T. A. Prince, and A. Wolszczan.
Old pulsars in the low-density globular clusters M13 and M53.
Nature, 349:47–49, January 1991.
173

[138] S. R. Kulkarni, R. Narayan, and R. W. Romani.
The pulsar content of globular clusters.
ApJ, 356:174–183, June 1990.
23

[139] A. G. Kuranov and K. A. Postnov.
Neutron stars in globular clusters: Formation and observational manifestations.
Astronomy Letters, 32:393–405, June 2006.
52, 53, 54, 60, 205

[140] B. Lanzoni, F. R. Ferraro, E. Dalessandro, A. Mucciarelli, G. Beccari, P. Miocchi, M. Bellazzini, R. M. Rich, L. Origlia, E. Valenti, R. T. Rood, and S. M. Ransom.
New Density Profile and Structural Parameters of the Complex Stellar System Terzan 5.
ApJ, 717:653–657, July 2010.
27

[141] T.-P. Li and Y.-Q. Ma.
Analysis methods for results in gamma-ray astronomy.
ApJ, 272:317–324, September 1983.
100, 126, 127, 143, 146, 147

[142] M. S. Longair.
High energy astrophysics. Vol.1: Particles, photons and their detection.
March 1992.
42

[143] M. S. Longair.
High energy astrophysics. Volume 2. Stars, the Galaxy and the interstellar medium.
1994.
70

[144] D. R. Lorimer.
The Galactic Population and Birth Rate of Radio Pulsars.
In F. Camilo & B. M. Gaensler, editor, *Young Neutron Stars and Their Environments*, volume 218 of *IAU Symposium*, pages 105–+, 2004.
173, 175, 177

[145] D. R. Lorimer, F. Camilo, P. Freire, M. Kramer, A. G. Lyne, R. N. Manchester, and N. D'Amico.

Millisecond Radio Pulsars in 47 Tucanae.
In M. Bailes, D. J. Nice, & S. E. Thorsett, editor, *Radio Pulsars*, volume 302 of *Astronomical Society of the Pacific Conference Series*, page 363, 2003.
26

[146] D. R. Lorimer, A. J. Faulkner, A. G. Lyne, R. N. Manchester, M. Kramer, M. A. McLaughlin, G. Hobbs, A. Possenti, I. H. Stairs, F. Camilo, M. Burgay, N. D'Amico, A. Corongiu, and F. Crawford.
The Parkes Multibeam Pulsar Survey - VI. Discovery and timing of 142 pulsars and a Galactic population analysis.
MNRAS, 372:777–800, October 2006.
176

[147] D. R. Lorimer and M. Kramer.
Handbook of Pulsar Astronomy.
2005.
180, 207

[148] A. G. Lyne, A. Brinklow, J. Middleditch, S. R. Kulkarni, and D. C. Backer.
The discovery of a millisecond pulsar in the globular cluster M28.
Nature, 328:399–401, July 1987.
183

[149] A. G. Lyne and R. N. Manchester.
The shape of pulsar radio beams.
MNRAS, 234:477–508, October 1988.
177

[150] A. G. Lyne, R. N. Manchester, D. R. Lorimer, M. Bailes, N. D'Amico, T. M. Tauris, S. Johnston, J. F. Bell, and L. Nicastro.
The Parkes Southern Pulsar Survey - II. Final results and population analysis.
MNRAS, 295:743–755, April 1998.
175

[151] Y. Lyubarsky and J. G. Kirk.
Reconnection in a Striped Pulsar Wind.
ApJ, 547:437–448, January 2001.
189

[152] Y. E. Lyubarsky.
Fast magnetosonic waves in pulsar winds.
MNRAS, 339:765–771, March 2003.
189

[153] Y. E. Lyubarsky.
The termination shock in a striped pulsar wind.
MNRAS, 345:153–160, October 2003.
197

[154] R. N. Manchester, G. B. Hobbs, A. Teoh, and M. Hobbs.
The Australia Telescope National Facility Pulsar Catalogue.
AJ, 129:1993–2006, April 2005.
175, 177, 182, 183, 184

[155] O. Maron, J. Kijak, M. Kramer, and R. Wielebinski.
Pulsar spectra of radio emission.
A&AS, 147:195–203, December 2000.
175

[156] A. McCann.
Discovery of the Crab Pulsar Above 100 GeV with VERITAS.
PhD thesis, McGill University, Canada, 2011.
16

[157] A. McCann, D. Hanna, J. Kildea, and M. McCutcheon.
A new mirror alignment system for the VERITAS telescopes.
Astroparticle Physics, 32:325–329, January 2010.
xxii, 79, 80, 81

[158] D. McConnell, A. A. Deshpande, T. Connors, and J. G. Ables.
The radio luminosity distribution of pulsars in 47 Tucanae.
MNRAS, 348:1409–1414, March 2004.
176

[159] D. E. McLaughlin.
Binding Energy and the Fundamental Plane of Globular Clusters.
ApJ, 539:618–640, August 2000.
20

[160] L. Mestel.
Pulsars-Oblique rotator model with dense magnetosphere.
Nature, 233:149–+, October 1971.

36

[161] L. Mestel and S. Shibata.
The Axisymmetric Pulsar Magnetosphere - a New Model.
MNRAS, 271:621–+, December 1994.
36, 37

[162] R. W. Michie.
On the distribution of high energy stars in spherical stellar systems.
MNRAS, 125:127–+, 1963.
52

[163] P. Morrison.
On gamma-ray astronomy.
Il Nuovo Cimento (1955-1965), 7:858–865, 1958.
10.1007/BF02745590.
3

[164] A. Muslimov and A. K. Harding.
Toward the Quasi–Steady State Electrodynamics of a Neutron Star.
ApJ, 485:735–+, August 1997.
37, 185

[165] A. G. Muslimov and A. K. Harding.
High-Altitude Particle Acceleration and Radiation in Pulsar Slot Gaps.
ApJ, 606:1143–1153, May 2004.
39

[166] A. G. Muslimov and A. K. Harding.
Particle Acceleration in Pair-starved Pulsars.
ApJ, 617:471–479, December 2004.
39

[167] A. G. Muslimov and A. K. Harding.
Pair-Starved Pulsar Magnetospheres.
ApJ, 692:140–148, February 2009.
39

[168] T. Nagai, R. McKay, G. Sleege, and et al.
Focal Plane Instrumentation of VERITAS.
In *International Cosmic Ray Conference*, volume 3 of *International Cosmic Ray Conference*, pages 1437–1440, 2008.
83

[169] K. Nakamura and Particle Data Group.
Review of Particle Physics.
Journal of Physics G Nuclear Physics, 37(7):075021–+, July 2010.
71

[170] L. Origlia, R. M. Rich, F. R. Ferraro, B. Lanzoni, M. Bellazzini, E. Dalessandro, A. Mucciarelli, E. Valenti, and G. Beccari.
Spectroscopy Unveils the Complex Nature of Terzan 5.
ApJ, 726:L20+, January 2011.
27

[171] F. Pacini.
Rotating Neutron Stars, Pulsars and Supernova Remnants.
Nature, 219:145–146, July 1968.
30

[172] Petter and Hofverberg.
Astrophysics with the h.e.s.s. cherenkov telescopes.
Nuclear Instruments and Methods in Physics Research Section A: Accelerators, Spectrometers, Detectors and Associated Equipment, 639(1):23 – 25, 2011.
¡ce:title¿Proceedings of the Seventh International Workshop on Ring Imaging Cherenkov Detectors¡/ce:title¿.
15

[173] J. D. H. Pilkington, A. Hewish, S. J. Bell, and T. W. Cole.
Observations of some further Pulsed Radio Sources.
Nature, 218:126–129, April 1968.
30

[174] G. Piotto, L. R. Bedin, J. Anderson, I. R. King, S. Cassisi, A. P. Milone, S. Villanova, A. Pietrinferni, and A. Renzini.
A Triple Main Sequence in the Globular Cluster NGC 2808.
ApJ, 661:L53–L56, May 2007.
18

[175] H. C. Plummer.
On the problem of distribution in globular star clusters.
MNRAS, 71:460–470, March 1911.
52

[176] D. Pooley and P. Hut.

Dynamical Formation of Close Binaries in Globular Clusters: Cataclysmic Variables.
ApJ, 646:L143–L146, August 2006.
172, 178, 179

[177] D. Pooley, W. H. G. Lewin, S. F. Anderson, H. Baumgardt, A. V. Filippenko, B. M. Gaensler, L. Homer, P. Hut, V. M. Kaspi, J. Makino, B. Margon, S. McMillan, S. Portegies Zwart, M. van der Klis, and F. Verbunt.
Dynamical Formation of Close Binary Systems in Globular Clusters.
ApJ, 591:L131–L134, July 2003.
20, 172

[178] M. Punch, C. W. Akerlof, M. F. Cawley, M. Chantell, D. J. Fegan, S. Fennell, J. A. Gaidos, J. Hagan, A. M. Hillas, Y. Jiang, A. D. Kerrick, R. C. Lamb, M. A. Lawrence, D. A. Lewis, D. I. Meyer, G. Mohanty, K. S. O'Flaherty, P. T. Reynolds, A. C. Rovero, M. S. Schubnell, G. Sembroski, T. C. Weekes, and C. Wilson.
Detection of TeV photons from the active galaxy Markarian 421.
Nature, 358:477, August 1992.
14

[179] J. Quinn, C. W. Akerlof, S. Biller, J. Buckley, D. A. Carter-Lewis, M. F. Cawley, M. Catanese, V. Connaughton, D. J. Fegan, J. P. Finley, J. Gaidos, A. M. Hillas, R. C. Lamb, F. Krennrich, R. Lessard, J. E. McEnery, D. I. Meyer, G. Mohanty, A. J. Rodgers, H. J. Rose, G. Sembroski, M. S. Schubnell, T. C. Weekes, C. Wilson, and J. Zweerink.
Detection of Gamma Rays with E¿300 GeV from Markarian 501.
ApJ, 456:L83, January 1996.
14

[180] W.L. Quirin.
Probability and statistics.
Harper & Row, 1978.
152

[181] S. M. Ransom.
Twenty Years of Searching for (and Finding) Globular Cluster Pulsars.
In C. Bassa, Z. Wang, A. Cumming, & V. M. Kaspi, editor, *40 Years of Pulsars: Millisecond Pulsars, Magnetars and More*, volume 983

of *American Institute of Physics Conference Series*, pages 415–423, February 2008.
23, 173

[182] S. M. Ransom, J. W. T. Hessels, I. H. Stairs, P. C. C. Freire, F. Camilo, V. M. Kaspi, and D. L. Kaplan.
Twenty-One Millisecond Pulsars in Terzan 5 Using the Green Bank Telescope.
Science, 307:892–896, February 2005.
26

[183] A. Ray and G. Benford.
Electron-positron cascade in pulsar outer gaps.
Phys. Rev. D, 23:2142–2150, May 1981.
40

[184] M. J. Rees and J. E. Gunn.
The origin of the magnetic field and relativistic particles in the Crab Nebula.
MNRAS, 167:1–12, April 1974.
186

[185] E. Roache, R. Irvin, J. S. Perkins, and et al.
Mirror Facets for the VERITAS Telescopes.
In *International Cosmic Ray Conference*, volume 3 of *International Cosmic Ray Conference*, pages 1397–1400, 2008.
76, 77

[186] G. B. Rybicki and A. P. Lightman.
Radiative Processes in Astrophysics.
Wiley-VCH Verlag GmbH, June 1986.
46, 60

[187] M. Salaris and A. Weiss.
Homogeneous age dating of 55 Galactic globular clusters. Clues to the Galaxy formation mechanisms.
A&A, 388:492–503, June 2002.
18

[188] M. Servillat, N. A. Webb, F. Lewis, C. Knigge, M. van den Berg, A. Dieball, and J. Grindlay.
A Dwarf Nova in the Globular Cluster M13.

ApJ, 733:106–+, June 2011.
177

[189] L. Sironi and A. Spitkovsky.
Acceleration of Particles at the Termination Shock of a Relativistic Striped Wind.
ApJ, 741:39–+, November 2011.
197

[190] I. A. Smith.
TeV gamma rays from millisecond pulsars and the detectability of globular clusters.
ApJ, 408:468–470, May 1993.
24

[191] D. N. Spergel.
Evacuation of gas from globular clusters by winds from millisecond pulsars.
Nature, 352:221, July 1991.
18

[192] A. Spitkovsky.
Time-dependent Force-free Pulsar Magnetospheres: Axisymmetric and Oblique Rotators.
ApJ, 648:L51–L54, September 2006.
30, 180

[193] B. W. Stappers, B. M. Gaensler, V. M. Kaspi, M. van der Klis, and W. H. G. Lewin.
An X-ray nebula associated with the millisecond pulsar B1957+20.
Science, 299:1372–1374, 2003.
31, 192

[194] B. W. Stappers, M. H. van Kerkwijk, B. Lane, and S. R. Kulkarni.
The Light Curve of the Companion to PSR J2051-0827.
ApJ, 510:L45–L48, January 1999.
31

[195] P. A. Sturrock.
A Model of Pulsars.
ApJ, 164:529–+, March 1971.
37

[196] P. H. T. Tam, A. K. H. Kong, C. Y. Hui, K. S. Cheng, C. Li, and T.-N. Lu.
Gamma-ray Emission from the Globular Clusters Liller 1, M80, NGC 6139, NGC 6541, NGC 6624, and NGC 6752.
ApJ, 729:90, March 2011.
14

[197] T. M. Tauris and R. N. Manchester.
On the Evolution of Pulsar Beams.
MNRAS, 298:625–636, August 1998.
177

[198] M. Tavani.
Gamma rays from globular clusters.
ApJ, 407:135–141, April 1993.
23

[199] D. J. Thompson, M. Bailes, D. L. Bertsch, J. Cordes, N. D'Amico, J. A. Esposito, J. Finley, R. C. Hartman, W. Hermsen, G. Kanbach, V. M. Kaspi, D. A. Kniffen, L. Kuiper, Y. C. Lin, A. Lyne, R. Manchester, S. M. Matz, H. A. Mayer-Hasselwander, P. F. Michelson, P. L. Nolan, H. Ögelman, M. Pohl, P. V. Ramanamurthy, P. Sreekumar, O. Reimer, J. H. Taylor, and M. Ulmer.
Gamma Radiation from PSR B1055-52.
ApJ, 516:297–306, May 1999.
186

[200] K. Tollefson and HAWC Collaboration.
HAWC: A Wide-Field TeV Gamma-Ray Observatory.
In *AAS/High Energy Astrophysics Division #11*, volume 42 of *Bulletin of the American Astronomical Society*, pages 703–+, February 2010.
6

[201] C. Venter and O. C. de Jager.
Estimates for Very High Energy Gamma Rays from Globular Cluster Pulsars.
In F. A. Aharonian, W. Hofmann, & F. Rieger, editor, *American Institute of Physics Conference Series*, volume 1085 of *American Institute of Physics Conference Series*, pages 277–280, December 2008.
24, 37, 55, 61

[202] C. Venter, O. C. De Jager, and A.-C. Clapson.

Predictions of Gamma-Ray Emission from Globular Cluster Millisecond Pulsars Above 100 MeV.
ApJ, 696:L52–L55, May 2009.
24, 37, 39, 133

[203] C. Venter, A. K. Harding, and L. Guillemot.
Probing Millisecond Pulsar Emission Geometry Using Light Curves from the Fermi/Large Area Telescope.
ApJ, 707:800–822, December 2009.
61, 185

[204] F. Verbunt and W. H. G. Lewin.
Globular Cluster X-ray Sources.
ArXiv Astrophysics e-prints, April 2004.
178

[205] VERITAS Collaboration, E. Aliu, T. Arlen, T. Aune, M. Beilicke, W. Benbow, A. Bouvier, S. M. Bradbury, J. H. Buckley, V. Bugaev, K. Byrum, A. Cannon, A. Cesarini, J. L. Christiansen, L. Ciupik, E. Collins-Hughes, M. P. Connolly, W. Cui, R. Dickherber, C. Duke, M. Errando, A. Falcone, J. P. Finley, G. Finnegan, L. Fortson, A. Furniss, N. Galante, D. Gall, K. Gibbs, G. H. Gillanders, S. Godambe, S. Griffin, J. Grube, R. Guenette, G. Gyuk, D. Hanna, J. Holder, H. Huan, G. Hughes, C. M. Hui, T. B. Humensky, A. Imran, P. Kaaret, N. Karlsson, M. Kertzman, D. Kieda, H. Krawczynski, F. Krennrich, M. J. Lang, M. Lyutikov, A. S. Madhavan, G. Maier, P. Majumdar, S. McArthur, A. McCann, M. McCutcheon, P. Moriarty, R. Mukherjee, P. Nuñez, R. A. Ong, M. Orr, A. N. Otte, N. Park, J. S. Perkins, F. Pizlo, M. Pohl, H. Prokoph, J. Quinn, K. Ragan, L. C. Reyes, P. T. Reynolds, E. Roache, H. J. Rose, J. Ruppel, D. B. Saxon, M. Schroedter, G. H. Sembroski, G. D. Şentürk, A. W. Smith, D. Staszak, G. Tešić, M. Theiling, S. Thibadeau, K. Tsurusaki, J. Tyler, A. Varlotta, V. V. Vassiliev, S. Vincent, M. Vivier, S. P. Wakely, J. E. Ward, T. C. Weekes, A. Weinstein, T. Weisgarber, D. A. Williams, and B. Zitzer.
Detection of Pulsed Gamma Rays Above 100 GeV from the Crab Pulsar.
Science, 334:69–, October 2011.
16, 30, 192

[206] R. F. Webbink.
Structure parameters of galactic globular clusters.
In J. Goodman & P. Hut, editor, *Dynamics of Star Clusters*, volume 113 of *IAU Symposium*, pages 541–577, 1985.
206

[207] T. C. Weekes.
Very high energy gamma-ray astronomy.
2003.
7, 97

[208] T. C. Weekes.
Revealing the Dark Tev Sky:. the Atmospheric Cherenkov Imaging Technique for Very High Energy Gamma-Ray Astronomy.
In K. Sato & J. Hisano, editor, *Energy Budget in the High Energy Universe*, pages 282–302, March 2007.
67, 70, 72

[209] T. C. Weekes, M. F. Cawley, D. J. Fegan, K. G. Gibbs, A. M. Hillas, P. W. Kowk, R. C. Lamb, D. A. Lewis, D. Macomb, N. A. Porter, P. T. Reynolds, and G. Vacanti.
Observation of TeV gamma rays from the Crab nebula using the atmospheric Cerenkov imaging technique.
ApJ, 342:379–395, July 1989.
14

[210] R. J. White.
Rise Time of the Simulated VERITAS 12 m Davies-Cotton Reflector.
In F. A. Aharonian, H. J. Völk, & D. Horns, editor, *High Energy Gamma-Ray Astronomy*, volume 745 of *American Institute of Physics Conference Series*, pages 797–802, February 2005.
76

[211] D. B. Wilson and M. J. Rees.
Induced Compton scattering in pulsar winds.
MNRAS, 185:297–+, October 1978.
187

[212] L. Zhang, K. S. Cheng, Z. J. Jiang, and P. Leung.
Gamma-Ray Luminosity and Death Lines of Pulsars with Outer Gaps.
ApJ, 604:317–327, March 2004.
40

[213] L. Zhang, J. Fang, and S. B. Chen.
High-Energy Properties of Pulsed Emission from Millisecond Pulsars.
ApJ, 666:1165–1173, September 2007.
40

[214] R. Zinn.
The globular cluster system of the galaxy. IV - The halo and disk subsystems.
ApJ, 293:424–444, June 1985.
172

[215] R. Zinn.
The Globular Cluster System of the Galaxy. IV. The Halo and Disk Subsystems: Erratum.
ApJ, 304:579, May 1986.
172